JAIST
JAPAN
ADVANCED INSTITUTE OF
SCIENCE AND TECHNOLOGY
1990

Mechanics of Wet Adhesion on Patterned Soft Surface, and Application to Development of Soft Robotic Hand

Nguyen Van Pho

Supervisor: Associate Professor Ho Anh Van
Second supervisor: Professor Yuzuru Takamura
Minor research supervisor: Professor Hiroshi Mizuta
School of Materials Science
Japan Advanced Institute of Science and Technology

This dissertation is submitted on June, 2020 for the degree of Doctor of Philosophy

I would like to dedicate this thesis to **my wife, my 5- month fetus** and **my loving family** who are always side by side with my life.

Abstract

Many animals and insects can firmly stick to their surrounding environments thanks to the adhesion mechanisms generated from their bodies. The wet adhesion principle of a tree frog's sole toe with a tree is among such examples. Herein, the sole toe of the tree frog has a microstructure in the contact interface comprising from a vast number of cells interspaced by a channel system. When contacting with surrounding environments, fluid inside the grooves is ejected to produce the wet adhesion, helping this animal to secure the substrate. Wet interfaces can facilitate the soft robotic fingers to archive an effect grasping thanks to increment of the adhesion interactions with the gripped object. Hence, the wet adhesion mechanism of the tree frog toe hinted us to develop the soft robotic hands for grasping the soft-fragile objects in wet environments. Thus, my thesis illustrates a mechanical approach understand the significant role of morphological design on rising the wet adhesion for secure grasping by the soft pads attached on the robotic finger's tips. To answer the given question we firstly constructed a model of contact mechanics for the wet interface between the soft pad and its surrounding substrates. Then, two conditions of these such pads were carried out in comparisons between: a pad with a normal surface (n-pad), and a pad with a micropatterned surface (m-pad). The latter was designed and estimated inspired by the wet adhesion principle between the surface of the tree frog's sole toes and their environments. In this analytical model, we proposed a method to investigate the contact force for two geometries of the substrates having: flat and curve contact interfaces.

For the flat contact interface, the adhesion and contact forces between the n- and m-pads with their substrate were estimated for both normal and tangential directions. These pads were cast from silicon rubbers. Additionally, a square-patterned mold, as the m-pad mold, comprising from 3600 85 μm$\times$85 μm cells interspaced by a channel network with 15 μm wide and 15 μm deep was fabricated from the electron beam lithography (EBL) technology. The obtained results of the normal and tangential contact forces for the m-pad and the n-pad were verified through the measurements in wet conditions. Validated results illustrated a good agreement with those of the estimation, revealing that the micropatterned morphology can enhance the contact force for the m-pad by two-fold in case the normal and 1.2- to 1.4-fold in case the tangential force.

Soft interfaces may change shape to adapt curved environments, thus, we proposed a method for evaluation of the adhesive ability of a soft curved interface with a specific micropattern in two cases: a concave, and a convex contact interfaces. This model was developed from the contact mechanics with adhesion in the flat contact interface. Herein, the adhesion force was focused on the normal direction in different contact scenarios. In addition, the micropatterned pad used in this analysis has 3600 cells each $85\,\mu$m$\times 85\,\mu$m separated by grooves $15\,\mu$m wide$\times 44\,\mu$m deep. This micropattern soft pad is able to change its form into a concave or a convex surface. We estimated the normal contact force in detachment and attachment phases between the micropattern soft pad and a substrate. This micropattern pad was compared with a similar pad without a micropattern for their adhesion ability at the interface between the pad and the substrate. Obtained results, have good agreement with the estimations, demonstrated the micro-patterned pad enhanced contact force approximately $1 \div 2$ times than that the normal surface.

Based on the results obtained from the model of the contact mechanics with adhesion, we proposed applications of the soft robotic hands. The first of them is a project of a manipulating robot in automatically attaching and detaching a contact lens from a 'human eye'. A contact lens presented a hemispherical thin shell was grasped by the soft fingers in three different environments: inside/outside the preservative liquid and as the contact lens stuck a hemispherical substrate mimicking a human eye. The experimental and estimated results were compared for two kinds of the finger's tips surfaces: normal and micropattern. The tested results illustrated a good contract with the calculation as the m-pad reduced the preload and deformation of the thin hemispherical shell 1.1-2 times lower than that of the n-pad. The next application is a soft robotic hand approaches to grasp and then release a food sample in wet condition. We showcased this scenario with a small block of fresh tofu $19.6\,$mm$\times 19.6\,$mm$\times 15\,$mm which is soft, fragile object that was grasped by a soft robotic hand including two symmetrical pressurized fingers which their tips deposited with two types of soft pads: a n- or m-pads. The micro-machined pattern comprises of 14400 square cells same dimensions as the previous m-pad, whereas each groove has its cross section 15μm in width and $44\,\mu$m in depth. Our estimation of the grasped force for both types of soft pads were conducted, then verified by actual application in griping the tofu block. Both estimated and experimental results reveal that the micropattern pad decreased the preload and deformation of the tofu block's surface $2.2\,$times lower than that of the flat one, for stable grasping of the tofu. The showcase in my thesis confirmed the potential of micro patterns grasping soft-fragile objects in wet environments without complicated control strategy, promising wider applications for robot in medical, human, service or food industry.

Key words: inspire tree frog's toe, wet adhesion, micropattern surface, grasping/manipulating soft objects, and soft robotic hands.

Declaration

This dissertation is the result of my own work and includes nothing which is the outcome of work done in collaboration. It is not substantially the same as any that I have submitted, or am concurrently submitting, for a degree or diploma or other qualification at the Japan Advanced Institute of Science and Technology or any other University or similar institution. I further state that no substantial part of my dissertation has already been submitted, or is being concurrently submitted, for any such degree, diploma or other qualification at the Japan Advanced Institute of Science and Technology or any other University or similar institution.

Nguyen Van Pho
2020

Acknowledgements

I have spent nearly three memorable years in pursuing the Ph.D. course at Materials Science School of JAIST with an interesting research story. Although this time is much challenging, it constitutes a wonderful part for my life. The significant contributions of this thesis to the literature remind that this study cannot be completed without the support of many people.

It was an unforgettable moment in 2017-June when my supervisor, Associate Professor Ho Anh Van, adopted me to become a first Ph.D student in Soft Haptics lab where I received much intensive supervisions from him. After arriving JAIST, he took me to introduce all of laboratories and fabrication areas, which gradually formed my significant research networks. During 3 years, with in-depth knowledge in Soft Robotics field he gave me a lot of valuable advice through discussions or seminars that fosters me to closely approach my research problem right the starting point. Thanks to his constructive suggestions I can overcome many big obstacles in research and stimulated my ambition in exploring novel ideas. Not only took care in my study Prof. Van, with all enormous enthusiasm, but also always encouraged me to improve my life through taking part in social activities, forums and conferences or doing oversea research in France. Inspired by working styles and learned a lot of useful research experiences from him gradually helps me undertake academic work confidently. Those such favours illustrate that *"how great his important role in my academic career is!"*. Thus, first of all I would like to sincerely thank Prof. Ho Anh Van for his long-term enthusiasm support.

To complete this research story I also acquired many useful suggestions from my other supervisors who are experts in my field. I am profoundly grateful to Associate Professor Fumihiko Asano-my second supervisor during 2017-2019, Professor Yuzuru Takamura-my second supervisor during 2019-2020, Professor Hiroshi Mizuta-my minor research advisor and Professor Christian Duriez-my direct supervisor of minor research in Inria, Lille, France. Additionally I would like to express sincere thanks to Professor Shinichi Hirai, Soft Robotics lab-Ritsumeikan university, for his value comments at the meetings of the international conferences. As well, I would like to thank the professors in my committee Professor Yuzuru Takamura, Professor Hiroshi Mizuta, Professor Mikio Koyano, and Professor Shinichi Hirai who spent long time for reading my thesis and pointed out my

limited points. Through the in-depth discussions with the them my thesis was gradually improved in several aspects that can enhance the impact of my research in future.

As a first Ph.D student in a robotics lab with the research content relating to many fields such as: mechanics, mechanical, robotics, materials and physics, it was too difficult for me to solve my problems in 3 years. To be honest, I had good chances to co-work with a large network of excellent scientists who enthusiastically supported me in research. Herein, I would like to thank Ph.D Huynh Van Ngoc (Mizuta's lab), Assistant Professor Phan Trong Tue (Takamura's lab), my co-authors, and Manoharan sensei (Mizuta's lab) who gave me valuable comments about dry adhesion and initially introduced me to enter JAIST Nano Tech Center. Also I sincerely thank Mr. Nguyen Dai Duong (Suzuki's lab) as well as Ph.D Ahmed Hammam (Mizuta's lab) for training me the photolythography machine and many other equip in the clean room. I acknowledge Associate Professor Yuki Nagao, Associate Professor Masashi Akabori and Mr. Notoya Osamu for respectively training me machines: laser scan microscope, electron beam lithography (EBL) and scanning electron microscopy (SEM). In additional I want to acknowledge the colleagues in Takamura's lab: Ph.D Nguyen Thanh Tung, Ms. Summamal Charernchai and Ph.D Hirose Daisuke who support me necessary chemicals for my fabrications. Furthermore, I want to thank my colleagues in Ho's lab for their supports in setup experiments.

I honestly acknowledge Ph.D Le Hoai Phuong, Associate Professor Pham Huy Hoang and Professor Bui Trong Hieu (Ho Chi Minh University of Technology) who strongly encouraged me in pursuing Ph.D and their enthusiastic recommendations to Prof. Ho Anh Van. Finally, I sincerely thank Assistant Professor Ito Asae (Yamaguchi's lab), my tutor, Ph.D Hoang Khanh Hung and Vietnamese Community at JAIST for supporting me in many aspects of my life.

Contents

List of Figures

List of Tables

Nomenclature

η	Viscosity coefficient (Pas)
γ	Surface tension (N/m)
$\hat{x}, \hat{z}$	Unit vectors in x and z directions
κ, κ_1	Bending stiffness (Nm^{-1}) of shell
μ, F_f	Coefficient and contact friction force (N) of shell-substrate
ρ_l, C	Mass density of the liquid (kgm^{-3}), drag coefficient
θ_i	Contact angles (rad), $i = 1, 2, 3$
Υ	State (entity) Υ for contact shell-substrate
Υ^*	State (entity) Υ for contact pad-shell (or pad-contact lens)
φ_0, φ	Bending angle (rad) at contact centers w/o and with p
a	Cell edge size (μm)
$a^{c(v)}$	States or entities a for the concave and convex pads, respectively
A_d	Cross section area of hemispherical shell (m^2)
d	Depth of groove (μm)
E, ν	Young's modulus (MPa), Poisson's ratio of shell
F^*_{wm}, F^*_{wn}	Wet adhesion force of m-pad and n-pad with shell (N)
F^c	Denoting force of the pads with concave surface
F^v	Denoting force of the pads with convex surface
F_b	Bouyancy force from the liquid for lifting the shell (N)

F_{ca} Capillary force (N)

F_{cm} Contact force of the micropattern pad (N)

F_{cn} Contact force of the normal pad (N)

F_d Drag force from the fluid to resist the shell's movement (N)

F_{gv} Viscosity force inside groove

F_g Grasp force for holding and lifting the shell (N)

$F_{i,n}, F_{i,t}$ Denoting force F_i in normal and tangential directions

F_{Lm} Laplace force of the m-pad (N)

F_L Laplace force (N)

F_p Peeling force (N)

F_r Resistance force acting on the shell (N)

F_{st} Surface tension force (N)

F_{vg} Viscosity friction force imposing on the groove side wall (N)

F_v Viscosity force (N)

F_{wm} Wet adhesion force of the m-pad (N)

F_{wn} Wet adhesion force of the n-pad (N)

F_w Wet adhesion force (N)

G Gravity force $G = mg$ (N)

h Interface gap between shell and substrate (μm)

h_p Peak interface gap (μm)

k Reduction coefficient of contact area shell-substrate

L The pad thickness (mm)

l_t The height level of liquid inside groove at time t (μm)

L_p The pad edge size (mm) (N)

m, g Mass of the shell (kg) and gravitational acceleration (ms^{-2})

$m-pad$ Pad with micropattern, and common name of m-pad-c and m-pad-v

$m-pad-c$ Micropattern pad has concave contact interface

$m-pad-v$ Micropattern pad has convex contact interface

N Number of cells

$n-pad$ Pad without any pattern, and common name of n-pad-c and n-pad-v

$n-pad-c$ Normal pad has concave contact interface

$n-pad-v$ Normal pad has convex contact interface

P Preload (N)

p Uniform applied preload (Pa), $p > 0$ pressing and $p < 0$ pulling the shell (or contact lens)

P_L Laplace pressure (Pa)

P_c Laplace pressure of cell(Pa)

P_g Laplace pressure inside groove (Pa)

R_l, R_m Latitude and mediator radii of shell initial state (m)

R_s Radius of the substrate (m)

R_1 Outside radius of capillary bridge (μm)

r_1 Outside and radius of groove capillary bridge (μm)

R_2 Inside radius of capillary bridge (μm)

r_2 Inside radius of groove capillary bridge (μm)

R_{lp}, R_{mp} Latitude and mediator radii of shell under applied p (m)

r_n Ratio of wet adhesion force $r_n = F^*_{wm}/F^*_{wn}$

r_{p1}, r_{p2} Reduction ratios of p between m-pad and n-pad in grasping cases: shell outside liquid and shell contacting substrate

r_{wc} Wet radius of cell (μm)

r_{wg} Wet radius of groove (μm)

r_w Wet radius (μm)

t Thickness of hemispherical shell (m)

t_l Thickness of fluid film (μm)

V Submerged volume of the shell inside the liquid (m^3)

v_x Pad velocities in x direction (mm/s)

v_z Pad velocities in z direction (mm/s)

w Width of groove (μm)

CHAPTER 1

INTRODUCTION

1.1 Traditional Robot

Under the rapid development of technology, robots gradually help human in enhancing labour productivity or handling tasks in dangerous environments thanks to it autonomous working ability [1–4]. Indeed, as shown in Figure 1.1(a), an underwater robot named Jaguar, which has a robotic arm put on an ocean vehicle, can work under deep sea or riverbed. In industry, many robots without taking up rest can create same products in production lines of factories such as: mechanical manufacturing, textile and garment, food productions. For example, an assembly robot co-works with a worker or other robots (welding robots, hangers) for making a complete car in Audi production line (Fig. 1.1(b)). In human daily life, the other robots work as servers or housemaids in cleaning tall buildings or rooms, shipping goods (Fig. 1.1(c)). And a vast number of applications in many aspects in figure 1.1(d-f) such as humanoid robot for interacting with human [5, 6], educational robots for teaching and training [7], drone for exploring space [8], surgery [9] and so on that have the present of these robots one can discuss outside this study.

The bodies of the aforementioned robots have been designed using rigid structure which are almost made from metals, strong plastics or rigid materials. This is appropriate with the adaptation of stability and durability in industrial environments. In other words, these robots highlights benefits for handling solid or stable objects; whereas, for this reason, it may not be friendly to interact with soft-fragile objects.

Demands of manipulating food products, fruits, human care or medical objects by automatic systems have been emergent recently. Such scenarios typically feature soft and fragile properties that themselves are easy to deform under being exerted by external loads. In addition, their surrounding environments always require materials during interacting.

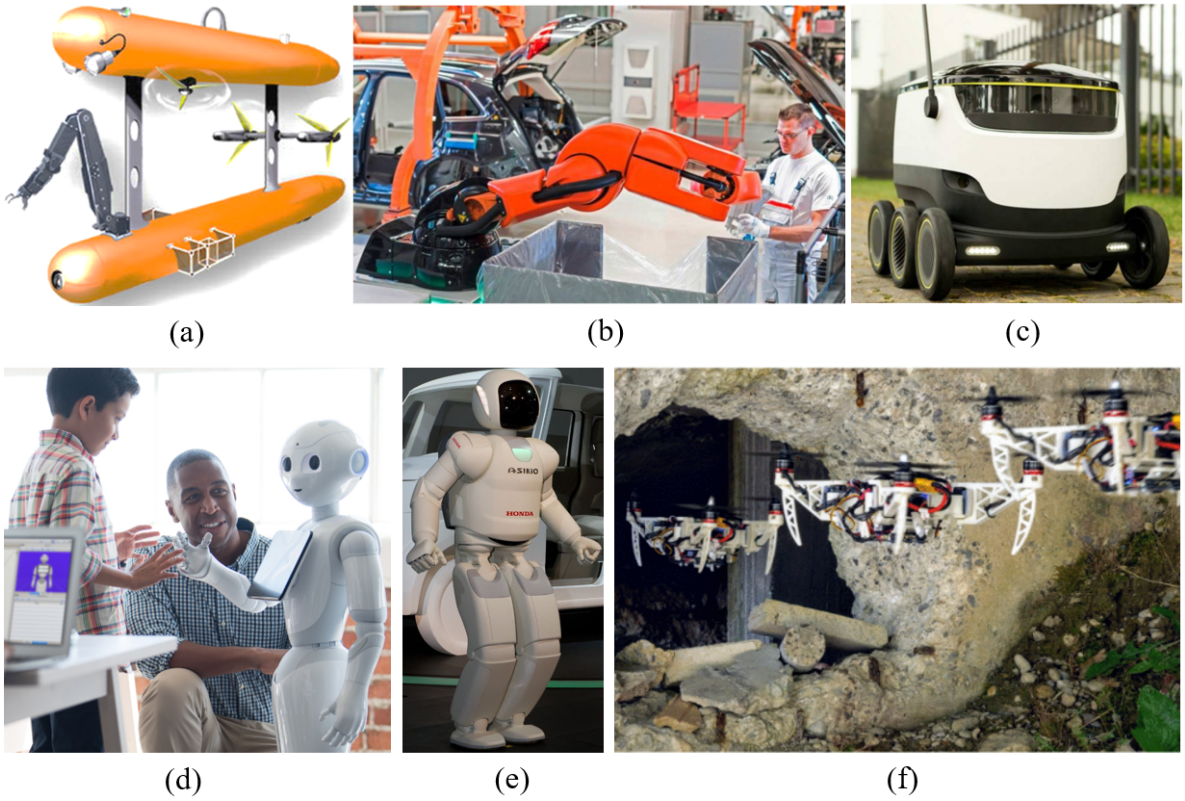

Figure 1.1: Several familiar examples of robotic application in industry and human daily life. a) Underwater robot manipulating in ocean or river [1], b) and c) assembly robot working at Audi's car production line and delivery robot for automatically shipping goods, those are found in [10]. d) and e) humanoid robots Pepper [11] and Asimo [12]. f) A drone for investigating space [13].

1.2 Soft Robotics

In order to solve the given problems it is necessary to change the operation principles or materials in designs of robots. That led to forming research on soft robotics, which is defined as a novel field of the robotics that uses highly compliant or soft materials as much as possible for constructing robot's bodies, mostly by mimicking living mechanisms [14–17]. These robots are inherently and physically soft and deformable, resulting in new functions that was not able to obtain in conventional rigid robots [18]. Thanks to soft-deformable ability of the body, the soft robots can endure large deformation in interaction with their surrounding environments, which may eliminate the risk of damage.

1.2.1 Morphological Design and Control

To design the soft robots one considers typically ideas started from mimicking principles of living organisms in nature (Fig. 1.2). In fact, it is nearly impossible to directly embed those mechanisms into an actual robot. Hence, it is necessary to convert selected mechanisms into

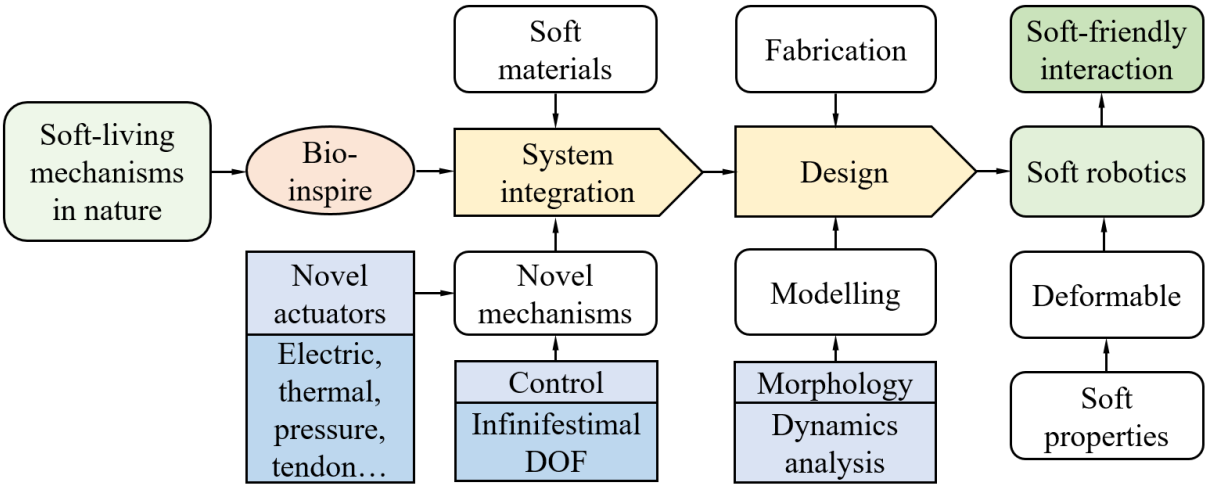

Figure 1.2: Step-by-step schema of soft robotics introduction.

those corresponding with the soft robots. These works include systematically synthesizing soft materials and novel mechanisms relating to the ways of control novel actuators. Afterward, this step provides necessary data for carrying out modelling, design and fabrication of the soft robots. The main components in Figure 1.2 can be stated in details as followed:

- *Materials:* To mimic the living mechanisms with minimizing the force acting on surrounding environments, the selected materials require the elastic and visco-elastic properties [16, 19, 20]. Such scenarios, the materials have low-modulus to adapt with deformation. Majidi [21] classified the range of soft and hard materials based on their Young modulus, in which the soft materials are recognized in $10^2 \div 10^6$ Pa. Currently, soft polymers and elastomers-like silicon rubber [22], and smart materials such as shape memory alloys (SMA) [23] and liquid crystal elastomers (LCEs) are of the most popular options for making the soft body [24].

- *Actuators*: To create motions and interactions with environment, soft robot's body needs a system of actuators. This system has to be compatible with the mentioned materials and compliant with the robot's surrounding environment. There are several ways of appropriate control that are utilized in the actuators. One first example is using dielectric elastomer actuators (DEAs) to vary the robot's morphology thanks to high-voltage electric field. This mechanism generates strong forces and obtains a rapid actuation rate ($10\,\text{ms} \div 1\,\text{s}$) [25]. However, according to Diaham [26], using DEAs usually appears leakage currents that may lead to electrical breakdowns, and needs pre-stretch for achieving a large deformation. Thermal actuator is typically shown in using shape memory polymers (SMPs) as the smart and re-configurable materials. When rising temperature, such kind of materials can revert to their initial shapes, thanks to their memory abilities. Applying these materials into the

corresponding actuators can reach the strains up to maximum 1000 [27], and perform energy density in a wide range $< 50\,kJm^3 \div 2\,MJm^3$. Pneumatic artificial muscles is also one of the most popular way to control soft robots. This method is based on alternating the pressure inside a Pneunet structure can shrink and extend through the signals of the external force like pneumatic or tendon [28, 29]. To control such muscles, one often utilizes proportional integral derivative (PID) controller as a primary algorithm [30].

- *Modelling:* Since the body of the soft robot comprises of the soft actuators and flexible materials, their behaviours during operation normally presents continuum states [18]. To modelling these structures, methods usually used are infinite degree of freedoms (DOF). Among them, using Finite Element Method (FEM) shows the most effective ways to solve the given problems. A vast of software is appropriate with the modelling and simulation of the soft robot such as: Comsol Multiphysics, Ansys, Abaqus. However, those may be much expensive and difficult for adapting the variation of diverse applications in this robotics field. Currently, stimulation using open source codes program is gradually developed by the community researchers around the world. One of those example is SOFA Framework (Simulation Open Framework Architecture) [31] which is utilized to model application in medical fields. This framework is useful for many simulating applications of the soft robotics such as: haptics, locomotion, manipulation, surgery and so on [32–34].

- *Design:* Designing the soft robots currently is carried out in the 3D computer aided design (CAD) softwares like Autocad, Solidworks, Autodesk Inventor and Catia. Besides soft and flexible characteristics, the design of the robot body also has to satisfy the durability and rigidity requirements during operations. Additionally, the outcomes of this process need objective to friendly interaction with their surrounding environments, for instance: human, medical fields, food.

- *Fabrication:* Nowadays, progress of making soft robotics has been conveniently performing, thanks to combining digital design and fabrication machines [18]. In fact, the manufacturing methods in [35], consisting of 3D printing with various materials [36], soft lithography [37] and shape deposition manufacturing (SDM) [38] created many prolific structures of soft robot through their rapid and adaptable abilities. Those techniques are integrated for generating other ways to stand for a range of applications in soft robot fields.

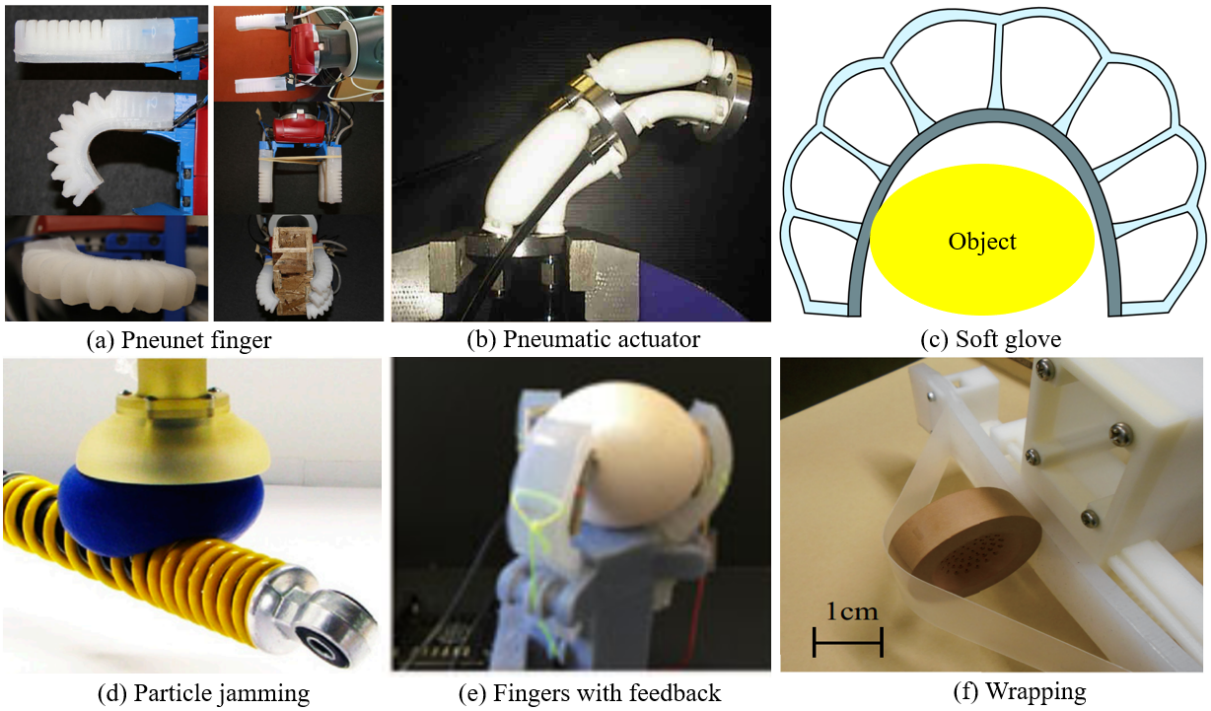

(a) Pneunet finger (b) Pneumatic actuator (c) Soft glove

(d) Particle jamming (e) Fingers with feedback (f) Wrapping

Figure 1.3: Applications of soft robotics in manipulation. Grasping objects by Pneunet finger a) [39], pneumatic actuator b) [40] and soft glove c) [41]. d) Gripping large object by a particle jamming [42]. Others grippers with novel mechanisms: soft fingers with contact feedback e) [43] and soft wrapping f) [44].

1.2.2 Applications

Although has been explored recently, soft robotics makes enormous contributions through a huge range of applications. It can be addressed at five major fields: manipulation, soft sensor, locomotion, medical and wearable devices and soft cyborgs.

1.2.2.1 Manipulation

Handling objects plays the canonical role in soft robotics [45]. Soft structures, which inherit the characteristics from living mechanisms, help traditional robots in overcoming the problems of gripping and manipulating complex objects. This is due to the compliant ability of soft bodies that allows them to easily approach various objects in the very simple ways (Fig. 1.3). Most popular example are the gripper designed with Pneunet fingers [39, 46], pneumatic actuator [40] and soft glove [41] as shown in Fig. 1.3(a-c). These can stably manipulate many complex objects, thanks to the flexibility in the finger's morphology these grippers advantages to adapt with various types of the objects. Universal jamming in Fig. 1.3(d) can replace multi-finger grippers to pick up and hold unfamiliar objects by changing their own shape. When contacting an object, sucking vacuum lets the jamming reduce itself volume and increase the density of particles inside. That leads to generating a grasp force in the jamming surface to keep the object. And many novel

grippers were proposed by Ho such as using principle of tendon [43] and wrapping [44] (Fig. 1.3(e-f)).

1.2.2.2 Soft Sensor

Basing on the compliance of the soft robotics, researchers fabricated many applications in sensor as shown in Fig. 1.4. Charbel [47] designed a soft pneumatic sensor for the interfaces between human and machine. This sensor can enhance the generic and interactive abilities during interactions. Authors in [48] fabricated sensor with high sensitive capacity by combination of fabric and microporous dielectric structure. A soft device is implanted to the the heart to tracking the failing heart as demonstrated in [49]. In studying friendly interaction with human and objects, Van and his colleagues illustrates many soft sensors for detecting touch [50–52].

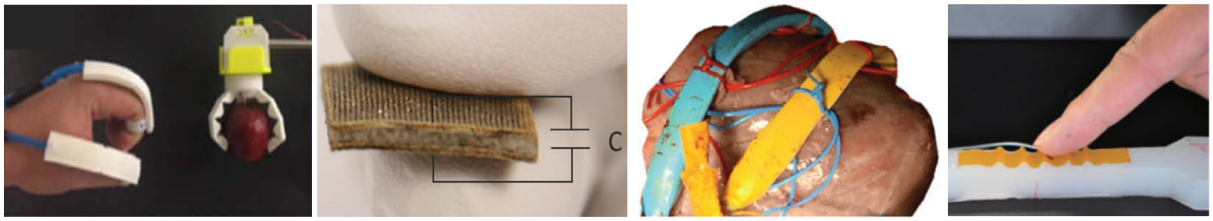

(a) Soft pneumatic sensing (b) Soft pressure sensor (c) Detecting failing heart (d) Wrinkle sensor

Figure 1.4: Applications of soft robotics in fabrication sensors. Grasping objects by Pneunet finger a) Creating sensitive by soft pneumatic [47]. b) Combining conductive fabric and dielectric layer comprising from microporus structure [48]. c) Tracking heart by soft robotic sensor embedded on it surface [49]. d) Detecting touch and force through wrinkles inspired by human skin [51].

1.2.2.3 Locomotion

Mimicking animal in locomotion for designing soft robots has been explored recently. There are abundant living mechanisms [53] that inspired the design of mobile robots introduced in [54]. For example, the locomotion robots can crawl thanks to the principles: two anchor [55] (Fig. 1.5(a)) or peristalsis [56]. Some soft legged robots have motions such as: hopping, running and walking with hexapod runner as an typical example introduced in [57]. Jumping gait is applied in soft mobile robot [58] as shown in Fig. 1.5(b) which can generate nine levels of stiffness. Gliding with the fixed wings [59] and flapping [60] can generate the thrust force to lift the robot up. In underwater locomotion, the soft robots usually mimic 4 swimming principles lift-power in Fig. 1.5(c), undulation [61], drag-power [62] and jet propulsion [63].

1.2.2.4 Medical and Wearable Devices

Thanks to friendly interactions with the objects, the soft robotics can avoid the poor outcome during operation. This characteristic is useful for applying to medical and wearable applications. Roche *et al* [64] attempted to make artificial heart from soft materials (Fig. 1.5(d)). Additionally, the applications of soft robotics are shown in wearable devices such as wearable keyboard [65](Fig. 1.5(e)) or ankle-foot rehabilitation [66].

1.2.2.5 Soft Cyborgs

Researchers has started to explore integrating the soft robotics with living materials. For instance, authors in [67] present the living materials utilized in fabricating cardiac fibers. Also, a microbial fuel cell can achieve strong artificial muscles for autonomous robots, thanks to digesting organic entities and creating electricity [68]. In [69], cardiomyocytes was utilized to power a soft robot mimicked swimming mechanism of jellyfish (Fig. 1.5(f)).

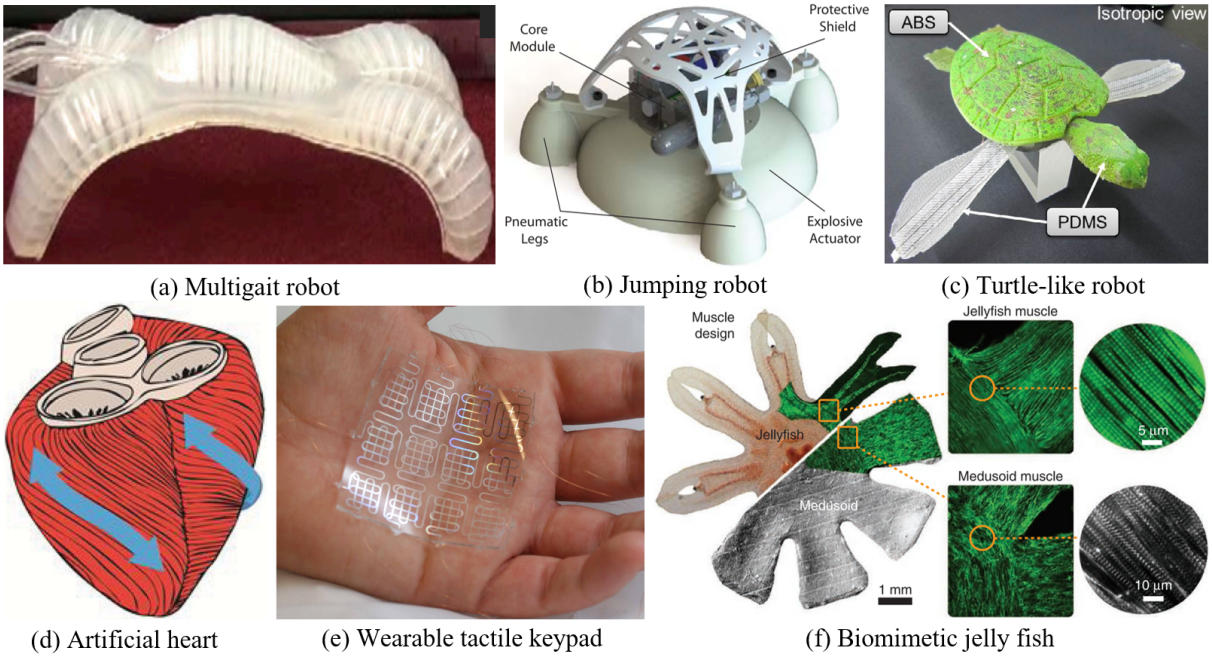

(a) Multigait robot (b) Jumping robot (c) Turtle-like robot

(d) Artificial heart (e) Wearable tactile keypad (f) Biomimetic jelly fish

Figure 1.5: Applications of soft robotics in locomotion, medical and wearable devices, and soft cyborgs. a) Soft mobile robot is actuated by pneunet structure [55]. b) Jumping robot which has various levels of stiffness [58]. c) A soft underwater locomotion robot inspires by a turtle [70]. d) Modelling and making an artificial heart by soft materials [64]. e) The thin sensitive keypad made by embedding a film of silicone rubber with conductive liquid inside micron grooves [65]. f) A jelly fish-like cybot which built from dissociated rat tissue and silicone polymer [69].

1.3 Soft Robotics in Grasping Soft-Fragile Objects

1.3.1 Research Question

Benefiting the interactions of the soft-bodies, manipulating soft-fragile objects becomes one of the most popular contributions in soft robotics shown in figure 1.6(a). In order to adapt various kinds of object, designing a universal robotic hand has to face with the challenge of broad ranges in shape, size, and stiffness of the handled articles. Particularly, while the features of rigid parts in industry are predetermined, objects in humans' daily life (like fruits and food) or in medical field (such as soft tissues or tools) exist in wet environments (mucus, blood, water and chemical liquids). That increases difficulties for soft robotic hands toward stable handling of those objects. One example of such cases is designing an autonomous gripper for helping the disable or patients to inserting and removing a contact lens from their eyes as shown in figure 1.6(c). Lifting off a tofu block from its container tray and subsequently positioning alternative places such as a lunch box in food production lines by a robotic hand/gripper is a similar application in Fig. 1.6(c). The contact lens and tofu block in this situation are soft-fragile with their surfaces are extremely slippery in liquid environments. However, because of different characteristics of materials, the contact lens and tofu themselves exhibit different behaviors during absorbing external forces. Herein, the contact lens is made from hydro gel having elasticity [71, 72]; whereas, the tofu has characteristics of rheology [73, 74]. In any situation, designing the corresponding soft robotic hands requires avoiding the risk of unexpected results during operations due to the grasped objects are soft and fragile, which are easily deformable and breakdown. In other words, the principle and structure of these soft robots have to exert a grasp force which is minimum to mitigate deformation and the slippage on the objects' surfaces. Thus, our research aims to *investigating efficient grasp mechanisms to the development of soft robot hands in manipulation applications* as shown in Fig. 1.6(b).

1.3.2 Attachments Mechanisms in Robotic

Locking surfaces by a soft robotic hand mimicking the living organisms has been explored for years. A vast number of studies discovered efficient mechanisms for different purposes of attachment that were based on imitation of biological attachment devices. The evolution in nature induces diverse skin of animals' body such as fingers or toes. Apical ridges on gecko's sole foot or spider foot hair in Fig. 1.7(a-b) can strengthen their dry stick to the contact interfaces in surrounding environment thanks to Van der Waals force exerted by atoms interactions [77]. Also, several primates promote the climbing ability [78] through the enhancement of attachment force with rough surfaces due to the asperities on their volar surfaces. Other biological principles can be found in [79] consisting of

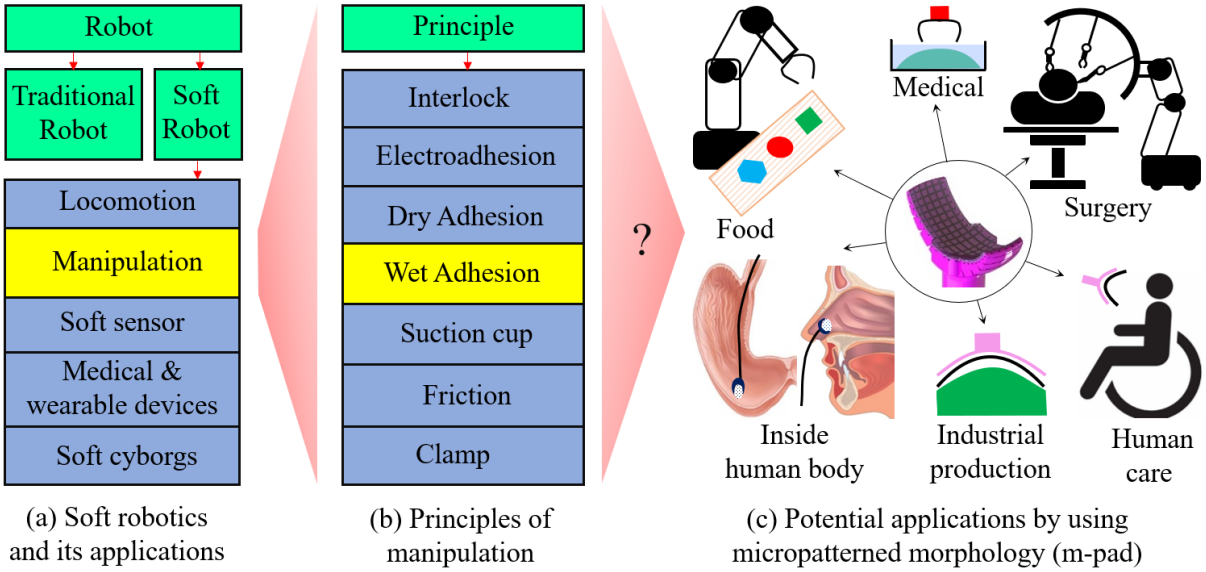

(a) Soft robotics and its applications

(b) Principles of manipulation

(c) Potential applications by using micropatterned morphology (m-pad)

Figure 1.6: Our research objectives. a) Contributions of soft robot in robotic field. b) Popular principles are utilized to manipulation applications. c) Potential applications of the soft robotics hand in actually gripping soft-fragile objects: food like tofu [75] and sushi, lunchbox, fruit in the production lines or restaurants, medical object such as contact lens [76], surgery devices of human soft tissues, human care, fragile products in industry, and objects inside human body.

electrostatic, interlocking, van der Waals, wet adhesion, frictional force and so on as shown in Fig. 1.6(b). Profitable attachment in anatomic characteristics has been imitated in roboticists to generate novel principles for various purposes. For instance, a patterned pad mimicked gecko foot [80] is utilized to facilitate a Stickybot for moving on walls. It is akin to amphibians' toes, the adhesive pads in [80] include a micropatterned morphology and secrete film. This design can strengthen sticky force between those pads and their corresponding environments. Although the biological adhesion was incorporated with the locomotion robots such as climbing, few adhesive constructions were applied to design of manipulation. Currently, handling objects is carried out by robotic hands or grippers through compressing forces to enlarge frictional force at corresponding contact positions. Traditional gripping approaches, nevertheless, are universally inappropriate to adapting objects having low-friction or wet surfaces. In this situation, applying adhesion can be applicable strategy to surmount such obstacle.

Pneumatic equipment affixed to robotic end-effectors [81] or suction cups embedded in and octopus-like robot [82] were employed for suction to or disengagement from various kinds of objects. However, they are unprofitable to grasping objects with coarse or hollow surfaces as pressure leakage. Despite benefiting in gripping large or curved objects [83], gecko-like pads are adaptable to dry couple surfaces. Fabricating a soft gripper actuated by a dielectric elastomer can produce strong electroadhesion between the contact interfaces of the gripper's pads and objects, achieving efficient grasp [84]. Authors in [85] demonstrate integrating the beneficial characteristics of electrostatic adhesives with dry adhesives to

enhance stick force on various roughness surfaces. However, this work needs an extremely high voltage (around 3.5 kV) to controlling its manipulation processes. That may induce bad influences for the handled objects during operation, especially in case interacting with wet conditions such as food or medical fields as shown in Fig. 1.6(e).

The aforementioned mechanisms exhibit their prolific advantages in grasping, however, it lacks of good adaption for handling soft-fragile objects in wet or moisture environments. In this situation, the structure of robotic hands mimicking biological principles needs to satisfy three main design conditions:

- Has an efficient grasp with minimum resultant force acting on the object,
- Is safe in wet environments,
- Generates friendly interactions.

In nature, wet attachments of animals bodies such as: tree frog or grasshoppers can help them obtain firm sticks to their surrounding environment both wet and dry without requiring high grasp force exerted from the bodies. Hence, mimicking the wet adhesion mechanisms of those living organisms, which is clarified in the next section, gives a practical guideline for answering the given question.

1.3.3 Wet bio-mechanism in Robotics

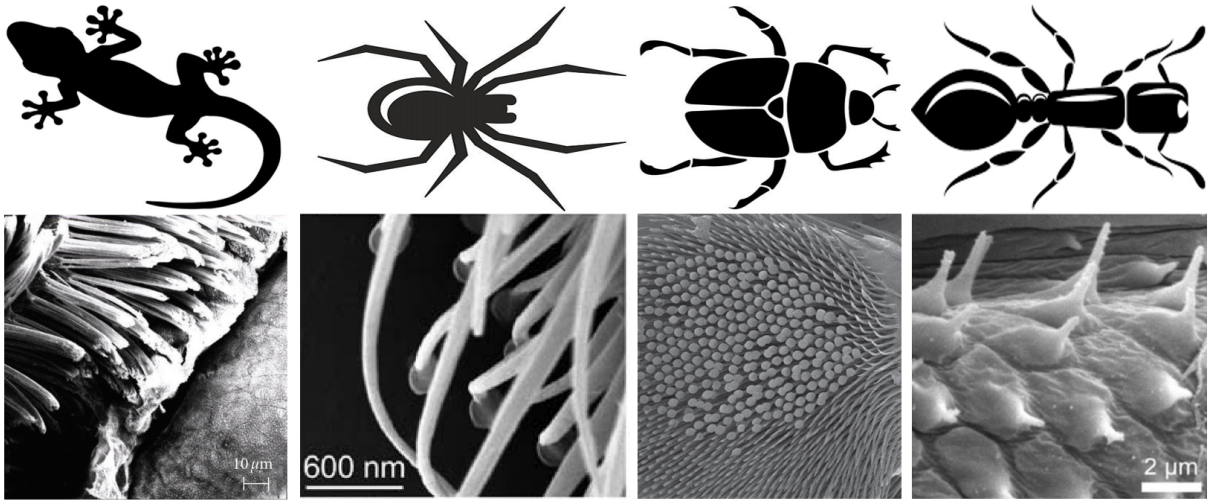

Figure 1.7: Microstructure inside animal and insects feet observed by SEM a) gecko [86], b) spider [87], c) beetle [88] and d) ant [89].

Many insects or animals such as grasshoppers [90], beetle [91], snail [92] and ant [93] have the wet adhesion principles generated by the liquid or mucus contained inside micro structures in their sole toes. When contacting with surrounding environments, the liquid

inside the micro structures of the insect feet demonstrated in Fig. 1.7(c-d) is delivered to fill the vacant space between the contact interface gaps that can enhance the sticky ability through the liquid capillary bridge. Additionally, authors in [94] present managing the ejection of fluid volume into the contact interface thanks to capillary suction in several species of stick insects and cockroaches. Snails can achieve good performance in locomotion due to varying the properties of their adhesive mucus. As sticking to a solid substrate, the adhesive liquid inside the snail's foot acts as solid material, whereas in locomotion state, this liquid behaves as a visco–elastic lubricant film [95, 96].

The sole surface of a tree frog toe pad in Fig. 1.8 comprises from a large number of polygonal blocks approximating $10\,\mu$m in diameter interspaced by a network of grooves approximating $40\,\mu$m in depth. Each of cell in Fig. 1.8(d) includes a nanoscale texture of minor cell and tiny groove in Fig. 1.8(e). When contacting to surrounding environments, the mucus inside these grooves is injected to cover the gap between two contact interfaces [97]. This principle can enhance the stick force for the toe pad during attachment in Fig. 1.9(a). Since the mucus film on the contact interface of those cells rapidly evaporates, the liquid exists mostly inside the groove system. Hence, such channels act as liquid containers for governing wet adhesion between the toe pad and corresponding environments. The toe pad structures of tree frog species are soft for interaction with the substrate, which the elastic modulus E_{tp} of the whole epidermis in low range $4 \div 61\,$kPa [98–100]. This modulus can reach up to 14000 [101] due to the structure of cytoskeleton. The mucus inside the pad grooves, which can sufficiently cover the separation gap between the contact interfaces [102], has the viscosity η=1.43 mPa and the contact angle $\theta << 10^{\circ}$ for species L.caerulea [103]. Generally, this mucus is usually considered a Newtonian property in calculation and independent from substrate adhesion characteristic [104].

Among the shown wet bio-attachments, the mechanism of tree frog is more advantageous to design of soft robotic hands, since morphology of its toe pad can generate soft characteristic to adapt with diverse substrate surfaces. Additionally, multilayers structure on its sole toe pad can enhance the frictional ability during grasping. And the ratio of the dimensions between one cell and one groove of the microstructure is much larger than other stick insects, which produces a higher stiffness in case the tree frog's pad than that of the others.

1.4 My Research Overview

1.4.1 Research Purpose

Inspired by the wet attachment principle of tree frog's toes in Fig. 1.9(a), our research aims to constructing an estimated model for evaluating grasp force in wet conditions in

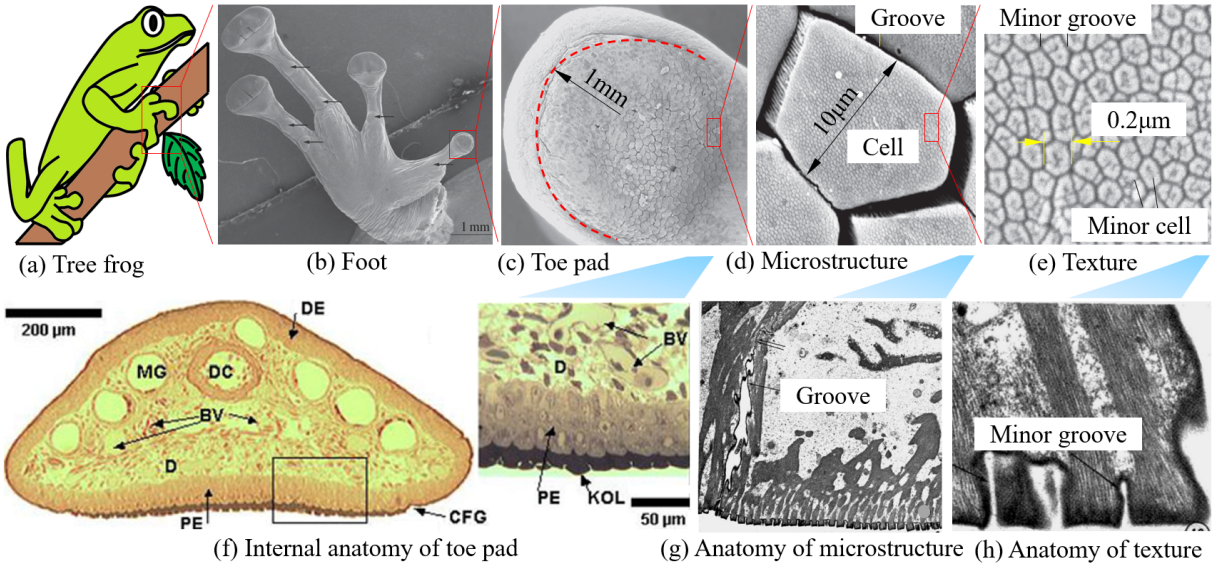

Figure 1.8: Toe pad morphology of a tree frog's toe. a) A tree frog with its feet b) are securely attaching to a tree (surrounding environment). Each foot b) includes four toe pads c) having a microstructure on the sole surface d). One cell (block) in d) consists of many minor cell e). Inside anatomy of f) the toe pad, g) the microstructure and h) the texture. In figure f), BV, CFG, D, DC, DE, KOL, MG and PE are respectively blood vessels, circum-feral groove, dermis, digital cartilage, dorsal epidermis, keratinised outer layer, mucous gland, and pad epidermis. Figures c-e) are adopted from [103]. SEM images in b), f) and g-h) are, in turn, after [98, 105, 106].

Fig. 1.9(b-c). Hence, two morphological cases of soft pad with: a micropatterned structure (m-pad) and a normal surface (n-pad) were fabricated and wiped with a thin film liquid to explore their underlying behaviors during contacting a substrate. In this scenario, the wet adhesion generated from capillary phenomenon and viscosity of the liquid film between the pad and the contact interface is similar to the secreted mucus inside the tree frog's toe pad [97, 103]. In our projects, those evaluations play a basic foundation to development of soft robotic hands that can grasp soft-fragile objects in wet conditions such as: contact lens and tofu in Fig. 1.9(d). In future, it is promising to make contributions in developing other soft robotic hand for universally manipulating various kind of objects.

1.4.2 Research Content

Our study is summarized as followed:

1. *Chapter 1*: shows the introduction of our research including: short review of traditional robot, introduction of soft robotic, overview of our research content, literature review of soft manipulation objects, and our research contributions to science and applications.

2. *Chapter 2*: presents the theoretical foundation of soft contact mechanics for wetting interface consisting of: contact mechanics models, capillary phenomenon, design pad

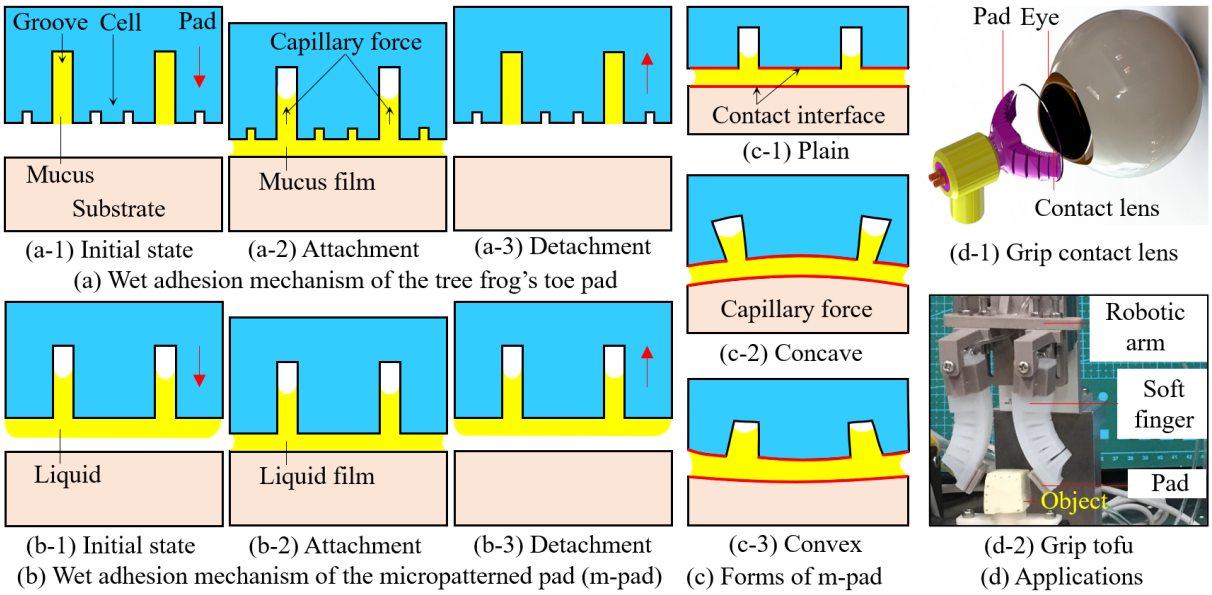

Figure 1.9: My research concept. a) Wet adhesion mechanism of the tree frog's toe pad with the substrate in three phases: a-1) initial state, a-2) attachment and a-3) detachment. b) Wet adhesion principle of the pad having micropatterned morphology (m-pad) [107, 108] in three phases: b-1) initial state, b-2) attachment and b-3) detachment. c) Wet adhesion the m-pad in b) in different forms of the contact interface: flat c-1), concave c-2) and convex c-3). In this figure, the contact interfaces shown in the red lines are the pairs of the surface in the pad and the substrate joining contact. d) Showcases of the soft robotics hand attaching micropatterned pad in actually gripping soft-fragile objects: contact lens d-1) and tofu d-2). Since our research is in the preliminary evaluation, it has not yet concerned the texture of the tree frog pad comprising from the minor cells and groove in Fig. 1.8(e) and Fig. 1.9(a). Also the contact interface of the m-pad was wiped with a thin liquid film for both cell and inside grooves. The red arrows show the moving direction of the pad; whereas, the substrate was stationary.

morphology, wet adhesion of normal surface in cases flat and curve, and mechanics of grasping with wet adhesion.

3. *Chapter 3*: proposes an analytical model for the adhesion generated in case the pad with micropatterned morphology (square pattern). Through estimated results, this chapter, the principal content of analytical model, also shows the role of the micropattern on strengthening the wet adhesion for the grasping interface.

4. *Chapter 4*: describes fabricating process of the soft robotic finger with two types of the pad: n-pad (the pad without any pattern) and m-pad (the pad has pattern structures).

5. *Chapter 5*: setups experiments using the fabricated pads in chapter 4 for validating the analytical in chapter 2-3.

6. *Chapter 6*: showcases the designs validated for the actual applications in handling contact lens and grasping tofu.

7. *Chapter 7*: gives our conclusions and discussions for the achieved works and the future plans for development of this projects.

1.4.3 Related Works

A few researches investigated the wet adhesion principle inspiring by the attachment of the tree frog's toes pad to the surrounding environment both in nature and in robotic applications. Firstly, the self-leaning mechanism to recover the mucus on the toe pad of the living tree frog was explored by Barnes and his colleagues in [109]. Authors in [110–112] provided some measurements of the grip force of the tree frog's pad to attaching the environment. The properties of the substrate encountered by those pads are concerned in prolific cases of random roughness: tree bark, leave, stone and so on as shown in [113–115]. When moving, the locomotion of tree frog usually includes three forms: walking, climbing and jumping [116]. The dynamic of alternating attachment and detachment in the toe pad is fast controlled under assuring condition of sufficient contact force [117]. Recently, Langowski and his team have given the analytical model for evaluating the wet adhesion of tree frog's toe pad in [118–120]. Although the theoretical models for evaluating the wet attachment of tree frog's toe pad were presented, such estimations were in preliminary evaluation without regarding the role of groove and micropatterned morphology.

Other researchers [121–124] explore the wet adhesion and friction enhancement of the nanoscale array mimicking the tree frog's toe, which the hexagonal pillars are made from rubber. Authors in [125] test the wet ability of micro pillar array, in attachment and climb mimicked a newt, in several cell shapes: hexagon, round, and hybrid of hexagon and round. The wet properties of hexagonal cell micropattern are experimentally evaluated in different wetting cases and the stiffness of polydimethylsiloxane (PDMS) [126]. The role of powering the wet adhesion for the micropatterned interfaces have been revealed though various testing evidences in silicon rubbers. Authors in [127] examined the wet friction force by alternating the hexagonal patterns in: shape, surface size, and depth of grooves. Herein, the wet frictional force of the m-pad is $4 \div 10$ times higher and $1 \div 2$ times lower than that of the n-pad in cases hydrophilic and hydrophobic respectively. In [128], the pad designed with micropatterned morphology enhanced with a similar increment ratio of the frictional force in case of wet contact; whereas, in dry contact, the m-pad was 1.6 times smaller than that of the n-pad. However, the analytical models for general evaluation are scarce.

In actual applications, the role of patterned morphology on strengthening the contact forces for soft fingertips illustrated in [129] through experimenting on resistance force exerted in different adhesion cases: wet and dry. However, the authors majorly focused on evaluating for large scale (millimeter) design of the pattern. Researchers in [130] improved motion ability of the climb robot by powering the wet adhesion force of an arthropods-like

pad with a square micropatterned morphology. According to [130], the testing results in case the m-pad produced increment of the adhesion roughly 4 times in normal and two folds bigger in tangential direction than that of the n-pad. Additionally, micro structure designs were applied to enhancing the efficient of intestine traction [131]. In another medical application, a surgical gripper with a biomimetic contact interface [132] can produce a powerful wet frictional force which was enough to hold soft tissues without any outcome risk. In [132], the frictional force with wet adhesion in grasp was investigated for a diverse morphology of the micropattern consisting of polygonal shapes such as: pentagon and hexagon, teeth and so on. In general, the increment ratio of the frictional force between the gripper having micropatterns and without any pattern was always higher than 1. Although concerning the wet adhesion properties in the given models, the mentioned researches [127, 128, 132] majorly concentrated on investigating for tangential direction of the wet frictional force.

The previous studies demonstrated a diverse amount of testing data to explore the role of wet adhesion of the m-pad during interaction with existence of the fluid film or mucus. In almost situations, comparing with the flat surface pad (n-pad) the pad having biomimetic morphology (m-pad) can strengthen a higher wet adhesion force in the contact both in tangential and normal direction. That provided potential results for applying to the development of soft robotic hand in manipulation like grasping. However, thoroughly investigating the analytical model for understanding the underlying physics and the significant role of micropatterned morphology in powering the wet adhesion were not completely proposed. Moreover, the micropatterned design for fabricating the actual applications in the soft robotics have just been emergent recently with a few showcases; whereas, currently, the need for autonomous grasping/manipulating soft-fragile objects becomes enormous.

1.4.4 Contributions

Motivation in solving the given problems, our study aimed to develop the novel soft robotic hand enabling grip/manipulation of the soft-fragile objects. In this scenario, the principle and morphological designs of the adhesive pads attached in the robotic fingers are inspired by the wet attachment of the tree frog's toe pad. Additionally, the role of micro pattern on enhancement of the grasp force/contact force was investigated through constructing theoretical model validated by experimental evidences. Our research makes meaningful contributions to science and tech as followed:

1. Studied the wet attachment mechanism of tree frog' toe pads for improving the adhesive ability of the pad in robotic finger.

2. Came up with a theoretical model for estimating the wet adhesion force in normal

and tangential direction for flat contact interface between the pads (m-and n-pad) and the substrate (Fig. 1.9(c-1)), which is potential for other related researchers to follow and develop their current works.

3. Developed the approximation of the wet adhesion in flat surface of of the pads (m-and n-pad) to two parallel curved contact interfaces between those pads with the curved substrates. Studying curved contact interfaces is more suitable for utilizing the actual applications of soft robotic manipulation because the object's surfaces may be not completely flat.

4. Presented a theoretical approach for gripping thin hemispherical shell in wet environment by the pad having micropatterned morphology. Our work is useful for evaluating the manipulation of thin soft objects by robotic fingertips with patterned structure in wet or moisture conditions.

5. Showed an analytical model for evaluating the grasping ability of a soft robotic finger's tip attaching micropatterned pad (m-pad) over a wet, fragile object such as a tofu block. This work is potential for extending to grasping soft-fragile objects in wet conditions by micropattern interface fixed on the fingertips.

6. Demonstrated some ways to making a soft robotic finger's tips attaching the bioinspired pad with an array of the cells and grooves in microscale.

CHAPTER 2

CONTACT MECHANICS FOR WET INTERFACES

This chapter mainly aims to investigating the mechanics of wet adhesion interaction between the pad with micopatterned morphology (m-pad) and the pad without any pattern (normal surface pad or n-pad) in contact with their substrate. Herein, the contact generally included two components wet and dry adhesion, in which the wet entity was.

2.1 Surface and Interfacial Forces

According to [133], the interfaces comprise of the region separated by a couple of phases among gas, solid, and liquid. Associating such phases forms interfaces: the solid–gas, the solid–liquid, and the liquid–gas ones. Also, we call the solid-solid interfaces for the solid behaviors. This section clarifies the surface and interfacial forces relating to the contact interfaces between the pads (m- and n-pad) and the substrate.

2.1.1 Adhesion Force

Adhesion is a physical phenomenon that between separated particles or surfaces exert an attractive energy to the others [133, 134]. The adhesion force includes four main types: dispersive, chemical, diffusive and mechanical. The magnitude of the adhesion force is equal to the total of the followed force components: electrostatic F_{els}, Van der Waal F_{vd} (in small distance), Casimir-Polder or Casimir F_{C-P} (in large distance), interlock F_{il}, capillary F_{ca} and hydrodynamics F_{hd}, and other forces [133, 135]. Hence, we can rewrite the adhesion force in Eq. (2.1):

$$\mathbf{F_a} = \mathbf{F_{els}} + \mathbf{F_{vd}} + \mathbf{F_{ca}} + \mathbf{F_{hd}} + \mathbf{F_{il}} + \vartheta\mathbf{F_o}, \tag{2.1}$$

with ϑF_o is the total of other forces. To detach the contact interfaces, the minimum external force F_{ex} has to be larger than the adhesion force F_a. Also the entities in right hand side of Eq. (2.1) are sequentially shown in the next followed sections.

2.1.2 Electrostatic Forces

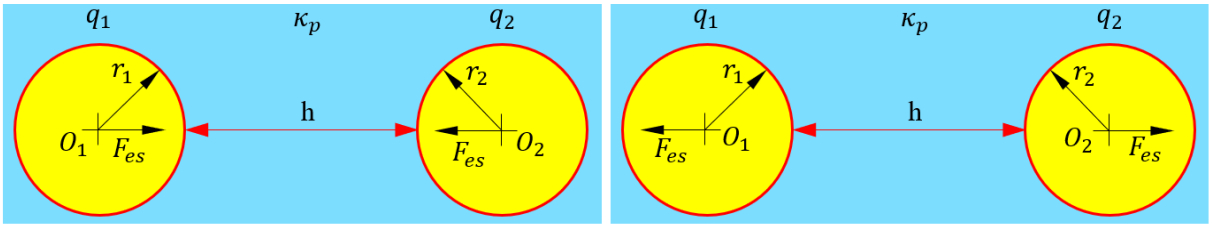

(a) Anti-polar $q_1 q_2 < 0$ (b) Uniform polar $q_1 q_2 > 0$

Figure 2.1: Electrostatic force between a couple of spherical particles in a medium permittivity κ_p. a) Two particles have the same electric charge's sign and b) different electric charge's sign.

Electrostatic force is produced on an object when the electrical charges having slow motion or stationary [136]. Depending on the polar states, the charges on the object's surface can execute attaching or releasing actions with higher strength comparing with the van der Waals force. Primarily, the electrostatic force can be calculated for all cases by using Coulomb law when the surface charges and volume of the investigating systems are determined. According to [137], we have the electrostatic force between two non-conductive spherical particles in Fig. 2.1 as followed:

$$F_{els} = \frac{1}{4\pi\kappa_0\kappa_p} \frac{q_1 q_2}{(r_1 + r_2 + h)^2} \overrightarrow{O_1 O_2}, \tag{2.2}$$

with r_1, r_2 and κ_0, κ_p are the radii of the particles, and permittivity of vacuum and medium, respectively. In Eq. (2.2), the electrostatic force performs the attachment action in case two particles are in the anti-polar charges (Fig. 2.1(a)), and reversed for the uni-polar charges being activated (Fig. 2.1(b)).

2.1.3 Van der Waals Forces

Van der Waals force which plays the primary role in the adhesion force between similar materials[138, 139] especially in dry contact interfaces, is an attractive force arise between atoms or molecules with a narrow distance (h<5 nm). Although van der Waals force is very important, it is quite weak [140] and rapidly vanishes as the distances of interacting molecules become larger. In the case without other acting force, the van der Waals contact distance is the atom gap when this force turn into repulsive rather than attractive [141]. The van der Waals force comprises of three sources of atomic interaction force: the London dispersion, Debye and the Keesom as shown in Fig. 2.2.

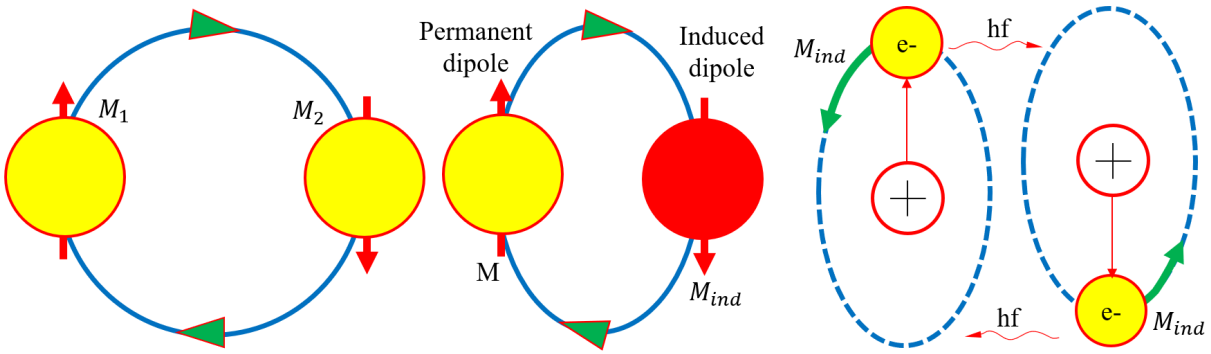

(a) Keesom interaction (b) Debye interaction (c) London interaction

Figure 2.2: Van der Waals interaction between a) two dipoles (Keemson interaction), b) a permanent and an induced dipole (Debye interaction) and c) a couple of induced dipole (London interaction).

2.1.3.1 Keesom Interaction

Keesom [142] is one component constituting van der Waals force generated by the attraction from one permanent dipoles to another, and depends on temperature parameter [143]. It can be explained by electrostatic charges produced among the interactions of molecular ions, dipoles, quadrupoles, and permanent multipoles (Fig. 2.2(a)). A couple of dipoles having free rotation usually appeals together due to the orientation of their opposite charges confronting directly. In addition, the thermal motion induces another fluctuation propelling them out of their preferential orientation. According to [144], the Keesom energy of the couple dipoles interaction from free rotational dipoles with their dipole moments $M1$ and $M2$ can be calculated in Eq. (2.3):

$$V_d = -\frac{M_1^2 M_2^2}{48(\pi\epsilon_0)^2 k_B T h^6}, \tag{2.3}$$

where k_B, T are respectively the Boltzmann constant ($k_B = 1.38064852.10^{-23}\, kgm^2/(Ks^2)$) and temperature. Those permanent dipoles aligning with the other generates a net attractive force denoted as Keesom force. This force majorly varies by the dipoles distance d and the thermal energy ($k_B T$).

2.1.3.2 Debye Interaction

Debye force [143] is the second entity of the van der Waals force that emerges from interactions between a permanent dipoles in free rotation state and a corresponding induced dipoles (Fig. 2.2(b)). Those induced dipoles arise as a permanent dipole drives the electrons of other molecule away. The permanent dipole molecule may generate a dipole for a neighbour molecule leading to reciprocal appeal. Also, this force cannot appear among atoms, and is independent to temperature variation since the free motion in

shift and rotation of the induced dipole around the molecule's polar. In case the dipoles freely rotate, the Debye interaction between the permanent dipole and the induced dipole (Helmholtz free energy) can be calculated in Eq. (2.4):

$$V_d = -\frac{M^2 M_{ind}}{16 E_f (\pi \epsilon_0)^2 h^6}, \tag{2.4}$$

where M_{int}, E_f are the induced dipole moment and electric field strength produced by the permanent dipole.

2.1.3.3 London Interaction

When the molecules have no permanent dipoles, an attractive force still arises between them, which explain how liquid condenses at low temperatures. The electron's fluctuation produces molecules dipoles changing overtime, which is not sufficient to orient themselves into alignment for forming attraction force. This force is the greatest contributor to van der Waals interaction, named as London dispersion or London interaction. London [145] showed a calculation of this force as followed:

$$V_d = -\frac{3 p_1 p_2}{32 (\pi \epsilon_0)^2 h^6} \frac{\hbar f_1 f_2}{f_1 + f_2}, \tag{2.5}$$

where p_1, p_2, h, f_1, f_2 are respectively the polarizabilities of the molecules, Plank constant $\hbar = 662607004.10^{-43}\, kgm^2/s$, and the electron's frequencies.

Hence, by totalling all items: the Keesom, the Debye, and the London dispersion interaction in Equations (2.3) to (2.5), the van der Waals interaction becomes:

$$V_{vd} = -\frac{1}{h^6}\left[\frac{M_1^2 M_2^2}{48 (\pi \epsilon_0)^2 k_B T} + \frac{M^2 M_{ind}}{16 E_f (\pi \epsilon_0)^2} + \frac{3 p_1 p_2}{32 (\pi \epsilon_0)^2} \frac{\hbar f_1 f_2}{f_1 + f_2}\right] = -\frac{C_{vd}}{h^6}. \tag{2.6}$$

Eq. (2.6) reveals that its entities on the right hand side have the same distance dependency: is inversely proportional to sixth power of the distance h ($\propto h^{-6}$). As the distance $h \leq 10$, the van der Waals force declines more rapidly with the proportion in case molecules is $\propto h^{-7}$ instead of $\propto h^{-6}$ at very smaller distances.

In soft robotics, Van der Waals force is dominantly investigated for the morphological designs inspired by the gecko's attachment [146–149] and may also contribute to tree frog's toe pad in dry attachment [103, 150]. We have two main ways for determining the van der Waals interaction between macroscopic solids: the microscopic and the macroscopic approach [151, 152].

2.1.3.4 Van der Waals Interaction-Microscopic Approach

The van der Waals energy between two macroscopic solids can be determined in case a single molecule M_1 separates a distance h from a planar surface extended from the molecules M_2 as shown in Fig. 2.3(a). Hence, the van der Waals energy is the total of the molecular interactions between M_1 and all M_2. Applying Eq. (2.6) to each molecular density ρ_{M_2} yields the van der Waals energy over the entire volume of the solid as followed:

$$V_{M_1/Plan(M_2)} = -C_{M_1M_2} \iiint_V \frac{\rho_{M_2}}{h_1^6} dV = -\frac{\pi \rho_{M_2} C_{M_1M_2}}{6h^3}. \tag{2.7}$$

In Eq. (2.7), the interaction energy between a molecule-a macroscopic body is proportional to h^{-3} which declines more slowly than that of between two molecules $\propto h^{-6}$.

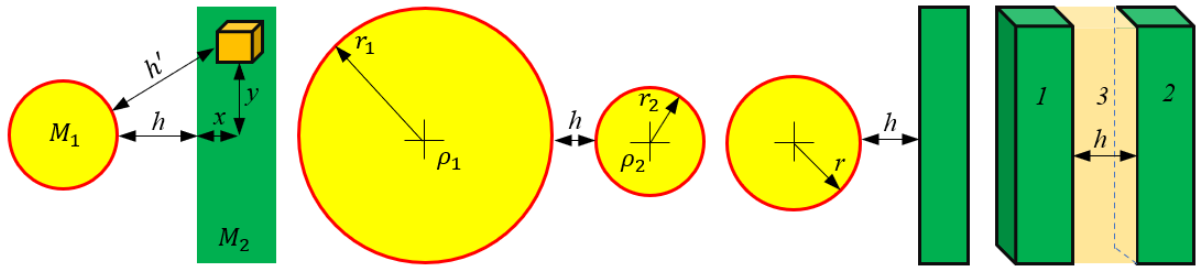

(a) Molecule M_1 and plane M_2 (b) Sphere and sphere (c) Sphere and plane (d) Plane and plane

Figure 2.3: Van der Waals interaction energy between a) a molecule M_1 and planar surface M_2, b) two sphere with radii r_1 and r_2, c) a sphere with radius r_1 and a planar surface, and d) Two parallel half-spaces with different materials of *1* and *2*.

Thus, the van der Waals energy per unit area between two infinitely extended solids: M_1, M_2 separated by a parallel gap of thickness h can be derived from Eq. (2.7):

$$w = \frac{V_{Plan(M_1)/Plan(M_2)}}{A} = -\int_0^\infty \frac{\pi \rho_{M_1} \rho_{M_2} C_{M_1M_2}}{6(h+x)^3} dx = -\frac{C_H}{6\pi h^2}. \tag{2.8}$$

In Eq. (2.8), ρ_{M_1} presents the molecular density in the solid M_1, and C_H is the Hamaker constant $C_H = \pi^2 C_{M_1M_2} \rho_{M_1} \rho_{M_2}$. As deriving the energy per unit area w in Eq. (2.8) yields the unit force in Eq. (2.9)

$$f_{vd} = -\frac{\pi^2 C_{M_1M_2} \rho_{M_1} \rho_{M_2}}{6\pi h^3}. \tag{2.9}$$

Similarly, Hamaker [153] showed methods to evaluating the van der Waals energy between solids with diverse geometries. Among such geometries, the van der Waals interaction between a couple of spheres or is one first significant case in Fig. 2.3(b). Herein,

the van der Waals interaction energy equals to:

$$V_{vd} = -\frac{C_H}{6}\left[\frac{2r_1r_2}{H^2-(r_1+r_2)^2} + \frac{2r_1r_2}{H^2-(r_1-r_2)^2} + ln\left(\frac{H^2-(r_1+r_2)^2}{H^2-(r_1-r_2)^2}\right)\right], \quad (2.10)$$

with $H = h + r_1 + r_2$. According to [154], as the electron orbitals begin to overlap which induces repelling between the molecules, the Eq. (2.10) need to be modified. Also in case the radii of the particles are much larger than then distance h ($h \gg r_1, r_2$), Eq. (2.10) is rewritten [155] as followed:

$$V_{vd} = -\frac{\pi^2 C_{M_1M_2}\rho_{M_1}\rho_{M_2}}{6h}\frac{2r_1r_2}{r_1+r_2}, \quad (2.11)$$

and we have the van der Waals force by the derivative of Eq. (2.11):

$$F_{vd} = -\frac{\pi^2 C_{M_1M_2}\rho_{M_1}\rho_{M_2}}{6h^2}\frac{2r_1r_2}{r_1+r_2}, \quad (2.12)$$

Thus, considering that $r_2 \longrightarrow \infty$, we have the energy and force of the van der Waals interaction between a sphere and a planar surface in Fig. 2.3(c) in Eq. (2.13):

$$V_{vd} = -\frac{\pi^2 C_{M_1M_2}\rho_{M_1}\rho_{M_2}r_1}{6h}, \& F_{vd} = -\frac{\pi^2 C_{M_1M_2}\rho_{M_1}\rho_{M_2}r_1}{6h^2}, \quad (2.13)$$

In actual conditions, the van der Waals interaction usually makes lower contribution because of the influence of contamination and roughness surface, which changes the contact distance h.

2.1.3.5 Van der Waals Interaction-Macroscopic Approach

The van der Waals interaction in the microscopic approach neglects the affect of neighbouring molecules. However, this assumption is not completely perfect. In fact, the actual the van der Waals interaction between two molecules varies by the appearance of a third one. Authors in [156] overcame the given question by utilizing the macroscopic theory (Lifshitz theory) that treated the solids as continuous matters with bulk characteristic, for instance, the refractive index and permittivity. The obtained results of Lifshitz theory showed a good agreement with Hamaker's works [153, 157]. However, determining the Hamaker constant is still carried out in a different approach. Herein, the Hamaker constant is influenced by the total of various frequencies. In Fig. 2.3(d), the interaction between a material *1* with material *2* across a medium *3* has the Hamaker constant as followed:

$$C_H \approx -\frac{3k_BT}{4}\left(\frac{\epsilon_1-\epsilon_3}{\epsilon_1+\epsilon_3}\right)\left(\frac{\epsilon_2-\epsilon_3}{\epsilon_2+\epsilon_3}\right) + \frac{3h}{4\pi}\int_{f_1}^{\infty}\left(\frac{\epsilon_1 if-\epsilon_3 if}{\epsilon_1 if+\epsilon_3 if}\right)\left(\frac{\epsilon_2 if-\epsilon_3 if}{\epsilon_2 if+\epsilon_3 if}\right)df. \quad (2.14)$$

Where $\epsilon_1, \epsilon_2, \epsilon_3$ are, in turn, the static dielectric permititivities at the frequency $f = 0$ of three mediums (Fig. 2.3(d)), and $\epsilon_1 if, \epsilon_2 if, \epsilon_3 if$ present respectively the mentioned permititivities at imaginary frequencies if. Also the frequency $f_1 = 2_B T/h = 3.9 \times 10^{13}$ Hz at 25$\circ$ C, which equals to a wavelength being 760 nm. And the two first entities on the right hand side of Eq. (2.14) illustrate the contributions of the Keesom and Debye energy.

Determining the Hamaker constant requires explicit dielectric parameters of three mediums. In case the frequencies begin the visible zone, the permittivity of nonconductive materials is calculated in Eq. (2.15):

$$\epsilon if = 1 + \frac{n^2 - 1}{1 + f^2/f_m^2}, \tag{2.15}$$

where n, f_m are the refractive index and the mean ionization frequency of the materials (with $f_m \approx 3.10^{15}$ Hz). Let us consider that those three materials have the same ionization frequencies, and their refractive indices be $n1, n2, n3$, an approximation of the non-retarded Hamaker constant can be shown as followed:

$$C_H = \frac{3k_B T}{4}.\frac{\epsilon_1 - \epsilon_3}{\epsilon_1 + \epsilon_3}.\frac{\epsilon_2 - \epsilon_3}{\epsilon_2 + \epsilon_3} + \frac{3\hbar f_m}{8\sqrt{2}} \frac{(n_1^2 - n_3^2)(n_2^2 - n_3^2)}{\sqrt{n_1^2 + n_3^2}\sqrt{n_2^2 + n_3^2}(\sqrt{n_1^2 + n_3^2} + \sqrt{n_2^2 + n_3^2})}. \tag{2.16}$$

The Hamaker constant in Eq. (2.16) helps one figure out attraction or repulsion through the Hamaker constant's signs (positive or negative). The Hamaker constant between similar materials is always positive, which is deduced from the Eq. (2.16) with $\epsilon_1 = \epsilon_2$ and $n_1 = n_2$. Also, for the interaction between two different medias in vacuum environment ($\epsilon_3 = n_3 = 1$), or a real gas, the van der Waals force performs attraction. In contrast, this force can revert to repulsion in the case of between different materials across a condensed phase. The van der Waals repulsion appears as medium *3* exerts a more powerful attraction to medium *1* comparing with to the medium *2* (Fig. 2.3). In additional, for a thin wetting layer spread on the solid interfaces, the van der Waals forces usually exert the repulsion for the interactions of the solid–liquid and the liquid–gas [158]. In case of the dielectric materials, Hamaker constant often values in range $10^{-21} \div 10^{-20}$ J; whereas, it is usually in the range of 10^{-19} J for the metal case.

2.1.4 Casimir Effect

The van der Waals interaction appears for two nearby atoms or molecules, it is absent in a larger distance. However, the correlated oscillations between the induced atomic dipole moments forms an attractive force between the couple of atoms. That is the Casimir-Polder force. According to [159, 160], the Casimir force generated between two plane as followed:

$$F_{CP} = -\frac{207\hbar c A_{CP}}{640\pi^2 h^4}, \tag{2.17}$$

with A_{CP} is the area generating Casimir force. From Eq. (2.17), the force F_{CP} depends on the area A_{CP} and is inversely proportional to fourth power of the distance h. Thus, at large distance h the van der Waals force F_{vd} in Eq. (2.1 is replaced by the Casimir force in Eq. (2.17).

2.1.5 DLVO Theory

The DLVO theory [161], which was proposed by the authors Boris Derjaguin and Lev Landau [158] and Evert Verwey and Theodoor Overbeek [162], illustrates the colloidal dispersion's stabilization through integration of the van der Waals attraction and the electrostatic double layer's repulsion. Taking into account both components, we can approximate the energy per unit area between two infinitely extended solids that are separated by a gap x

$$V_{DPVO}(x) = 64 c_0 k_B T \lambda_d \tanh^2(\frac{e\psi_0}{4k_B T}) e^{-x/\lambda_d} - \frac{\pi C_{M_1 M_2} \rho_{M_1} \rho_{M_2}}{12x^2}. \tag{2.18}$$

Here, c_0, ψ_0, λ_d are bulk concentration of the salt, surface potential at radius particle r_p and Debye length [133]. The DLPO force results better in estimation for the surface distances up to 5 nm.

2.1.6 Steric Forces

According to [138], steric effects is the stable suspensions generated from adsorbing polymers coating on the particle surfaces. Steric stabilization requires the thickness of polymer film and its refractive index are sufficient to remain the particles out of range of the Lifshitz-van der Waals force. The interaction energy generated between polymer layers and the particles in an aprotic solvent, which depends on the Flory–Huggins's parameters, can be calculated [163] in Eq. (2.19):

$$V_{Str} = V_f^2 (0.5 - \chi)(2t_p - 2r + H)^2 . \frac{\pi r k_B T}{V_p}, \tag{2.19}$$

where, χ, V_p, V_f, t_p are, in turn, the polymer-solvent interaction parameter, polymer's partial molar volume, ratio volume of chains in the absorbed layer and polymer layer thickness, respectively.

2.1.7 Non-DLVO Forces

Besides aforementioned forces, there are other forces also contribute to colloidal stability such as "non-DLVO" forces. The two first examples of these such forces are hydrophilic and hydrophobic force, and magnetic or electric dipoles interactions linked with ferromagnetism or ferroelectricity [164, 165].

2.1.7.1 Hydrophylic Interaction

Hydrophilic interactions presenting for the wetting ability is generated in polar chemical liquid like water [166]. In fact, the atom O in a H_2O molecule is further electronegative than H which the shared electrons of an oxygen-hydrogen bond take longer time in approaching to the O. This mechanism induces the partial polarization between atom O taking on a negative and the atom H having a positive. Also, the bonds in a H_2O molecule is always available due to its orientation angle is 105°. Additionally, other polar molecules can generate ionic bonds to water. Generally, molecules of the proteins and biology that discloses to environment shows normally hydrophilic property.

2.1.7.2 Hydrophobic Interaction

Hydrophobic interactions [167] pushed from a volume of water arise from the uncharged property of the involved chemical groups like *CH3*. In this example, the bonds in the C atom are fully resided in, which produces non-polar states. Hence, one H_2O molecule possessing polarization property is inapplicable to associate with such non-polar group (*-CH3*). That induces unstable association between the water molecules which can force hydrophobic areas into a like association regions under the repulsion of the neighbour water molecules. As a result, this mechanism creates a hydrophobic pocket or an envelope in carbohydrate or a protein.

2.1.8 Interlock Force

Mechanical interlocking (or "hooking") [168] illustrates the adhesive liquid remaining in various crevices after flowing into and becoming hard in there. This constructs a structure to restrict the separations between the surfaces. Although interlocking has meaningful contributions to the adhesion force, it is an intuitive concept which depends on the roughness of the contact interfaces, the materials properties and the external acting forces. In other words, it is complicated to build a theoretical model for this force.

2.1.9 Capillary Force

Capillary is the phenomenon which the liquid can move in narrow regions without requiring the support sources from external forces. Capillary forces influencing in microscale, arise at the solid-gas-liquid interfaces to obtaining the minimum surface energy [169, 170]. Inside a liquid volume, each liquid molecule has cohesive forces with its surrounding molecules. However, there are no liquid neighbour molecules for that of at the interface. This induces producing more powerful attraction with surrounding molecules on and below the interface (Fig. 2.4(a)). Integrating surface tension and adhesive forces between the interaction of the liquid-walls can push the liquid to move up (water) or down (mercury) as the tube's diameters are small enough.

Capillary phenomenon has significant contributions to the wet adhesion of surface-surface and particle-surface [171]. To investigate the underlying physical properties of capillary forces, we step-by-step approach the theories shown in the below sections.

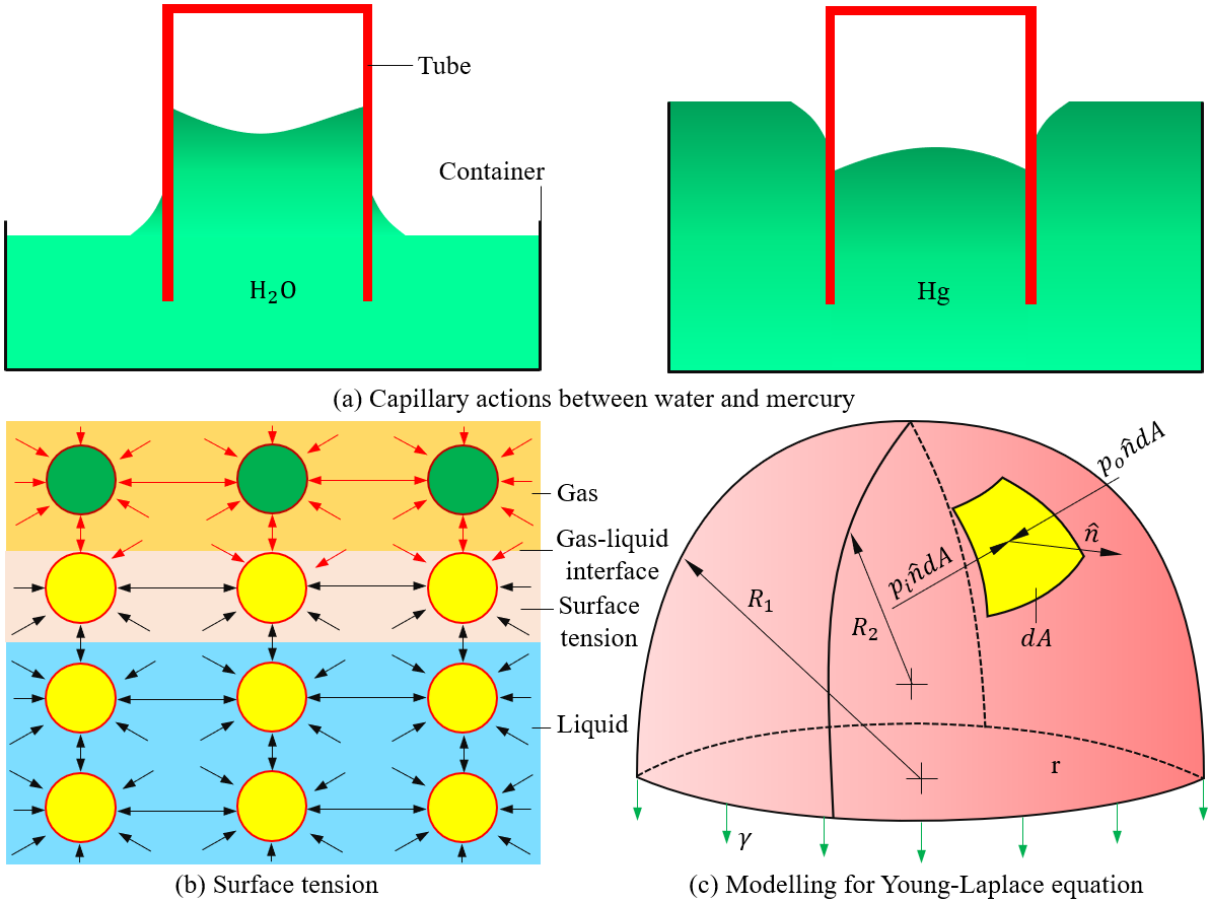

(a) Capillary actions between water and mercury

(b) Surface tension

(c) Modelling for Young-Laplace equation

Figure 2.4: Schematic demonstration of capillary phenomenon. a) Capillary in side a small tube between water and meniscus. b) Liquid surface tension of the liquid-gas interface. c) Model applies to deriving Young-Laplace force.

2.1.9.1 Surface Tension

Surface tension is one of the important concepts in capillary theory. One can find out the underlying physics of this definition through exploring a gas-liquid interface in microscale. Herein, surface tension is resulted from the imbalance attraction between molecules originated from declining in surface energy. The molecules inside the liquid volume impact to the others thanks to attracting forces like hydrogen bonds or van der Waals. However, at the gas-liquid interface in Fig. 2.4(b), the molecules having stronger bonds form a different layer which is harder to enter into the liquid surface than its inside volume. In this scenario, the molecules joining in stronger attractions generate the surface tension with higher values than that of the rests. Let us denote γ is the surface tension, the work dW produced from an area dA is:

$$d_W = \gamma dA. \tag{2.20}$$

In Eq. (2.20), the surface tension's γ is presented in energy per area (J/m^2) or force per length (N/m). Also, the surface tension depends on the state of the liquid and gas, and temperature.

2.1.9.2 Young-Laplace Equation

As equilibrium state, meniscus curvature forms convex or concave shapes (Fig. 2.4(c)) depending on the different pressure between the inside and outside the liquid-gas interface (p_i, p_o). According to [169], the Young-Laplace theory can estimate the relation between different pressure and the meniscus curvature in Eq. (2.21):

$$P_L = p_o - p_i = \gamma \nabla . \hat{n} = -\gamma \left(\frac{1}{R_1} + \frac{1}{R_2} \right), \tag{2.21}$$

with R_1, R_2 are the principal radii of the meniscus curvature. As shown in Fig. 2.5(a), the radius R_1 takes "positive" sign in contrast to that of R_2; whereas, the signs of R_1, R_2 are shifted in Fig. 2.5(b). This is caused from the different pressure between inside and out side the liquid-gas interface.

Equation 2.21 is also called as Young-Laplace equation, and P_L is Laplace pressure.

In addition, we have some basic implications for the Young–Laplace equation as followed:

- One can estimate the Laplace pressure after having the parameters of the meniscus curvatures.
- If there are no impact of the external forces, the Laplace pressure takes the same value at each point inside the capillary bridge. Hence, as P_L is constant, the capillary curvature is same everywhere.

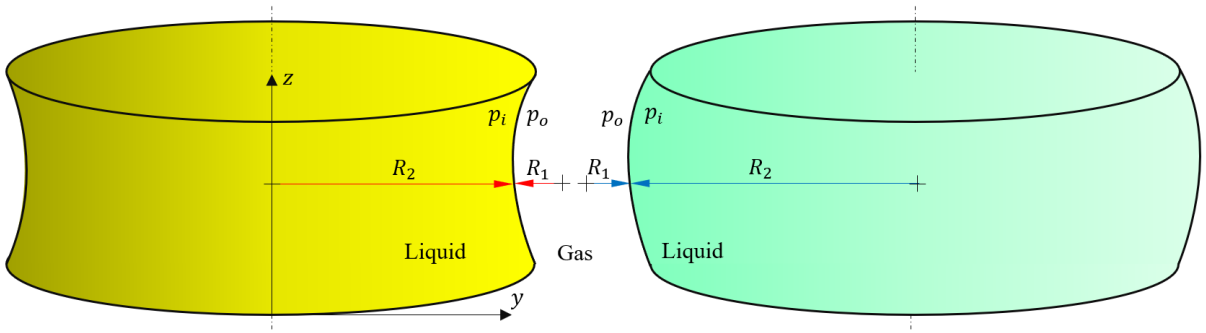

(a) Capillary curvature with $p_i > p_o$ (b) Capillary curvature with $p_i < p_o$

Figure 2.5: Curvature shapes of the capillary bridge under pressure differences. a) The inside pressure value is larger than that of the outside. b) The inside pressure value is smaller than that of the outside.

- The Young–Laplace equation (2.21) facilitates us to determine a liquid surface's shape in the equilibrium. For instance, when the different pressure and boundary conditions are explicit, the geometry of the capillary bridge can be obtained.

Practically, the meniscus curvature in Eq. (2.21) is normally determined through a coordination function of x, y, z with $z = f(x, y)$ [172]. In this scenario, the capillary curvature relates to the second derivative of x, y which gives their radii R_1, R_2 by Eq. (2.22):

$$R_1 = \frac{\ddot{x}}{(1+\dot{x}^2)^{1.5}}, \& R_2 = \frac{\dot{x}}{y\sqrt{1+\dot{x}^2}}. \tag{2.22}$$

2.1.9.3 Kelvin Equation

The Young–Laplace equation in previous section has no concern the properties of material or estimated conditions. Kelvin equation [173] displays problems relating to the liquid's vapor pressure. The vapor pressure depends on the capillary curvature, which takes higher value in a drop comparing with that of a plain surface, and decreases a bubble. In this section, the Kelvin equation shows the relation of the vapor pressure and the the capillary curvature in Eq. (2.23):

$$RT.ln\frac{p_0^K}{p_0} = \gamma V_c \left(\frac{1}{R_1} + \frac{1}{R_2}\right). \tag{2.23}$$

Here, R, p_0^K, p_0, V_m are respectively the universal gas constant, vapor pressure of the curve and flat surface, and the volume of capillary. The Kelvin equation in Eq. (2.23) is also utilized in explaining the capillary condensation.

2.1.9.4 Contact Angle

As dropping a volume liquid on a solid surface, the interface edge of solid-liquid forms a contact angle (Fig. 2.6). This angle is determined through measuring the angle at the line at the cross interface of gas-liquid-solid. Also the contact angle can indicate the wet ability of the solid surface with the liquid volume through the Young-Laplace law [174] in Eq. (2.24):

$$\gamma_{SL} + \gamma_{LG} \cos\theta = \gamma_{SG}, \tag{2.24}$$

with $\gamma_{SL}, \gamma_{SG}, \gamma_{LG}$ are respectively the interfacial surface tension of the solid-liquid, solid-gas and liquid-gas.

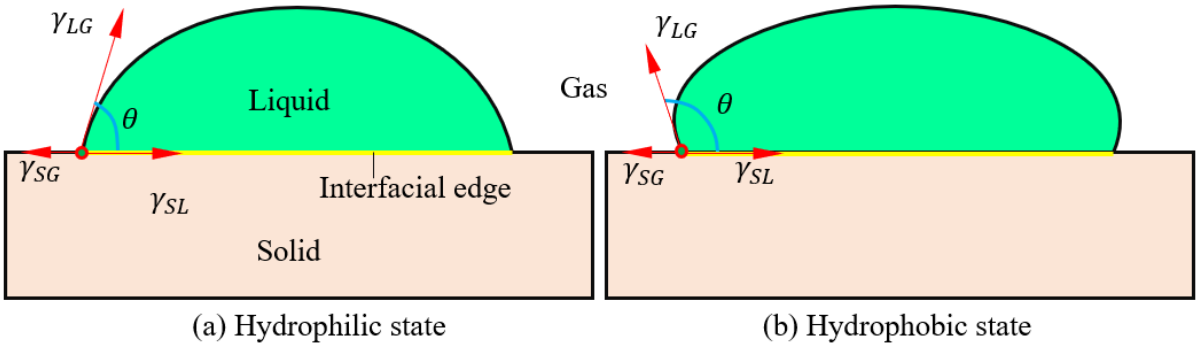

Figure 2.6: Schematic illustration of dropping a liquid volume on a plain surface of the solid with contact angle θ. Contact angle in hydrophilic a) and hydrophobic state b).

Additionally, the contact angle θ in Eq. (2.23) shows the wet ability of the liquid in spreading over the solid surface by the value of θ. As shown in Fig. 2.6(a), in hydrophilic state the contact angle of $\theta < 90°$, which has stronger wet adhesion force than that of the contact angle in hydrophobic state (Fig. 2.6(b)). Also, reducing the contact angle value can enhance the wet adhesion ability of the solid surface. This can be explained by the cohesive force influenced by the hydrophilicity and hydrophobicity in section 2.1.6. Furthermore, an interface comprising from liquid-solid-gas with a given temperature and pressure parameters takes a unique contact angle value in equilibrium condition.

2.1.9.5 Surface and Adhesion Energy

In liquids, when calculating the amount of energy dW to rise the small surface area dA, we can use the Eq. (2.20) with regarding $\gamma_{LG} = \gamma$. In other words, the surface energy and surface tension of the liquid are directly proportional. However, it has some problems when applied to solids, since the solid surface area may rise in two ways. Herein, the first question is the increment of number molecules N at the solid surface as well as in the liquid case, and the rest one is the surface stretching from the elastic. Thus, it is necessary

to concern the elastic and plastic contributions in the surface energy, or we have:

$$\frac{dW}{dA} = E_S \frac{\partial N}{\partial A} + N \frac{\partial E_S}{\partial A}, \tag{2.25}$$

with E_s is the excess energy of each molecules. In case having only a plastic deformation, the surface area A_m of each molecule is constant. That leads to the surface energy $dW/dA = \gamma_{SG}$ is similar to the liquid case, which can be also called *"surface tension"*. As investigating a purely elastic, the number of molecule N is constant; whereas alternating surface area A_m induces the changes of the surface area of the solid. Hence, let us denote ϵ_{elas} is the elastic strain, applying Eq. (2.25) applying this scenario yields:

$$\left.\frac{dW}{dA}\right|_{elas} = \gamma_{SG} + \frac{\partial \gamma_{SG}}{\partial \epsilon_{elas}} = \Gamma, \tag{2.26}$$

In Eq. (2.26), the entity Γ is also called *"surface stress"*. Therefore, in case a new surface area resulted from the contributions of the elastic and plastic variation generally has its surface energy in Eq. (2.27):

$$\frac{dW}{dA} = \gamma_{SG} \frac{d\epsilon_{plas}}{d\epsilon_{tot}} + \Gamma \frac{d\epsilon_{elas}}{d\epsilon_{tot}}, \tag{2.27}$$

with $\epsilon_{tot} = dA/A, \epsilon_{plas}$ are, in turn, the total strain and the plastic strain. Therefore, the variation in Gibbs energy (dW) needs enlarging surface against the γ_{SG} and Γ.

In order to determine the adhesion force, let us split two blocks of different materials 1 and 2, and bring them into contact. Hence, according to [175, 176], the different energy balancing to the adhesive energy equal to:

$$W_h = \left.\frac{dW}{dA}\right|_1 + \left.\frac{dW}{dA}\right|_2 - \gamma_{12}, \tag{2.28}$$

with γ_{12} is the interfacial energy at the contact between materials 1 and 2. Eq. (2.28) is Dupré work for adhesion. Because of the influence of the roughness and contamination on the surface, experimentally results of the adhesion energy may take lower values than estimations.

2.2 Adhesion of Pads with A Substrate Surface

When a pad covered by a thin fluid film contacts a substrate surface, the liquid film forms a capillary bridge inside the contact interface. From Eq. (2.1), we can consider the adhesion force F_a between the pad and the substrate in general calculation majorly comprises of two components wet F_w and dry adhesion F_d, whereas the interlock force F_{il} appears in

Table 2.1: List of abbreviations

n-pad	Pad with normal surface or w/o any patterns
n-pad-c	n-pad with concave surface
n-pad-v	n-pad with convex surface
m-pad	Pad with micropatterned surface
m-pad-c	m-pad with concave surface
m-pad-v	m-pad with convex surface
$F_{i,n}, F_{i,t}$	Force F_i in normal and tangential directions (N)
F_{in}, F_{im}	Force F_i in case n- and m- pads (N)
$F_{in,n}, F_{im,n}$	Force F_i in case n- and m- pads in normal direction (N)
$F_{in,t}, F_{im,t}$	Force F_i in case n- and m- pads in tangential direction (N)
$F_i\langle c-o\rangle$	Force F_i in cases complete wet without dry adhesion (N)
$F_i\langle c-w\rangle$	Force F_i in cases complete wet with dry adhesion (N)
$F_i\langle p-o\rangle$	Force F_i in cases partial wet without dry adhesion (N)
$F_i\langle p-w\rangle$	Force F_i in cases partial with dry adhesion (N)
$F_{in}^{c(v)}$	Force F_i in case n-pad-c and n-pad-v (N)
$F_{im}^{c(v)}$	Force F_i in case m-pad-c and m-pad-v (N)
$F_{in,n}^{c(v)}$	Normal force F_i in case n-pad-c and n-pad-v (N)
$F_{in,t}^{c(v)}$	Tangential force F_i in case n-pad-c and n-pad-v (N)
$F_{im,n}^{c(v)}$	Normal force F_i in case m-pad-c and m-pad-v (N)
$F_{im,t}^{c(v)}$	Tangential force F_i in case m-pad-c and m-pad-v (N)
γ	Surface tension (N/m)
η	Viscosity coefficient (Nsm^{-2})

case tangential direction:

$$\mathbf{F_a} = \mathbf{F_{a,n}} + \mathbf{F_{a,t}} = \mathbf{F_w} + \mathbf{F_d} + \mathbf{F_{il}} + \vartheta\mathbf{F_o}. \tag{2.29}$$

Where $F_{a,n}, F_{a,t}$ are the adhesion in normal and tangential directions. In this scenarios, we use the abbreviations for other forces following the rules in the table 2.1. In Eq. (2.29), the dry adhesion F_d is the total of the electrostatic F_{els}, van der Waals F_{vd} and Casimir F_{CP} forces; whereas, wet adhesion force F_w is the sum of the capillary F_{ca} and viscosity forces F_v (one type of hydrodynamic force F_{hd}). According to [108, 177, 178], the force F_w is the total of three primary components: Laplace force F_L, surface tension F_{st} and viscosity force F_v. Hence, the forces F_d and F_w are described by the following equation:

$$\begin{cases} \mathbf{F_d} = \mathbf{F_{d,n}} + \mathbf{F_{d,t}} = \mathbf{F_{vd}} + \mathbf{F_{CP}} \\ \mathbf{F_w} = \mathbf{F_{w,n}} + \mathbf{F_{w,t}} = \mathbf{F_L} + \mathbf{F_{st}} + \mathbf{F_v}. \end{cases} \tag{2.30}$$

From Eq. (2.30), we get the capillary force by

$$\mathbf{F_{ca}} = \mathbf{F_{ca,n}} + \mathbf{F_{ca,t}} = \mathbf{F_L} + \mathbf{F_{st}}. \tag{2.31}$$

When the pad contacts with the substrate, the total force generated by the external entities called F_{ex} such as: peeling force $F_p = F_{p,n} + F_{p,t}$ and compress force acting on the pad (preload P) balances the resistant entities, for example, the adhesion force F_a and the friction force F_f. Summing them yields the contact force F_c as followed:

$$\mathbf{F_c} = \mathbf{F_{c,n}} + \mathbf{F_{c,t}} \begin{cases} \mathbf{F_{c,n}} = \mathbf{P} + \mathbf{F_a} \\ \mathbf{F_{c,t}} = \mu \mathbf{F_{c,n}} + \mathbf{F_{a,t}} \end{cases}, \tag{2.32}$$

with μ is the friction coefficient. In this thesis, two kinds of the pad: n- and m-pad are used to constitute the contact mechanic with the adhesion in two cases of contact interfaces: flat and curved (in table 2.2). In this scenario, the interface gap h is assumed same value at all points inside the contact.

Table 2.2: Two contact interfaces of the n- and m-pad

Types of pad	Flat contact interface	Curved contact interface
n-pad	n-pad (Fig. 2.7)	n-pad-c and n-pad-v (Fig. 2.11)
m-pad	m-pad (Fig. 3.1)	m-pad-c and m-pad-v (Fig. 3.2)

Equations (2.30) to (2.33) illustrate the forces in general case for both n- and m-pad. In addition, t hese equations play the primary role for calculations of the resultant and contact force both flat and curved contact interface will be shown in the next following sections.

2.3 Adhesion of Normal Pad in Flat Surfaces

This section studies the adhesion between the n-pad and a flat substrate as shown in Fig. 2.7(a). In this scenario, the pad is wiped a thin film of liquid before approaching to contact with the substrate. After making a contact with the substrate, the liquid film forms a capillary bridge inside the contact interface. In microscale, the contact interfaces usually have various surface roughness which induces different states for the wet contact (Fig. 2.7(b-c)). The wet adhesion depends on various parameters such as: properties of liquid, vapor, substrate, and interface gap h [177]. Simply, if the capillary bridge curvatures are already known, one can can calculate the force F_w.

2.3.1 Attachment Phase

As contacting with a flat-rigid substrate, the liquid film spreads to fill the vacancies between the contact interface [97], which produces wet adhesion for bonding the surfaces together (Fig. 2.7). Depending on the surface properties of the pad and the substrate and the liquid characteristic, the attachment phase may include four cases: wet without dry

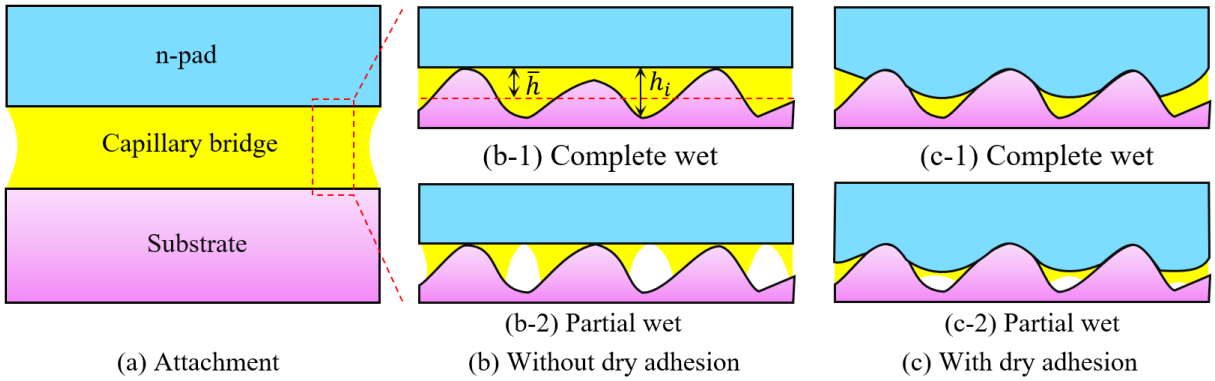

Figure 2.7: Schematic illustration of the wet adhesion between the n-pad (normal pad or a pad without any patterns) with a plain substrate. a) The general model of the wet adhesion for flat contact interface in attachment phase. b) Insets exaggerate one unit region of a) in case without dry adhesion: complete b-1) [177, 179] and partial wet b-2) [180]. c) Insets exaggerate one unit region of a) in case with dry adhesion: complete c-1) [177, 179] and partial wet c-2) [180].

adhesion as the n-pad is complete flat (Fig. 2.7(b)) and wet with dry adhesion as the n-pad has deformation (Fig. 2.7(c)). In addition, the volume of liquid film affect on the fully filling the empty space to achieve complete wet (Fig. 2.7(b-1),(c-1)) or partial wet (Fig. 2.7(b-2),(c-2)). Such cases of the adhesion are illustrated in table 2.3

Table 2.3: Four states of wet adhesion

With dry adhesion	Without dry adhesion
Complete wet	Complete wet
Partial wet	Partial wet

2.3.1.1 Wet Without Dry Adhesion

When having no deformation, the contact can be considered only appearing at the top points of the roughness surface as shown in Fig. 2.7(b). In other words, the dry adhesion may exist at these points with the adhesion area $A_d \sim 0$.

Complete Wet In case complete wet in Fig. 2.7(b-1), let us consider h being the separation gap between two surfaces with $h = \bar{h} = \int h_i dA_w / N_p \langle i \rangle$ is the median value of the n-pad surface to the substrate surface. $N_p \langle i \rangle$ is the number of points with the interface gap h_i on the wet area A_w, and this couple surfaces are assumed to completely parallel.

By replacing the Eqs. (2.21,2.24) into Eq. (2.31) for the n-pad with its wet radius r_w

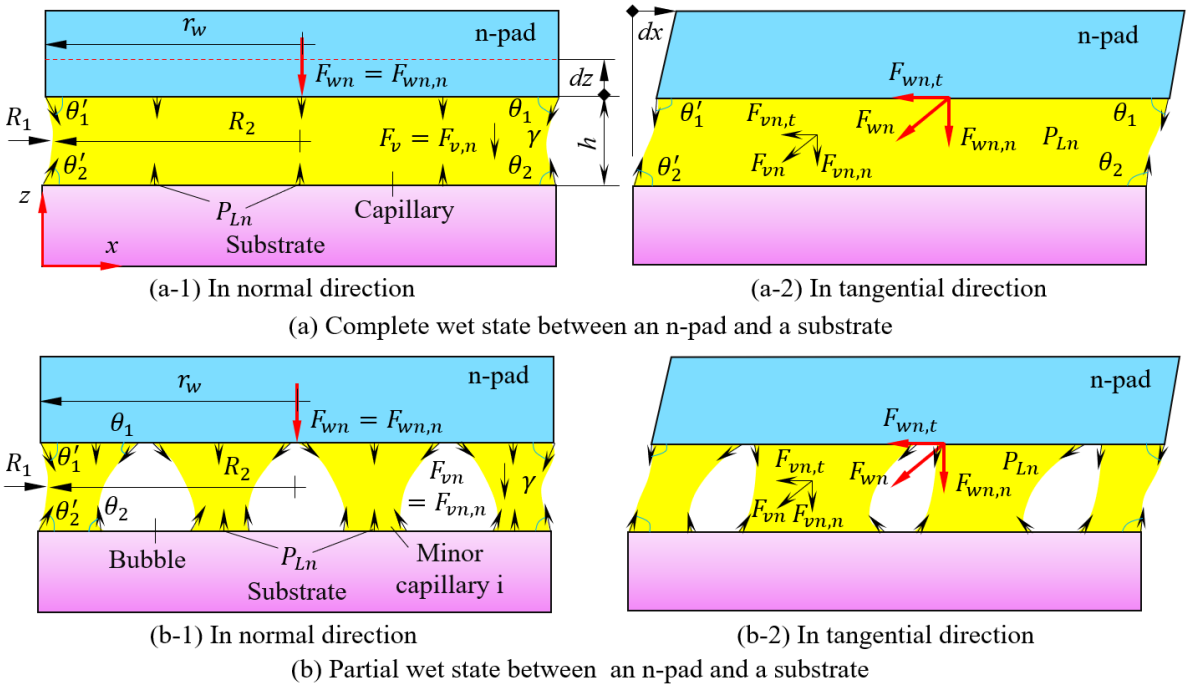

(a-1) In normal direction (a-2) In tangential direction

(a) Complete wet state between an n-pad and a substrate

(b-1) In normal direction (b-2) In tangential direction

(b) Partial wet state between an n-pad and a substrate

Figure 2.8: Mechanics of the wet adhesion between the n-pad and a flat substrate at interface gap h. a) The complete wet state between the n-pad and the substrate in a-1) normal and a-2) tangential direction. b) The partial wet state between the n-pad and the substrate in b-1) normal and b-2) tangential direction. For normal direction, the red dot line show varying interface gap h with a small distance dz. In addition, θ_1, $\theta_{1'}$, θ_2 and $\theta_{2'}$ are the contact angles of the liquid capillary bridge. In case there are no tangential movement, we can consider θ_1=$\theta_{1'}$, θ_2=$\theta_{2'}$.

yields the capillary force for normal direction as followed:

$$F_{can,n}\langle c-o\rangle = \left[\underbrace{\gamma \iint_{A_w}\left(\frac{1}{R_1}+\frac{1}{R_2}\right)dA_w}_{\text{Laplace force}} + \underbrace{\gamma P_w \sin\theta_1}_{\text{Normal surface tension force}}\right]\hat{z}, \tag{2.33}$$

and in case thermaldynamic law, the radius $r_L = 1/R_1 + 1/R_2$ also called as Kelvin radius [181] is additionally regarded the temperature in Kelvin equation Eq. (2.23). Thus, we can rewrite Eq. (2.33) by:

$$F_{can,n}\langle c-o\rangle = \gamma\left(\iint_{A_w}\frac{V_c}{RT\ln(p_0^K/p_0)}dA_w + P_w\sin\theta_1\right)\hat{z}, \tag{2.34}$$

Here, the wet perimeter of the n-pad P_w is equivalent to $2\pi r_w$. Eq. (2.34) can result a precise estimation of the normal capillary force. However, it is too complicated to determining exactly the pressure ratio p_0^k/p_0, especially in microscale of interface gap h. In this scenario, the Young-Laplace equation (Eq. (2.33) is more practical to calculating $F_{can,n}$ by determining the capillary curvature R_1, R_2. Hence, replacing Eq. (2.22) into the

Eq. (2.33) yields the force $F_{can,n}$ as followed:

$$F_{can,n}\langle c-o\rangle = \gamma\left[A_w\left(\frac{(1+\dot{x}^2)^{1.5}}{\ddot{x}} - \frac{y\sqrt{1+\dot{x}^2}}{\dot{x}}\right) + P_w\sin\theta_1\right]\hat{z}. \tag{2.35}$$

To solve Eq. (2.33) it has to face with a challenge of the uncertain state of the capillary curvature which cannot show the accuracy functions x, y at each point [182]. However, in the actual contact model, the interface gap h is infinitesimal to the dimension of the n-pad (r_w) or we have $1/R_2 << 1/R_1$. Simply, let us assume that the capillary curvature has round shape with radius R_1 is approximately tangential to the surface tension force F_{stn} and neglect $1/R_2$. Thus, Eq. (2.35) becomes:

$$F_{can,n}\langle c-o\rangle = \left(\underbrace{\gamma A_w\frac{cos\theta_1 + cos\theta_2}{h}}_{\text{Laplace force}} + \underbrace{\gamma P_w\sin\theta_1}_{\text{Normal surface tension force}}\right)\hat{z}, \tag{2.36}$$

As can be seen, if the radius r_w is a constant amount for the defined pad, the force $F_{ca,n}$ in Eq. (2.36) depends on the variations: surface tension γ, interface gap h and the contact angles θ_1, θ_2. Firstly, the surface tension γ explained in Eq. (2.20) is determined by Eötvös or Guggenheim–Katayama [183] as followed:

$$\gamma = \begin{cases} k(T_C - T)V_c^{-2/3}, & \textit{Eötvös} \\ \gamma_0(1 - T/T_C)^n, & \textit{Guggenheim–Katayama} \end{cases}, \tag{2.37}$$

with T_C, n are respectively the critical temperature and the empirical factor. Since our study applying to interaction with food or human which organic is usually chosen for the liquid film, the corresponding model uses the surface tension γ by following Guggenheim–Katayama in Eq. (2.37) with $n = 11/9$. The change of the contact angle θ depending on many parameters which was explored by many researchers. Among them, Souza and his colleagues [184, 185] give a vast number of experimental evaluations for the thick liquid films. Authors in [186, 187] develop Young-Lalace equation in Eq. (2.24) for calculating the contact angles by:

$$\cos\theta = \frac{\gamma_{SG} - \gamma_{SL}}{\gamma_{LG}} + \frac{\gamma_l}{\gamma_{LG}R_2}, \tag{2.38}$$

with R_2, γ_l are the droplet radius and line tension [188]. Eq. (2.38) can be applied to the droplet or large interface gap h; whereas, for the narrow interface gap, it is difficult to use. Hence, in this thesis, we consider the contact angle, in static state, $\theta_1 = \theta_2 = \theta$ and in normal direction $\theta_1 = \theta_{1'} = \theta_2 = \theta_{2'}$ in Fig. 2.8(a-1)(b-1). By projecting the vectors in Eq. (2.31) in the tangential direction (Fig. 2.8(b-1)(b-2)) we have the tangential capillary

force $F_{can,t}$ as followed:

$$F_{can,t}\langle c-o\rangle \approx 0.5\gamma P_w(cos\theta_{1'} - cos\theta_1)\hat{x}. \tag{2.39}$$

In case of static condition, the viscosity force F_{vn} is neglected. Thus the wet adhesion F_{wn} is equal to capillary force F_{can}. Therefore, Eq. (2.36 and 2.39) already determine the force $F_{wn,n}$ and $F_{wn,t}$ in Eq. (2.30).

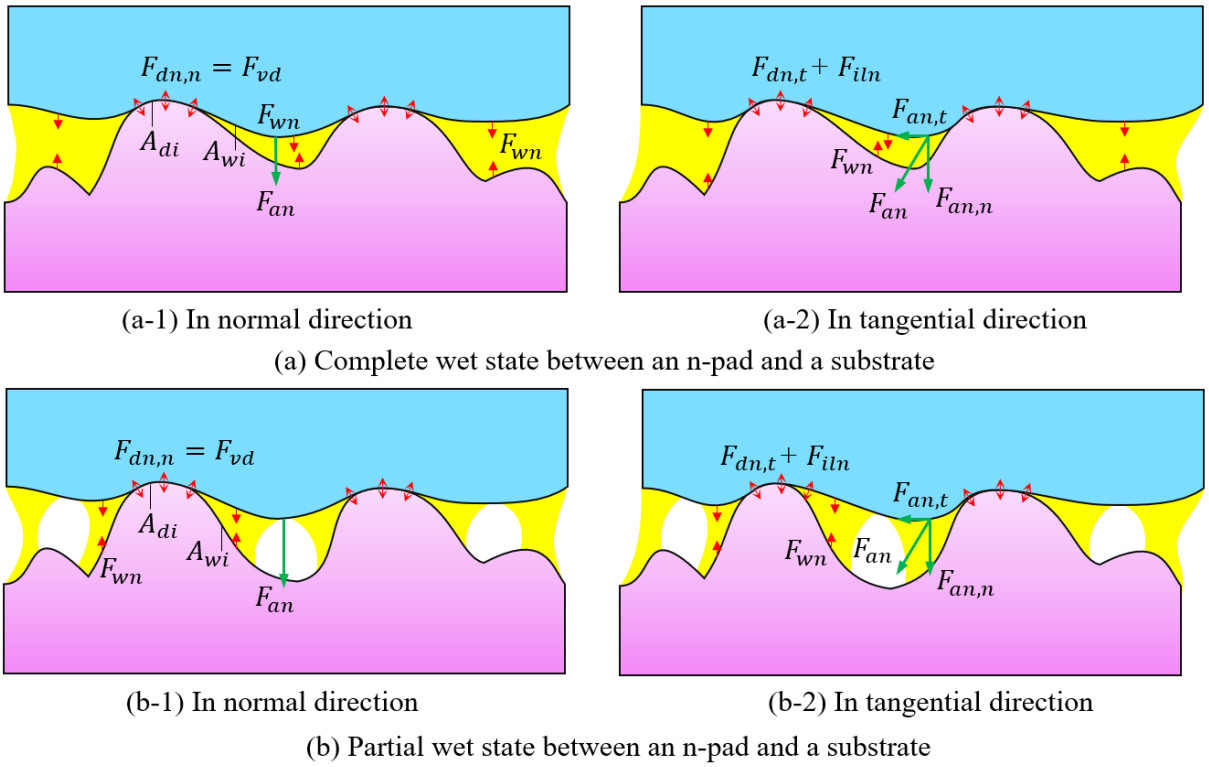

Figure 2.9: Mechanics of the adhesion between the n-pad and a flat substrate at interface gap h. a) The dry and wet adhesion in case complete wet state between the n-pad and the substrate in a-1) normal and a-2) tangential direction. b) The dry and wet adhesion in case partial wet state between the n-pad and the substrate in b-1) normal and b-2) tangential direction. In this figure, the areas of dry and wet contact at position i are, in turn, A_{di} and A_{wi}.

Partial Wet In case partial wet in Fig. 2.7(b-2), let us assume that between each trough of the substrate surface and the n-pad forms a bubble which locally separates the capillary bridge into the minor capillary bridges (Fig. 2.8(b-1)). Since every minor capillary also have the solid-liquid-gas interface, calculating the wet adhesion force for them is similar to the entire n-pad in case complete wet. Thus, by applying Eqs. (2.31, 2.36 and 2.39) to the partial wet case, the normal wet adhesion force is:

$$F_{wn,n}\langle p-o\rangle = \gamma\pi N_n\langle i\rangle r_{wi}\left(r_{wi}\frac{cos\theta_{1i} + cos\theta_{2i}}{h_i} + 2\pi\sin\theta_{1i}\right)\hat{z} = F_{can,n}\langle p-o\rangle, \tag{2.40}$$

and the tangential wet adhesion force equals to:

$$F_{wn,t}\langle p-o\rangle \approx \gamma\pi N_n\langle i\rangle r_{wi}(cos\theta_{1'i} - cos\theta_{1i})\hat{x} = F_{can,t}\langle p-o\rangle. \tag{2.41}$$

Herein, $N_n\langle i\rangle$ is the total number of minor capillaries i with its wetting radius, area and perimeter are, in turn, $r_{wi}, A_{wi} = \pi r_{wi}^2, P_{wi} = 2\pi r_{wi}$.

2.3.1.2 Wet With Dry Adhesion

When the deformation appears on the n-pad interface or the substrate surface is extremely smooth, the liquid is pushed out of the contact areas as shown in Fig. 2.7(c). Then the interface comprises of two contact regions: wet and dry. Thus, dry adhesion force is concerned in this scenario. Since the design materials in our research are nonconductive, the adhesion force F_{an} in Eq. (2.1) includes the van der Waal, Casimir and interlock forces.

Complete Wet Depending on the wet ability and the surface roughness of the contact interface's components, the liquid may exist or vanish at dry regions (Fig. 2.9). Generally, the van der Waal interaction between the n-pad and the substrate can be considered as macroscopic approach which using the Hamaker constant in Eq. (2.16). Hence, by replacing this constant to Eq. (2.9) and applying it to this contact, the van der Waals force F_{vdi} at each position i can be given by:

$$F_{vdi} = -\frac{0.75k_BT\phi_\epsilon + 0.265\hbar f_m\phi_n}{6\pi h^3}A_{di}. \tag{2.42}$$

Where $\epsilon_p\langle i\rangle, \epsilon_s, \epsilon_{lg}$ are respectively the permittivity of the pad, substrate and the liquid (or gas), $\phi_\epsilon = (\epsilon_p\langle i\rangle - \epsilon_{lg})(\epsilon_s - \epsilon_{lg})/[(\epsilon_p\langle i\rangle + \epsilon_{lg})(\epsilon_s + \epsilon_{lg})], n_s, n_{lg}$ are, in turn, the retractive indices of the pad, substrate and the liquid (or gas), and $\phi_n = (n_p^2 - n_{lg}^2)(n_s^2 - n_{lg}^2)/[\sqrt{n_p^2 + n_{lg}^2}\sqrt{n_s^2 + n_{lg}^2}(\sqrt{n_p^2 + n_{lg}^2} + \sqrt{n_s^2 + n_{lg}^2})]$.

In normal direction, the dry adhesion force F_{dn} can neglect the effect of the interlock force F_{iln} (Fig. 2.9(a-1)(b-1)); whereas,the wet adhesion force F_{wn} is calculated for the rest regions of the n-pad. Thus, applying Eqs. (2.36) and (2.42) yields the normal adhesion force between the n-pad and substrate as followed:

$$F_{an,n}\langle c-w\rangle = \left[F_{wn,n}\langle c-o\rangle + F_{dn,n}\right]\hat{z}. \tag{2.43}$$

Where the dry adhesion force $F_{dn,n} = N_d^n\langle i\rangle F_{vdi}$ and $N_d^n\langle i\rangle$ is the total number of the dry contact position i with area A_{di}. Also, the wet area in this scenario is $A_w = \Sigma A_{wi} = \pi r_w^2 - N_p\langle i\rangle A_{di}$.

When the n-pad is impacted by the tangential external force, the dry adhesion force additionally includes interlock force F_{iln} [189] as shown in Fig. 2.9(a-2)(b-2). Walraven presents the force F_{iln} in case the rigid materials like steel and concrete which is not completely suitable to use for our study which design soft materials. Additionally, as aforementioned in section 2.1.7, this force is extremely intuitive and relates to the contact mechanics. Apply Eqs. (2.39) and (2.42), the tangential adhesion force equals to:

$$F_{an,t}\langle c-w\rangle = \left[F_{wn,t}\langle c-o\rangle + F_{dn,t} + F_{ils}\right]\hat{x}. \tag{2.44}$$

Partial Wet When the liquid film can not entirely cover the contact surface of the substrate in Fig. 2.9(b-1)(b-2), the bubbles also separate the capillary bridge into the minor capillaries. However, the number of the minor capillaries $N_n\langle i\rangle$ may differ with that of the dry contact positions $N_p\langle i\rangle$. Hence, combining Eqs. (2.40), (2.42) and (2.29) derives the normal adhesion force as followed:

$$F_{an,n}\langle p-w\rangle = \left[F_{wn,n}\langle p-o\rangle + F_{dn,n}\right]\hat{z}. \tag{2.45}$$

Similarly, by synthesizing Eqs. (2.41), (2.42) and (2.29) we have the tangential adhesion force as followed:

$$F_{an,t}\langle p-w\rangle = \left[F_{wn,t}\langle p-o\rangle + F_{dn,t} + F_{iln}\right]\hat{x}. \tag{2.46}$$

Equations (2.33) to (2.46) are used to calculate the total adhesion between the n-pad and the flat substrate in static condition. They also play the key role for the evaluation in curved and micropatterned contact interfaces in the following sections. Also, in the attachment, the contact force is considered in normal direction where $F_{cn} = F_{cn,n}$ balancing against the adhesion force $F_{an} = F_{an,n}$; whereas, the tangential contact force $F_{cn,t}$ is neglected.

2.3.2 Detachment Phase

This section shows investigating the dynamics of the adhesion between the n-pad and the flat substrate under the normal peeling force $F_{p,n}$ in normal direction. Herein, the n-pad moves with a distance dz in z axis in their corresponding velocity v_z. Also, we neglect the n-pad's acceleration a_z and the substrate is stationary. In this scenario, the force $F_{p,n}$ equals to the force $F_{an,n}$. Also, the contact force F_{cn} mentioned in Eq. (2.32) is equivalent

to the adhesion force in the following equation:

$$F_{cn} = F_{cn,n} = F_{an,n}, \tag{2.47}$$

In dynamic state, the wet adhesion force F_{wn} in Eq. (2.47) also adds an entity: the viscosity force F_{vn} as mentioned in Eq. (2.30). The force F_{vn} comprises of normal and tangential components $F_{vn,n}$ and $F_{vn,t}$ which is shown as followed:

$$\begin{aligned} \mathbf{F_{vn,n}} &= \frac{\mathbf{3\pi\eta r_w^4}}{\mathbf{4dt}}\left(\frac{\mathbf{1}}{\mathbf{h^2}} - \frac{\mathbf{1}}{\mathbf{h_0^2}}\right)\hat{\mathbf{z}}, Normal \text{ [190]} \\ \mathbf{F_{vn,t}} &= \frac{\eta \mathbf{A_w}}{\mathbf{h}}.\frac{\mathbf{dx}}{\mathbf{dt}}\hat{\mathbf{x}}, Tangential \text{ [93]}. \end{aligned} \tag{2.48}$$

The force $F_{vn,n}$ becomes Stefan force $F_{vn,n} = [1.5\pi\eta r_w^4/h^3](dz/dt)$ [130, 191] as the displacement dz is infinitesimal to h. Hence, we can use the capillary number n_{ca} to evaluating the effect of the viscosity component comparing with the surface tension on the contributions to the force F_{wn} [174]. This number is given in Eq. (2.49)

$$n_{ca} = \eta v/\gamma. \tag{2.49}$$

As the n-pad detaches from the substrate in normal direction, the interface gap h increases, which abates the adhesion force of the contact $F_{an,n}$. The dry adhesion force $F_{dn,n}$ decreases rapidly; whereas, the wet adhesion force $F_{wn,n}$ gradually reduces until the capillary bridge completely vanishes. There are two principal states of the capillary bridge in this scenario: collapses the wet area in the substrate into the center region (Fig. 2.10(a)) as low Laplace pressure, and separates into minor capillaries (Fig. 2.10(b)) as high Laplace pressure. Hence, by replacing Eqs. (2.46) and (2.48) into Eq. (2.29) the normal adhesion in case the n-pad in case partial wet adhesion is generally given by:

$$\begin{aligned} F_{an,n}\langle c - w\rangle = \Bigg[\gamma\left(\iint_{A_w} \frac{cos\theta_{1i} + cos\theta_{2i}}{h_i} dA_w + N_n\langle i\rangle P_{wi}\sin\theta_{1i}\right) \\ + F_{dn,n} + \frac{3\pi\eta r_{2n}^4}{4dt}\left(\frac{1}{h^2} - \frac{1}{h_0^2}\right)\Bigg]\hat{z}. \end{aligned} \tag{2.50}$$

In case of complete wet adhesion with narrow interface gap h, we can assume that the capillary majorly separated by the break bubbles [107] having the contact angles $\theta_{bn1}, \theta_{bn2}$ and the radius r_{bn} (Fig. 2.10(b)); whereas, the influence of collapsing the capillary into the center substrate in Fig. 2.10(b) is neglected. In this scenario, the force $F_{wn,n}$ rapidly declines after reaching the peak of interface gap h_p as the minor capillary bridges become

weak. For sake of simplicity, we can consider the bubble radius at position i being $r_{bni} \sim 0.5h_{bni}(1/\sin\theta_{bn1i} + 1/\sin\theta_{bn2i})$ with $h_{bni} = f_n(hi)$. Hence, the wet area at each minor capillary bridge A_{wi} is estimated in:

$$A_{wi} = \pi\left[r_{wi} - \frac{g_{h_i} f_n(h_i)}{4}\left(\frac{1}{\sin\theta_{bn1i}} + \frac{1}{\sin\theta_{bn2i}} - \frac{1}{\tan\theta_{bn1i}} - \frac{1}{\tan\theta_{bn2i}}\right)\right]^2. \tag{2.51}$$

Where $g_{hi} = \{0, 1\}$ is the function of bubble disappearance or appearance at position i

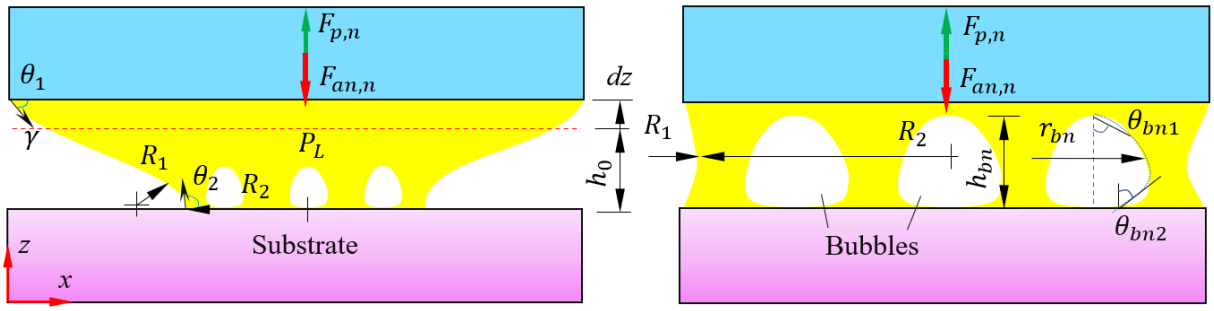

(a) Weak wet adhesion (b) Strong wet adhesion

Figure 2.10: Schematic illustration of the adhesion between the n-pad and the planar substrate at the interface gap $h = h_0 + dz$ under pulled by a normal peeling force $F_{p,n}$. a) The capillary bridge in case the system of the substrate and the liquid film have weak wet adhesion (low Laplace pressure [177]). In this scenario, the wet area on the substrate becomes more narrow and bubble appear on the interface line [184]. In case strong wet adhesion (high Laplace pressure [177]) b), the capillary bridge is interspaced by the minor capillary bridges [192, 193]. Differences in suction due to pad morphology, liquid characteristics and substrate's surfaces caused the bubbles to vary in shape and partly affected the number of minor bridge capillaries. Because wet adhesion force on the pad is larger than the substrate, fractures tend to occur initially at the lower part of the bridge near the substrate's surface. Also the bubbles were considered spherical stimulated in the dot lines with radius r_{bn}.

corresponding value 0 or 1 respectively. Hence, by replacing Eqs. (2.45), (2.48) and (2.51) into Eq. (2.29) the normal adhesion generated by the n-pad in case partial wet adhesion is generally given by:

$$F_{an,n}\langle p - w\rangle = \left[F_{can,n}\langle p - w\rangle + \frac{3\pi\eta N_n\langle i\rangle r_{wi}^4}{4dt}\left(\frac{1}{h^2} - \frac{1}{h_0^2}\right) + F_{dn,n}\right]\hat{z}. \tag{2.52}$$

2.3.3 Tangential Direction

When the n-pad moves on x direction with velocity v_x as shown in Fig. 2.8(a-2)(b-2), the tangential adhesion force $F_{an,t}$ sums up the forces: dry adhesion $F_{dn,t}$, wet adhesion $F_{wn,t}$ and interlock force F_{iln}. Thus, by replacing Eqs. (2.46), (2.48) and (2.51) into Eq. (2.29)

the tangential adhesion in case the n-pad in case complete wet adhesion is generally given by:

$$F_{an,t}\langle c-w\rangle = \left[F_{can,t}\langle c-o\rangle + F_{iln} + \frac{\eta A_w}{h}.\frac{dx}{dt} + F_{dn,t}\right]\hat{x}. \tag{2.53}$$

and that of in case partial wet is:

$$F_{an,t}\langle p-w\rangle = \left[F_{can,t}\langle p-o\rangle + F_{iln} + N_n\langle i\rangle\frac{\eta A_{wi}}{h_i}.\frac{dx}{dt} + F_{dn,t}\right]\hat{x}. \tag{2.54}$$

The interlock force F_{iln} in equation 2.54 is complicated for calculation, thus it is normally transferred into an amount of the friction force F_{fn}. In case the contact interface has smooth surfaces (small surface roughness), we can neglect the force F_{iln}

In general, this section constitutes the adhesion model of the contact interface between the n-pad and a flat surface of the substrate by utilizing the principles and theoretical foundations. This analytical model sets up an estimation to describe the contact mechanics for the curved and micropatterned contact interfaces in the next steps.

2.4 Adhesion of Normal Pad in Curved Surfaces

Previous sections show the theoretical foundation for estimating the adhesion in case the flat contact interface. In fact, the contact interface in the actual applications of soft robots is not always flat because of the diverse shapes of the manipulated objects (substrates). Such prolific cases of the substrate's shape require the soft pad to have suitable morphology for achieving the effective adaptions. There are several research on the estimation of the wet adhesion or dry adhesion between a sphere and a flat substrate [194–196]; whereas, that of two curved contact interfaces is scarce. Thus, this section aims to develop the model of adhesion for the couple of curved contact interfaces between the n-pad and the substrate. There are two cases of the n-pad's morphology are investigated: concave (n-pad-c) and convex (n-pad-v) as shown in Fig. 2.11. To avoid replicate explanations we denote $a^{c(v)}$ presents the entities a^c for the n-pad-c and a^v for the n-pad-v, respectively.

2.4.1 Attachment Phase

The n-pad c(v) comes to make contact with their corresponding hemispherical substrates having convex and concave shape with radii R_s. In this scenario, α_1, α_2 are the angles between the tangential line and x-axis at the interface line solid-liquid-gas of the n-pad-c(v) and the substrate. Also z_c, the curvature function of the capillary, has its variation x_c.

However, Eq. (2.22) is complicated to calculate $z_c(x_c)$. Simply, let us consider the surface of the n-pad is parallel with the substrate's surface, which has the consistent interface gap h in the entire contact area. By drawing a normal line between the couple of contact interfaces AD and $AC \perp EC$ yields $AD = AB \sin\alpha_2$, and $AB = AE \sin\alpha_1 - R_2^c + x_s$. Thus, we have $DE = AE(1 - \sin\alpha_1 \sin\alpha_2) + (R_2^c - x_s)\sin\alpha_2$. Then, the interface gap h can be determined as: $h \approx DE/\cos\alpha_1 = [AE(1 - \sin\alpha_1 \sin\alpha_2) + (R_2^c - x_s)\sin\alpha_2]/\cos\alpha_1$. In addition, from $AE = CE/\cos\alpha_1 = R_1^c[\cos(\theta_1 - \alpha_1) + \cos(\theta_2 + \alpha_2)]/\cos\alpha_1$ derives $h = \{R_1^c[\cos(\theta_1 - \alpha_1) + \cos(\theta_2 + \alpha_2)](1 - \sin\alpha_1 \sin\alpha_2)/\cos\alpha_1 + (R_2^c - x_s)\sin\alpha_2]\}/\cos\alpha_1$. Hence, the outside radius of the capillary bridge in case the n-pad-c R_1^c equals to:

$$R_1^c = \frac{[h\cos\alpha_1 - (R_2^c - x_s)\sin\alpha_2]\cos\alpha_1}{[\cos\beta_1^c + \cos\beta_2^c](1 - \sin\alpha_1\sin\alpha_2)}, \beta_1^c = \theta_1 - \alpha_1, \beta_2^c = \theta_2 + \alpha_2. \tag{2.55}$$

It is similar to determining R_1^c, the outside radius of the capillary bridge in case the n-pad-v R_1^v becomes:

$$R_1^v = \frac{[h\cos\alpha_1 - (R_2^v - x_s)\sin\alpha_2]\cos\alpha_1}{[(\cos\beta_1^v + \cos\beta_2^v)(1 - \sin\alpha_1\sin\alpha_2)]\cos\alpha_1}, \beta_1^v = \theta_1 + \alpha_1, \beta_2^v = \theta_2 - \alpha_2. \tag{2.56}$$

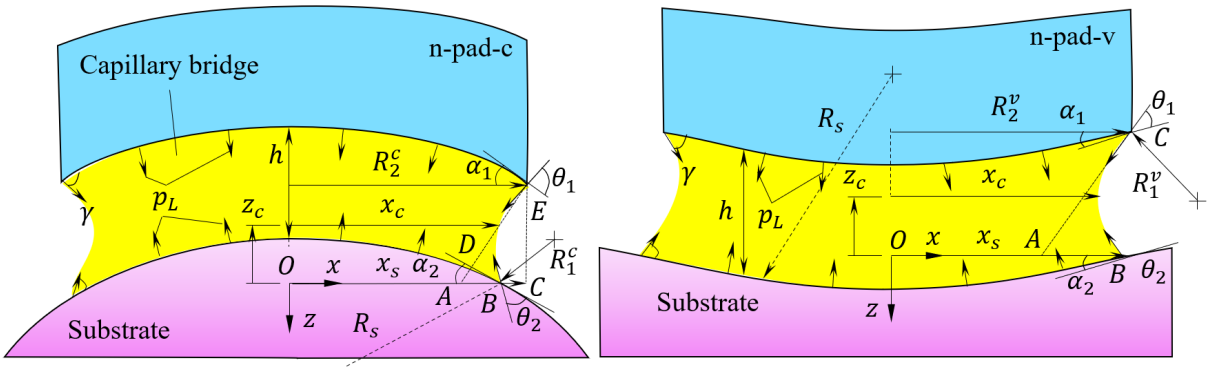

(a) Concave contact interface (b) Convex contact interface

Figure 2.11: Mechanics scheme of the curved contact interfaces between the normal pad and a hemispherical substrate at the interface gap h. There are two cases of the pad: a) concave normal pad (n-pad-c) and b) convex normal pad (n-pad-v).

The radii $R_1^{c(v)}$ in Eqs. (2.55) and (2.56) are usually infinitesimal to x_c (or $R_2^{c(v)}$) at small interface gap h. Thus, the entity $1/x_c$ can be neglected in Laplace force. Replacing Eqs. (2.55) and (2.56) into Eq. (2.33) yields the normal wet adhesion force $F_{wn,n}^{c(v)}$ for the

n-pad-c and the n-pad-v as followed:

$$F_{wn,n}^{c(v)}\langle c-o\rangle = \left(\underbrace{\pi\gamma 2R_2^{c(v)}\sin\beta_1^{c(v)}}_{\text{Surface tension force}} + \underbrace{\iint_{A_w^{c(v)}} \frac{R_2^{c(v)}}{R_1^{c(v)}} dA_w^{c(v)}}_{\text{Laplace force}} \right) \hat{z}. \tag{2.57}$$

The surface roughness affects on the adhesion in case of curved contact interface, which is similar to the flat contact interface as mentioned in section 2.3. In this scenario, the normal adhesion is also concerned with or without dry adhesion as shown in Fig. 2.7. For the complete wet case without dry adhesion, the normal adhesion force $F_{an,n}^{c(v)}$ is determined in Eq. (2.57). In case partial wet without dry adhesion, there are $N_n\langle i\rangle$ minor capillary bridges instead of one capillary. Hence, the radii $R_1^{c(v)}, R_2^{c(v)}$ in Eq. (2.57) is replaced by the minor capillary curvature's radii $r_{1i}^{c(v)}, r_{2i}^{c(v)}$ at each position i. By synthesizing Eq. (2.40) and (2.57) derives the normal adhesion force $F_{an,n}^{c(v)}$ in Eq. (2.58):

$$F_{wn,n}^{c(v)}\langle p-o\rangle = \gamma\pi N_n\langle i\rangle r_{wi}^{c(v)} \left(r_{wi}^{c(v)} \frac{r_{2i}^{c(v)}}{r_{1i}^{c(v)}} + 2\pi\sin\beta_{1i}^{c(v)} \right) \hat{z}. \tag{2.58}$$

For complete wet with dry adhesion, combining Eq. (2.43) and (2.57), the normal adhesion force $F_{an,n}^{c(v)}$ can be given by:

$$F_{an,n}\langle c-w\rangle = \left(F_{wn,n}^{c(v)}\langle c-o\rangle + F_{dn,n}^{c(v)} \right) \hat{z}. \tag{2.59}$$

And in case the partial wet with dry adhesion, combining Eq. (2.45) and (2.57) yields the normal adhesion force $F_{an,n}^{c(v)}$ as followed:

$$F_{an,n}\langle p-w\rangle = \left(F_{wn,n}^{c(v)}\langle p-o\rangle + F_{dn,n}^{c(v)} \right) \hat{z}. \tag{2.60}$$

2.4.2 Detachment Phase

Under normal peeling force $F_{p,n}$, the normal adhesion force $F_{an,n}^{c(v)}$ is in dynamic state. Herein, the wet adhesion forces $F_{wn,n}^{c(v)}$, one major component of the force $F_{an,n}^{c(v)}$, additionally include viscosity forces $F_{vn,n}^{c(v)}$. Since, the liquid film is very thin and the interface gap h is infinitesimal, we can assume that the capillary bridge is separated by minor capillary bridges as shown in Fig. 2.12(b) and neglect another case in Fig. 2.12(a). Thus, the normal wet adhesion forces $F_{an,n}$ in Eq. (2.58) can be rewritten in the general case as followed:

$$F_{wn,n}^{c(v)} = F_{can,n}^{c(v)} + F_{vn,n}^{c(v)}. \tag{2.61}$$

In any situations, the bubbles appear inside the capillary bridge. Thus, we can apply the calculation of the partial wet with dry adhesion to estimating the normal adhesion between the n-pad-c(v) and their corresponding substrate. Hence, in the dynamic state, synthesizing Eqs. (2.48), (2.57) and (2.61) derives the normal wet adhesion forces for the n-pad-c and the n-pad-v in:

$$F_{an,n}^{c(v)} = \left[F_{wn,n}^{c(v)} \langle p - w \rangle + \frac{3\pi\eta N_n \langle i \rangle (r_{wi}^{c(v)})^4}{4dt} \left(\frac{1}{h^2} - \frac{1}{h_0^2} \right) + F_{dn,n}^{c(v)} \langle p - w \rangle \right] \hat{z}. \tag{2.62}$$

In Eq. (2.62), the wet area A_{wi} is determined in Eq. (2.51); whereas A_{di} may be value zero. In general, equation (2.62) can estimate the adhesion forces respectively generated by the n-pad-c(v) with convex and concave surfaces of the substrate. In these equations, parameters of angles α_1, α_2, θ_1, and θ_2, associated with pad form, differ between two cases of the n-pad: concave and convex. Accordingly, the obtained results described in this section are theoretical foundations in the mechanics of wet contact between curved surfaces. We applied these estimations for the pads with micropatterns in the following sections.

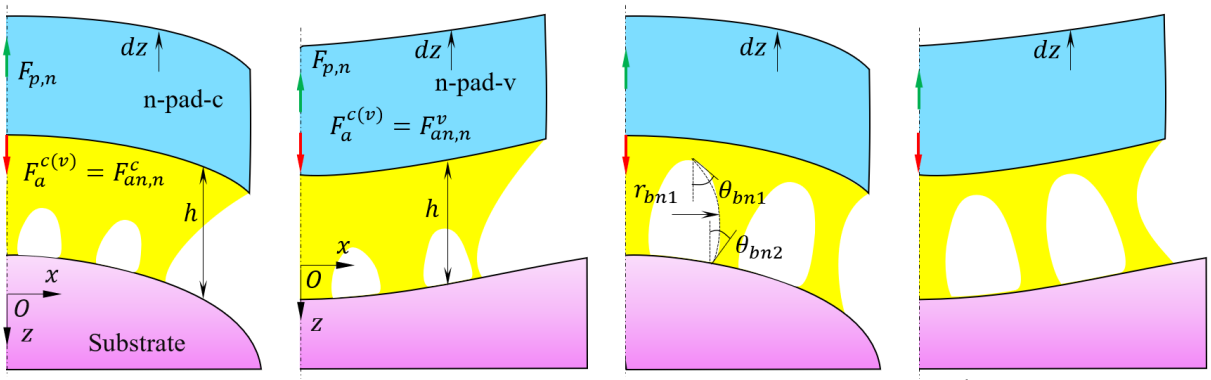

(a-1) Concave (a-2) Convex (b-1) Concave (b-2) Convex

(a) Weak wet adhesion (b) Strong wet adhesion

Figure 2.12: Schematic illustration of normal adhesion for the curved contact interface between the n-pad and the hemispherical substrates at interface gap $h = h_0 + dz$ under pulled by a normal peeling force $F_{p,n}$. a) The capillary bridge as the system of the substrate and the liquid film has weak wet adhesion (low Laplace pressure). In case strong wet adhesion (high Laplace pressure) b), the capillary bridge is interspaced by the minor capillary bridges, forming minor capillary bridges in the fluid film. a-1) and b-1) show the adhesion of the n-pad-c; whereas, a-2) and b-2) illustrate the adhesion of the n-pad-v.

2.5 Contact Mechanics

Solid shows behaviors under interaction with external force, and deformation is one of the most important feature among them. In particularly, in manipulating soft-fragile objects

by soft robotic hand, deformation of the soft matters should be focused. Thus, this section illustrates the underlying physic of soft contact mechanic through theoretical foundation to utilizing in grasping with wet adhesion.

2.5.1 Stress and Strain

A bar has its own characteristic as: length l_b, cross-sectional area A_b, Young modulus E_b, Poisson ratio υ_b is under external force F_{ex} being perpendicular to A_b. Hence, we have basic relations as followed:

$$\sigma_A = F_{ex}/A_b = E_b\epsilon_l \tag{2.63a}$$

$$\epsilon_{l_b} = \Delta l_b/l_b\epsilon_{w_b} = \Delta w_b/w_b \tag{2.63b}$$

$$\epsilon_{w_b} = \upsilon_b\epsilon_{l_b}, \tag{2.63c}$$

with σ_A, ϵ_{l_b} are the normal stress and strain at section A_b, and υ_b is the Poisson ratio.

2.5.1.1 Isotropic Materials

The relation between the stress and strain of an elastic material is normally described by Hook's law. In 3D elasticity, we have:

$$\begin{Bmatrix} \sigma_{11} \\ \sigma_{22} \\ \sigma_{33} \\ \sigma_{23} \\ \sigma_{13} \\ \sigma_{12} \end{Bmatrix} = \frac{E}{(1+\upsilon)(1-2\upsilon)} \begin{bmatrix} 1-\upsilon & \upsilon & \upsilon & 0 & 0 & 0 \\ \upsilon & 1-\upsilon & \upsilon & 0 & 0 & 0 \\ \upsilon & \upsilon & 1-\upsilon & 0 & 0 & 0 \\ 0 & 0 & 0 & 0.5-\upsilon & 0 & 0 \\ 0 & 0 & 0 & 0 & 0.5-\upsilon & 0 \\ 0 & 0 & 0 & 0 & 0.5-\upsilon & \end{bmatrix} \begin{pmatrix} \upsilon_{11} \\ \upsilon_{22} \\ \upsilon_{33} \\ 2\upsilon_{23} \\ 2\upsilon_{13} \\ 2\upsilon_{12} \end{pmatrix} \tag{2.64}$$

2.5.1.2 Anisotropic Materials

For an anisotropic materials, the stress–strain relation is the derivation of a strain energy density function (U) by the formulation: $\sigma_{ij} = \partial U/\partial\epsilon_{ij}$. In this scenario, the Hook's law

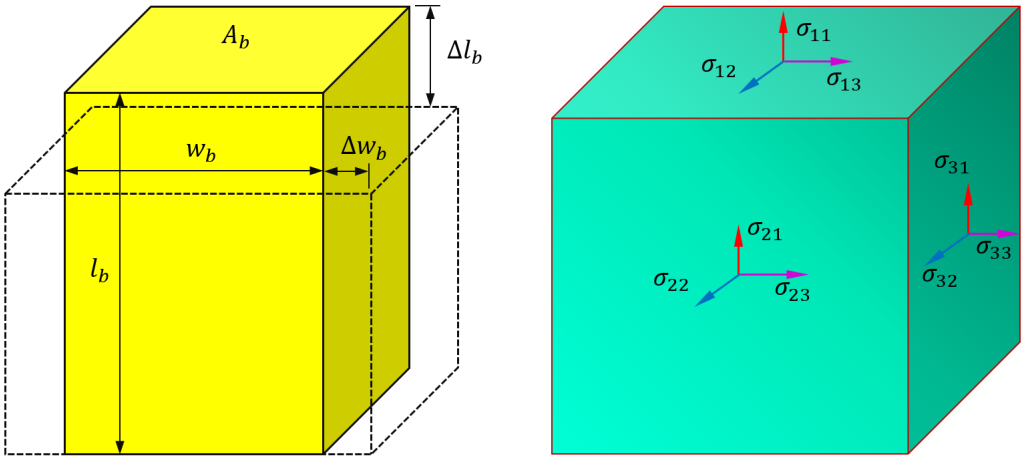

(a) Deformation of a bar (b) Stress tensor

Figure 2.13: Schematic illustration of the deformation for a bar a) and stress tensor b).

is rewritten in Eq. (2.65):

$$\begin{Bmatrix} \sigma_1 \\ \sigma_2 \\ \sigma_3 \\ \sigma_4 \\ \sigma_5 \\ \sigma_6 \end{Bmatrix} = \begin{bmatrix} s_{1111} & s_{1122} & s_{1133} & s_{1123} & s_{1131} & s_{1112} \\ s_{2211} & s_{2222} & s_{2233} & s_{2223} & s_{2231} & s_{2212} \\ s_{3311} & s_{3322} & s_{3333} & s_{3323} & s_{3331} & s_{3312} \\ s_{2311} & s_{2322} & s_{2333} & s_{2323} & s_{2331} & s_{2312} \\ s_{3111} & s_{3122} & s_{3133} & s_{3123} & s_{3131} & s_{3112} \\ s_{1211} & s_{1222} & s_{1233} & s_{1223} & s_{1231} & s_{1212} \end{bmatrix} \begin{pmatrix} \upsilon_1 \\ \upsilon_2 \\ \upsilon_3 \\ 2\upsilon_4 \\ 2\upsilon_5 \\ 2\upsilon_6 \end{pmatrix}, \tag{2.65}$$

with $S = [s_{ijkl}]$ is the stiffness tensor which has $s_{ijkl} = s_{klij}$.

2.5.2 Contact Model in Normal Direction

Contact model is utilized for investigating the mechanics of grasping/handling objects during their interactions with the soft robotic fingers or bodies. The main objective in our research is focusing on manipulating soft-fragile objects in wet conditions. However, it is developed to universally handle others rigid objects in diverse environment. In this thesis, the materials for making the soft pads in directly contacting with the substrates is soft such as: silicon rubber; whereas, the objects is generally soft (tofu, contact lens) or rigid (hard contact lens, medical equipment).

The adhesion force F_{an} helps the soft robotic finger to achieve a stickier attachment with the substrate, which can reduce the compress stress on the handled objects exerted by the external force from the fingers. However, in actual grasp, to get an effective manipulation the grasp force F_{gn} may need the squeezing force F_s (in my thesis we use preload P as a case of F_s) combining with the adhesion force F_{an} as shown in Fig. 2.14.

In general, the grasp force is in the following relation:

$$\mathbf{F_{gn}} = \mathbf{F_{cn,n}} + \mathbf{F_{cn,t}} = \mathbf{F_{an}} + \mathbf{F_s}. \tag{2.66}$$

The grasp force F_{gn} in Eq. (2.66) generates the normal and shear stress on the object's surface which affects on the safe condition of manipulation. Hence, it is necessary to investigate the role of the grasp force F_{gn} on the contact mechanics of the interface between the pad and the substrate. In this scenario, the contact force F_{cn} exerted by the grasp force comprising from the normal $F_{cn,n}$ and tangential (shear) $F_{cn,t}$ force. There are several theories related to contact mechanics given in [197–199].

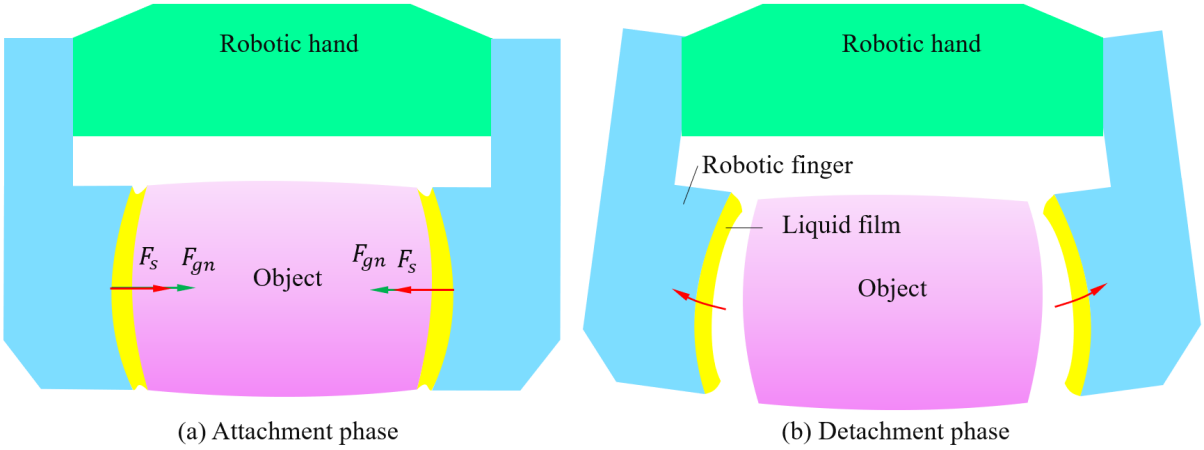

Figure 2.14: Schematic illustration of grasping object by the soft robotic hand with each of its finger tip fixes with a soft adhesive pad. a) The finger attaches and grips an object through a grasp force F_{gn}. b) The finger detaches from the object.

2.5.2.1 Hertz Contact Model

The first theoretical model of contact mechanics was proposed by Hertz [197], which showed the non-adhesive contact between two elastic bodies without roughness surface and small strain. These bodies with their radii r_1, r_2 come into contact under the squeezing force F_s, and their deformation are determined through elastic energy. In Fig. 2.15(a), the contact radius r_3 equals to:

$$r_3 = \left[\frac{0.75 F_s r_1 r_2}{r_1 + r_2} \left(\frac{1 - \upsilon_1^2}{E_1} + \frac{1 - \upsilon_2^2}{E_2} \right) \right]^{1/3}. \tag{2.67}$$

Also the penetration δ between two surface is:

$$\delta = \left(\frac{r_1 + r_2}{4 r_1 r_2} \right)^{1/3} \left[0.75 F_s \left(\frac{1 - \upsilon_1^2}{E_1} + \frac{1 - \upsilon_2^2}{E_2} \right) \right]^{2/3}. \tag{2.68}$$

In case a sphere contacts a half space in Fig. 2.15(b), the penetration δ in Eq. (2.68) becomes:

$$\delta = \left(\frac{r_1 + r_2}{4r_1 r_2}\right)^{1/3} \left[\frac{0.75F_s}{\sqrt{r_1}}\left(\frac{1-\upsilon_1^2}{E_1} + \frac{1-\upsilon_2^2}{E_2}\right)\right]^{2/3}. \tag{2.69}$$

Then, the contact pressure is distributed on the distance r_{3i} from the center of the contact region.

$$\sigma_i = \frac{F_s}{\pi r_3^2}\left[1 - \left(\frac{r_{3i}}{r_3}\right)^2\right]. \tag{2.70}$$

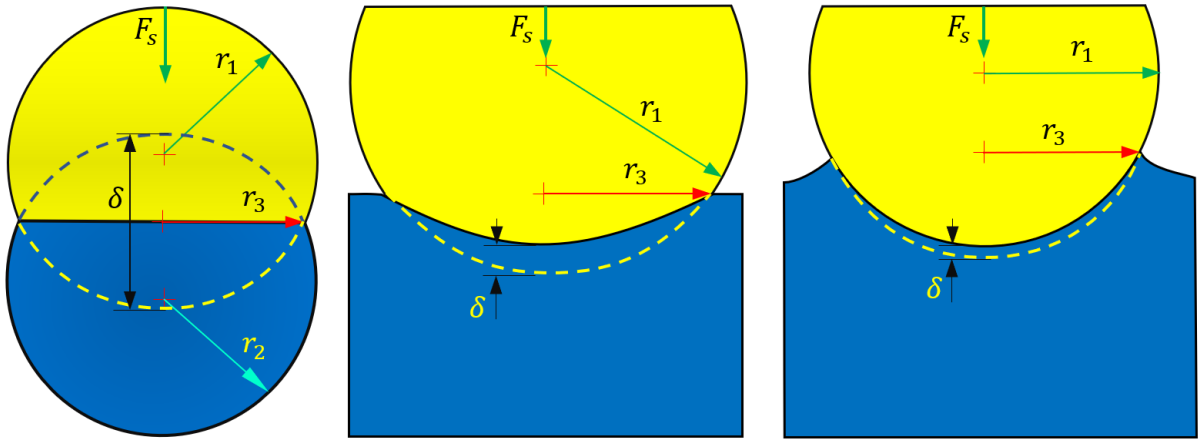

(a) Sphere-sphere (b) Sphere-half space (c) Sphere-half space contact in JKR

Figure 2.15: Schematic illustration of contact model proposed by Hertz and JKR in different types of the Hertzian contact model between a) sphere and sphere and b) sphere and half space. c) sphere and half space in JKR contact model.

2.5.2.2 JKR Model

Hertz constructed a contact model between two elastic solid bodies without concerning the adhesive properties of surface roughness. Later, Johnson, Kendall and Robert [200, 201] have done this work by accounting the adhesive forces in the contact evaluation. This model called JKR theory based on the energy relation of the adhesion and elastic deformation. In Fig. 2.15(c), the adhesive neck forms a contact area differing from the Hertizan model, the circular contact radius in this case equals to [197]:

$$r_3 = \left[\frac{3r_1}{8}\left(\frac{1-\epsilon_1^2}{E_1} + \frac{1-\epsilon_2^2}{E_2}\right)^{1/2}\left(\sqrt{8\gamma_{12}\pi} + \sqrt{8\gamma_{12}\pi + \frac{16F_s}{3r_1}}\right)\right]^{3/2}, \tag{2.71}$$

with γ_{12} is the relative energy between two objects. The adhesion force is:

$$F_a = -1.5\gamma_{12}\pi r_1, \tag{2.72}$$

and the penetration depth δ equals to:

$$\delta_{min} = \left[\frac{3\pi^2\gamma_{12}^2 r_1}{64}\left(\frac{1-\epsilon_1^2}{E_1} + \frac{1-\epsilon_2^2}{E_2}\right)^2\right]^{1/3}, \tag{2.73}$$

Hence, the pressure distribution is determined in:

$$\sigma_i = \frac{1}{\pi}\left(\frac{1-\epsilon_1^2}{E_1} + \frac{1-\epsilon_2^2}{E_2}\right)^{-1}\left[\left(\frac{\delta}{r_3} - \frac{r_3}{r_1}\right)\left(1 - \frac{r_i^2}{r_3^2}\right)^{-1/2} + \frac{2r_3}{r_1}\left(1 - \frac{r_i^2}{r_3^2}\right)^{1/2}\right], \tag{2.74}$$

2.5.2.3 Greenwood and Williamson Model

The JKR theory (Fig. 2.16(a)) developed the previous work of Hertz. However, it did not concern on the roughness surface of the objects. Greenwood and William proposed a new approach by assuming the asperity height of the object surface is a probability distribution ζ_h [202]. From Gaussian distribution, we have:

$$\zeta_h = \frac{1}{\sqrt{2\pi}h^*} exp\left(-\frac{h^2}{2h^{*2}}\right), \tag{2.75}$$

with h^* is the root-mean-square of the summit height. Hence, the normal stress equals to:

$$\sigma_n = \frac{4}{3}\left(\frac{1-\epsilon_1^2}{E_1} + \frac{1-\epsilon_2^2}{E_2}\right)^{-1} N_0 \int_\delta^\infty (h-\delta)^{1.5} r_1^{0.5}\zeta_h dh. \tag{2.76}$$

Where N_0 is the number of asperities in a unit area. From Eq. (2.76), one can add the adhesion force for the contact model according to [202, 203].

2.5.2.4 Bush, Gibson and Thomas Model

In this model (Fig. 2.16(b)), the asperities in the roughness surface were modeled as paraboloids with their curvature radii: r_1, r_2. According to [204, 205], the probability distribution in Eq. (2.75) becomes:

$$\zeta_h = \frac{\sqrt{27}}{16\pi^2 m_2 m_4\sqrt{m_0 m_4}} m_3^{0.5} exp\left[-m_3\left(\frac{h}{m_0^{0.5}} + \frac{3(r_{1i}+r_{2i})}{4\sqrt{\chi m_4}}\right)^2\right](r_{1i}-r_{2i}) \\ r_{1i}r_{2i} exp\left[-\frac{3[(r_{1i}+r_{2i})^2 - 8r_{1i}r_{2i}}{16m_4}\right]. \tag{2.77}$$

In Eq. (2.77), m_0, m_2, m_4 are, in turn, the zero, second and fourth moments of surface roughness spectrum, $\chi = m_0 m_4 / m_2^2$, and $m_3 = m_0 m_4 / (2m_0 m_4 - 3m_2^2)$. By using equation (2.77), the normal pressure in the contact area A_c can be calculated in:

$$\sigma_c = \frac{F_s}{A_c} = \int_u^\infty dh \iint_\omega dh dr_2 F_{si} \zeta_h. \tag{2.78}$$

Here, ω is the domain of $\{r_1, r_2\}$ and F_{si} is the squeezing force acting on one asperity.

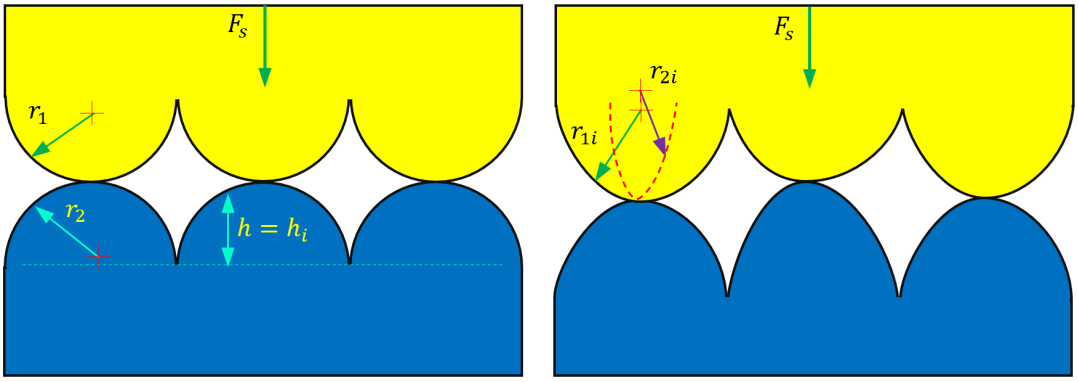

(a) GW model (b) BGT model

Figure 2.16: Schematic illustration of contact model proposed by Greenwood-Williamson a) and Bush-Gibson-Thomas b).

The BGT model showed that the true contact area A_c is proportional to the squeezing force F_s. However, this theory is appropriate to the simple surface roughness and neglects long-range elastic coupling.

2.5.2.5 Persson Model

Previous contact theories considered that in the contact interfaces the actual contact area is smaller than that of the nominal one. In the Persson theory [206, 207], the contact mechanics eliminates the mentioned assumption by limiting case of the contact between a rigid rough surface and a flat elastic half-space as shown in Fig. 2.17. Here, as increasing the magnification ζ, there only several asperities joint to the contact. ζ, the reference length, is the ratio of the lateral size l_c of the nominal contact area and the shortest wave length roughness at λ: $\zeta = l_c/\lambda = q/q_{l_c}$. The stress distribution at ζ is:

$$\sigma_\zeta = \frac{1}{A_0} = \int_{A_c} dx^2 \delta(\sigma - \sigma_\zeta(x)), \tag{2.79}$$

with A_0, $\sigma_\zeta(x)$, and $\delta(\sigma - \sigma_\zeta)$ are, in turn, the unit nominal contact area, the interface stress, and delta function.

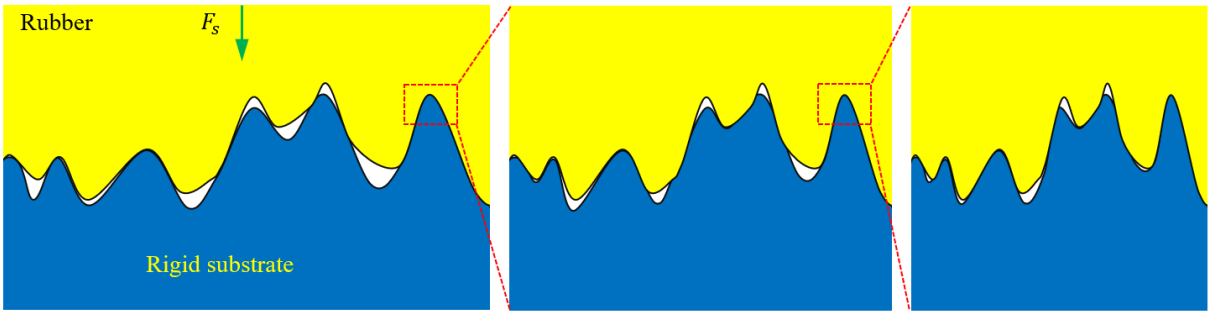

Figure 2.17: Schematic illustration of contact model proposed by Persson in various magnifications a) actual scale, b) scale = 10, and c) scale = 100. This image is after [207].

For entire contact, the distribution stress satisfies the following different equation:

$$\frac{\partial \sigma_\zeta}{\partial \zeta} = \frac{\pi}{4}\left(\frac{1-\epsilon_1^2}{E_1} + \frac{1-\epsilon_2^2}{E_2}\right)^{-2} q_{L_c} q^3 C(q) \frac{\partial^2 \sigma_\zeta}{\partial^2 \sigma}. \tag{2.80}$$

Here, $q_{L_c} = 2\pi/L_c$, $q = \upsilon 2\pi/L_c$, and $C(q)$ is the surface roughness power spectrum:

$$C(\mathbf{q}) = \frac{1}{4\pi^2}\int d^2x \langle h(\mathbf{i})h(0)\rangle e^{-i\mathbf{q}.\mathbf{i}}, \tag{2.81}$$

with $h(\mathbf{i})$ is the height of the surface at the point $i = (i_x, i_y)$ above a reference plane having averaging h_i $\langle h(i)\rangle = 0$. Also, $\mathbf{q} = (q_x, q_y)$ is the frequency or wavevector space. For a self-affine fractal surface, the power spectrum is approximated by:

$$C(q) \propto q^{-2(H+1)}. \tag{2.82}$$

Here, H is the Hurst exponent in the relations of fractal dimension utilizing $D_f = 3 - H$.

2.5.3 Contact Model in Tangential Direction

Tangential contact force $F_{c,t}$ plays an important role in holding objects. In this section, the two bodies come into contact with the contact interface is smooth.

2.5.3.1 Without Slippage

Let us assume that a two opposite contact surface have their displacement dx and $-dx$ for the other and there are no slippage between them (Fig. 2.18(a)). According to [197, 208], the tangential stress distribution at point i is given by:

$$\tau_i = \tau_0 \left[1 - \left(\frac{r_{isi}}{r_{is}}\right)^2\right]^{-0.5}. \tag{2.83}$$

and by denoting G_1, G_2 are the shear modulus of two objects yields the relative displacement between two bodies in the form:

$$u_{rel} = 0.25\pi\tau_0 r_{is}\left(\frac{2-\upsilon_1}{G_1} + \frac{2-\upsilon_2}{G_2}\right). \tag{2.84}$$

2.5.3.2 With Slippage

In this scenario, two spheres, under a squeezing force F_z and simultaneously pulled in the tangential direction with a force $F_{p,t}$, have dry friction with frictional coefficient μ_{isn}, μ_o (Fig. 2.18(b)). According to Coulomb's law [209, 210] the friction force inside the contact equals to:

$$F_{fn} = \begin{cases} \mu_{isn}F_{c,n}, & v_x = 0, dx = 0 \\ \mu_{on}F_{c,n}, & v_x > 0, dx \neq 0 \end{cases}. \tag{2.85}$$

Hence, the tangential stress τ is the sum of two stress components: τ_i and τ_o with:

$$\tau_i = \tau_{i0}\left[1 - \left(\frac{r_{isi}}{is}\right)^2\right]^{0.5} = \mu_{isn}\sigma_i. \tag{2.86}$$

and

$$\tau_o = \tau_{o0}\left[1 - \left(\frac{r_{oi}}{r_o}\right)^2\right]^{0.5} = \mu_o\sigma_i\frac{r_o}{r_{is}}, \tag{2.87}$$

with σ_i is obtained in Eq. (2.74).

Hence, as beginning slide ($r_o = 0$), the body can be displaced in the tangential direction by at the most

$$d_x = \frac{3(2-\upsilon)\mu_{isn}F_s}{16Gr_3}. \tag{2.88}$$

Also the total tangential contact force becomes:

$$F_{c,t} = \mu_{i,o}F_s\left[1 - \left(\frac{r_o}{r_{is}}\right)^3\right]. \tag{2.89}$$

2.6 Contact Mechanics With Wet Adhesion of Normal Pad

Sections 2.2 and 2.3 mentioned the adhesion of the contact between the n-pad and the substrate in cases: flat and curved interface. In such works, we also propose the contact without concerning the deformation of the pad and the substrate. In actual applications of

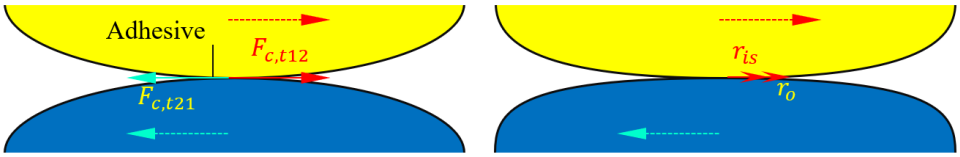

(a) Incipient slip (b) Over slippage

Figure 2.18: Schematic illustration of contact model in tangential direction with a) incipient slippage and b) overt slippage. In this scenario, the contact interface is considered having round shape. Additionally, in figure b), the contact interface includes two regions: without slippage (r_{is}) and slippage (r_o).

soft manipulation, to obtain an efficient grasp the soft robotic fingers require the squeezing force F_s (or preload P) in Eq. (2.66) acting on the objects. Therefore, in this section, we aim to develop our previous works by applying the contact theories to the adhesion model in microscale. For simplicity, the entire n-pad is compressed by a uniform preload $P = A_w.p$ instead of concentration squeezing force F_s. As aforementioned, the n-pad wiped by a thin liquid film before approaching to contact with the substrate. Depending on the film thickness and the roughness surface of the substrate, this liquid can completely or partly cover entire vacant space inside the interface gap. In addition, contact theory of Persson is appropriate to roughness surfaces especially having sine wave. However, the actual soft fragile objects usually have random surfaces with diverse roughness and the deformation is small. For simplicity, we can use the JKR model for calculating the contact mechanics with adhesion.

2.6.1 Contact Mechanics with Wet Adhesion of N-pad in Flat Interface

2.6.1.1 Normal Direction

Complete Wet As shown in Fig. 2.19(a), the the liquid film can cover whole the empty space of the contact interface. We have to consider two conditions of the liquid film: without squeeze out and squeeze out. Determining these conditions in microscale is too complicated.

In case the liquid is not squeezed out, applying Eqs. (2.43) and (2.66) to (2.32) yields the normal contact force $F_{cn,n}$ as followed:

$$F_{cn,n}\langle c-w\rangle = \left(F_{an,n}\langle c-w\rangle + P\right)\hat{z}. \tag{2.90}$$

The force $F_{cn,n}$ in Eq. (2.90) can reach maximum value because the liquid film generate the wet adhesion for entire contact area. In case the liquid is squeezed out, the Laplace

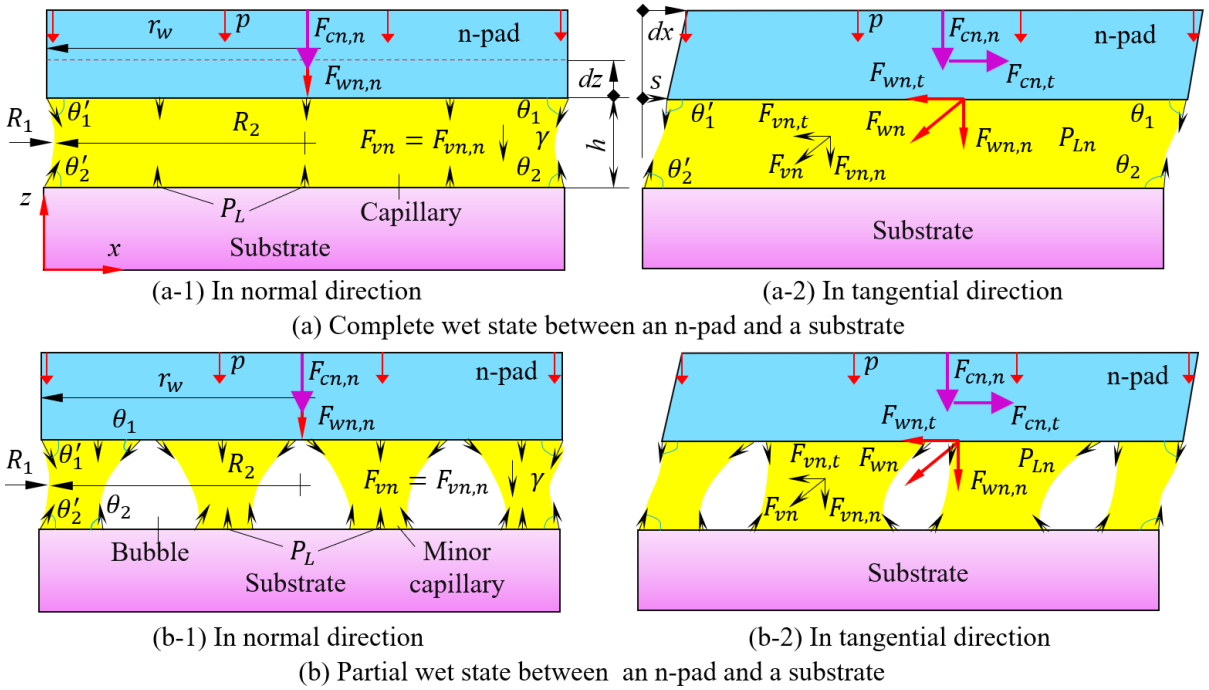

Figure 2.19: Mechanics of the wet adhesion between the n-pad and a flat substrate at interface gap h under distribution preload pressure p. a) The complete wet state between the n-pad and the substrate in a-1) normal and a-2) tangential direction. b) The partial wet state between the n-pad and the substrate in b-1) normal and b-2) tangential direction. For normal direction, the red dot line show varying interface gap h with a small distance dz. In addition, θ_1, $\theta_{1'}$, θ_2 and $\theta_{2'}$ are the contact angles of the liquid capillary bridge.

pressure in Eq. (2.90) becomes negative, which reduce the contact force between the pad and the substrate.

Partial Wet In a similar way, the normal contact force between the n-pad and the substrate in case partial wet is synthesized from Eqs. (2.45), (2.66) and (2.32) in the form:

$$F_{cn,n}\langle p - w\rangle = \left(F_{an,n}\langle p - w\rangle + P\right)\hat{z}. \tag{2.91}$$

2.6.1.2 Tangential Direction

From Eq. (2.85), the tangential contact force $F_{cn,t}$ depends greatly on the normal contact forces $F_{cn,n}$ in Eq. (2.90). We also investigate the force $F_{cn,t}$ in both incipient and overt slippage case.

Incipient Slip The slippery displacement of the contact interface between the n-pad and the substrate is zero, as the tangential peeling force $F_{p,t}$ is not larger than the tangential contact force $F_{cn,t}$. Hence, we can eliminate the viscosity force component $F_{vn,t}$ in the wet

adhesion force $F_{wn,t}$; whereas the surface tension force $F_{stn,t}$ cancels together because the symmetrical contact angle.

By replacing Eqs. (2.85), (2.90), and (2.66) into Eq. (2.32) derives the tangential contact force $F_{cn,t}$ for the contact between the n-pad and the substrate in case complete wet as followed:

$$F_{cn,t}\langle c-w\rangle = \mu_{isn}F_{cn,n}\langle c-w\rangle\hat{x}. \tag{2.92}$$

Also, by replacing Eqs. (2.85), (2.91) and (2.66) into Eq. (2.32) yields the tangential contact force in case partial wet as followed:

$$F_{cn,t}\langle p-w\rangle = \mu_{isn}F_{cn,n}\langle p-w\rangle\hat{x}. \tag{2.93}$$

Overt Slippage When the tangential peeling force $F_{p,t}$ is larger than the contact force $F_{cn,t}$, the slippage gradually appears between the n-pad and substrate surface. Let us denote this slippery displacement is s under conditions: the pad displacement dx and slippery velocity v_x. This motion is simultaneously restricted by the tangential viscosity force $F_{vn,t}$ and the overt slippage friction force $F_{f,o}$. Additionally, the contact angles become more vertical slope which rises the tangential surface tension force $F_{stn,t}$. In addition, the capillary with it radius curvature is in the form: $R_1 = R_1^s = 0.5h\{\cos[\theta_1 + \arctan(s/h)]\cos[\arctan(s/h)]\}^{-1} = 0.5h\{\cos[\theta + \arctan(s/h)]\cos\arctan(s/h)\}^{-1}$ and R_2 is infinitely great with R_1 [107]. Therefore, rising s leads to increasing R_1 which declines the force $F_L = \gamma A_w R_1^{-1}$ of the normal contact force $F_{cn,n}$ - one of the principal component of tangential contact force $F_{cn,t}$.

Synthesizing Eqs. (2.44), (2.85), (2.90) and (2.66) into Eq. (2.32) we have the tangential contact force between the n-pad and substrate $F_{cn,t}$ in case complete wet given by:

$$F_{cn,t}\langle c-w\rangle = \left[\mu_{on}\left(F_{an,n}\langle c-w\rangle + P\right) + F_{an,t}\langle c-w\rangle + \frac{\eta A_w v_x}{h}\right]\hat{x}. \tag{2.94}$$

Also, by replacing Eqs. (2.46), (2.85), (2.91) and (2.66) into Eq. (2.32) yields the tangential contact force in case partial wet as followed:

$$F_{cn,t}\langle p-w\rangle = \left[\mu_{on}\left(F_{an,n}\langle p-w\rangle + P\right) + F_{an,t}\langle p-w\rangle + N_n\langle i\rangle\frac{\eta A_{wi} v_x}{h_i}\right]\hat{x}. \tag{2.95}$$

2.6.2 Contact Mechanics with Wet Adhesion of N-pad in Curved Interface

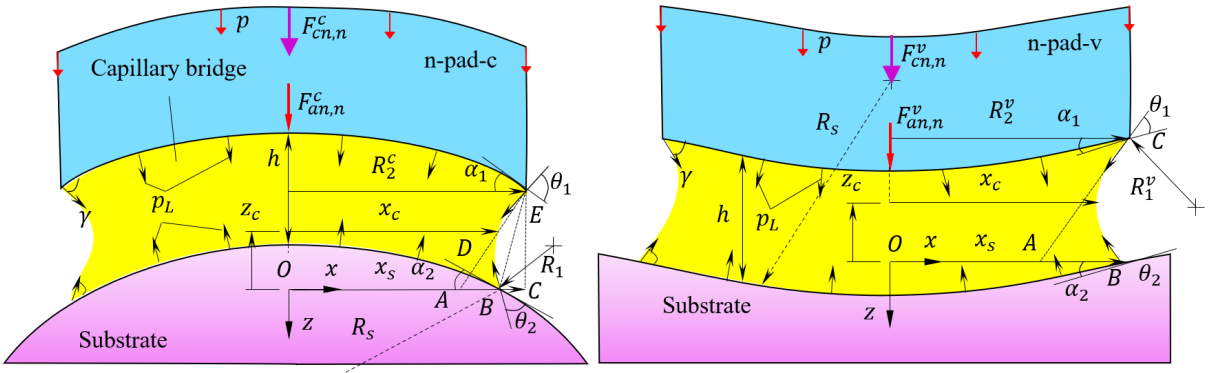

(a) Concave contact interface (b) Convex contact interface

Figure 2.20: Mechanics of the curved contact interfaces between the normal pad and a hemispherical substrate at the interface gap h under preload $P = p.A_w$. There are two cases of the pad: a) concave normal pad (n-pad-c) and b) convex normal pad (n-pad-v).

Since the estimation of tangential contact force between the n-pad and the substrate in curved contact interface is too complicated, we focus on constitute the contact model in normal direction. As shown in Fig. 2.20, the preload P is assumed to equally distributed on the entire contact area of the pads.

2.6.2.1 Complete Wet

It is similar to the flat contact interface case, we have to consider two conditions of the liquid film: without squeeze out and squeeze out. In case the liquid is not squeezed out, applying Eqs. (2.59) and (2.66) to Eq.Eq. (2.32) yeilds the normal contact force $F^{c(v)}_{cn,n}$ as followed:

$$F^{c(v)}_{cn,n}\langle c-w\rangle = \left[F^{c(v)}_{an,n}\langle c-w\rangle + P\right]\hat{z}. \tag{2.96}$$

In case the liquid is squeezed out, the Laplace pressure in Eq. (2.96) becomes negative, which reduce the contact force between the pad and the substrate.

Partial Wet In a similar way, the normal contact force between the n-pad-c(v) and the substrate in case partial wet is synthesized from Eqs. (2.60), (2.66) and (2.32) by the form:

$$F^{c(v)}_{cn,n}\langle p-w\rangle = \left[F^{c(v)}_{an,n}\langle p-w\rangle + P\right]\hat{z}. \tag{2.97}$$

In summary, chapter 2 shows our construction of modelling the contact mechanics between the n-pad (the pad without any patterns) and the substrate in flat and curved contact interfaces. Also this chapter concentrates on calculating the contact force F_{cn} generated by the preload P (squeezing force) of the n-pad. It creates a theoretical foundation for determining the contact mechanics in case micropatterned surface in following chapters.

CHAPTER 3

CONTACT MECHANICS OF WET ADHESION WITH PATTERNED MORPHOLOGY

In this chapter, we introduce proposal of our analytical model of wet adhesion between a contact of a pad designed with micropatterned morphology (m-pad) and a substrate. There are two cases of contact interfaces investigated: flat and curved.

3.1 Design of Patterned Morphology

3.1.1 Flat Contact Interface

As shown in Fig. 3.1, the n- and m-pad have the same overall dimensions with the pad thickness and the edge are t_l, L_p. The m-pad interface includes N square cells (blocks) interspaced by $2N(1-1/\sqrt{N})$ grooves (channels). Hence, the pad edge size is in form $L_p = \sqrt{N}(a+w) - w$. Inspired by the wet attachment of tree frog toe with its surrounding environment, the m-pad in Fig. 3.1(b) is wiped by a thin fluid film with the same thickness t_l at the its contact interface comparing with that of the n-pad. Also, the liquid is available inside the grooves for reducing evaporation and governing the wet adhesion force.

As the n- and m-pad make contact with their corresponding substrate, their contact interfaces form the liquid capillary generating the wet adhesion for enhancement of the contact forces F_{cn}, F_{cm}. For the n-pad, the wet adhesion is already investigated in chapter 2. In case the m-pad, applying Young-Laplace equation (2.21) we have the fluid pressure inside the groove and at the contact interface are γ/r_1 and γ/R_1. Herein, the radii: r_1 approximates to $0.5w/cos\theta_3$ and R_1 equals to $h/(cos\theta_1 + cos\theta_2)$ [108]. As the interface gap h is larger than the groove width w, the pressure inside the groove is larger than

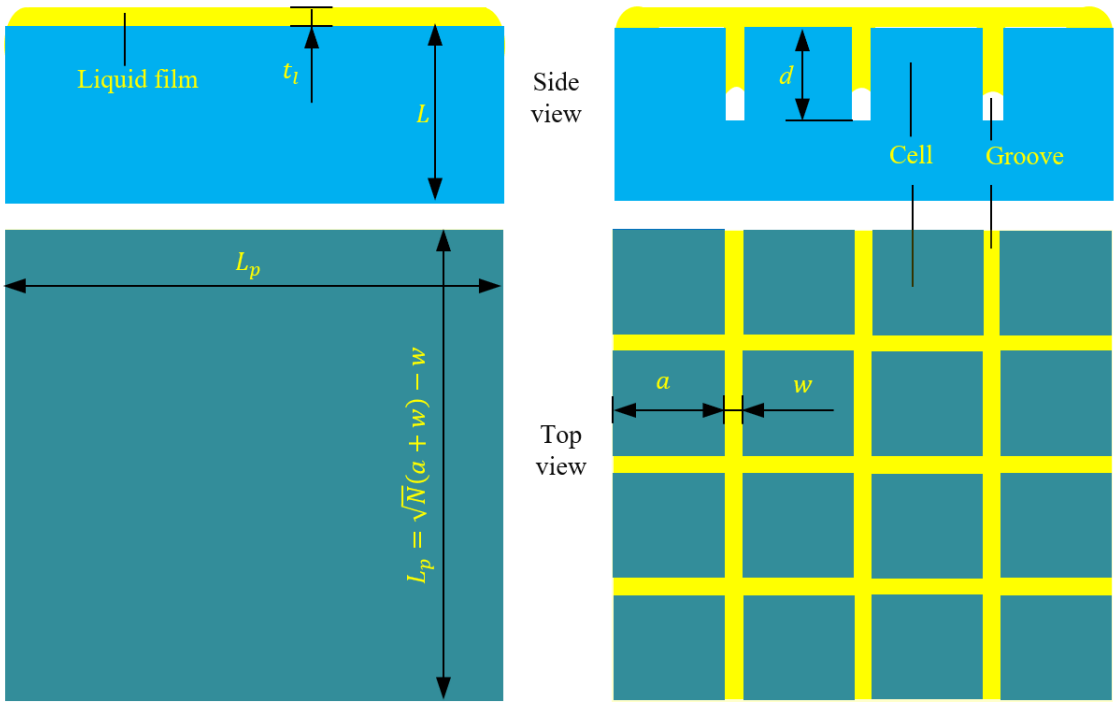

Figure 3.1: Morphological designs of a normal pad (n-pad) and a micropatterned pad (m-pad) in flat contact interface have the same overall dimensions. a) The n-pad (normal surface) is wiped by a thin liquid film. b) The m-pad with an array of N square cells with edge a interspaced by a network of grooves with cross section dimensions w, d are for the width and depth.

that of at the interface, causing liquid evacuation onto the interface [97]. This mechanism strengthens the wet adhesion F_{wm} at the contact interface between the m-pad and substrate. Therefore, for designing a micropatterned morphology, one should concern the groove width in condition of being smaller than the interface gap h. In addition, the liquid film t_l is sufficiently thin to achieve an efficient enhancement of the wet adhesion.

3.1.2 Curved Contact Interface

The m-pad depicted in figure 3.2(a) was designed based on the Fig. 3.1. It comprises of a plain square with N square cells and $2N(1 - 1/\sqrt{N})$ grooves. The width and depth of a groove are denoted as w and d, respectively, and e_c represents the length of a side of a square cell. The length of the pad is equal to $L_p = \sqrt{N}(a + w) - w$. When bent, the soft pad exhibits a concave or convex shape with different radii R_s (according to the substrate) (Fig. 3.2(b) and (c)). The pad was covered of approximate thickness t_l liquid over its entire surface and inside each groove.

When flexed, the micropattern is deformed and the grooves of m-pad-c are compressed to reduce the size of section w_1^c below that of $\bar{w}^c$ (Fig. 3.2(b)); whereas in m-pad-v, w_1^v is larger than $\bar{w}^v$. Since the walls of each groove are not parallel when the pad

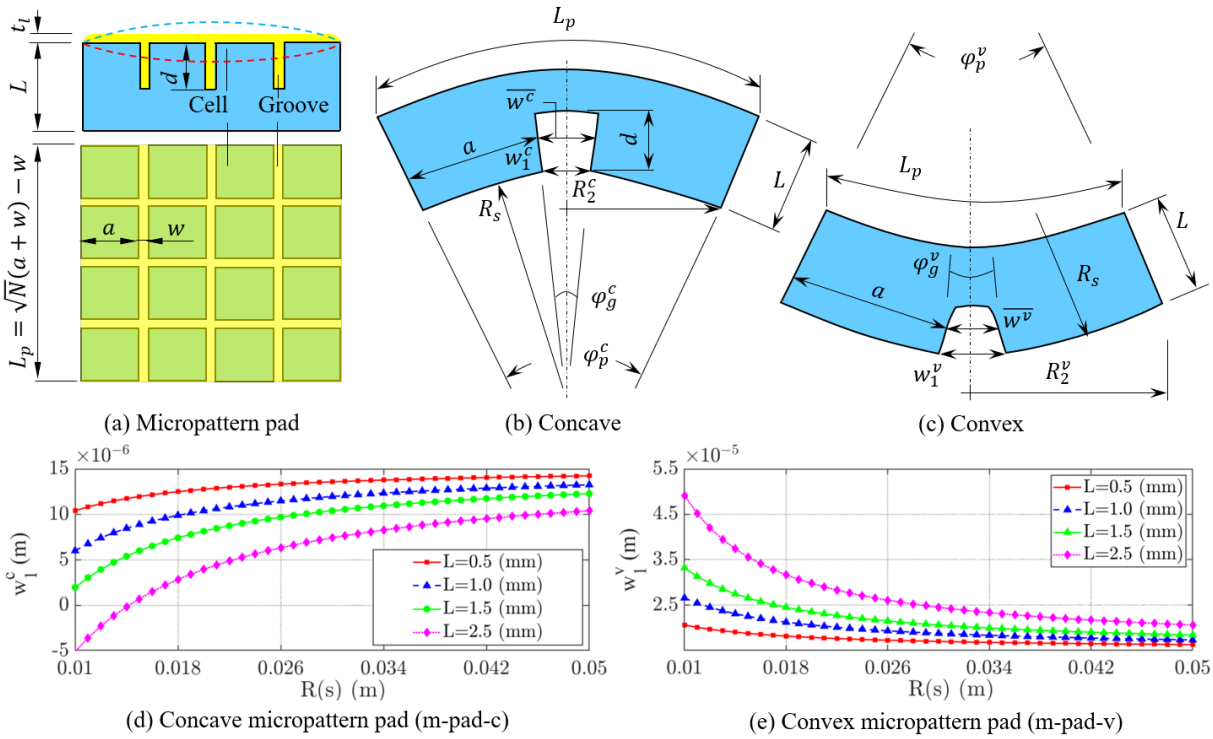

Figure 3.2: Form of m-pad under differential bending states. a) M-pad in a resting state with red and blue curves representing its concave and convex interfaces in a flexed state. Form of the m-pad when flexed to adapt to substrate surface a) concave and b) convex surfaces. d) and e) variations of the groove's width in cases: the m-pad-c and the m-pad-v by changing the pad thickness L and the substrate radius R_s.

is flexed, we approximate the width of a groove as the mean value $w^{c(v)} = \bar{w}^{c(v)}$ at the mid-depth of the groove $(0.5d)$. Let us assume the two boundary walls of the pad and the grooves have their extent lines intersecting at the center of the pad with radius R_s, with $\varphi_p^{c(v)}$, and $\varphi_g^{c(v)}$ denoting the bending angles for each pad and groove respectively, we get $\varphi_p^c = 2\arcsin(R_2^c/R_s)$ for m-pad-c, and $\varphi_p^v = 2\arcsin(R_2^v/R_s)$ for m-pad-v. Hence, with a curve length of L_p, we get $\varphi_g^c = [L_p/(R_s+L) - aN^{0.5}R_s^{-1}]/(N^{0.5}-1)$, $w_1^c = [L_pR_s/(R_s+L) - aN^{0.5}]/(N^{0.5}-1)$, $\bar{w^c} = [L_p(R_s+0.5d)/(R_s+L) - aN^{0.5}]/(N^{0.5}-1)$ in m-pad-c; whereas in m-pad-v with $\varphi_g^v = [L_p/(R_s - L) - aN^{0.5}R_s^{-1}]/(N^{0.5}-1)$, $w_1^v = [L_pR_s/(R_s-L) - aN^{0.5}]/(N^{0.5}-1)$, and $\bar{w^v} = [L_p(R_s-0.5d)/(R_s-L) - aN^{0.5}]/(N^{0.5}-1)$. If $aN^{0.5} \geq R_sL_p/(R_s+L)$, the contact between m-pad-c and the substrate can be considered completely cells-substrate (*i.e.*, the grooves were closed due to concave flexing). As the m-pad and the substrate come into contact, the Laplace pressure of the liquid inside groove P_g and cells P_c are $\gamma/r_1^{c(v)} \sim 2\gamma cos\theta_3/w$ and $\gamma/R_1^{c(v)} \sim \gamma(cos\theta_1 + cos\theta_2)/h$. If $w^{c(v)} < h$, the Laplace pressure P_g is greater than pressure P_c, causing rapid evacuation of liquid onto the surfaces. This enhances capillary force $F_{cam}^{c(v)}$ at the interface between m-pad and substrate. Therefore, the micropattern was designed so that the groove width is smaller than the interface gap $w^{c(v)} < h$.

Figure 3.2(d-e) shows affects of L and R_s on varying the morphology of groove w for m-pad cases under bending. As $R_s \to \infty$ or the curved surfaces gradually change to flat, $\bar{w}$ of both m-pad-c and m-pad-v is proximate 15 μm equaling to the value of w in flat case (no bending). In contrast, $\bar{w}$ of m-pad-c reduces rapidly, corresponding to decline R_s; whereas $\bar{w} \to \infty$ for the m-pad-v. In case $\bar{w} \leq 0$, the m-pad-c becomes n-pad-c, which satisfies the condition $aN^{0.5} \geq R_s L_p/(R_s + L)$, and if $w \to \infty$, then the m-pad-c becomes n-pad-c (the groove disappears). Also there has slight difference between w_1 and $\bar{w}$ because the entity $0.5d$ is infinitesimal to R_s, L_p, and L. Decreasing L leads to reducing trend of $\bar{w}$ in both cases of m-pad. Thus, we neglect calculation of the models as w are much smaller than 15 μm.

3.2 Adhesion of Micro-patterned Pad with Flat Interface

In general, the adhesion generated on the contact between the m-pad and the substrate is the integration of the cells and the adjacent grooves. Hence, applying Eq. (2.29) to the adhesion force F_{am} in case m-pad we have:

$$\mathbf{F_{am}} = \mathbf{F_{am,n}} + \mathbf{F_{am,t}} = \mathbf{F_{dm}}\,|_{\{\mathbf{cell,groove}\}} + \mathbf{F_{wm}}\,|_{\{\mathbf{cell,groove}\}} + \mathbf{F_{ilm}}\,|_{\{\mathbf{cell,groove}\}}. \quad (3.1)$$

The groove in Fig. 3.3 majorly affects the wet adhesion force F_{wm} and the interlock force F_{iln}. Therefore, we can neglect the role of the groove on varying the van der Waal force F_{vdm} and Casimir force F_{C-P}; whereas the cells have the same role as that of the surface of the n-pad. Additionally, Eq. (3.1) is also used for estimating the adhesion in case the curved contact interface.

3.2.1 Normal Adhesion

Similar to the adhesion model in case the n-pad, the contact between the m-pad and the substrate also includes two states: complete wet (the fluid covers entire empty space inside the interface gap h in Fig. 3.3(a)) and partial wet (the fluid covers entire empty space inside the interface gap h in Fig. 3.3(b)).

3.2.1.1 Complete Wet

As shown in Fig. 3.3(a), when the micropatterned pad comes to contact with the flat substrate, four types of contact zone generally forms: A_1- the dry adhesion with without liquid film, A_2- the wet adhesion,A_3- the dry adhesion with an extreme thin liquid film

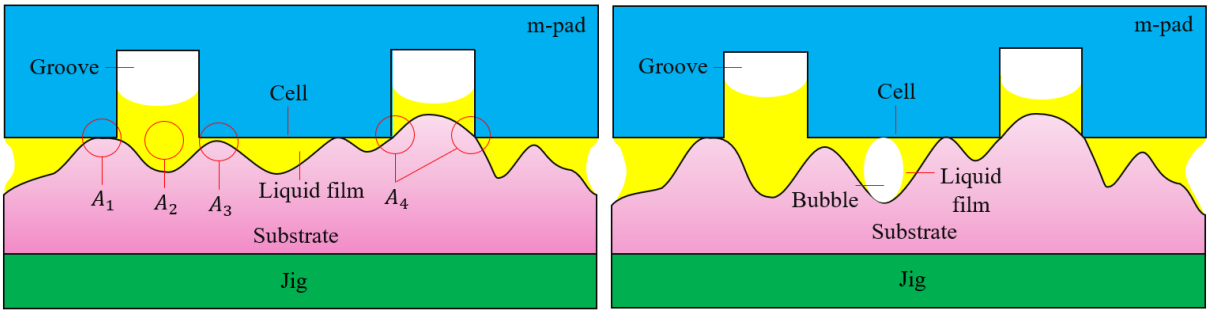

Figure 3.3: Mechanics of the adhesion between the m-pad and a flat substrate at interface gap h. a) The dry and wet adhesion in case complete wet state between the m-pad and the substrate. b) The dry and wet adhesion in case partial wet state between the m-pad and the substrate. In this figure, the areas of dry and wet contact at position i are A_{di} and A_{wi}.

and A_4- the dry adhesion with without liquid film and interlock force. These zones depend on the roughness surface of the substrate, and the properties of the liquid film and the m-pad's morphology. In fact, the cell surface can be considered being completely flat because it is very small and is fabricated by accuracy methods as illustrated in chapter 4. Thus, the surface roughness of the substrate is randomly chosen.

When the liquid film fills entire space inside the interface gap, we can neglect the fluid motion. Herein, for simplicity, the wet adhesion approximates the total of the cells and the grooves.

Attachment State without Preload In static state (Fig. 3.4(a-1)) where there are no change of velocity v_z, the normal viscosity force in grooves $F_{gv,n}$ is infinitesimal; whereas the Laplace force F_L and surface tension F_{st} play the key role on the wet adhesion force F_{wm}. Since the groove network are adjacent to each cell and the fluid can entirely move inside this system, the adhesion also regard the static capillary interaction produced by these channels. In this scenario, the Laplace pressure P_{Lm} includes: pressure inside the groove P_g and the pressure of the cell P_c. In case h is tiny and the groove width satisfies $w < \{a, h\}$, P_g strengthens the Laplace pressure surround the the grooves, while P_c shows the Laplace pressure between the cells and their corresponding substrate. By denoting $n_c = 1 - 1/\sqrt{N}$, the Laplace force F_{Lm} [107] produced by N cells and $2n_cN$ channels is taken in the form:

$$F_{Lm} = \left[\underbrace{\gamma \left(L_p^2 - Na^2 \right) \frac{2cos\theta_3}{w}}_{\text{Groove}} + \underbrace{N\gamma a^2 \frac{cos\theta_1 + cos\theta_2}{h}}_{\text{Cell}} \right] \hat{z}. \tag{3.2}$$

Additionally, each groove has an amount of its surface tension as followed:

$$F_{gs,n} = 2a\gamma \cos\theta_3. \tag{3.3}$$

Hence, replacing Eqs. (3.3), (3.2) to Eq. (2.29) with wet radius of cell $r_{wc} = a\pi^{-0.5}$ and neglecting the curvature radius of the capillary bridge in the grooves r_2, we have the normal wet adhesion force in case m-pad is:

$$F_{wm,n}\langle c-o\rangle = 4N\gamma\Bigg[A_{wg}\frac{\cos\theta_3}{2w} + A_{wc}\frac{\cos\theta_1+\cos\theta_2}{4h} + \underbrace{a\frac{\sin\theta_1}{\sqrt{N}}}_{\text{Surface tension force of cell}} + \underbrace{an_c\cos\theta_3}_{\text{Surface tension force of groove}}\Bigg]\hat{z}. \tag{3.4}$$

As shown in Eq. (3.4), when rising the interface gap h, the normal wet adhesion force declines. Therefore, keeping h as narrow as possible can enhance the force $F_{wm,n}$.

By applying Eqs. (2.43) and (3.4) to Eq. (3.1) yields the normal adhesion force in case the m-pad $F_{am,n}$ in:

$$F_{am,n}\langle c-w\rangle = \left(F_{wm,n}\langle c-o\rangle + F_{dm,n}\right)\hat{z}. \tag{3.5}$$

Attachment State under Preload In order to calculate the normal contact force $F_{cm,n}$ between the m-pad and the substrate, the uniform preload p is also imposed on the entire m-pad with its area is L_p^2 (Fig. 3.4(a-2)). Due to the compression of preload $P = pL_p^2$, the gap h is smaller that induces changing the m-pad morphology. The liquid film quickly suffices the empty space inside the contact [206] and the groove network governs achieving equilibrium state in the entire contact area. Hence, reducing the interface gap h means rising the Laplace force F_{Lm}, whereas the fluid motion does not exist both inside the channels and in the cell which allows us to eliminate the viscosity component $F_{vm,n}$. The contact force generated from the m-pad in normal direction $F_{cm,n}$ additionally consists of the surface tensions inside the grooves $F_{gs,n}$ and the m-pad periphery F_{stm}. The deformation of the m-pad can make the groove width w become narrower, which varies the adhesion properties in the contact area between the m-pad and the substrate. This leads to vanishing of the bubbles inside the contact. By accounting the preload P in Eq. (3.4) we have the normal contact force in case the m-pad $F_{cm,n}$ as followed:

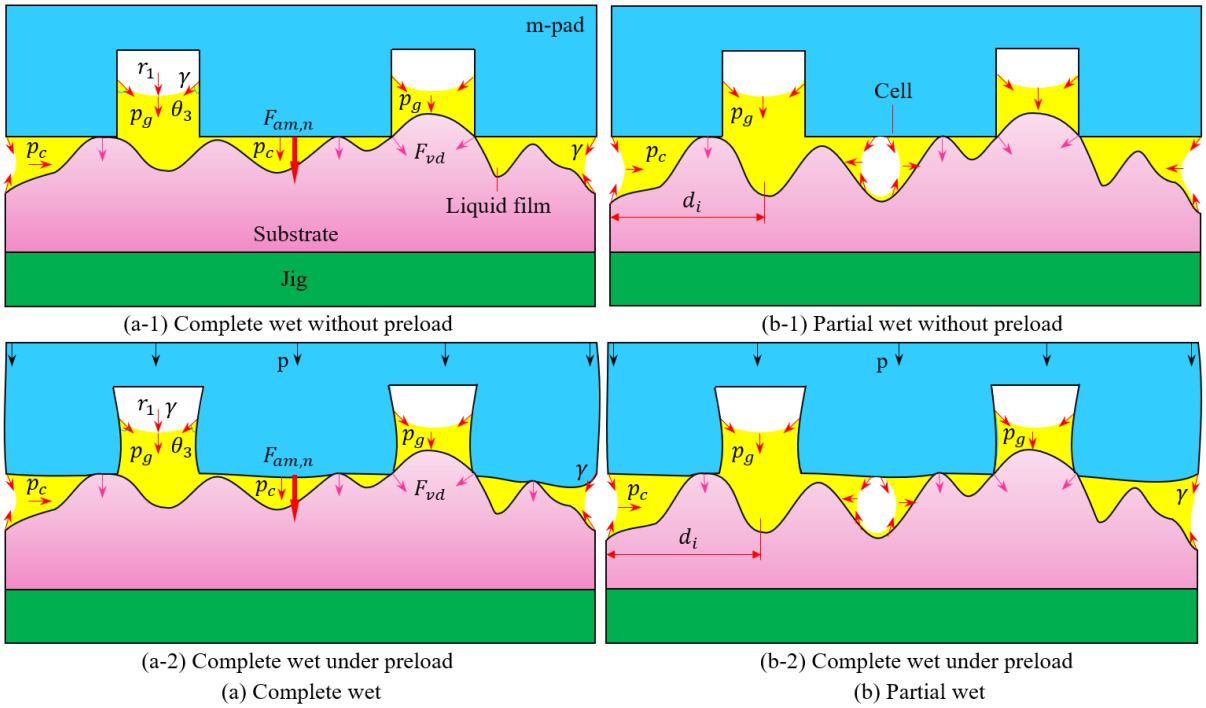

Figure 3.4: Mechanics of the adhesion between the m-pad and a flat substrate at interface gap h. a) The adhesion in case complete wet state between the m-pad and the substrate in a-1) without preload and a-2) under preload. b) The adhesion in case partial wet state between the m-pad and the substrate in b-1) without preload and b-2) under preload.

$$F_{cm,n} = [P + F_{am,n}\langle c - w \rangle]\,\hat{z}. \tag{3.6}$$

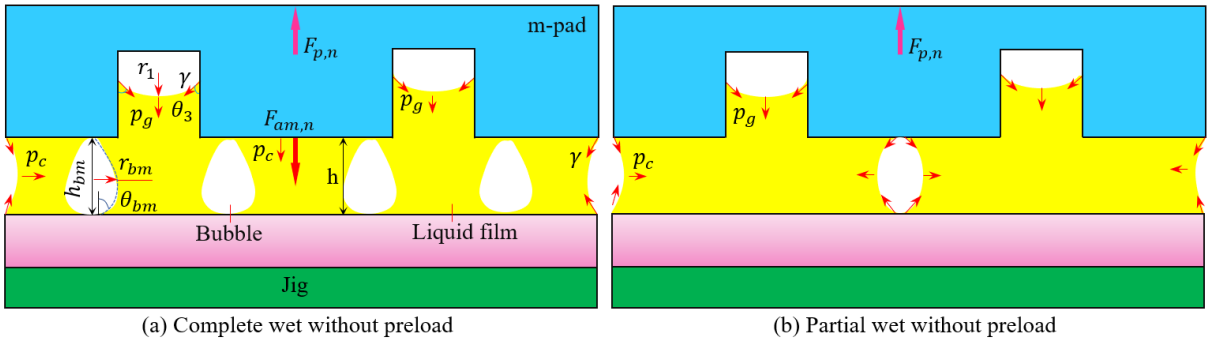

Figure 3.5: Mechanics of the adhesion between the m-pad and a flat substrate under peeling force $F_{p,n}$ at interface gap h. a) The adhesion between the m-pad and the substrate in case complete wet state a) and partial wet b).

Detachment State When increasing the interface gap h, the normal wet adhesion force in case m-pad $F_{wm,n}$ starts to drop after passing their maximum value at the peak interface gap h_p. At this point, the gradual appearance of bubbles separate the capillary bridge into minor bridges as in Fig. 3.4(b-1). It is similar to modelling the bubble in case the

n-pad, we also have the wet radius of minor capillary bridge i as followed:

$$A_{wi} = \pi \left[r_{wi} - \frac{g_{h_i} f_m(h_i)}{4} \left(\frac{1}{\sin\theta_{bm1i}} + \frac{1}{\sin\theta_{bm2i}} - \frac{1}{\tan\theta_{bm1i}} - \frac{1}{\tan\theta_{bm2i}} \right) \right]^2. \tag{3.7}$$

In normal detachment phase, the m-pad interface does not directly contact with its substrate, the normal wet adhesion force $F_{wm,n}$ majorly depends on the minor capillary bridges. Determining the force $F_{wm,n}$ in this scenario is similar to that of the Eq. (3.4) with regarding A_{wgi}, A_{wci} use Eq. (3.6). By replacing the wetting areas in Eq. (3.7) into Eq. (3.5), the normal adhesion of the contact between the m-pad and the substrate becomes:

$$F_{am,n}\langle c - w \rangle = \left\{ \gamma \left[\iint_{A_w} \left(A_{wgi} \frac{\cos\theta_3}{2w} + A_{wci} \frac{\cos\theta_1 + \cos\theta_2}{4h} \right) dA_w + 8N\pi r_{wci} \left(\frac{\sin\theta_1}{\sqrt{N}} + n_c \cos\theta_3 \right) \right] + F_{vm,n} + F_{vg,t} + F_{dm,n} \right\} \hat{z}, \tag{3.8}$$

with $F_{vm,n} = [0.75N\pi\eta r_{2i}^4/dt](1/h^2 - 1/h_0^2)$ and $F_{vg,t} = Nn_c\eta A_{wgi} v_{gl}/w$.

3.2.1.2 Partial Wet

Attachment State Without Preload As the liquid partially fills the interface gap as shown in Fig. 3.4(b-1), the bubbles appear inside the capillary which randomly form the minor capillaries. However, since the liquid is contained inside the grooves and in continuity condition, we can assume that those such bubbles only exist at the contact interface between the cells and substrate. Also the wet adhesion force F_{wm} also comprises of the capillary force generated by the cells and the grooves. In this scenario, the fluid flows both inside the channels and in the cell surfaces before reaching equilibrium state. Thus, the kinetics of fluid motion should be investigated for estimation of the adhesion interaction.

Let us assume that the liquid film between the m-pad and the substrate is a Newtonian and imcompressible fluid, which can be used the Navier-Stocke equation in the form:

$$\rho_l \left(\frac{\partial v_f}{\partial t} + v_f . \nabla v_f \right) - \eta \nabla^2 v_f = -\nabla p_f - \nabla \Im + F_g, \tag{3.9}$$

where $\nabla\Im, F_g, t$ the thermaldynamic work, the gravity force and time, and v_f, p_f, ρ_f present the velocity, pressure and mass density of the fluid. In tiny interface gap h we can neglect the gravity force F_g and the thermal dynamic $\nabla\Im$ in Eq. (3.9); whereas for the

imcompressible continuity fluid flow with a constant velocity, we have:

$$\nabla v_f = \frac{\partial v_f}{\partial x} + \frac{\partial v_f}{\partial y} + \frac{\partial v_f}{\partial z} = 0. \tag{3.10}$$

Combining Eq. (3.9) and (3.10) we can rewrite the Navier-Stokes equation in the form of:

$$\rho_l \frac{\partial v_f}{t} + \nabla p_f - \eta \nabla^2 v_f = 0. \tag{3.11}$$

In Fig. 3.4(b-1), if the liquid at one groove i flows with a symmetrical distance d_i and the interface gap h_i is smaller than w, the fluid flows out of the groove due to $p_g < p_c$. According to [211], we have the travel distance of the fluid between the cell and the substrate in the following relation:

$$\frac{\partial p_f}{\partial x} = \frac{\gamma(\cos\theta_1 + \cos\theta_2)}{h_i d_i}. \tag{3.12}$$

The velocity of the fluid in z-direction can be approximated in:

$$v_{fz} = 6\bar{v}_{f_{x,y}} z(h_i - z)/h_i^2, \tag{3.13}$$

with $\bar{v}_{f_{x,y}}$ is the mean velocity of the fluid in x, y directions. From Eq. (3.12), we have the peak and mean velocity of the fluid as followed:

$$\begin{aligned} max\{v_{fz}\} &= \frac{\gamma(\cos\theta_1 + \cos\theta_2)h_i}{8\eta d_i}, \\ \bar{v}_{f_{x,y}} &= \frac{\gamma(\cos\theta_1 + \cos\theta_2)h_i}{12\eta d_i}. \end{aligned} \tag{3.14}$$

In addition, the pressures p_{c_i}, p_{g_i} at $x_i = d_i$ are $\gamma(\cos\theta_1 + \cos\theta_2)/h_i$ and 0, and that of at the center groove $x_i = 0$ are 0 and $2\gamma(\cos\theta_3)/w$. Thus, we have:

$$\frac{\partial p_f}{\partial x} \sim \frac{\gamma}{d_i}\left(\frac{\cos\theta_1 + \cos\theta_2}{h_i} - \frac{2\cos\theta_3}{w}\right). \tag{3.15}$$

Hence, by replacing Equations (3.13) to (3.15) into Eq. (3.11) with regarding the v_f in equilibrium state derives:

$$\frac{\gamma}{d_i}\left(\frac{\cos\theta_1 + \cos\theta_2}{h_i} - \frac{2\cos\theta_3}{w}\right) \approx \frac{12\eta}{h_i^2}\frac{dd_i}{dt}, \tag{3.16}$$

with $dd_i = \bar{v}_{f_{x,y}}$. From Eq. (3.16), we have the travel distance in the form:

$$d_i = h_i\sqrt{\left(\frac{\cos\theta_1 + \cos\theta_2}{h_i} - \frac{2\cos\theta_3}{w}\right)\frac{\gamma dt}{6\eta}}. \tag{3.17}$$

Eq. (3.17) shows the relation between the travel distance d_i and other parameters in the wet adhesion system. It also presents the time t, which is used to calculate the mean velocity $\bar{v}_{f_{x,y}}$. In this scenario, the pressure of the contact between cell-substrate and groove-substrate are equal to $\gamma[(\cos\theta_1 + \cos\theta_2)/h - cos\theta_3/w]$ as shown in Eq. (3.15). Hence, by combining Eqs. (3.1) and (3.15) yields the normal adhesion force between the m-pad and the substrate in case partial wet without preload as followed:

$$F_{am,n}\langle p - w\rangle = \left\{ 4\gamma \sum_{i=1}^{Nn_c} \left[A_{wi}\langle d_i\rangle \left(\frac{\cos\theta_1 + \cos\theta_2}{4h} - \frac{\cos\theta_3}{2w} \right) + a\cos\theta_3 \right.\right. \\ \left.\left. + P_{wi}\langle d_i\rangle \sin\theta_1 \right] + F_{dm,n} \right\} \hat{z}. \tag{3.18}$$

Here, $A_{wi}\langle d_i\rangle, P_{wi}\langle d_i\rangle$ are the wetting area and periphery at the groove having travel distance of liquid d_i. In case the groove width is smaller than the interface gap h_i, the fluid flows backward the groove because the suction pressure inside the channel is higher than that of the cell. Hence, the normal adhesion force in Eq. (3.18) is rewritten by:

$$F_{am,n}\langle p - w\rangle = \left\{ 4\gamma \sum_{i=1}^{Nn_c} \left[A_{wi}\langle d_i\rangle \left(\frac{\cos\theta_3}{2w} - \frac{\cos\theta_1 + \cos\theta_2}{4h} \right) + P_{wi}\langle d_i\rangle \sin\theta_1 \right.\right. \\ \left.\left. + a\cos\theta_3 \right] + F_{dm,n} \right\} \hat{z}. \tag{3.19}$$

Attachment State Under Preload When imposing the uniform preload p (Fig. 3.4(b-2)) in the entire m-pad, the interface gap h reduces because the morphological deformation of the m-pad makes its own surface easily in contact with the substrate asperities. If the liquid film can sufficiently fill in the empty space, the adhesion in this scenario is calculated in a similar way to the complete wet case. As a result, let us assume that the liquid generated a partial wet for the contact interface. By combining Eqs. (3.1) and (3.18) yields the normal adhesion in case $w > h$ as followed:

$$F_{cm,n} = \left\{ P + 4\gamma \sum_{i=1}^{Nn_c} \left[A_{wi}\langle d_i\rangle \left(\frac{\cos\theta_1 + \cos\theta_2}{4h} - \frac{\cos\theta_3}{2w} \right) + P_{wi}\langle d_i\rangle \sin\theta_1 \right.\right. \\ \left.\left. + a\cos\theta_3 \right] + F_{dm,n} \right\} \hat{z}, \tag{3.20}$$

and in case $w < h$ we have:

$$F_{cm,n} = \left\{ P + 4\gamma \sum_{i=1}^{Nn_c} \left[A_{wi} \langle d_i \rangle \left(\frac{\cos\theta_3}{2w} - \frac{\cos\theta_1 + \cos\theta_2}{4h} \right) + P_{wi} \langle d_i \rangle \sin\theta_1 \right. \right.$$
$$\left. \left. + a\cos\theta_3 \right] + F_{dm,n} \right\} \hat{z}. \qquad (3.21)$$

As the surface roughness of the substrate is random, the conditions $w < h$ and $w > h$ may happen at the same time. Thus, in a specific case, the eqs. (3.20) and (3.21) can be utilized together. Furthermore, eqs. (3.18) to (3.21) reveal that in case partial wet the micropattern can enhance or weaken the wet adhesion between the m-pad and the substrate comparing with that of the n-pad. It is resulted in the ratio of w/h.

3.2.1.3 Detachment Phase

When peeling the m-pad from the substrate under the normal peeling force $F_{p,n}$, the van der Waals force and Casimir force rapidly drop; whereas the wet adhesion gradually declines before passing the peak interface gap. In this scenario, the minor capillaries already appear, we may neglect the bubble appearance as mentioned in the complete wet case. Hence, by applying Eq. (3.19) to (3.8) derives the normal adhesion force in the following form:

$$F_{am,n}\langle p - w \rangle = \left\{ 4\gamma \sum_{i=1}^{Nn_c} \left[A_{wi} \langle d_i \rangle \left(\frac{\cos\theta_3}{2w} - \frac{\cos\theta_1 + \cos\theta_2}{4h} \right) + P_{wi} \langle d_i \rangle \sin\theta_1 \right. \right.$$
$$\left. \left. + a\cos\theta_3 \right] + \sum F_{vm,n}\langle i \rangle + \sum F_{vm,n}\langle i \rangle + F_{dm,n} \right\} \hat{z}. \qquad (3.22)$$

In detachment phase, the interface gap h is much larger than the groove width w, Eq. (3.22) is applied to the partial wet in condition $w < h$. In case $w > h$, the normal adhesion can be calculated Eq. (3.18).

3.2.2 Tangential Direction

As shown in Figs. 3.6 and 3.7, the m-pad is simultaneously exerted by two orthogonal forces preload P and the peeling force $F_{p,t}$ in normal and tangential direction, respectively. The slide trend is restricted by the integration of the friction force F_{fm} and the adhesion force F_{am}. It is similar to the estimation in case the n-pad, the difference of the tangential contact force $F_{cm,t}$ and the tangential peeling force $F_{p,t}$ also induces two cases of tangential motion: incipient slippage and over slippage.

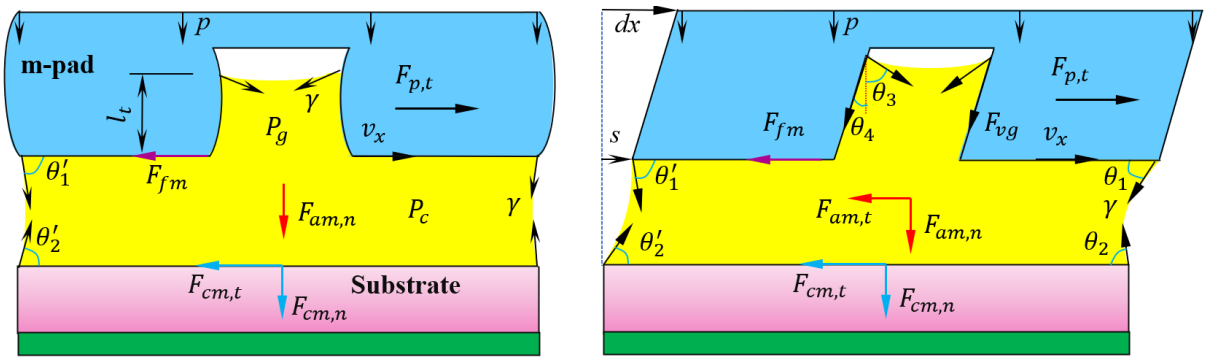

(a) Incipient slip (b) Overt slippage

Figure 3.6: Scheme illustration of the adhesion between the m-pad and a flat substrate under tangential peeling force $F_{p,t}$ in case complete wet. a) The tangential adhesion between the m-pad and the substrate in case incipient slippage a) and over slippage b).

3.2.2.1 Complete Wet

Incipient Slippage As the relation $F_{p,t} < F_{cm,t}$ appears, the slippery displacement between the contact interface of the m-pad and the substrate s is closed to zero in Fig. 3.6(a). We can neglect the tangential viscosity force $F_{vm,t}$ on both the cells and inside the channels. Additionally, the total tangential surface tension $F_{stm,t}$ is zero due to their symmetry vectors. Therefore, the tangential contact force $F_{cm,t}$ is calculated by replacing the right hand side of Eq. (3.6) into Eq. (2.85):

$$F_{cm,t} = \mu_{ism} \left(P + F_{am,n} \langle c - w \rangle\right) \hat{x}. \tag{3.23}$$

Overt Slippage As the tangential peeling force $F_{p,t}$ is larger than the tangential contact force $F_{cm,t}$, slippage s between the contact interface of the m-pad and substrate appears; whereas, the m-pad has a displacement dx under a slip velocity v_x (Fig. 3.6(b). In this scenario, the friction force $F_{fm,o}$ and the adhesion force F_{am} resists the overt slippage motion. Also the wet adhesion force F_{wm} additionally have the tangential viscosity force $F_{vm,t}$ in the cell surface and inside the grooves. At that time, the contact angles $\theta_1, \theta_{1'}, \theta_2, \theta_{2'}$ change, which vary the surface tension force $F_{stm,t}$ in tangential direction. The liquid inside the channels flows out that exerts the viscosity force F_{vg} on the groove side walls of the m-pad.

By synthesizing Eqs. (3.6), (2.41) (2.48) and (2.85) with the denotation $\theta_4 = \arctan(s/l_t)$ we have the tangential contact force in case the m-pad contacting with the substrate as followed:

$$F_{cm,t} = \Bigg[P\mu_{om} + 4N\mu_{om}\gamma \sum_{i=1}^{N} \Bigg(A_{wgi}\frac{\cos\theta_3}{2w} + A_{wci}R_i^s + a\frac{\sin\theta_1}{\sqrt{N}} + an_c\cos\theta_3 + F_{vg,t}\cos\theta_4 \Bigg) + F_{vg,t}\sin\theta_4 + \frac{L_p^2 v_x}{h} + F_{dm,n} \Bigg] \hat{x}. \tag{3.24}$$

3.2.2.2 Partial Wet

In case the liquid partially covers the contact interface as shown in Fig. 3.7, the minor capillaries are assumed to have the same contact angle with $\theta_1, \theta_{1'}, \theta_2, \theta_{2'}$. We also investigate the contact force $F_{cm,t}$ in conditions: incipient slip and over slippage.

Incipient Slip In incipient slip state, where the slip does not appear between the contact interface $s = 0$ (Fig. 3.7(a)), the viscosity forces at the cell surfaces and inside grooves are neglected. In this scenario, the peeling force balances against the tangential contact force. Thus, by synthesizing Eq. (3.21) into Eq. (2.85), we have the tangential contact force $F_{cm,t}$ in case $w < h$ in the form:

$$F_{cm,t} = \mu_{ism}\left(P + F_{am,n}\langle p - w\rangle\right)\hat{x}. \tag{3.25}$$

In case $h < w$, the calculation in Eq. (3.25) is the combination of Eqs. (3.20) into Eq. (2.85).

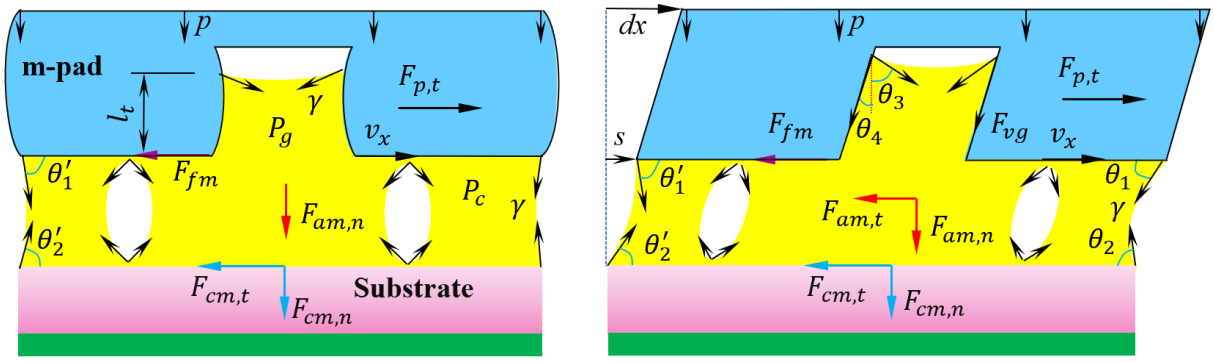

(a) Incipient slip (b) Overt slippage

Figure 3.7: Scheme illustration of the adhesion between the m-pad and a flat substrate under tangential peeling force $F_{p,t}$ in case partial wet. a) The tangential adhesion between the m-pad and the substrate in case incipient slippage a) and overt slippage b).

Overt Slippage When the force $F_{p,t}$ is larger than the the contact force generated from the friction and the adhesion force, it appears a slip with a distance s between the m-pad

and the substrate as shown in Fig. 3.7(b). In this situation, we consider the slipped distance s is small, and each minor capillary have four contact angles $\theta_1, \theta_{1'}, \theta_2, \theta_{2'}$. Hence, by synthesizing Eqs. (2.41), (2.48), and (3.21) into Eq. (2.85), the tangential contact force $F_{cm,t}$ in this situation becomes:

$$F_{cm,t} = \Bigg\{ \mu_{om} P + 4\mu_{om} \sum_{i=1}^{Nn_c} \gamma \Bigg[A_{wi} \langle d_i, R_i^s \rangle \left(\frac{\cos\theta_3}{2w} - \frac{\cos\theta_1 + \cos\theta_2}{4h} \right) + P_{wi} \langle d_i, R_i^s \rangle \frac{\sin\theta_1}{n_c} + F_{vg,t} \cos\theta_4 + a\cos\theta_3 \Bigg] + 2Nn_c \left(F_{vg,t} \sin\theta_4 + \frac{A_{wi} \langle d_i, R_i^s \rangle v_x}{h_i} \right) + F_{dm,n} \Bigg\} \hat{x}. \tag{3.26}$$

In this section, the contact between the m-pad and the substrate have a higher interlock force F_{il} than that of the n-pad case due to the asperities of the surface roughness are easier to penetrate the grooves. For simplicity, this force is considered as a component of friction force F_{fm} with $\mu_{om} \geq \mu_{on}$ and $\mu_{ism} \geq \mu_{isn}$, and neglected in the calculations.

3.3 Adhesion of Micro-patterned Pad with Curved Interface

In this section, two different kinds of the curved contact interface are investigated to understanding physic of the adhesion between the contact of the m-pad and the substrate. Herein, the m-pad having two curved interface concave and convex shape, respectively called m-pad-c and m-pad-v (Fig. 3.2) make contact with their corresponding hemispherical substrates (Fig. 3.8). In addition, each couple of surfaces in each curved interface is assumed to be parallel (interface gap h is same in the entire contact). In this scenario, we also limit our research in constructing contact model in the normal direction.

3.3.1 Normal Attachment Without Preload

When contacting with the substrate without preload P, the m-pad-c(v) are considered having no deformation. In this situation, we also calculate the adhesion in two cases: the liquid fully or partially covers the empty space of the interface gap.

3.3.1.1 Complete Wet

In Fig. 3.8(a) where the attachment velocity of the m-pad-c(v) v_z is approximately zero, it is possible to neglect the normal viscosity forces in grooves $F_{gv,n}^{c(v)}$; whereas the Laplace forces $F_{Lm}^{c(v)}$ and the surface tension forces $F_{stm}^{c(v)}$ are primary components of the wet adhesion. In

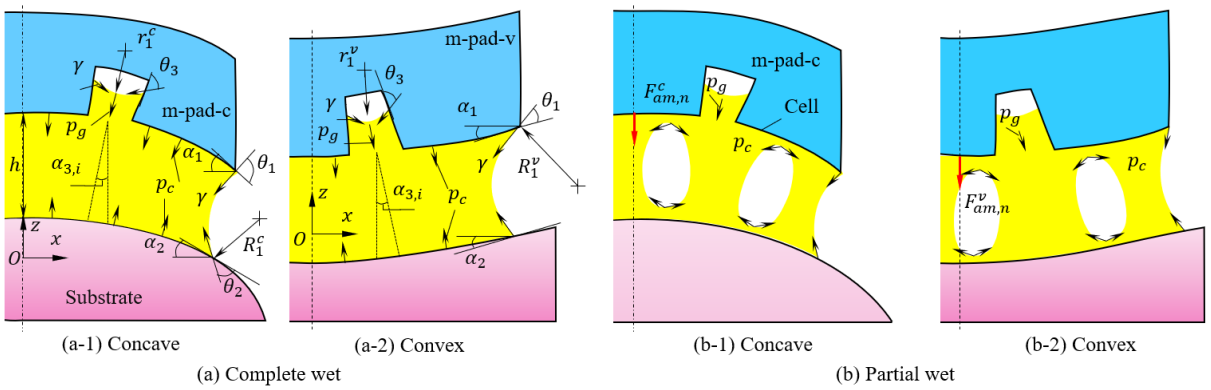

Figure 3.8: Scheme illustration of the adhesion between the micropatterned pad with concave and convex interface in contacting with their corresponding substrate. The m-pad-c(v) make complete wet a) and partial wet b) with the substrate. a-1) and b-1) show the contact model of the m-pad-c; whereas a-2) and b-2) demonstrate the contact model of the m-pad-v.

this scenario, the Laplace pressures $P_{Lm}^{c(v)}$ consist of two components, pressure within the groove channel P_g and that outside P_c which act together. Hence, the Laplace forces for m-pad-c and m-pad-v can be estimated as:

$$F_{Lm}^{c(v)} = \gamma \left[\underbrace{2w_1^{c(v)}(a + w_1^{c(v)}) \cos\theta_3 \sum_{i=1}^{2Nnc} \frac{\cos\alpha_{3i}}{\bar{w}^{c(v)}}}_{\text{Groove}} + \underbrace{a^2 \sum_{i=1}^{N} \frac{\cos\alpha_{3j}}{R_1^{c(v)}}}_{\text{Groove}} \right] \hat{z}, \tag{3.27}$$

where α_{3i}, α_{3j} are in turn the inclined angle of the groove i and the cell j comparing with z-axis. For two consecutive grooves or cells, the deviations are $\alpha_{3i} = i(a + w_1^{c(v)})/R_s$ and $\alpha_{3j} = (j + 0.5)(a + w_1^{c(v)})/R_s$. Additionally, on the assumption that the contact angles between two side walls of a groove always equal θ_3, we determine the surface tension force for each groove in the normal direction $F_{gs,n}^{c(v)} = 2a\gamma \cos\alpha_{3i} \cos(\theta_3 \pm 0.5\varphi_g^{c(v)})$ with sign " $+$ " and " $-$ " being respective to cases: m-pad-c and m-pad-v. The whole pattern of the m-pads including N cells and $2Nn_c$ grooves has a normal surface tension as followed:

$$F_{gs,n}^{c(v)} = 2a\gamma \cos(\theta_3 \pm 0.5\varphi_g^{c(v)}) \sum_{i=1}^{2Nn_c} \cos\alpha_{3i}\hat{z}. \tag{3.28}$$

By denoting $F_{stm,n}^{c(v)} = 2\pi\gamma R_s \sin\alpha_2 \sin\beta_1^{c(v)}\hat{z}$ derived the normal wet adhesion forces as followed:

$$F_{wm,n}^{c(v)} = F_{Lm}^{c(v)} + F_{gs,n}^{c(v)} + F_{stm,n}^{c(v)}. \tag{3.29}$$

By replacing Eqs. (2.42) and (3.29) into Eq. (3.1) yields the normal adhesion force $F_{am,n}^{c(v)}$ in the form:

$$F_{am,n}^{c(v)}\langle c-w\rangle = \left(F_{wm,n}^{c(v)} + F_{dm,n}^{c(v)}\right)\hat{z}, \tag{3.30}$$

3.3.1.2 Partial Wet

The similar approach in the contact between the m-pad and the substrate in case flat interface, when the fluid partially covers the empty space inside interface gap, the liquid film also separated into many minor capillary bridges (Fig. 3.8(b)). In this scenario, we also assume that each groove creates a minor capillary which interspaces with the other through a bubble at the middle of the cell. As the interface gap h_i of the minor capillary i is smaller than the width of the groove w, the liquid inside the channel is sucked out. Thus, to calculate the normal adhesion force $F_{am,n}^{c(v)}$ it can apply Eq. (3.18) to Eq. (3.30) as shown in the form:

$$F_{am,n}^{c(v)}\langle p-w\rangle = \left\{\gamma\left[\sum_{i=1}^{Nn_c} A_{wi}\langle d_i\rangle\cos\alpha_{3i}\left(\frac{1}{R_1^{c(v)}} - \frac{2\cos\theta_3}{\bar{w}^{c(v)}}\right) + \sum_{i=1}^{Nn_c} P_{wi}\langle d_i\rangle\sin(\theta_1+\alpha_{3i}) + \cos\left(\theta_3 \pm 0.5\varphi_g^{c(v)}\right)\sum_{i=1}^{2Nn_c}\cos\alpha_{3i}\right] + F_{dm,n}^{c(v)}\right\}\hat{z}. \tag{3.31}$$

In case $w < h$, we have:

$$F_{am,n}^{c(v)}\langle p-w\rangle = \left\{\gamma\left[\sum_{i=1}^{Nn_c} A_{wi}\langle d_i\rangle\cos\alpha_{3i}\left(\frac{2\cos\theta_3}{\bar{w}^{c(v)}} - \frac{1}{R_1^{c(v)}}\right) + \sum_{i=1}^{Nn_c} P_{wi}\langle d_i\rangle\sin(\theta_1+\alpha_{3i}) + \cos\left(\theta_3 \pm 0.5\varphi_g^{c(v)}\right)\sum_{i=1}^{2Nn_c}\cos\alpha_{3i}\right] + F_{dm,n}^{c(v)}\right\}\hat{z}. \tag{3.32}$$

3.3.2 Normal Attachment Under Preload

In this scenario, we investigated the normal contact force $F_{c,n}^{c(v)}$ when imposing the uniform preload p on the whole interface of a pad $\pi(R_2^{c(v)})^2$ (Fig. 3.9). Under compression by preload $P = p\pi(R_2^{c(v)})^2$, h reduced, changing the morphological structure of the pad; simultaneously the liquid moves rapidly to fill the space between the two surfaces, while the groove channels continuously suck and distribute fluid throughout the entire contact area until equilibrium is reached. Normal compressed deformation can narrow the width of the grooves $\bar{w}^{c(v)}$ to enhance the contact area of the pad with the substrate, resulting in disappearance of the bubbles.

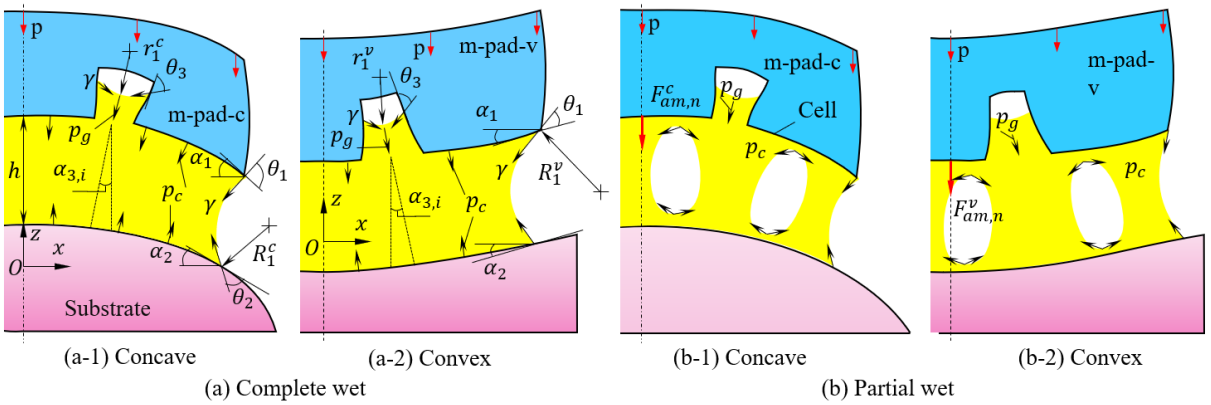

Figure 3.9: Scheme illustration of the adhesion between the micropatterned pad with concave and convex interface in contacting with their corresponding substrate under an imposed preload P. The m-pad-c(v) make complete wet a) and partial wet b) with the substrate. a-1) and b-1) show the contact model of the m-pad-c; whereas a-2) and b-2) demonstrate the contact model of the m-pad-v.

Complete Wet In case complete wet state (Fig. (3.9(a)), adding the preload P to Eq. (3.30) yields the normal contact forces for the m-pad-c and the m-pad-v as followed:

$$F_{cm,n}^{c(v)} = \left(P + F_{am,n}^{c(v)} \langle c - w \rangle\right) \hat{z}, \tag{3.33}$$

Partial Wet As the liquid partially covers the interface gap (Fig. (3.9(b)), adding the preload P to Eq. (3.31) yields the normal contact forces for the m-pad-c and the m-pad-v in condition $h < w$ as followed:

$$F_{cm,n}^{c(v)} = \left(P + F_{am,n}^{c(v)} \langle p - w \rangle\right) \hat{z}. \tag{3.34}$$

Additionally, determining the normal adhesion force of the contact between the m-pad-c(v) and the substrate in case partial wet with $w > h$ is similar to that of in case $h < w$. Herein, we also add the preload P to Eq. (3.36) for this calculation.

Eq. (3.33) and (3.34) show a method to determine contact force in the case of wet adhesion under preload P. In this study, we consider the preload P sets a maximum value which does not generate the large deformation for the pad's surface during contacting. This value depending on the material property and morphology of the pad and the roughness of the substrate can be evaluated in experiments. In actual application, reducing P applied to the surface of a substrate is necessary to save objects. Thus, it is possible to neglect the case of a large preload.

3.3.3 Detachment Phase

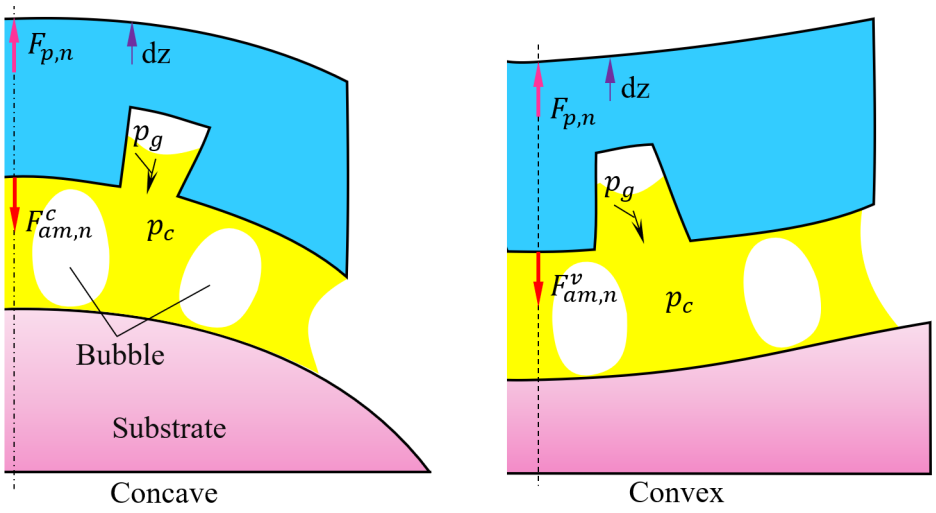

Figure 3.10: Scheme illustration of the adhesion between the micropatterned pad with concave a) and convex interface b) under normal peeling force $F_{p,n}$ in case complete wet.

In this scenario, we investigated the adhesion force in the normal direction satisfies starting to detach the substrate under peeling force $F_{p,n}$ as shown in Fig. 3.10. As mentioned in the previous section, in this case, the contact forces $F^{c(v)}_{cm,n}$ are the total of $F^{c(v)}_{am,n}$ and the peeling force $F_{p,n}$. When the relation $||F^{c(v)}_{cm,n}|| \leq ||F_{p,n}||$, the forces $F^{c(v)}_{cm,n}$ become zero. In detachment phase, the normal adhesion force $F_{am,n}$ also means the normal contact force $F_{cm,n}$. Hence, we focus on estimating the normal adhesion forces $F^{c(v)}_{am,n}$ while the peeling force $F_{p,n}$ is considered as a given external force. Herein, the normal adhesion is estimated in dynamic case ($v_z \neq 0$).

3.3.3.1 Complete Wet

In case complete wet, the normal wet adhesion forces start to decrease after reaching their maximum at peak interface gap h_p due to the appearance of minor capillary bridges separated by bubbles inside the capillary bridge (Fig. 3.10), whereas the dry adhesion force $F_{am,n}$ drops quickly. In this scenario, the wet area $A^{c(v)}_{wi}$ of each minor capillary bridge can be determined in the same method as mentioned in Eq. (3.7). Then, combining Eq. (3.30) with applying Eq. (2.47) for the grooves and cells yields the normal adhesion forces of the m-pad-c and the m-pad-v as followed:

$$F_{am,n}^{c(v)}\langle c-w\rangle = \Bigg\{\gamma\Bigg[A_{gi}^{c(v)}\langle g_i\rangle\cos\theta_3\sum_{i=1}^{2Nnc}\frac{\cos\alpha_{3i}}{\bar{w}_i^{c(v)}} + A_{ci}^{c(v)}\langle c_i\rangle\sum_{i=1}^{N}\frac{\cos\alpha_{3j}}{R_1^{c(v)}} + 2a\gamma\cos\left(\theta_3 \pm 0.5\varphi_g^{c(v)}\right)\sum_{i=1}^{2Nn_c}\cos\alpha_{3i}\Bigg] + 2al_{ti}v_{gli}\sum_{i=1}^{2Nn_c}\frac{\cos\alpha_{3i}}{\bar{w}_i^{c(v)}} + \sum_{i=1}^{N(2n_c+1)}\frac{3}{4}\frac{\pi(r_{wi}^{c(v)})^4}{dt}\left(\frac{1}{h_i^2}-\frac{1}{h_i^0}\right) + F_{dm,n}^{c(v)}\Bigg\}\hat{z}, \tag{3.35}$$

where $A_{gi}^{c(v)}$ and $A_{ci}^{c(v)}$ are the wetting area of the minor capillary at the groove i and cell i. Additionally, l_{ti}, v_{gli} are, in turn, the height and the velocity of liquid inside the grooves i.

In the detachment phase, the wet adhesion force of the n-pad depends on parameters of the pad and substrate liquid and interface gap h; whereas that of the m-pad varies with the micropattern. These findings suggest a need to evaluate the normal contact force when applying preload P to the model.

3.3.3.2 Partial Wet

During detachment phase with partial wet, the minor capillary already exists in the small interface gap h. Thus, the normal wet adhesion $F_{wm,n}^{c(v)}$,in this scenario, additionally comprises of the normal viscosity force $F_{vm,n}^{c(v)}$. Hence, by using Eq. (3.36) with applying Eq. (2.47) for the grooves and minor capillaries derives the normal adhesion forces of the m-pad-c and the m-pad-v in condition $w < h$ as followed:

$$F_{am,n}^{c(v)} = \Bigg\{\gamma\Bigg[\sum_{i=1}^{Nn_c}A_{wi}\langle d_i\rangle\cos\alpha_{3i}\left(\frac{2\cos\theta_3}{\bar{w}^{c(v)}}-\frac{1}{R_1^{c(v)}}\right) + \sum_{i=1}^{Nn_c}P_{wi}\langle d_i\rangle\sin(\theta_1+\alpha_{3i}) + \cos\left(\theta_3 \pm 0.5\varphi_g^{c(v)}\right)\sum_{i=1}^{2Nn_c}\cos\alpha_{3i}\Bigg] + \sum_{i=1}^{N(2n_c+1)}\frac{3}{4}\frac{\pi(d_i^{c(v)})^4}{dt}\left(\frac{1}{h_i^2}-\frac{1}{h_i^0}\right) + 2al_{ti}v_{gli}\sum_{i=1}^{2Nn_c}\frac{\cos\alpha_{3i}}{\bar{w}_i^{c(v)}} + F_{dm,n}^{c(v)}\Bigg\}\hat{z}. \tag{3.36}$$

In detachment phase, we consider that the groove width h is smaller than the interface gap h. Thus, it may neglect the calculation of the normal adhesion in condition $h < w$.

CHAPTER 4

FABRICATION OF PATTERNED SURFACE

This chapter shows the process of fabricating the micropatterned and normal pads mentioned in previous chapters. Those pads were cast from silicon rubbers in assembled molds comprising of the inserted pad molds and a finger mold. In this scenario, the molds have two types: micropattern and normal surface (without any patterns); while, there is one type of the finger mold.

4.1 Micro-patterned Mold's Fab

In this dissertation, we used the pieces silicon wafer made from P-type (100) with its resistivity at 0.005 m for creating the sample mold of our experiments. An original silicon wafer having around 110 mm diameter was cut into small square pieces in size of $14{\times}14\,mm^2$ to make a substrate for the micropattened mold in size $6{\times}6\,mm^2$. Hence, this substrate was patterned by utilizing one of the two methods: photo-lithography and electron beam lithography (EBL). Also, fabricating these such microppaterned molds were completely carried out in JAIST Nano Tech Center.

4.1.1 Photo-Lithography

1. Small pieces of silicon wafers were soaked and ultrasonically vibrated in acetone at room temperature in 5 mins. This process was repeated again by using isopropanol as shown in Fig. 4.1(a). Then, these wafer substrates were treated in oxygen plasma at the machine Plasma etching system Samco FA-1 under conditions: power: 30 W, pressure: 3 Pa and time: 5 mins as shown in Fig. 4.1(b). The purpose of these steps was to eliminate the organic residues on the silicon surface where the micropattern

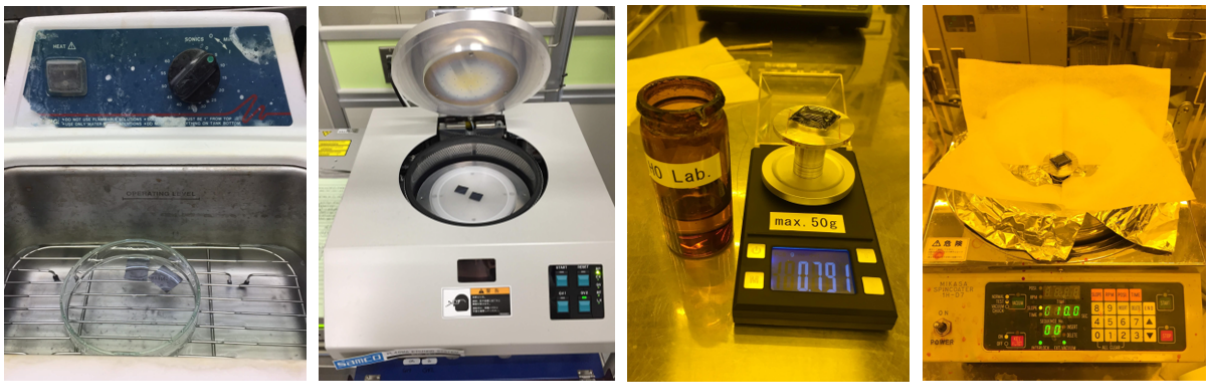

(a) Clean sample (b) Oxyplasma treatment (c) Weigh resist (d) Spin coating

(e) Photo-lithography (f) Beaking (g) Develop

Figure 4.1: The process of fabricating a micropatterned mold by using photo-lithography technology. a) Clean the slicon wafer in chemical liquid under vibration condition. b) Remove the organic on the wafer surface in oxyplasma treatment. c) and d) Weigh the resist SU8-3050 and carry out spin coating. e) Exposure the sample in lithography machine MLA-150. f) Beaking the sample after exposure process. g) Develop the sample. Whole of this process was performed in JAIST Nano Tech Center.

was created later [107, 108].

2. The Wafer substrate put in the holder of the spin coating machine was dropped with a developer liquid Su-8 3050 with a thickness $\sim 2\,\text{mm}$ through weighing in a milligram scale (Fig. 4.1(c)). Then, the group of the substrate lying on the holder was put on the rotational axis of the spin coating machine (Fig. 4.1(d)) and started the spin coating process.

3. The wafer substrate obtained in step 2 was input in the center of the lithography machine Heidenberg MLA150 (Fig. 4.1(e)). Hence, a design of the micropattern output from Autocad software was input and setup the exposure conditions in the lithography machine. The exposure laser created square pattern with line widths of 15 μm on negative resist Su-8 3050 [212].

4. After exposure and exposure bake (Fig. 4.1(f)), the wafer substrate was developed in Su-8 developer in 10 min (Fig. 4.1(g)) for generating the micro-patterned structure

with the depth was 44 μm.

5. The silicon substrate with micropattern was washed by water and dried with N_2 before testing in the laser scan microscope Keyence VK-9710.

4.1.2 Electron Beam Lithography

1. The pieces of silicon wafer were prepared by cleaning and removing the organic residues on their surface as well as the step 1 in lithography technology.

(a) ELS 7500 (b) Resistance heating evaporation

Figure 4.2: The main machines for fabricating a micropatterned mold by using electron beam lithography technology. a) The E-beam lithography ELS 7500 machine and b) Resistance heating evaporation. Both of them are in JAIST Nano Tech Center.

2. The wafer substrate was carried out spin coating by dropping positive resist polymethyl methacrylate/methyl methacrylate (PMMA/MMA). Then, the substrate was generated a square-patterned mask with a 15 μm pattern line width by utilizing E-beam lithography (EBL) technology in the ELS 7500 machine as shown in Fig. 4.2(a). In this step, we can also use the ELS 3700 machine for large scale of the micropattern.

3. The silicon wafer patterned in the second step was deposited with a thin silver layer via the thermal deposition in resistance heating evaporation machine (Fig. 4.2(b)). Then, we carried out a lift-off process for the obtained substrate in acetone and isopropanol at 60° C for 30 mins each.

4. In this phase, the wafer substrate deposited by the silver layer was soaked in an etching solution consisting of acid HF at 4.8 M and H_2O_2 at 0.3 M during 120 min.

In addition, one can find out the principle of silver etching of silicon substrate wafer through several previous research such as [213–215].

5. Finally, the wafer substrate was immersed in DI water, and soaked in $DI - HNO_3$ 63% at volume ratio 1:1 during 5 mins for dissolving the catalyst Ag. Then, this substrate was cleaned with DI water again, and flowed by the gas N_2 for drying.

4.1.3 Test Micropatterned Mold

After finishing the fabrication, the mold samples were tested through observing in optical and electron laser microscope. Figure 4.3 shows the testing results of two micropattern: square and hexagonal cell. Herein, the square pillar is the basic shape for preliminary investigation (entirely used in our current research); while, the hexagonal pattern is the research objectives we aim to carry out (shortly introduced in my first publication [108]). In this figure, the micropatterns achieved high accuracy both in the edge length and the cell shapes. Additionally, many texture structures exist in the cell surfaces as shown in Fig. 4.3(a-3)(b-3), which can generate variations of the contact models.

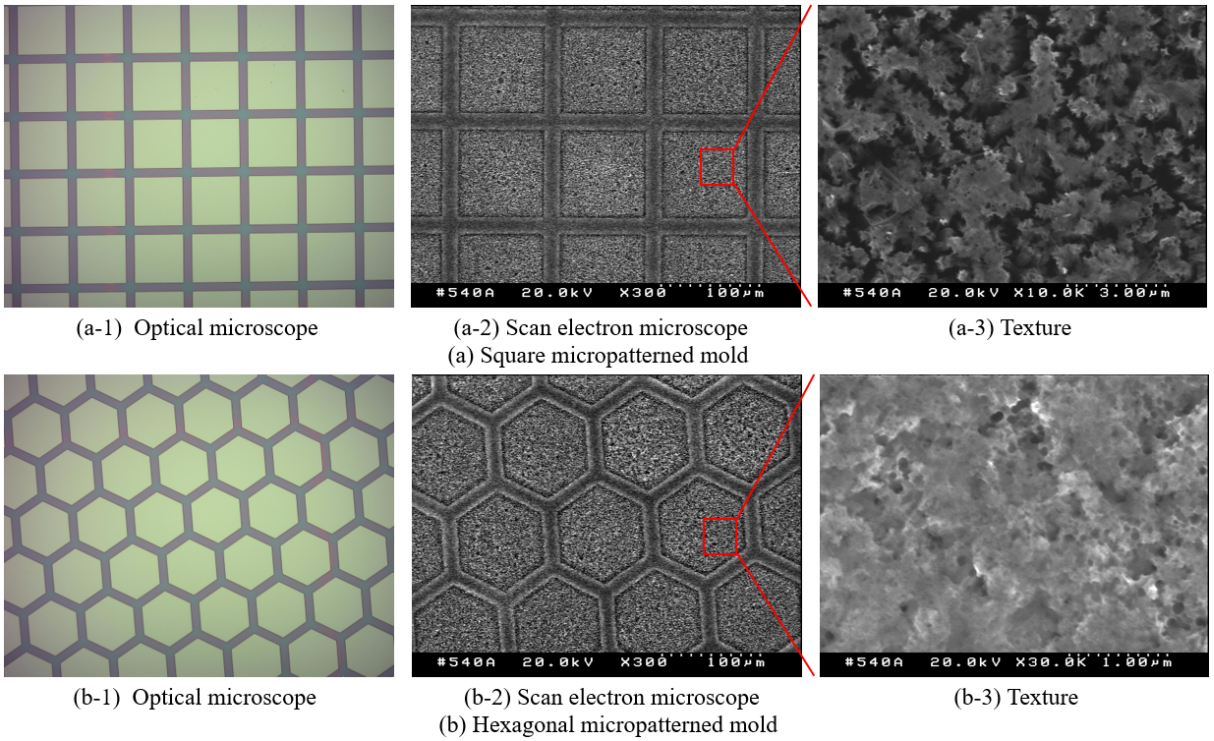

(a-1) Optical microscope (a-2) Scan electron microscope (a-3) Texture

(a) Square micropatterned mold

(b-1) Optical microscope (b-2) Scan electron microscope (b-3) Texture

(b) Hexagonal micropatterned mold

Figure 4.3: Testing the micropatterned molds through observing in optical and scan electron microscopes (SEM). The testing samples include two types of micropatterned morphology a) square and b) hexagon cells with their images output from optical microscope: a-1) and b-1), SEM a-2) and b-2). Also, the inset pictures a-3) and b-3) show the textures on each cell surface of the patterns observed in the SEM.

Both two methods of fabricating the micropatterned mold gave the high accuracy

in the final products. The lithography technology is more simple and cheaper than the electron beam lithography, because it reduces many steps in fabrication. Furthermore, the lithography technology can expose the laser on the resist Su-8 which generates a very high thickness of the groove depth. This is very convenient to design the soft pads with diverse micropatterned morphology in a short time. However, the electron beam lithography can achieve a smaller scale of the micropattern.

4.2 Fabricate Pads for Flat Contact Interface

4.2.1 Micropatterned Pad

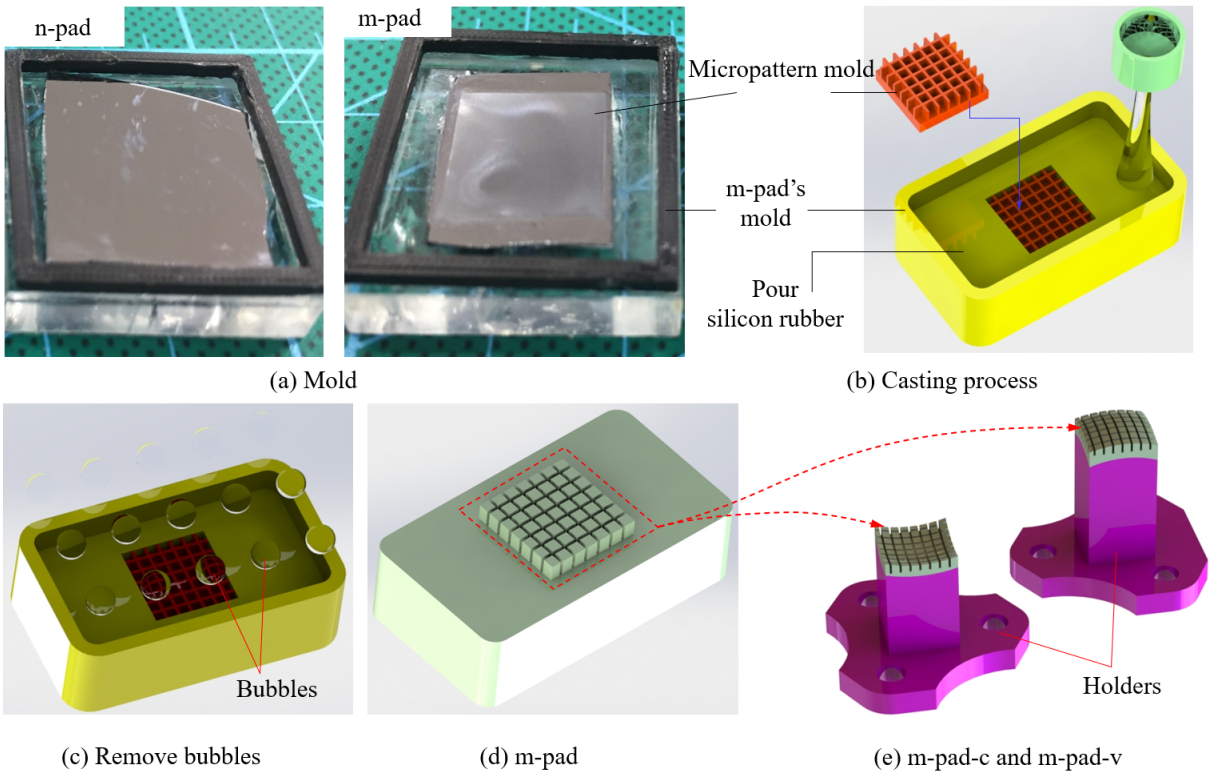

Figure 4.4: Process of making the micropatterned and normal pads. a) The molds of the m-pad were fixed in the pad's molds. b) Cast silicon rubber in the m-pad mold, this process is also applied to the case of n-pad. c) Remove air bubbles. d) m-pad after casting. e) Make m-pad in concave and convex surfaces.

The micropatterned mold deposited in the silicon wafer in the previous steps was fixed in a pad mold (Fig. 4.4(a)) which its walls were created by the 3D printing technology (using Zotrax 3D printer M200) and the base plate made from mica plastic. Then, the two liquid ingredients of each silicon rubber, for instance, Dragon Skin or Ecoflex of Smooth-on company, were mixed with the weight ratio 1:1 in the plastic tank as shown in Figure 4.4(b). To archive a good quality outcome these blends were carefully stirred so that they can completely dissolve.

After that, those blends were poured into the m-pad mold and sucked for removing the air bubble inside a vacuum machine in 10 mins (Fig. 4.4(c)). Then, the silicon rubbers were carefully removed from the m-pad's mold after becoming solid during several hours in the atmosphere (Fig. 4.4(d)). We also can reduce elapse time of changing states of the silicon rubbers from the liquid to solid thanks to heating.

4.2.2 Normal Pad

In this case, to make a n-pad mold the silicon substrate without fabricating any micropatterns on it surface was fixed on the pad mold which had same structure as the m-pad's mold as shown in Fig. 4.4(c). Then, we poured the liquid silicon rubbers into the n-pad mold and replicated the same steps as well as the m-pad for creating the n-pad.

4.2.3 Test Sample

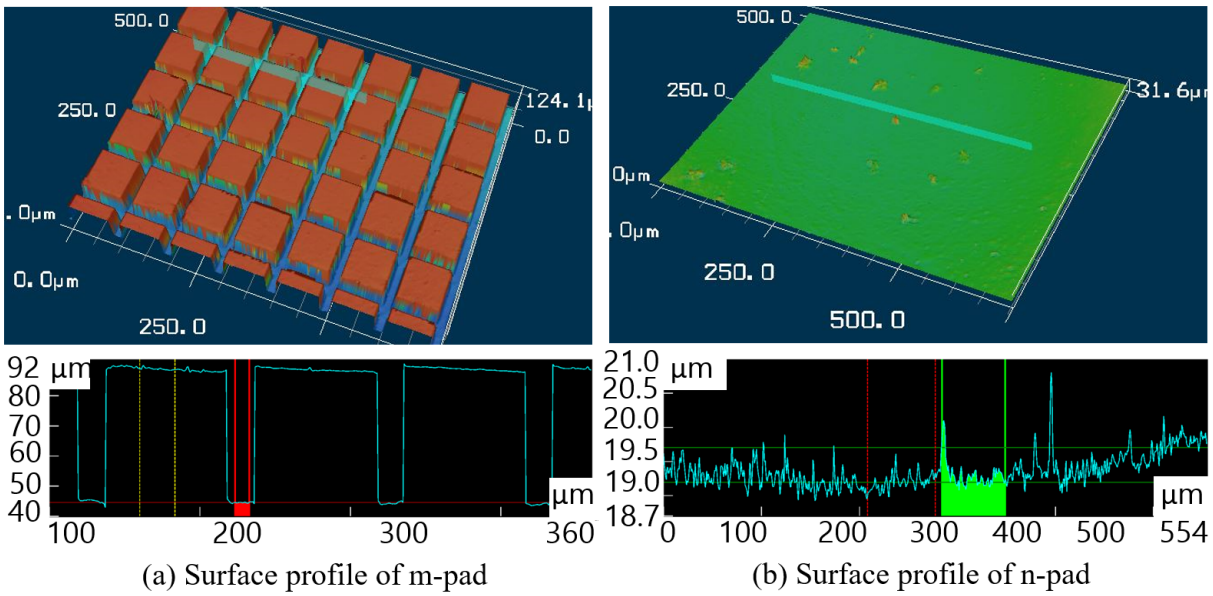

Figure 4.5: Testing the surface profiles of the pads by observing in 3D laser microscope for a) micropatterned pad and b) normal pad.

The m- and n-pads were observed in laser scan microscope Keyence VK-9710 as shown in Fig. 4.5. As can be seen, the surface profile on each cell of the m-pad are almost flat; whereas, the surface profile of the n-pad has higher roughness. However, these roughness is much smaller than the depth of the grooves. Herein, the asperities are random and appear in several places, which occupies an infinitesimal area comparing with entire contact surface of the n-pad. The grooves of the m-pad have the same sizes of their width (about 16 μm) and depth (about 44 μm). In addition, the walls of the grooves are orthogonal to the cell surfaces. The small slop angle on the cell's surfaces comes from the deformation

of the soft pad when fixed in the table of the microscope, and the errors of fabricating the pad molds.

4.3 Fabricate Pads for Curved Contact Interface

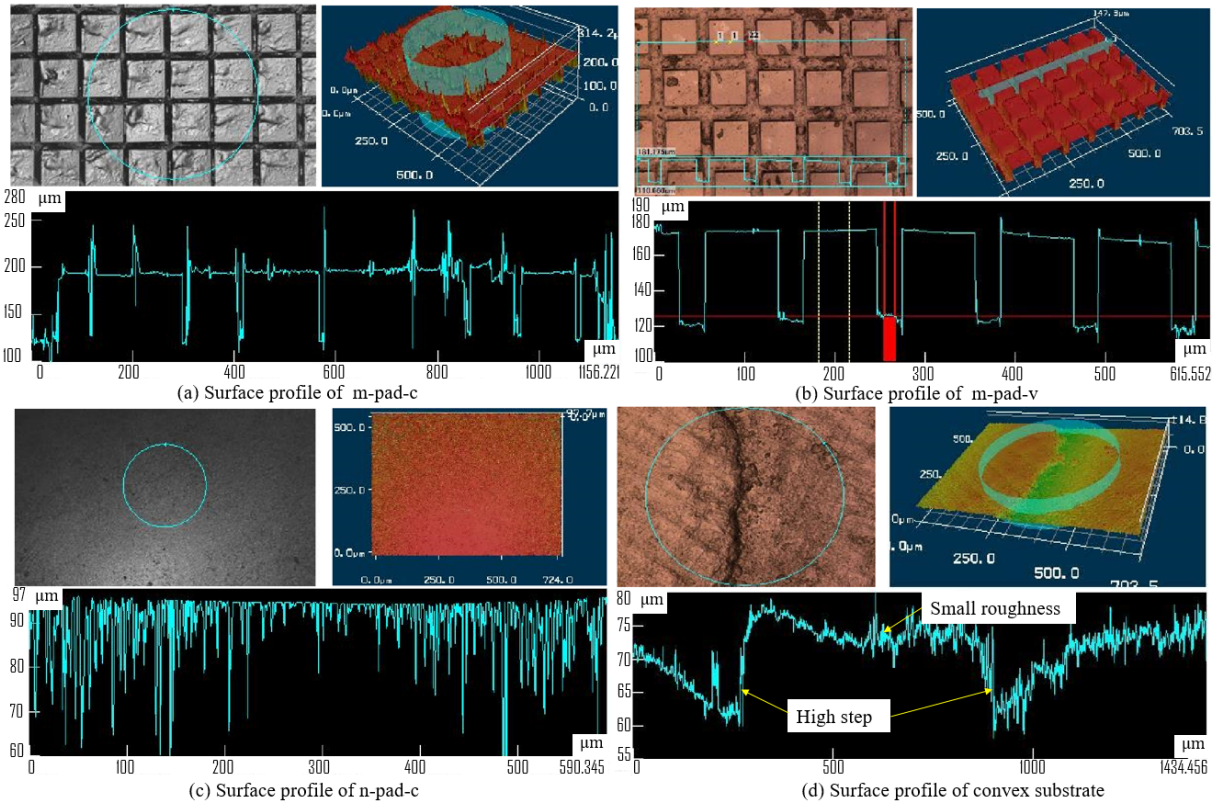

Figure 4.6: Testing the surface profiles in curved contact interfaces by observing in 3D laser microscope for a) m-pad-c, b) m-pad-v, c) n-pad-c and d) the hemispherical convex substrate.

The pads having curved contact interfaces as mentioned in figure 3.2 comprised from two primary parts: the soft pad made from silicon rubbers, and the holder parts having rigid structure for forming the curved interface of the pads (Fig. 4.4(e)). Herein, the soft pads were fabricated in the same way as the case of flat contact interface; whereas, the holders were precisely printed by the Zotrax Inspire 3D printer machine. Then, the soft pads were fixed into the holder through a thin film of glue.

Fig. 4.6 shows the surface profiles of the pads and the substrate in curved contact interfaces, which were observed in laser scan microscope Keyence VK-9710. Because the grooves collapsed in concave surface which affected on scattering laser, the image of surface profile in case the m-pad-c is not clear (Fig. 4.6(a)). In case the m-pad-v, the groove width expanded at the contact interface positions (Fig. 4.6(b)). The surface of the n-pad-c had small roughness (Fig. 4.6(c)); whereas, the surface roughness was high for the substrate surface (Fig. 4.6(d)). This is due to the resolution of the 3D printer.

CHAPTER 5

RESULTS

This chapter shows the role of the micropaterned morphology on enhancement of the wet adhesion for grasping soft-fragile objects, which is illustrated through comparison of the adhesion and contact forces in two contact cases of the pads: the n-pad (the pad without any pattern) and m-pad (the pad with micropattern) mentioned in mentioned in chapter 2 and 3. The comparisons were performed in estimations and then validated by experiments. In this scenario, the fabricated pads in chapter 4 were treated in oxygen plasma before setting up experiments. In addition, in case the flat contact interface, we carried out the validation for the adhesion model in both tangential and normal directions; whereas, it was performed in normal direction for the curved contact interface.

5.1 Contributions of Dry Adhesion in Wet Contact

The dry adhesion has contributions to the adhesion through the van der Waals and Casimir forces. Since the roughness surfaces of the grasped objects are usually large (in micro scale) and random, the contact between the pads and the substrate with nanoscale may almost appear at the asperities. Let us assume that the total dry area A_{di} is same for the n- and m-pad, and the parameters of the dry adhesion are as chosen in table 5.1. The materials of the pad, liquid and substrate are silicon rubber, water, and polyetylen, and the calculations are performed at room temperature 20°. Replacing parameters in table 5.1 into Eqs. (2.17) and (2.42) yields the Casimir and van der Waals forces as shown in Fig. 5.1. Between the contact of the pads and the substrate contains a liquid film, which enlarges the interface gap h. Also the surface roughness of the substrate in Fig. 5.1(a) is in microscale (roughness at planes and the depth of hollows are about 7.5 μm and 50 μm). Thus, we can consider the maximum interface gap h in cases van der Waals and Casimir force being respectively 7 nm and 50 nm that appear at the planes.

Table 5.1: Parameters of the dry adhesion forces

Permitivity (F/m) [216]			Refractive index			Ionization frequency (Hz)
ϵ_p	ϵ_{lg}	ϵ_s	n_p [217]	n_{lg} [218]	n_s [219]	f_m [133]
3.5	80.2	2.25	1.4	1.33	1.5	$\sim 3.10^{15}$

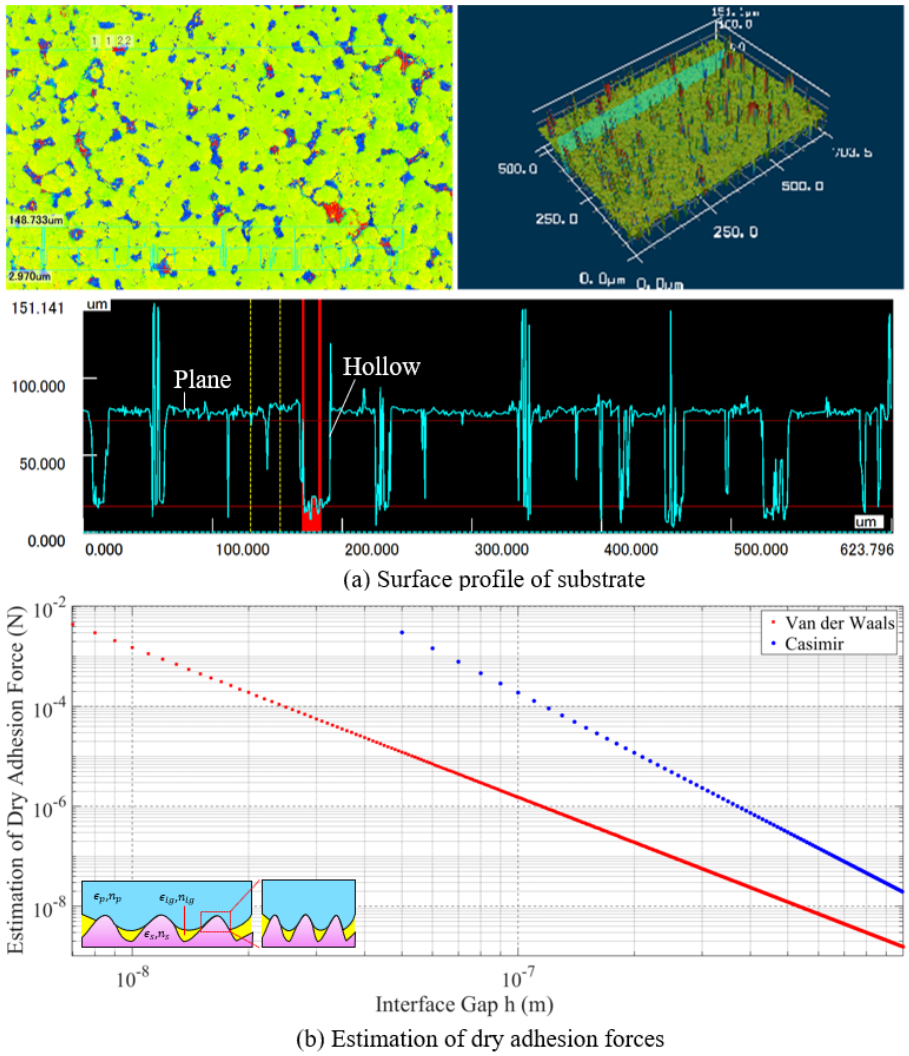

Figure 5.1: Estimated results of van der Waals and Casimir forces by varying interface gap h. a) Surface profile of the plastic substrate observed in laser scan microscope Keyence VK-9710. b) The Casimir and van der Waals forces are calculated according to Eqs. (2.17) and (2.42). The total area of dry adhesion A_{di} is assumed to 6.9% of the contact area L_p^2.

As shown in Fig. 5.1, the van der Waals and Casimir forces respectively reach 0.0045 N and 0.003 N at the interface gaps $h = 7$ nm and 50 nm. Those forces drop rapidly when increasing h. Since it is extremely complicated to determine the total of dry adhesion area, we investigate the contribution of the dry adhesion force (van der Waals and Casimir forces) through the ratio between the dry adhesion area and the contact area corresponding with 6.9, 14 and 30 %. In table 5.2, the contribution of the dry adhesion force are the ratios between the van der Waals or Casimir forces with the normal adhesion force measured

in Fig. 5.9. These ratios are directly proportional with the percentage of dry area, and achieves higher value (two fold) in case n-pad than that of the m-pad. The contribution of the dry adhesion force is significant at the percentage of dry area being 30 %. However, the surface roughness of the substrate is in microscale, the percentage of dry area is about 6.9 % or lower. In other words, the dry adhesion force makes not much significant contribution comparing with the wet adhesion in the wet contact ($F_{dn} << F_{wn}, F_{dm} << F_{wm}$). Hence, we can neglect the dry adhesion force in validating the adhesion force $\langle F_{an}, F_{am} \rangle$.

Table 5.2: Contribution of dry adhesion in adhesion force

Percentage of dry area	n-pad case		m-pad case	
$\sum A_{di}/L_p^2$	van der Waals	Casimir	van der Waals	Casimir
6.9%	6 %	4.2 %	3 %	2 %
14 %	12.17 %	8.48 %	6.06 %	4.04 %
30 %	26.1 %	18.26 %	13 %	8.7 %

5.2 Validate Adhesion Between The Pads and Substrate In Flat Interface

The adhesion force of the contact between the n- and m-pad with their corresponding substrates are investigated in chapter 2 and 3. In this section, we aim to evaluate the role of micropatterned morphology on enhancement of the adhesion force in the contact/grasping through comparison the corresponding entities between the n- and m-pad case. To be convenient for comparisons it is assumed that the pads are made from isotropic materials having same properties everywhere. Thus, we have some initial conditions such as: h is a constant in one contact, in normal direction the contact angle are same: $\theta_1 = \theta_2 = \theta_{1'} = \theta_{2'} = \theta_3 = \theta$, in tangential direction the contact angle are: $\theta_1 = \theta_{2'} = \theta, \theta_2 = \theta_{1'} = \pi - \theta, \theta_3 = \theta$, and $\theta_{bn} = \theta_{bm} = 0.5\pi - \theta$. Such comparisons were performed for both flat and curved contact interface.

Table 5.3: Parameters using in estimation of adhesion force.

Water		Dragon Skin 30		m-pad		
γ	η	ν	E	L_p	$a \times w \times d$	N
0.073 N/m	1 mPas	0.5	592.95 kPa	6 mm	85× 15 × 44 (μm)	3600 cell

5.2.1 Compare Adhesion Between N- and M-pad in Flat Interface

In this scenario, we carry out the comparisons of the adhesion force and contact force generated by the normal and micropatterned pad during contacting with their substrate having flat interface. These comparisons include both normal and tangential direction of the contact.

5.2.1.1 Normal Adhesion Without Preload

When the number of cells micropattern become enormous ($N \to +\infty$), the entity $N^{-0.5}$ closes to zero that leads to eliminateing infinitesimal entities such as: $wN^{-0.5}$, and $\sin\theta N^{-0.5}$ from the calculations. Let us neglect the dry adhesion component $F_{dn} = F_{dm}$ in comparison of the adhesion force and majorly concentrate on estimating the increment ratio of the normal wet adhesion force between the m- and n-pad. The increment ratio of the normal adhesion force in case attachment w/o preload $r_s = F_{am,n}/F_{an,n}$ as followed:

$$r_s = \frac{h}{w} + \frac{2n_c wh + a(w-h)}{aw(1+w/a)^2}, \tag{5.1}$$

with $F_{an,n}, F_{am,n}$ are obtained from Eqs. (2.43) and (3.5).

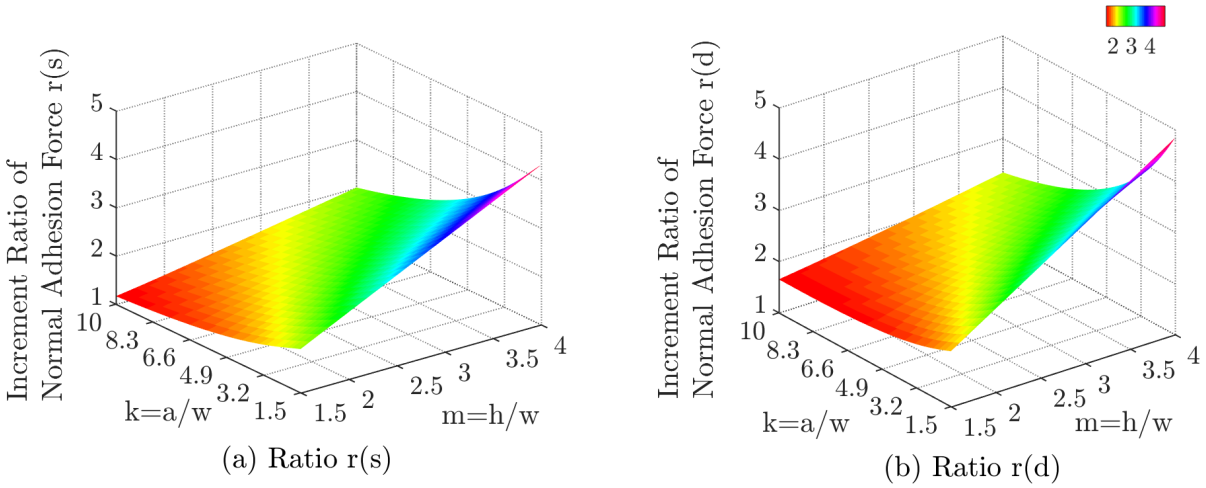

(a) Ratio r(s) (b) Ratio r(d)

Figure 5.2: The role of the parameters m, k on the increment ratio of the normal wet adhesion force r_s and r_d of a m-pad with its interface morphology including $N = 3600$ square cells (Fig. 3.1(b)) and the n-pad (Fig. 3.1(a)) at same contact area. Variations of the increment ratio for r_s a) using Eq. (5.1) and r_d b) using Eq. (5.3). The initial conditions for comparison between two cases of those such pad are: water at room temperature is the liquid film with $\gamma = 0.07286\,\mathrm{N/m}$, $\eta = 0.001\,\mathrm{Pas}$ (in table 5.3) and contact angle $\theta \sim 0.86$. The ranges of investigation for both r_s and r_d are investigated in complete wet with normal velocity of the pad for r_d is $v_z = 0.5\,\mathrm{mm/s}$.

In equation (5.1), the ratio r_s depends on interface gap h and the pad morphology: edge length a, width of the groove w and the number of cell N; whereas h is an independent

variant. Let us denote $k = a/w$ and $m = h/w$ $(m, k > 1)$, now Eq. (5.1) is rewritten in the form:

$$r_s = 1 + \frac{(m-1)(2/k + 1/k^2) + 2n_c m/k}{(1+1/k)^2}. \tag{5.2}$$

From Eq. (5.2) with $n_c \approx 1$, the increment ratio r_s majorly depends on the ratios k and m. In condition m is higher than 1, the ratio r_s is certainly larger than 1. In other words, the wet adhesion force generated by the m-pad and the substrate is higher than that of the n-pad and the substrate. As shown in Fig. 5.2(a), r_s always positions upper than plane $z = 1$ in the entire investigated region. Also, the ratio r_s shows more directly proportional trend for the ratio m than that of the ratio k.

5.2.1.2 Normal Adhesion in Detachment Phase

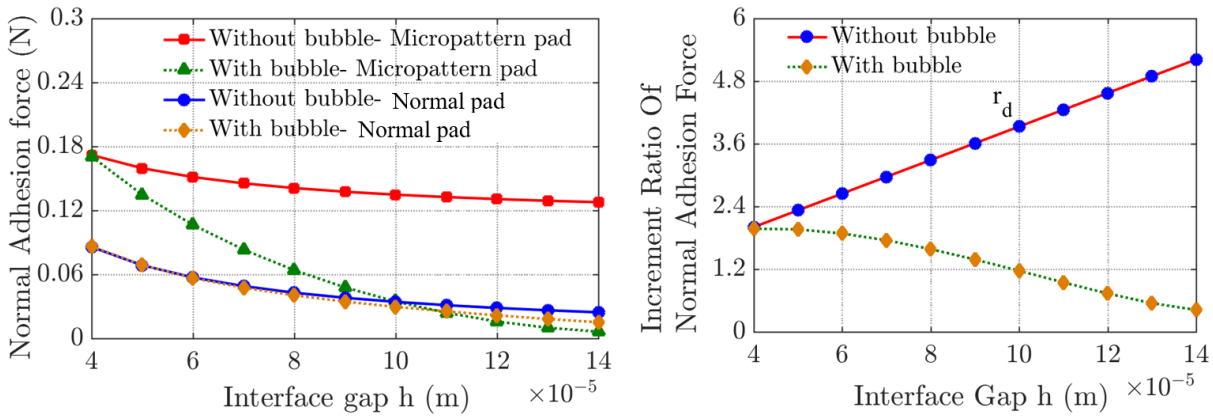

(a) Magnitude (b) Ratio

Figure 5.3: Normal wet adhesion forces of the n- and m-pads by varying the interface gap h. a) The magnitude of the normal wet adhesion forces for the n- and m-pads. In this figure, the solid lines correspond to the estimations in case without bubble using Eqs. (2.52) and (3.8) for the n- and m-pads in case without bubbles ($g = 0$); whereas, the dot lines show the calculation using Eqs. (2.52) and (3.8) in case with bubbles ($g = 1$). In addition, N_n for the n-pad case was assumed to be equal $4Nn_c$ for having the same number of bubbles in case the m-pad. b) The increment ratios of normal wet adhesion output from a) for the detachment phase r_d without bubbles, and the ratio $F_{am,n}/F_{an,n}$ with bubbles.

As $w < \langle a, h \rangle$, the micropattern morphology can strengthen the normal wet adhesion in 1.5÷3 fold bigger than that of the surface without any patterns as shown in Fig. 5.2(b). Also, the comparison in case $g_h = 1$ is not carried out due to many confounding parameters consisting of the angles θ_{bn}, θ_{bm}, the radii of the bubbles r_{bn}, r_{bm}, and the number of bubbles N_n.

The viscosity forces $F_{vm,n}$ and $F_{vn,n}$ depend on many parameters such as the pad velocity v_z, liquid velocity inside groove v_{gl}, interface gap h, the edge length a, and the width of channel w. Thus, it is complicated to achieve a precise comparison between

$F_{wm,n}$ and $F_{wn,n}$. In this situation, let us consider $v_{gl} << v_z$ and $\eta << \gamma$, and thereby eliminate the infinitesimal entities. Hence, the increment ratio of normal wet adhesion force for the contact between the n- and m-pad with the substrate in detachment phase $r_d = F_{am,n}/F_{an,n}$ can be written as followed:

$$r_d \approx \frac{[(1+w/a)^2-1]/w + (1+2n_c h)/(ah) + \phi_n[L_p(1+w/a)]^2/(2\gamma cos\theta)}{(1+w/a)^2[1/h + \phi_n L_p^2/(2\gamma cos\theta)]}. \tag{5.3}$$

Where $\phi_n = [0.75\pi\eta r_w^4/dt](1/h^2 - 1/h_0^2)$, and $F_{an,n}, F_{am,n}$ are obtained from Eqs. (2.52) and (3.8).

During detachment phase, the ratio r_d in Eq. (5.3) shows its dependence on the normal velocity of the pads v_z. Hence, by replacing the ratios: m and k into Eq. (5.3) we have the ratio r_d in the form:

$$r_d = 1 + \frac{(m-1)(2/k + 1/k^2) + 2n_c m/k]}{(1+1/k)^2[1 + 3N\eta v_z(k/m + 1/m)^2/(4\pi\gamma\cos\theta)]}. \tag{5.4}$$

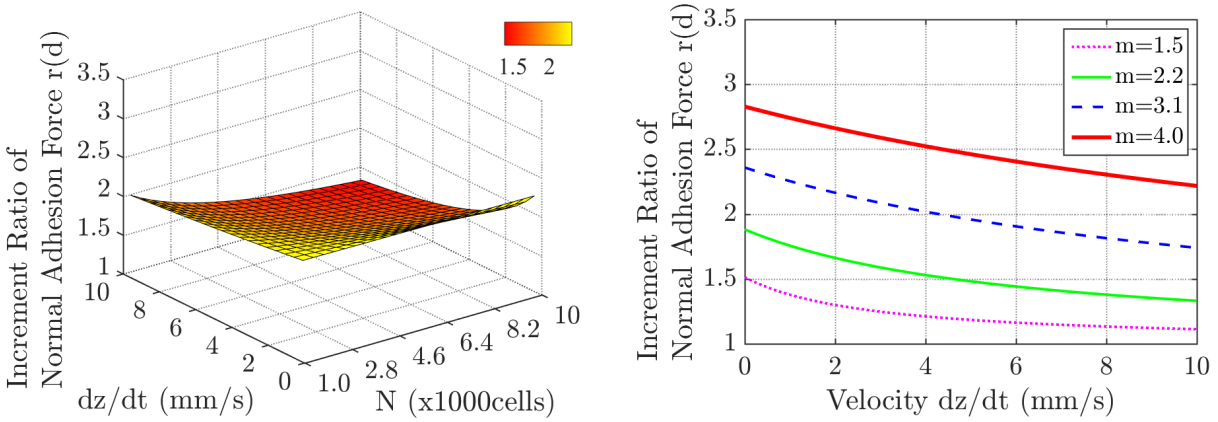

(a) Variants dz/dt and N

(b) Variants dz/dt and m

Figure 5.4: Influence of variables and the pad's morphology on the increment ratio of normal wet adhesion force r_d in Eq. (5.4) between m- and n-pad in case without bubbles. a) Influence of the variables: the number of cells N and the pad velocity v_z on the variation of the ratio r_d. Herein, the ratios $\langle m, k\rangle$ value, in turn, 3 and 85/15. b) Influence of the ratio m and the pad velocity v_z on variation of the ratio r_d. In this scenario, the lines illustrate the different values of m, while k is unchanged; whereas, other conditions are identical to those in previous estimations.

From equation (5.4), it can be seen that the ratio r_d majorly depends on $\langle m, k, N, v_z\rangle$; whereas, $\langle \eta, \theta, \gamma\rangle$ are unchanged at each specific cases of the liquid and the pads ($i.e$ material). When the liquid film is water, the amount $3\eta/(4\pi\gamma\cos\theta) \sim 0.005$ in the denominator of equation (5.4) becomes infinitesimal to 1. In Fig. 5.3(b), the normal wet adhesion force of the m-pad is bigger than that of n-pad in condition without bubble, and even with bubbles at very narrow gap h. Also, the increment ratio r_d equals to r_s if Nv_z

closes to zero. There are some slight differences of the calculation results between r_s and r_d observed in the entire investigated range as shown figure 5.2. In general, those such differences take value around 20%, but is down to 10%, corresponding to v_z, which sets values, in turn, 0.01 m/s and ~ 0 as shown in figure 5.4(b). A low velocity multiplied by N and a tiny wet area A_w cannot significantly strengthen the viscosity force. In case as described in figure 5.4(a), the increment ratio r_d is inversely proportional to the number of the cells N and the pad velocity v_z. Therefore, we can eliminate the viscosity force as determining contact, which depends on each specific cases.

In the detachment phase, the estimated results of the normal wet adhesion in case the micropatterned pad show a higher value than that of the flat surface pad (n-pad). That is to say, interactions between the pad morphology and wet adhesion have significant contributions for enhancement of the adhesion force during detachment.

5.2.1.3 Normal Adhesion With Preload

When the pads are compressed by the preload, besides effected by the parameters such as the ratios $\langle k, m \rangle$, the contact forces in normal direction $F_{cn,n}, F_{cm,n}$ additionally accords with the preload P. The normal contact force in the preload condition is compared through constructing the increment ratio of normal contact force: $r_p = F_{cm,n}/F_{cn,n}$ as followed:

$$r_p = 1 + \frac{2\gamma \cos\theta[(2 + 2n_c - 1/m)/(kw) + 1/(mw)]}{p(1 + 1/k)^2 + 2\gamma \cos\theta(1 + 1/k)^2/(mw)}, \tag{5.5}$$

with $F_{cn,n}, F_{cm,n}$ are obtained from Eqs. (2.90) and (3.6).

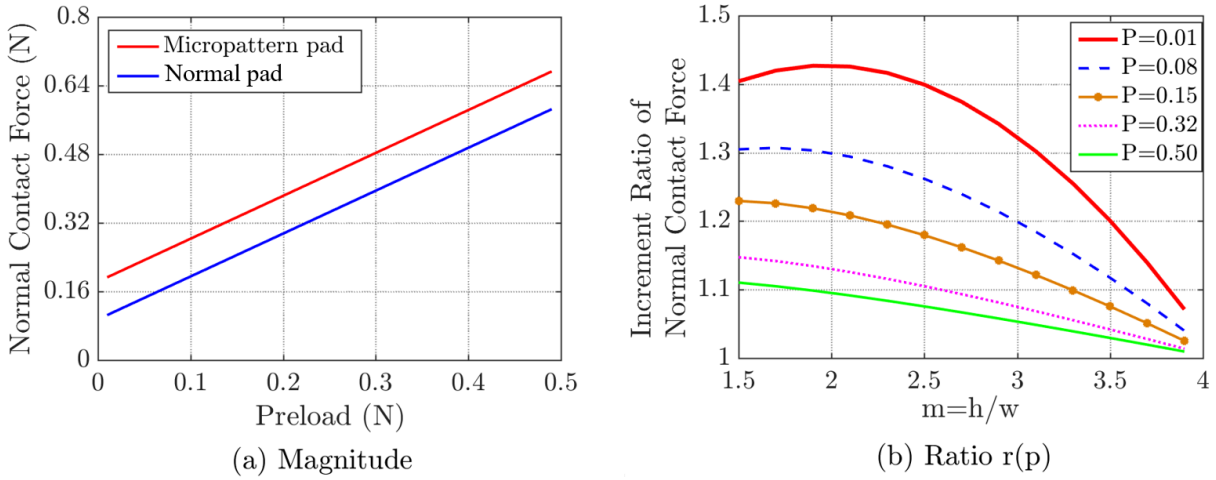

(a) Magnitude (b) Ratio r(p)

Figure 5.5: Schematic illustration of the normal contact forces of the pad having micropaterned morphology $F_{cm,n}$ in equation (3.6) and the normal pad $F_{cn,n}$ in equation (2.92), and the increment ratio r_p in attachment phase under compressed by preload P. a) The influence of the preload P on the contact forces in normal direction. The conditions were set at $h = 40\,\mu$m, $w = 15\,\mu$m and $a = 85\,\mu$m. b) The influence of P and m on the change of the increment ratio r_p in equation (5.5).

Equation (5.5) acts as the function comprising of the variables $\langle m, k, w, p\rangle$. Since the term $1/m$ has smaller value than 1, the value of the right hand side in equation (5.5) is larger than 1. The ratios $\langle m, k\rangle$ remain their same roles in both the presence or absence of the preload P. The increment ratio r_p consists of w depending on $\langle k, p\rangle$, relating to the others through the material and morphology of the pads. In case p has extremely large value comparing with the other parameters, the increment ratio r_p closes to 1; whereas, r_p is approximate to r_d at small value of p. The preload P influences both the normal contact force as shown in Fig. 5.5(a) and its increment ratio r_p as shown in Fig. 5.5(b). Rising p associates with declining the interface gap h. Also, this may stop when h achieves its minimum value even though going on rising the compression. In this scenario, a rising amount of p induces a decrease amount of the ratios of $F_{cm,n}/F_{cn,n}$ and F_a/P. Wipping surface of the pads with a thick liquid film and applying a large preload can lose the effects of wet adhesion interaction in which the liquid film produces a positive pressure to detach instead of stick the contact surfaces.

5.2.1.4 Tangential Direction

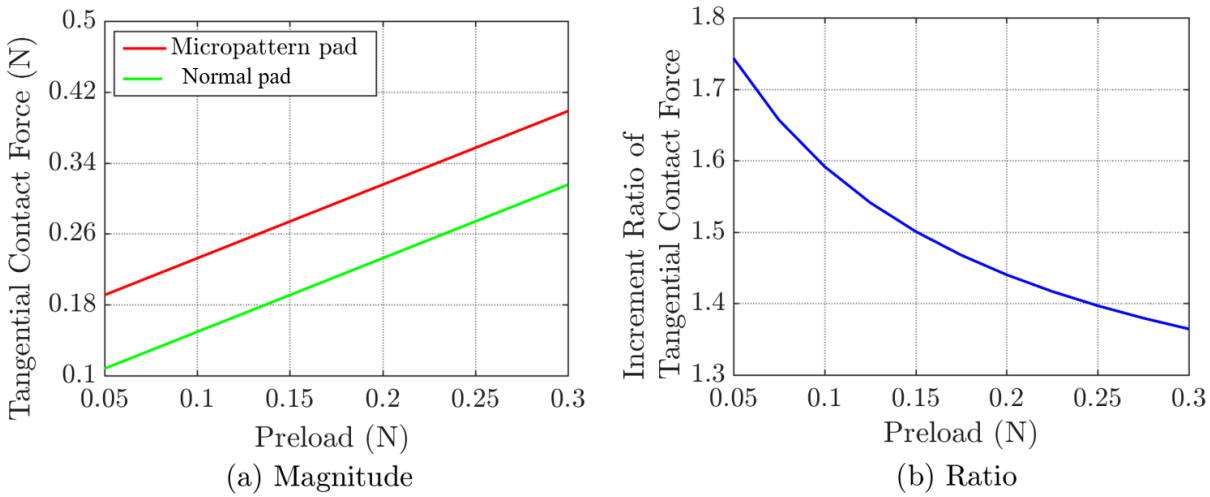

Figure 5.6: Calculating the tangential contact forces of the contact between the pads having micropattern or normal surface and their substrate. a) The magnitude of the contact force $F_{cm,t}$ and $F_{cn,t}$ use, in turn, equations (3.23) and (2.92). b) Influence of the preload P on the increment ratio between $F_{cm,t}$ and $F_{cn,t}$ output from a). Herein, the parameters of the liquid film use to those as the previous estimations; whereas, other parameters are set up as followed: $v_x = 0.0005\,\mathrm{m/s}$, $\mu_{ism} = \mu_{isn} = 0.83$ and $h = 40\,\mu\mathrm{m}$.

The contact forces in tangential direction $F_{cm,t}, F_{cn,t}$ are compared by using the data in Eqs. (3.23) and (2.92) respectively for the cases: micropatterned pad and normal pad (Fig. 5.6). In this scenario, we also eliminate the term $F_{vg,t} = \eta N n_c A_{wgi} v_{gl}/w$ due to the aforementioned reasons. Hence, through the simplification of the calculation, the increment ratio of tangential contact force of the contact between the m- and n-pads with

their substrates $r_t = F_{cm,t}/F_{cn,t}$ is given in the form:

$$r_t \approx 1 + \frac{4\mu_o m\{(1+n_c)\cos\theta - 0.5w/R_1 - 0.5v_x\eta w(\mu_o\gamma)^{-1}\}/(hk)}{mw\gamma^{-1}(1+1/k)^2(\mu_o p + \psi) + \mu_o w/R_1^s}. \tag{5.6}$$

When the pad velocity in tangential direction v_x becomes infinitesimal under conditions of $\mu_o m > 1, \eta << \gamma$, the entity $0.5\psi_1 w(\mu_d\gamma)^{-1} = 0.5v_x\eta/(m\mu_d\gamma)$ closes to zero. In addition, the term $0.5w/R_1$ equals to $\cos[\theta + \arctan(s/h)]\cos[\arctan(s/h)] < \cos\theta$ being smaller than $(1+n_c)\cos\theta$. This leads to the increment ratio r_t is bigger than 1 or $F_{cm,t} > F_{cn,t}$. At the tiny values in the conditions such as: velocity and displacement of the pads in tangential direction v_x, dx, the wetting area A_w, and viscous coefficient η, the tangential contact forces $F_{cn,t}, F_{cm,t}$ majorly depends on the forces: preload P and the capillary force F_{ca}.

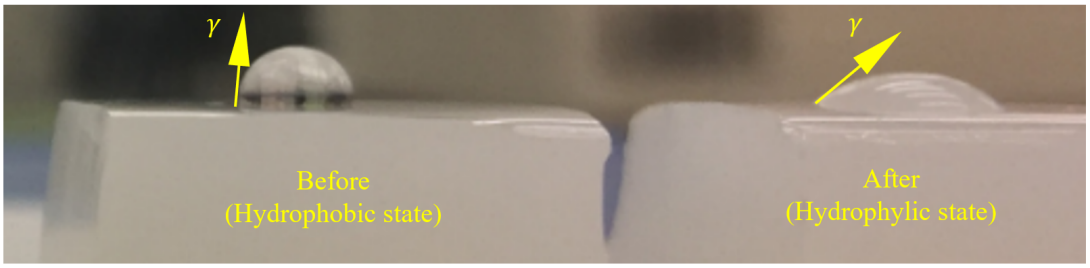

Figure 5.7: Enhancement of wet adhesion ability by performing oxygen plasma treatment for converting the pad's surface from hydrophobic state into hydrophilic state [108].

Figure 5.6(a) illustrates the estimated results with the datum are output from equations (3.23) and (2.92) in the same investigating conditions. Also, the curve representing the increment ratio (figure 5.6(b)) matches the outcomes of the ratio $F_{cm,t}/F_{cn,t}$ of tangential contact force in case incipient slip. Rising the preload P leads to strengthening the tangential contact forces $F_{cm,t}$ and $F_{cn,t}$. However, it makes the ratio $F_{cm,t}/F_{cn,t}$ become down to 1. This trend is roughly similar to that of the increment ratio r_p (equation (5.5)).

5.2.2 Evaluation Experiment Setup

To strengthen the ability of the adhesion in which the wet component was dominant, we carried out the oxygen plasma treatment on the n- and m-pads obtained in chapter 4. Herein, the condition was setup as following machine Plasma Etching Samco FA-1, power 30 W, pressure 3 Pa and during 15 min. This work can change the surface properties of those such pads from hydrophobic state to hydrophilic state as shown in Fig. 5.7. As aforementioned in previous sections, when the contact angle reduces, the wet adhesion capacity becomes more powerful, which was proved through measuring the contact angle after dropping a water drop on the pad's surface (Fig. 5.7).

The adhesion of the soft pads with and without the micropattern in wet contacting

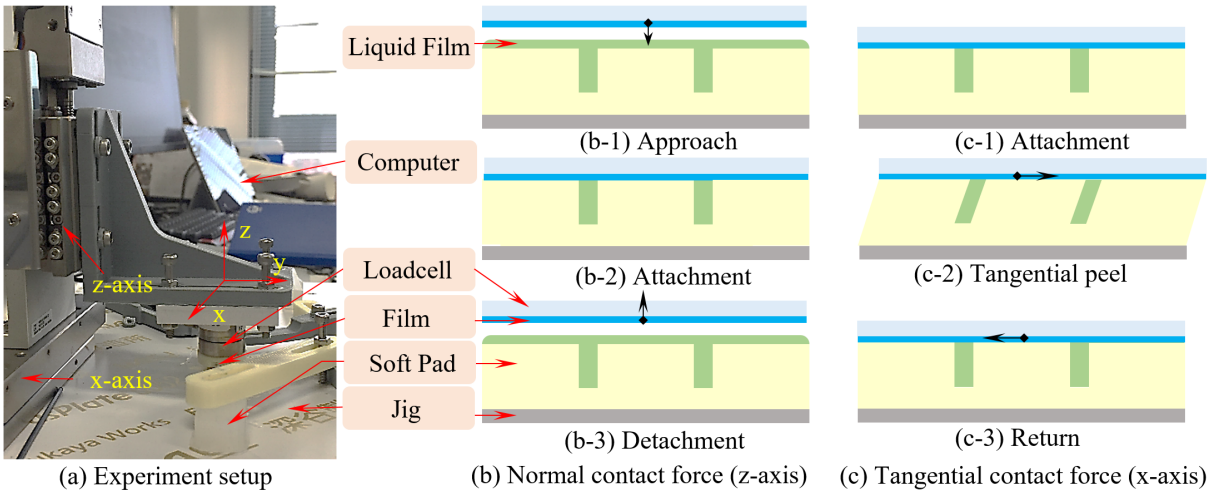

Figure 5.8: Schematic illustration of experimental setup for measuring the adhesion and contact forces in case flat contact interface. a) Scheme of measurement system. b) Testing the contact and adhesion forces in normal direction. b-1) The initial state of the experiment - the film substrate separated from the m-pad at an interface gap h at about 0.2 mm. b-2) Downward moving of the film substrate in z direction with the constant velocity $v_z = 0.3$ mm/s for compressing the liquid film and the pad or generating the preload, b-3) upward moving of the film substrate under various velocities v_z corresponding to every experiment time to generate the peeling force. c) The process of testing the contact forces in tangential direction. c-1) The loadcell exerting various values of the preloads onto the m-pad, during the maintained condition in 5 sec, c-2) The displacement of the film substrate with $dx = 0.4$ mm along the tangential direction or x-axis at different values of velocities v_x at 0.1, 0.2, 0.3 and 0.5 mm/s, c-3) returning the film substrate to the initial state as shown in c-1).

with their substrates were experimentally validated. In this scenario, a plastic film with a thin thickness was firmly fixed in a 6-axis load-cell ATI-Nano17, which then was affixed to a linear stage running in z-axis under control of a stepping motor Suruga Seiki D212. Output datum were recorded by utilizing an analog-to-digital (ADC) converter National Instrument connected with Matlab program executing in Windows 10 operation system (Fig. 5.8(a)). Both the n- and m-pads were wiped with a thin film of water and waited in several minutes for covering whole wetting area. These pads were completely fixed on a jig during experimental process under contact and peeling off motions from the plastic film. The film substrate was initially distanced an interface gap about 0.2 mm from the pad's contact interface. And then, this film moved with the constant values of the substrate velocity v_x and v_z at 4 levels of the preload P of, in turn, $0.05\,N \longrightarrow 0.08\,N \longrightarrow 0.12\,N \longrightarrow 0.2\,N \longrightarrow 0.3\,N$. In addition, five trials were carried out under corresponding conditions.

5.2.2.1 Normal Force

The normal adhesion played a key role in validating the total adhesion force. Hence, We performed the variation of the normal adhesion force through testing the contact forces in

the normal direction under various conditions of the preload P and normal peeling force $F_{p,n}$. The plastic film acting as the substrate (object), was initially separated at a gap h from the pad's contact interface such that it was enough for the subsequent capillary bridge can completely break (Fig. 5.8(b-1)). This plastic film rapidly translated downward to build up contact with the n- or m-pads under the specific preloads P, gone after a brief pause of 5 sec as shown in figure 5.8(b-2). The purpose of this brief pause was to ensure that the thin film of liquid had enough time to completely cover the empty space inside the interface gap. Then, the loadcell moved upward along z-axis at velocity v_z for executing the normal detachment phase until the capillary bridge completely broke as described in figure 5.8(b-3).

5.2.2.2 Tangential Force

In this scenario, the experimental system for evaluating the normal adhesion force was kept for validating the tangential contact force $\langle F_{rn,t}, F_{rm,t} \rangle$. Herein, we additionally controlled the motion of the loadcell on the x-direction. As shown in Fig. 5.8(c-1), the contact force in tangential direction was initially paused for 5 sec under the same conditions of the preload P as utilized for measuring the normal contact and adhesion forces in Fig. 5.8(b-2). After that, the plastic film moved forward 0.4 mm along the x-axis at 4 different levels of the velocity (Fig. 5.8(c-2)) under constant preload conditions. And finally, this film returned backward to its initial state as shown in figure 5.8(c-3).

5.2.3 Evaluation Results

5.2.3.1 Normal Force

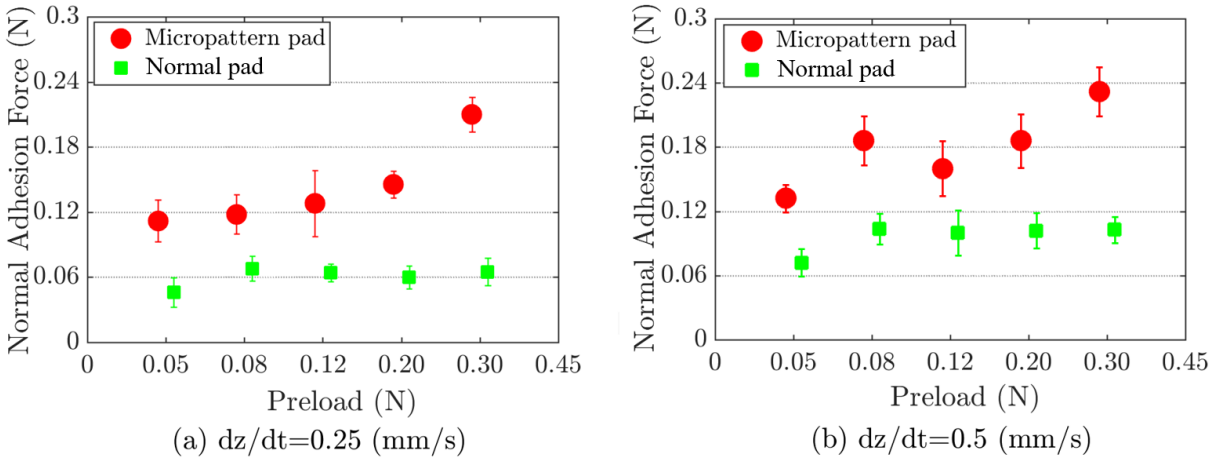

Figure 5.9: Experimental validation of the normal adhesion force of the micropatterned and normal pads with the substrate at different velocities v_z of *a*) 0.25 mm/s and *b*) 0.5 mm/s.

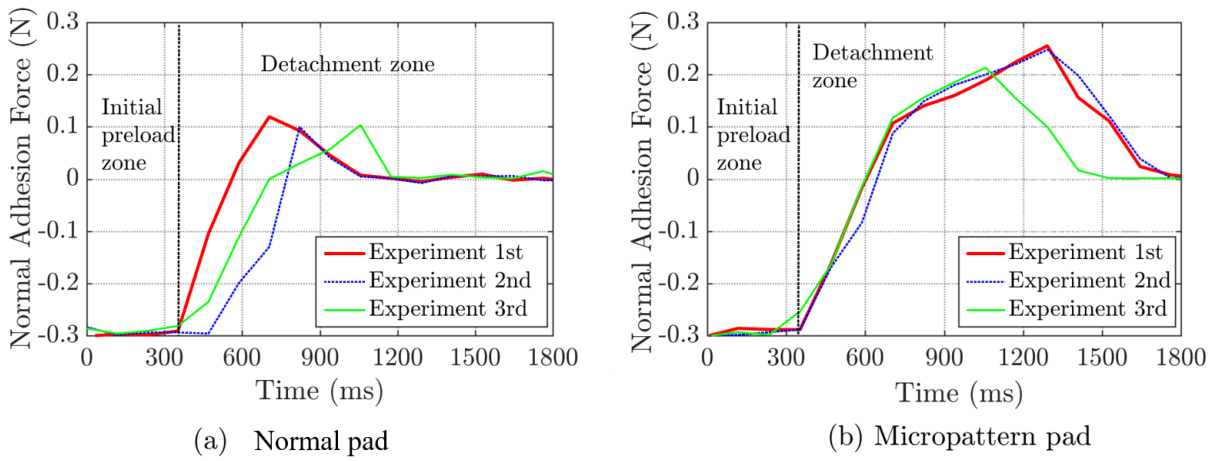

Figure 5.10: Illustration of the adhesion force over time in normal direction for normal a) and micropatterned pad b) at the film velocity $v_z = 0.5\,\text{mm/s}$ under the preload $P = 0.3\,\text{N}$. These graphs demonstrate the experimental results of multiple tests carried out under the same conditions. In addition, the m-pad was initially compressed by the preload $P = 0.3\,\text{N}$. After that, the plastic film moved upward to determine the normal adhesion force $\langle F_{an,n}, F_{am,n} \rangle$. This force rapidly rose to reach the peak gap h_p before quickly falling from starting appearance of the bubbles. Over time, the forces $\langle F_{an,n}, F_{am,n} \rangle$ closed to zero as the capillary bridge completely broken.

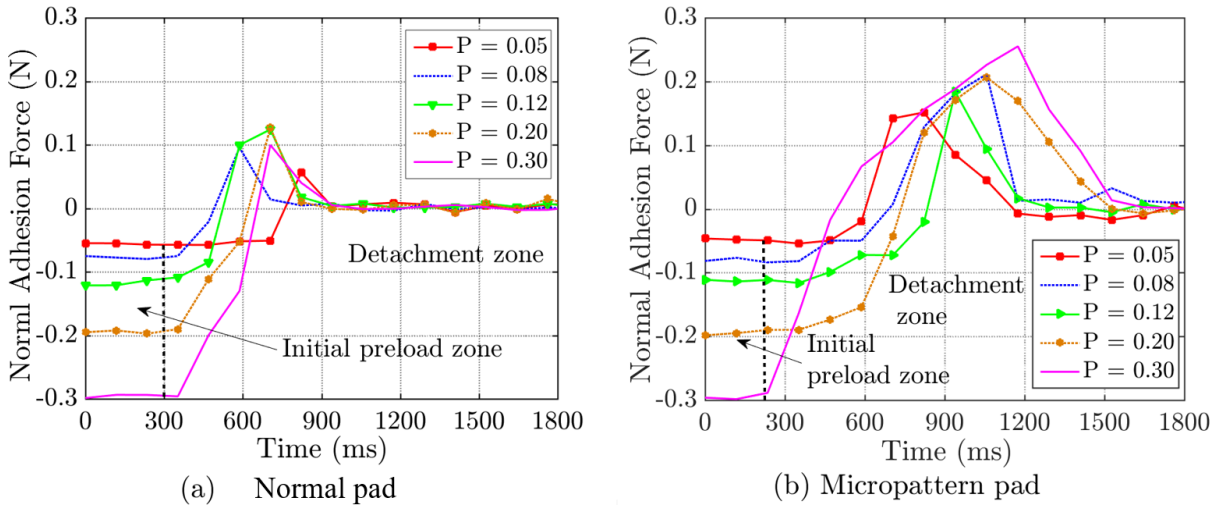

Figure 5.11: Experimental validation of the normal adhesion forces for the normal a) and micropatterned pad b) under five levels of the preloads P of $0.05\,N \longrightarrow 0.08\,N \longrightarrow 0.12\,N \longrightarrow 0.20\,N \longrightarrow 0.30\,N$ and the film velocity $v_z = 0.5\,\text{mm/s}$.

As shown in figure 5.9, the mean values of normal adhesion forces for the contact cases of the n- and m-pads gradually increased when the preload P rises in range $0.06 \div 0.26\,\text{N}$. Also the normal pad showed that the smallest value of the normal adhesion force was about $0.1\,\text{N}$, while the pad having micropatterned design achieved the normal adhesion force roughly $200\,\%$ higher. This finding showed an agreement with the estimated outputs in the previous chapters. Since the contact interface of the m-pad comprising from the array of the cells interspaced by the channel network possessed a softer property than that of

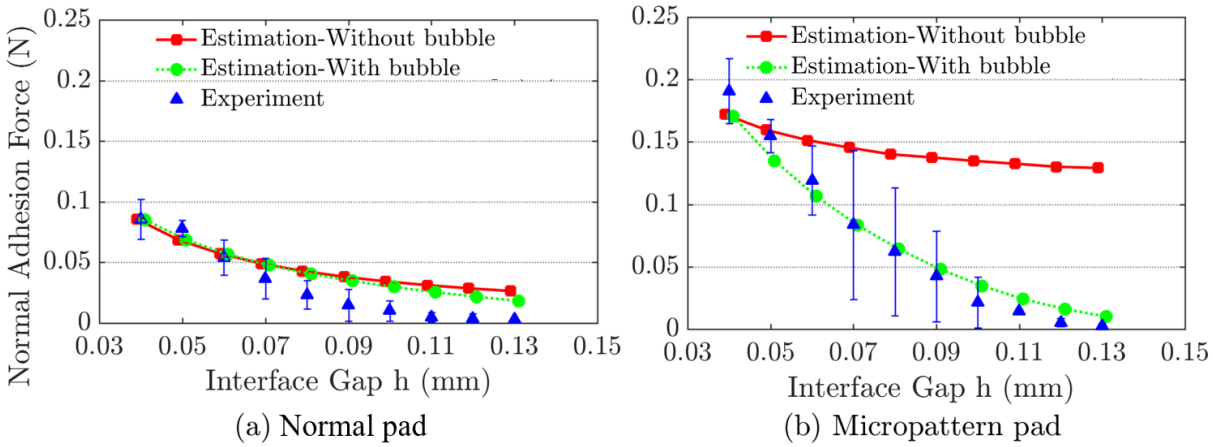

Figure 5.12: The estimated and tested results of the normal adhesion forces $\langle F_{an,n}, F_{am,n} \rangle$. a) Normal and b) micropatterned pad after passing the peak of the interface gap $h_p \sim 40\,\mu$m at the substrate velocity $v_z = 0.5\,$mm/s and the preload $P = 0.2\,$N. In addition, the estimated results were output from equations (2.50)and (3.8) with g_h= 0 and 1 for, in turn, without bubble and with bubble case.

the n-pad, applying a greater preload P induced a larger deformation for the morphology of the pad having micropatterned design. That is, in case the m-pad, the normal reaction force was lower than that of the n-pad. This can be explained through the system of the grooves helped the pad stiffness to become softer, enhancing the ability of absorbing the external forces such as the preload P. Thanks to this property the micropatterned pad can help to decrease the risk of large deformation in gripping soft-fragile objects by reducing the normal resultant force, as well as strengthening the wet adhesion force.

Consequently, upon rising of the compression of the preload (P), the interface gap h between the pads and the substrate became gradually smaller, facilitating the liquid film to quickly cover the vacant space inside the contact. Moreover, the preload P affected the contact interface between the pads and their substrate, even when their couple surfaces of the contact were not completely in parallel. This leads to strengthening the adhesion in normal direction $\langle F_{an,n}, F_{am,n} \rangle$. It was clearly illustrated in figure 5.9 as the preload P increased in range $0.05 \div 0.3\,$N. Whereas, it needs a stronger force to achieve entire contact area between the normal pad and its substrate in case the objects are not completely smooth. Therefore, the network of channels show its significant roles in both enhancing the wet adhesion and reducing the resultant force in the contact.

The normal adhesion forces in case the normal pad were found to reach peak at about $0.7\,$N as shown in figure 5.9(a-b), while those in case the pad having micropatterned design were directly proportional to P, with the average values of the peaks setting about $0.18\,$N. In addition, the peaks of the gap h_p had slight differences in time of magnitude and appearance among the experiment times. Fig. 5.10 demonstrated the variations needed to verify the dynamic lines of the normal adhesion force $\langle F_{an,n}, F_{am,n} \rangle$ over time for replicated experiments in the same conditions.

Although the dynamic performance was not completely identical, the normal adhesion force curves for the two types of the pad increased before archiving their interface peaks, contrary to the phase of bubble appearance after passing the peaks. Since the adhesion force in normal direction was dominant, the m-pad stuck the substrate in a longer time than that of the n-pad before entering the bubble phase as shown in figures 5.10 and 5.11. Generally, the average values of the normal adhesion times of the normal and micropatterned pads were, in turn, set about 250 ms and 400 ms, while the average values of the dropping time in the bubble phase for these pads was evaluated about 160 ms. Altering the preload P influenced to the normal adhesion force, varying its configuration and magnitude partly as shown in figure 5.11, which made it specify the distribution region of the peak gap h_p in lieu of fixation points.

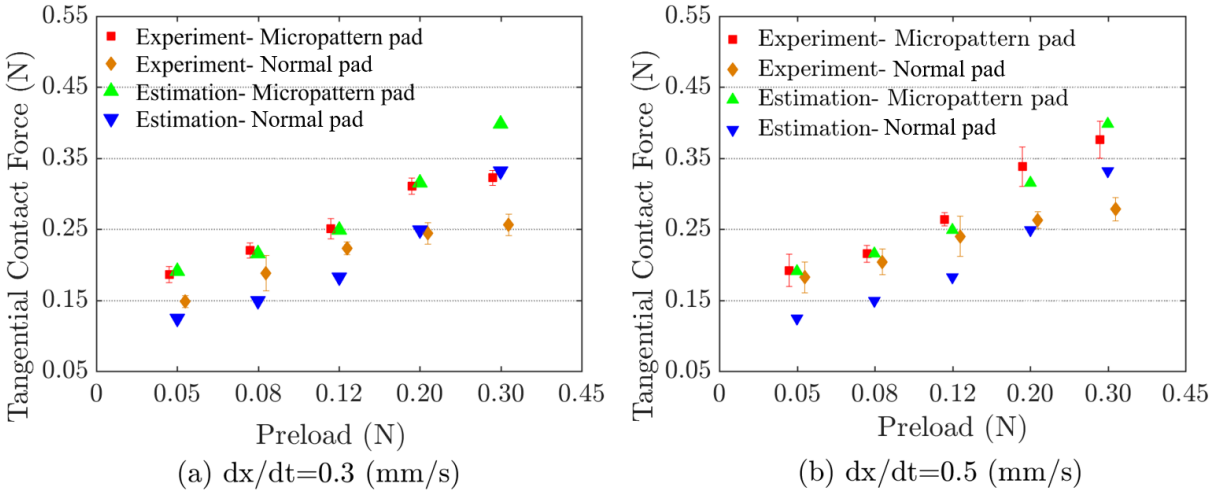

(a) dx/dt=0.3 (mm/s) (b) dx/dt=0.5 (mm/s)

Figure 5.13: Experimental validation of calculating the tangential contact forces for the contact between the micropatterned and normal pads with their substrate at different velocities a) v_x = 0.3 mm/s and b) v_x = 0.5 mm/s. In addition, the estimated results were output from equations (2.92) and (3.23) in case complete wet with dry adhesion.

Figures 5.11 and 5.12 demonstrated that the peak gaps in obtained results of the experiments were in distributed range h=40÷60 μm. Thus, considering the mean interface gap h_p for all cases valued around 40 μm allowed us to perform the estimated and tested validations for the adhesion forces in normal direction as shown in figure 5.12. The calculated plots for the n- and m-pads illustrate that the measurement values of the normal adhesion force $\langle F_{an,n}, F_{am,n} \rangle$ at a narrow interface gap h= 40÷60 μm matched with those in case without bubbles, and that for the bubble curves were in range of h >60 μm.

As a result, to achieve the accurate reflection of the experimental validations the normal adhesion force $\langle F_{an,n}, F_{am,n} \rangle$ in equations 2.50 and 3.8 should be divided into two cases corresponding to with and without bubbles. Although there were several regions illustrated slightly small deviations when the gap h became increasing, the calculations obtained from equations (2.50) and (3.8) showed a good agreement with the experimental

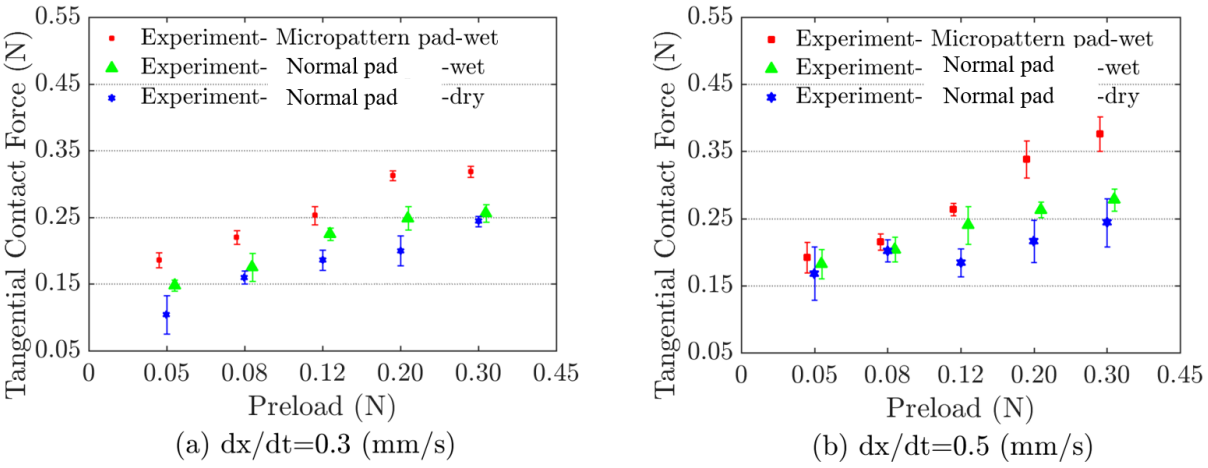

(a) dx/dt=0.3 (mm/s) (b) dx/dt=0.5 (mm/s)

Figure 5.14: Experimental comparisons of the tangential contact forces for the contact between the micropatterned and normal and micropatterned pads with their substrate in wet (for two kinds of the pads) and dry (for the normal pad) conditions at different velocities of a) $v_x = 0.3\,\text{mm/s}$ and b) $v_x = 0.5\,\text{mm/s}$.

validations.

5.2.3.2 Tangential Force

Figure 5.13 shows the variations of the tangential contact forces $\langle F_{cn,t}, F_{cm,t} \rangle$ at various value of the preload P for the micropatterned and normal pads under different tangential velocity of the film. Generally, the tangential contact forces $\langle F_{cn,t}, F_{cm,t} \rangle$ were directedly proportional to the preload P. In this scenario, the contact force shows more linear relation with the preload P in case the contact of micropattern pad than in case the normal pad. Furthermore, the tangential contact force of the micropatterned pad was $20 \div 40\,\%$ larger than that of the normal pad in wet and $45 \div 60\,\%$ larger in dry conditions (figure 5.14). These differences also increased when the preload P rose. In addition, the tangential contact force in case the normal pad was found to stick the substrate surface $5 \div 20\,\%$ more firmly in the wet than the dry adhesion. The calculated curves were almost fit to the tested results, however, matches were closer in case the pad having micropatterned morphology than in case the pad without any patterns. The tangential contact forces $\langle F_{cn,t}, F_{cm,t} \rangle$ were not completely linear relation with the preload P, since it depended on many parameters such as the characteristics of the liquid, pad morphology, pad materials and film velocity.

In addition, other aspects of tangential contact forces in experimental relationship with the preload P and the film velocity in tangential direction v_s were illustrated in figure 5.15. Herein, there were slightly changes with varying tangential velocity v_x; whereas, the preload P made the significant changes for those such forces. In this situation, the deviations oscillated in the range of v_x $0.1 \div 0.3\,\text{mm/s}$ on the contrary to the value of $v_x = 0.5\,\text{mm/s}$. As explanations for the estimations output from the equations (3.23)-(2.92), the

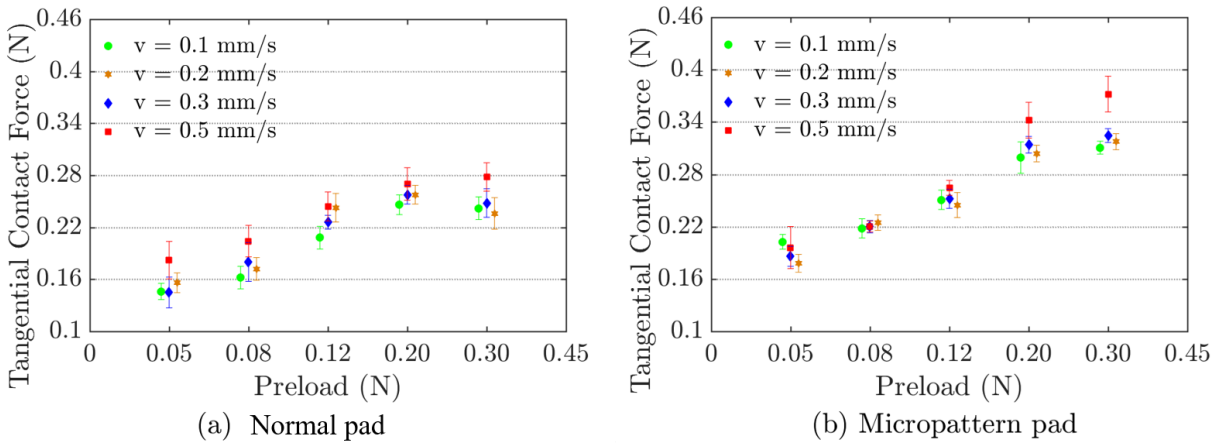

Figure 5.15: Experimental comparisons of the tangential contact forces for the contact between the micropatterned and normal pads with their substrate. a) The normal and b) micropatterned pads as a function of variables: the preload P and various levels of the film velocity v_x = 0.1, 0.2, 0.3, and 0.5 mm/s.

tangential velocity v_x partly influenced in the tangential contact force $\langle F_{cn,t}, F_{cm,t} \rangle$, even though that was neglected in this research. Moreover, the dependence of contact force on preload in tangential direction was larger in case the micropattern pad than the normal pad as shown in Fig. 5.15. At each value of the preload P at the velocity level of the plastic film $v_x = 0.5$ mm/s, the contact forces $\langle F_{cn,t}, F_{cm,t} \rangle$ were directly proportional to P (see figures 5.13-5.15). During the contact in wet condition, the tangential contact force balancing with the total external force was the key factor for the prevention of slipping. For the tested results under the tangential displacement dx=0.4 mm, we had tangential contact forces as shown in figure 5.16 slightly reduced, corresponding to the increment of the displacement. Herein, the state of this contact can be in the incipient slip situation because the n- and m-pads made from soft materials were deformed due to the shear stress.

In summary, the experiments validating the normal adhesion and tangential contact forces illustrates tested values were always higher for the pad having micropatterned morphology than that of the pad without any patterns. Additionally, the experimental results closely matched the estimated models constructed in chapters 2 and 3. For the contact having wet adhesion, the very low velocities of the plastic film v_x and v_z multiplied by the group consisting of a tiny wet area A_w and a low viscosity coefficient η induces an infinitesimal value of the outcome product, can be negligible and also had not much important contribution to the final calculations (very low capillary number). The viscosity force, in this research, may be much strengthened by choosing another liquids having the very high values of the viscosity coefficients instead of water. Hence, it can significantly enhance the adhesion force, enlarging the balance with the other components of the contact forces. Also, the obtained results showed that the adhesion and contact forces were majorly dependent on many factors such as: the adhesion conditions, preload P, and the pad's

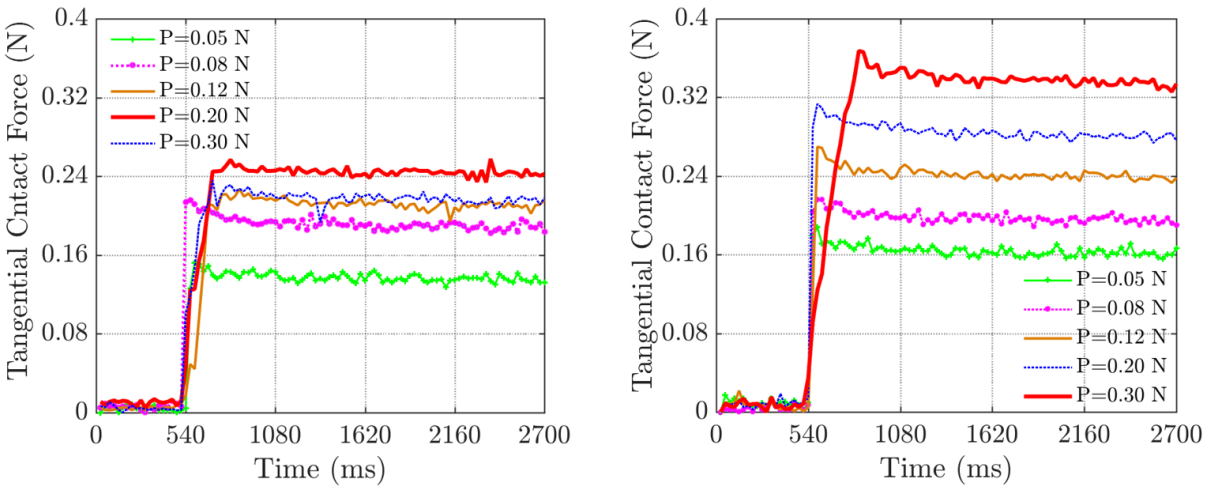

(a) Normal pad (b) Micropattern pad

Figure 5.16: Experimental results of the tangential contact forces over time in case the contact between the a) normal pad and b) micropatterned pad with their substrate under various levels of the preloads of $0.05\,N \longrightarrow 0.08\,N \longrightarrow 0.12\,N \longrightarrow 0.20\,N \longrightarrow 0.30\,N$ at the constant velocity of the plastic film $v_x = 0.5\,\text{mm/s}$.

morphology and materials. Moreover, the interactions between the cells interspaced by the groove network with the wet adhesion produces effects of the enhancement of the contact forces. Finally, the suction force was much greater inside than outside the grooves in case the interface gap h is extremely larger than the width of the groove w, but hugely rising the number of the channels may decline the Laplace force of the contact between the cell-substrate. Thus, the mechanics of the contact having wet condition should be developed through optimum designs of the pad's morphology and choosing the appropriate liquids for the capillary.

5.3 Validate Adhesion Between The Pads and Substrate In Curved Interface

In this section, we performed experiments for evaluating the normal adhesion force of the couple contact interfaces for the m-pad and n-pad in two cases: concave and convex surfaces. Herein, the obtained results were applied into validating the theoretical model in the previous sections.

5.3.1 Compare Adhesion Between N- and M-pad in Curved Interface

In this scenario, the estimated results derived from the analytical models in previous sections are shown in some specific cases. Since the contact angles $\theta_{1,2}$ depend on various

parameter of liquid, substrate, and pad [184, 185], it is complicated to apply precisely in this model. However, we can consider $\theta_3 \approx \beta_1 = \beta_1^*$ according to [220]. In addition, other parameters are set up as $\alpha_1 \approx \alpha_2$, $R_2 \approx x_s$, $\gamma = 0.073\,\mathrm{N/m}$, $\eta = 0.001\,\mathrm{Pas}$, $L_p = 6\,\mathrm{mm}$, $N = 3600\,\mathrm{square\ cell}$, $a = 85\,\mu m$, and $w = d = 15\,\mu m$ (in flat contact interface) as shown in table 5.3.

5.3.1.1 Normal Adhesion Without Preload

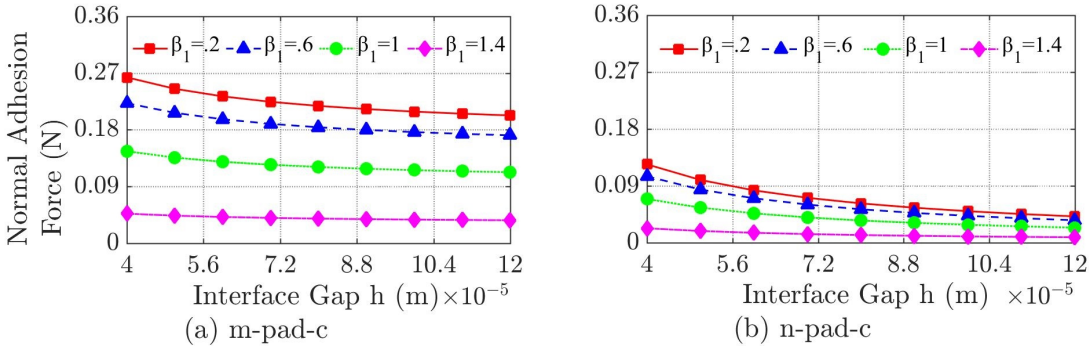

Figure 5.17: Comparison of normal wet adhesion forces of the micro-patterned pad in concave shape (m-pad-c) (Eq. (3.30)) and normal pad in concave shape (n-pad-c) (Eq. (2.59)) b) at angle $\beta_1 = 0.2$, 0.6, 1 and 1.4 rad. R_s was set 15 mm.

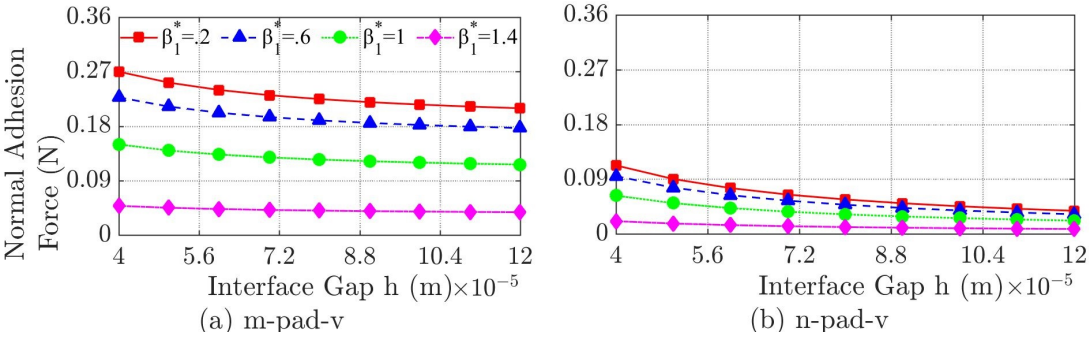

Figure 5.18: Estimated comparison of normal wet adhesion forces between the a) m- and b) n-pad in convex shape (m-pad-v and n-pad-v) in contacting with their substrate. In this scenario, the adhesion forces are derived from Eqs. (3.30) and (2.59) in condition of angle $\beta_1^* = 0.2$, 0.6, 1 and 1.4 rad. R_s was set 14.3 mm.

Since the contact angles $\theta_{1,2}$ present the ability of wet adhesion of the pad-liquid-substrate, the normal forces in Figs. (5.17) and (5.18) drop rapidly as β_1 and β_1^* increase to 1.4 rad. Also the normal adhesion of the m-pad is about two-fold bigger than that of the n-pad (Fig. 5.19). In general, these forces gradually reduce to zero for the n-pad when increasing the interface gap h in contrast to m-pad. The forces in m-pad-v is slightly higher than that of m-pad-c because of rising contact area.

Although the normal adhesion force in Figs. 5.20 and 5.21 has the similar trends compared with the influence of the angles β_1 and β_1^* in previous graphs, the angle α_1

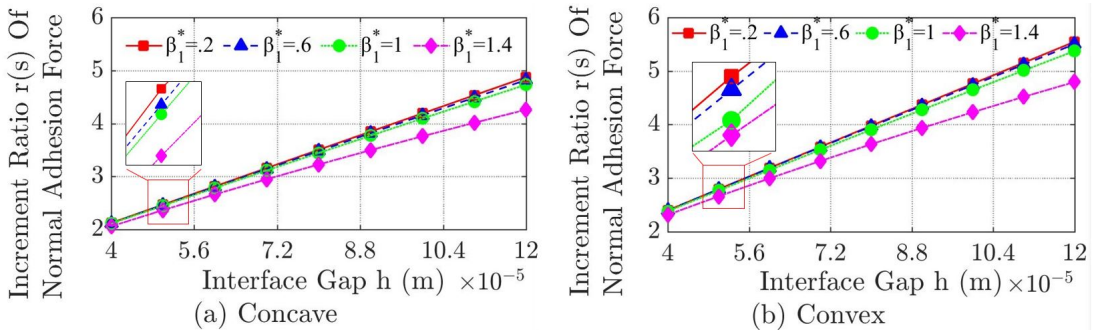

Figure 5.19: Effect of the interface gap h on the ratio of normal adhesion force between two cases a) m-pad-c (derived from Eq. (3.30)) and b) n-pad-c (derived from Eq. (2.59)).

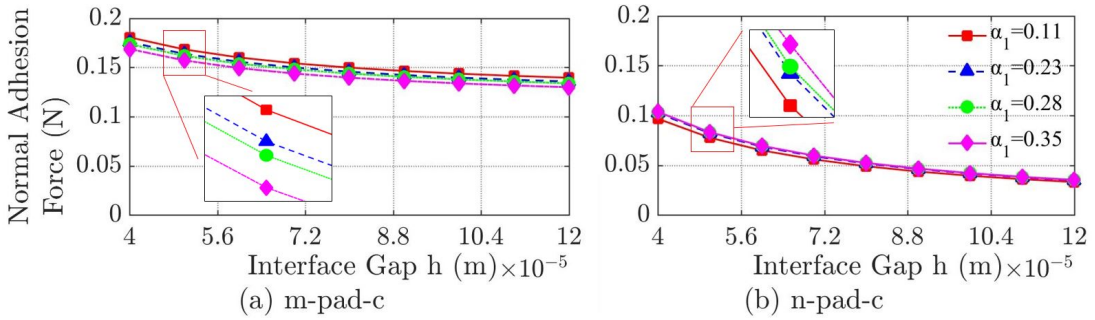

Figure 5.20: Effect of interface gap h on the normal wet adhesion force of a) m-pad-c (derived from Eq. (3.30)) and b) n-pad-c (derived from Eq. (2.59)) at angle $\alpha_1 = 0.11$, 0.23, 0.28 and 0.35 rad. In this graph, the parameters are fixedly chosen such as the angle $\beta_1 = 0.86$ rad, $L = 1$ mm.

affects slightly the resulted forces. In case the pads contact the substrates in small area (L_p is small), the radius R_2, which presents the wet area and wet periphery, has not much change even if α_1 increases. The wet adhesion forces in all cases decrease as the angle α_1 (radius R_s) rises. The ratio r_s in Fig. 5.22 show that the m-pad enhance the normal adhesion force about 2 times comparing with the n-pad. Also this ratio in convex case is slightly higher than concave case. Consequently, based on simulated results, in static state, the normal wet adhesion force varies directly according to the variants contact angle and substrate's radii. Also the force generated in convex m-pad is slightly higher than that of the concave one.

5.3.1.2 Detachment Phase

In dynamic state, viscosity force F_v appears, enhancing the normal wet adhesion force. Figures 5.23 and 5.24 shows variation of normal wet adhesion force according to the angle β_1, β_1^* associated with the substrate's radii R_s. The normal adhesion forces in these figures vary directly according to both β_1 and β_1^*, where the variants β_1 and β_1^* affect significantly on the normal adhesion forces in contrast to the substrate's radii R_s. As $\beta_1 = \beta_1^* = 1.4$ rad, the normal adhesion forces of m-pad and n-pad set the lowest value smaller than 0.06 N;

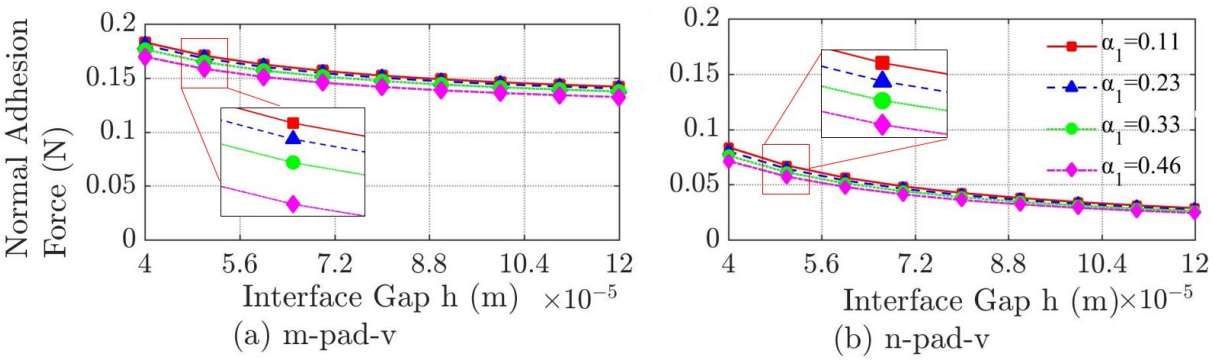

Figure 5.21: Effects of interface gap on the normal wet adhesion force of a) m-pad-v (derived from Eq. (3.30)) and b) n-pad-v (derived from Eq. (2.59)) at angle $\alpha_1 = 0.11$, 0.23, 0.33 and 0.46 rad. In this graph, the angle β_1 and the thickness of pads L are chosen as previous graph.

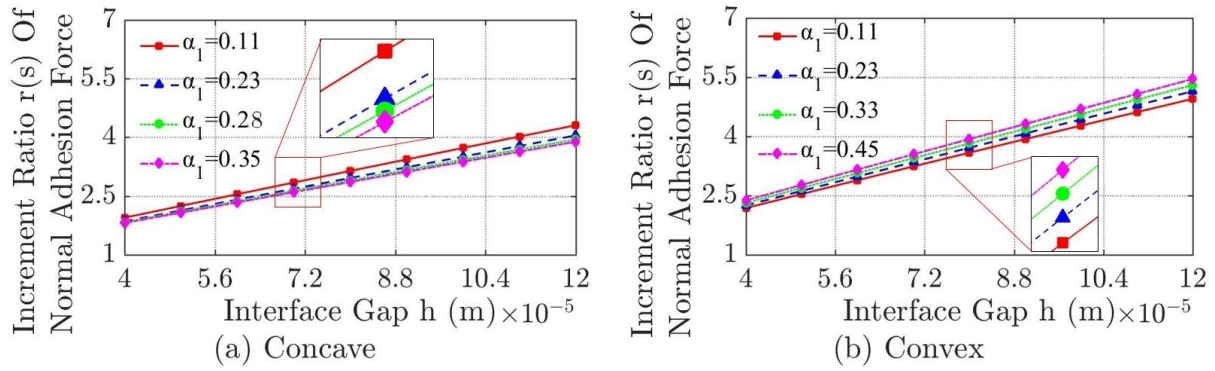

Figure 5.22: Affect of interface gap h on the ratio of normal adhesion force between a) m-pad-c (derived from Eq. (3.30)) and b) n-pad-c (derived from Eq. (2.59)) at changing angle α_1.

whereas, it increases 4 times for $\beta_1 = \beta_1^* = 0.2$ rad. On the other hand, the forces rise slightly as the radii R_s change from 10 to 30 mm.

For lower viscosity liquid (η puts small value), the viscosity forces depend on the velocity v_z and contact areas (or R_2). Since interface gap h values micro scale, it is difficult for the pads to reach high velocity in narrow gap. In fact, v_z can set at high value after the pad moving in a larger gap, *i.e.* the capillary bridge become weaker and broken. Thus, in this model we consider the velocity v_z being small that leads to infinitesimal entities of viscosity force comparing with Laplace force. Hence, the normal adhesion forces in dynamic state (Figs. 5.23 and 5.24) has not much difference from that of static state.

As h becomes larger, the Laplace pressure approaches zero, accompanied by gradual breakage of the capillary bridge. Therefore, the normal adhesion forces close to zero with an interface gap $h \geq 0.12$ mm as shown in Fig. 5.25. Moreover, determining exactly the peak of interface gap h_p or the event when bubbles appear is extremely complicated because this state depends on various parameters in the contact model. Thus, the estimated results of the normal adhesion forces in Fig. 5.25 include two types of curves: without bubbles (solid line) and with bubbles (dash line) for the m-pad-c and n-pad-c. In general, the normal

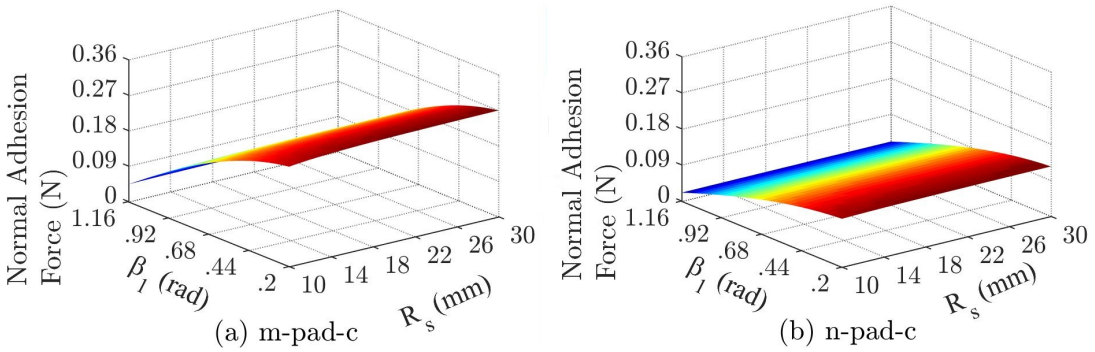

Figure 5.23: Influence of the angle β_1 and the substrate's radii R_s to the normal adhesion force for a) m-pad-c (derived from Eq. (3.35)) and b) n-pad-c (derived from Eq. (2.62)) with $g_h = 0$. In this graph, we set values of $R_s = 15\,\text{mm}$ and the velocity $v_z = 0.0005\,\text{m}s^{-1}$.

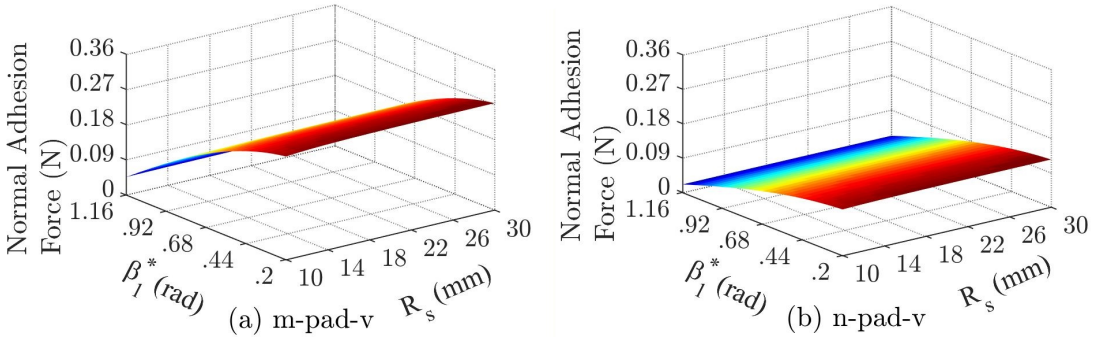

Figure 5.24: Influence of the angle β_1^* and the substrate's radii R_s to the normal adhesion force for a) m-pad-v (derived from Eqs. (3.35)) and b) n-pad-v (derived from Eq. 2.62)) with $g_h = 0$. Other conditions was set as same as Fig. 5.23, and $R_s = 14.3\,\text{mm}$.

adhesion force corresponds to an event without bubbles if the interface gap h is small and with bubbles if h is large. Additionally, the normal wet adhesion forces drop to zero in case the contact angle is very large since the ability of wet adhesion reduce significantly. The ratios in Fig. 5.25(c) also reduce to zero accompanied by the trend of normal force.

5.3.1.3 Normal Adhesion with Preload

Under impact of the preload P, the m-pad-c has higher value of the normal contact force comparing with that of normal pad. The preload P effects importantly both in the normal contact force in Fig. 5.26(a-b) and the ratio r_s in Fig. 5.26(c). In fact, these forces vary directly to the preload and the angle β_1 partly. With strong influence, the preload plays principal role in the normal contact force that leads to 1 in the ratio in Fig. 5.26(c) as P rises. Increasing P in small range is associated with decrease of h, however, the pads will be deformed extremely large that can destroy the structure of the micro pattern if we continue compressing. Also covering the pad surface with a thick liquid under the effects of a huge preload P may reduce the wet adhesion effects. In this case, rather than acting as a suction pressure, the liquid generates a push force to detach the contact.

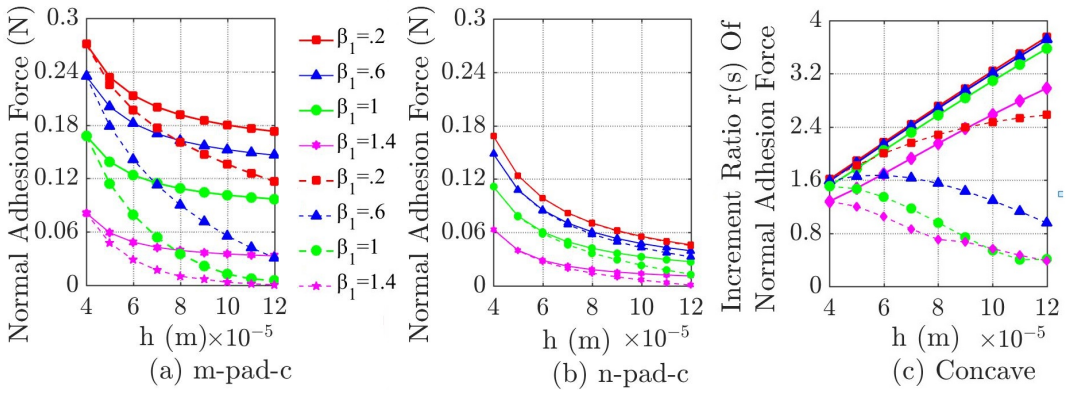

Figure 5.25: Normal adhesion forces of the n- and m- pads in the same area by change in the interface gap h. Normal adhesion force of a) m-pad-c (derived from Eq. (3.35)) and b) n-pad-c (derived from Eq. (2.62)). c) Ratio of normal adhesion force between m-pad-c and n-pad-c In this graph, the solid and dash lines in turn show the results in case of without $g_h = 0$ and with bubbles $g_h = 1$ (Eqs. (3.35) and (2.62)).

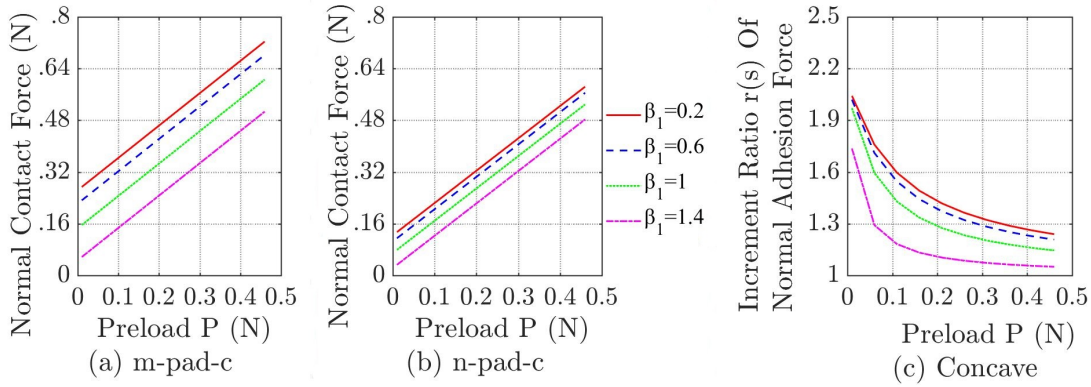

Figure 5.26: Influence of the preload P to the normal contact force of a) m-pad-c (derived from Eq. (3.33)) and b) n-pad-c (derived from Eq. (2.96)). c) The ratio of normal contact force directly divided from a) and b).

In addition, the contact interface of the m-pad was softer than that of the n-pad since the structure of the micro pattern, which makes the pad easier to deform and better absorb external loads like P. Thus the normal reaction force of the contact can be lower for the the micropattern surface than for the normal when applying a higher preload. This property may decline the risk of deformation of a grasped soft and fragile objects under impact of resultant normal force, as well as enhance wet adhesion.

In summary, in all case of contacts: "detachment phase" and "attachment phase", the normal contact force of m-pad always higher than that of the n-pad. In addition, the normal wet adhesion forces generated in convex pads are slightly larger comparing with the concave pad in the same estimated condition in this study. In other words, micro-patterned structure plays an important role on enhancing the wet adhesion force for m-pad. Finally, with the small values of contact area, dimension of the pads, and other parameters of the liquid related to the ability of wet adhesion, the normal contact force

depends majorly on the contact angle, preload; whereas R_s and $\alpha_{1,2}$ affect partly on it.

5.3.2 Setting Experiment

To enhance the wet adhesion ability, the pads were treated with oxygen plasma in the condition: 10 Pa×10 min×30 W (Fig. 5.27(a)). Additionally, we also measured the contact angles of the pad and the substrate.

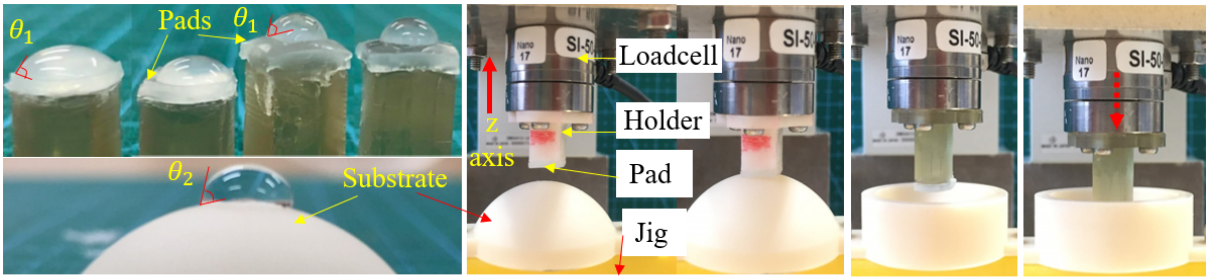

(a) Contact angles (b) Experimental setup

Figure 5.27: Scheme of experimental set-up for measuring the normal adhesion force. a) The contact angles θ_2 for the pads is roughly equal to 72°; whereas that of the substrate is 80°. In b), the loadcell translates in z-direction for two case of the pads: n-pad and m-pad with concave and convex contact interfaces. In this scenario, the substrate radii for the m(n)-pad-c were R_s=10.26 and 15.33 mm, and for the m(n)-pad-v were R_s=7.55 and 14.34 mm. An addition, the contact interfaces between the pads and the substrates are considered being coincident to have the same radii.

Figure 5.27(b) shows the experimental set-up for evaluating the normal adhesion force of the wet contact between each the two case of pads (the m-pad and the n-pad) and the substrates. Herein, we fixed the holders of the concave and convex pads in the loadcell ATI-Nano-17 which can translate in z-direction through a linear stage controlled by Suruga Seiki D212. Also the curved substrate were fixed in a jig such that can form the contact interface with the pads. Additionally, both of the pads and the substrate were accurately adjusted for getting the largest contact area. Datum were collected through utilizing an ADC analog-to-digital converter National Instrument connected with Matlab software operated in Windows 10. Such experimental apparatus were already introduced in [107]. Then, the surfaces of the pads were wiped with a 0.2 mm thickness of thin film water and waited for the grooves sucking water in 5 minutes. The pads were set at an initial gap of 1 mm from the substrate interfaces and a constant velocity was sequentially applied at 4 different values of the normal velocity v_z, corresponding with the unchanged preload P values of 0.1, 0.22, 0.33, 0.45 and 0.6 N. In this study, we performed the test for two radius levels R_s of each type of the substrates: 10.26 and 15.33 mm for the concave pad, and 7.55 and 14.34 mm for the convex pad. Five trials were performed under each condition.

5.3.3 Results

Since the contact angles θ_1 and θ_2 depend on parameters of liquid, substrate, and pad [184, 185], it is complicated to model the results precisely. However, we can consider $\theta_3 \approx \beta_1 = \beta_1^*$ as previously described [220] and $\alpha_1 \approx \alpha_2$, $R_2 \approx x_s$. In addition, other parameters are given in table 5.3.

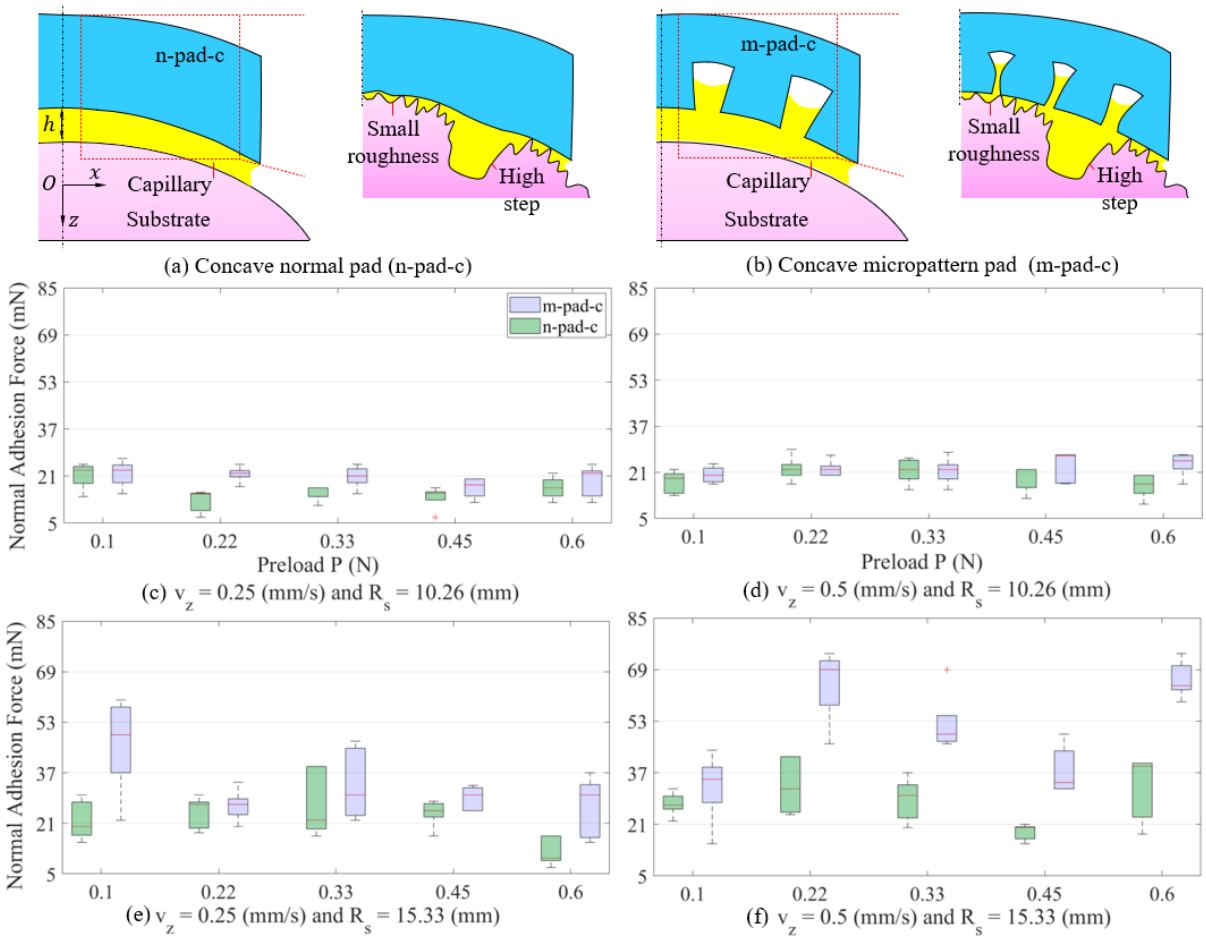

Figure 5.28: Comparisons of the normal adhesion force for the wet contact between the concave pads (a) n-pad-c and b) m-pad-c) and the substrate in varying preload P and velocity v_z. There are two levels of substrate radius: c) and d) R_s=10.26 mm, ($\alpha_1 = 20°$, w_1^c=6.2 μm and $\bar{w^c}$=6.4 μm), and e) and f) R_s=15.33 mm (α_1= 10.526°, w_1^c=9.538 μm and $\bar{w^c}$=9.552 μm).

In figure 5.28, the experimental data of the normal adhesion during detaching the substrates of the m-pad-c is 1÷2 times higher than that of the n-pad-c. Also the preload P and the velocity v_z have not much singnificant affect on the varying of the the force $F_{w,n}$ for the pads with R_s= 10.26 mm; whereas, these factors enhance $F_{w,n}$ more than 200 % for the m-pad-c (Fig. 5.28(c-d)). Thanks to increasing R_s the angle α_1 and shrinking the groove both reduce as aforementioned in chapter 3, from the formulation $w_1^c = [L_p R_s/(R_s + L) - aN^{0.5}]/(N^{0.5} - 1)$. The applied preload P in z- direction makes the cells themselves axial compress and slip further the center axis of the m-pad-c. For the sake

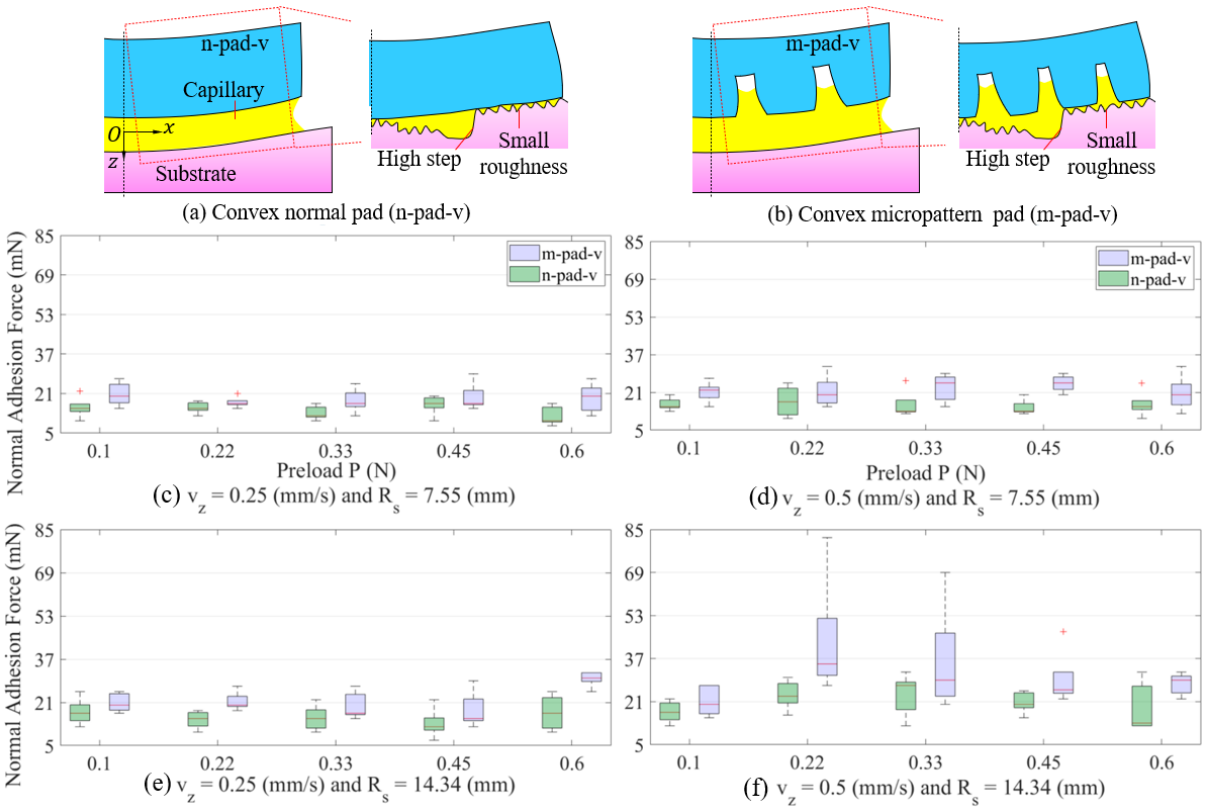

Figure 5.29: Comparisons of the normal adhesion force for the wet contact between the convex pads (a) n-pad-v and b) m-pad-v) and the substrate in varying preload P and velocity v_z. There are two levels of substrate radius: c) and d) R_s=7.55 mm, ($\alpha_1 = 26.24°$, w_1^v=30.78 μm and $\bar{w}^v$=30.44 μm), and e) and f) R_s=14.34 mm ($\alpha_1 = 12.858°$, w_1^v=22.064 μm and $\bar{w}^v$=21.73 μm).

of simplicity, the lateral deformation Δa of each cell's edge can equal to $\nu P \cos\alpha/(NEa^2)$. However, Dragon Skin 30 has large deformation under impact of the preload P that gennerates the convex shape instead of plain for each side wall of the cells. Applying calculations in [221, 222] with assuming all cells of the m-pad-c completely contact the substrate, the entity Δa of each cell roughly becomes $a(1/\sqrt{1 - P\cos\alpha_1/(NEa^2)} - 1)$. Hence, the reducing values of w_1^c are respectively 0.26 μm and 0.27 μm (4.2 % and 2.8 %) for the m-pad-c with R_s= 10.26 mm and 15.33 mm. In fact, the contact surfaces of the substrates are not perfectly smooth, as shown in Fig. 5.27(d), for completely contacting with the pads. Because of these errors in printing at changing each layer, the cells can major have parallel contact at the small roughness; whereas, it is too difficult to completely approach at the areas having the high steps (~16 μm). As a result, the grooves of the m-pads at the small roughness areas of the substrate have much larger deformations comparing with that of the rests. In other words, the corresponding cells are not separated (become flat surface) as increasing preload P that leads to the small increasing wet adhesion in case R_s= 10.26 mm (Fig. 5.28(a-b)). In Fig. 5.28(c-d), the preload P does not shrink the grooves so large that can disappear the pattern or significantly changes the pad

morphology. Thus, the normal adhesion force of the m-pad-c in this case is higher than that of the case R_s=10.26 μm.

The normal adhesion force in case the convex pads in Fig. 5.29 gives similar results as of the concave pads. The testing data of the m-pad-v is 1÷2 times higher than that of the n-pad-v. Also, the preload P and the velocity v_z have not much significant affect on the varying of the the force $F_{a,n}$ for the pads with R_s= 7.55 mm; whereas, these factors enhance $F_{a,n}$ more than 200 % for the m-pad-c with R_s= 14.34 mm (Fig. 5.29(c-d)). The reducing values of w_1^v are respectively 0.248 μm and 0.27 μm (0.8 % and 1.2 %) for the m-pad-v with R_s= 7.55 mm and 14.34 mm. Since the high steps of substrate surface are around 16 μm, the width of the grooves of the m-pad-v is too large to enhance the wet adhesion. In this scenario, the suction force of the groove can be considered to neglected in case R_s= 7.55 mm. On the contrary, the m-pad-v having R_s= 14.34 mm can rise the Laplace force F_{Lm}^v inside the grooves corresponding with the flat surface area of the substrate thanks to significantly reducing the groove's width under high applied preload P.

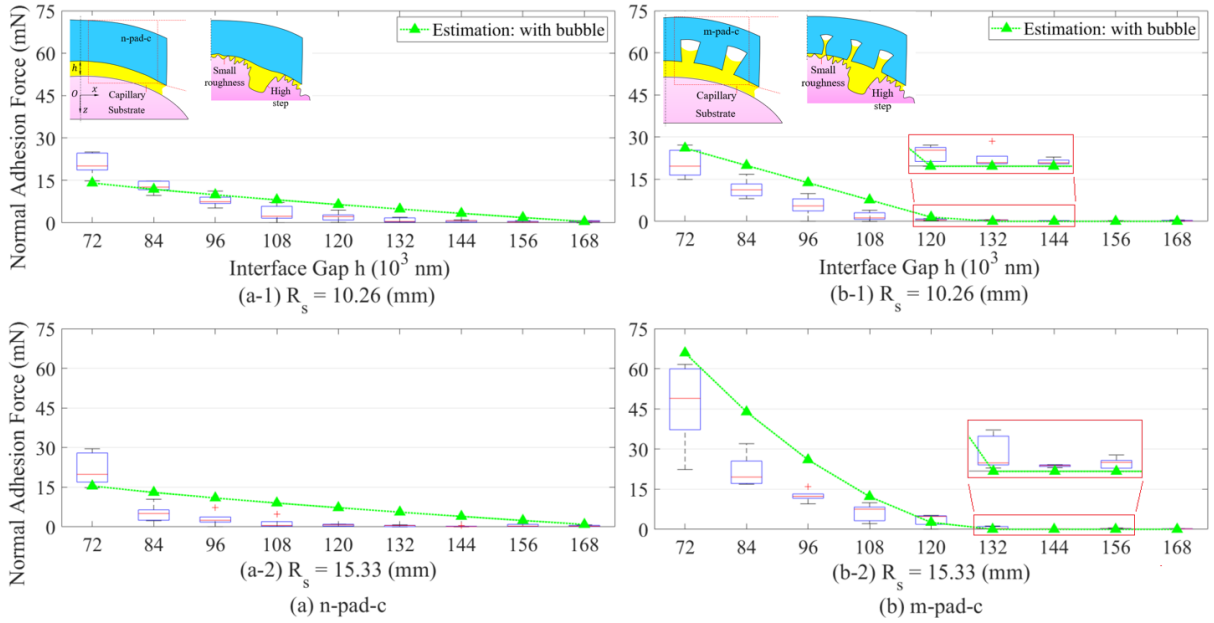

Figure 5.30: Comparisons of the normal adhesion force for the wet contact between the concave pads and the substrate in varying interface gap h with the conditions: P= 0.1 mN and v_z=0.25 mm/s. a) The n-pad-c and b) m-pad-c respectively consist of two levels of the substrate radii: R_s=10.26 mm a-1) and b-1), and R_s=15.33 mm a-2) and b-2). Also the estimation curves are obtained from Eqs. (3.33) and (2.96) for in turn the m-pad-c and n-pad-c.

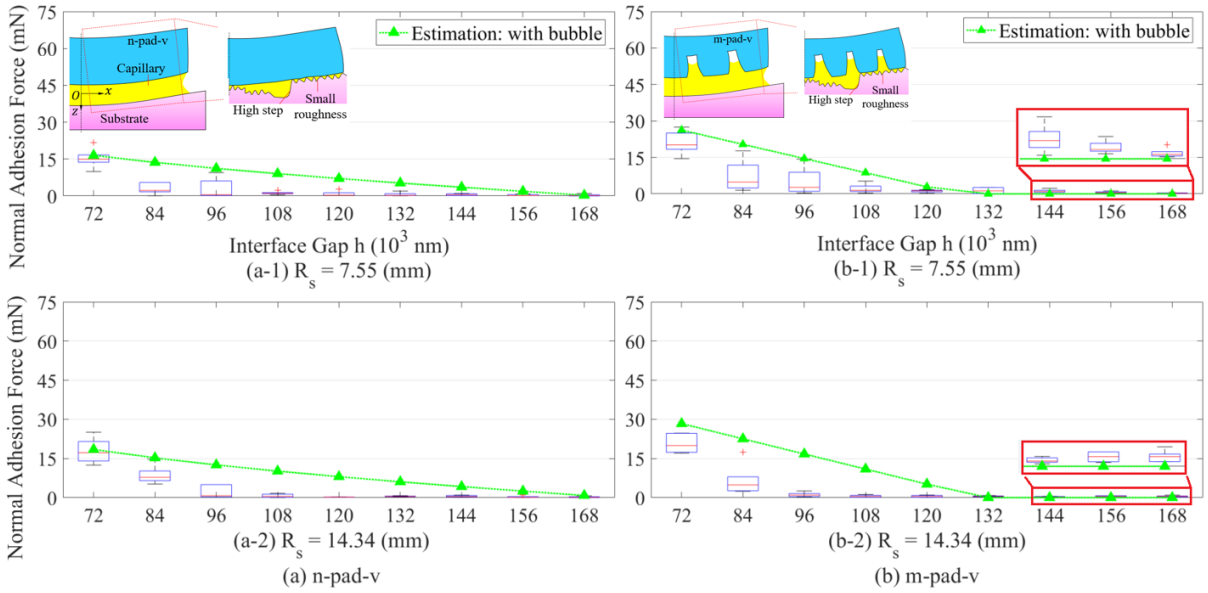

Figure 5.31: Comparisons of the normal adhesion force for the wet contact between the convex pads and the substrate in varying interface gap h with the conditions: P= 0.1 mN and v_z=0.25 mm/s. a) The n-pad-v and b) m-pad-v respectively consist of two levels of the substrate radii: R_s=7.55 mm a-1) and b-1), and R_s=14.34 mm a-2) and b-2). Also the estimation curves are obtained from Eqs. (3.33) and (2.96) for in turn the m-pad-v and n-pad-v.

In spite of having not much significant contribution to the force components, the velocity v_z integrating the preload P effects arranging the contact states of the m-pad-c and m-pad-v, which varies the groove's width and the interface gap h between the pads and the substrates as well as generates the high values of the normal adhesion force: 0.73 and 0.81 mN in Figs. 5.28(c) and 5.29(d). Hence, the results of the normal adhesion force $F_{w,n}$ in case P= 0.1 mN and v_z=0.25 mm/s are applied to validate the theoretical model as shown in Figs. 5.30 and 5.31. The forces $F_{w,n}$ reach maximum at the interface gap $h \approx$72 μm when the network of the grooves and cells nearly return the initial states without deformation. The large interface gap generates the break bubbles inside the capillaries between the couple interfaces, which can validate the estimations through the Eqs. (3.33) and (2.96) in comparison. In almost cases, the peaks interface gap h_p of the estimation are good agreement with the experiment. The small errors gradually appear at the interface gap in 84$\div$120 μm as the break bubbles become too large before separate the capillary bridges.

In summary, the obtained results show that the geometrical parameters such as: R_s, L, L_p and the patterned morphology have significant contributions to varying the normal adhesion force. Also the surface characteristics (roughness and adhesive ability) of the substrate impact on the pad morphologies during contacting. As well, the liquid film significantly effects on evaluating the model. Because this study applies one kind of the liquid, we consider neglecting the investigation the water's factors. Finally, the

micropattern structure plays an important role in enhancing the wet adhesion force-one of the principal components of the contact force in modelling the grasp. Hence, our model in this study is appropriate for development of designing the soft robotics hand applied into grasping objects which have curved surfaces in actual applications.

CHAPTER 6

APPLICATIONS

Previous chapters showed that the micropatterned morphology can help the m-pad achieve a stronger wet adhesion force in contacting with its substrate than that of the n-pad. In this chapter, we introduce the actual applications of grasping/manipulating soft fragile objects by the soft robotic hands, whose fingers had the micropatterned designs. In this scenario, there were two types of the objects grasped: contact lens-a showcase of the thin shell objects [76] and tofu-a showcase of the rheological objects. In any situations, compress force acting on the object's surfaces were investigated and compared between two cases of the contact: the m- and n-pads.

6.1 Design of Soft Robotic Hand for Gripping Thin Shell

A contact lens immersed in a preservative liquid was taken out and attached to a substrate's surface mimicking a 'human eye' by a soft robotic hand or soft gripper. Afterward, the such gripper or robotic hand can remove the contact lens from the substrate and place it in the tank with the preservative liquid. Herein, the contact lens should be gripped with a minimum force for avoiding large deformation. Therefore, we built an analytical model of the robotic hand, with the finger's tips having micropatterned and normal surfaces, gripping a thin-deformable shell (with the contact lens is a showcase) and carried out the investigation of the grasp forces generated by two such pads during operation.

6.1.1 Mechanics of Bending a Thin Hemispherical Shell

First of all, we can define a hemispherical object as a thin shell when the ratio $t/R_m < 1/20$ happens [223]. Hence, all cases of the thin shell in this section are assumed to satisfy the given condition. As illustrated in figure 6.1(a), the thin hemispherical shell is under

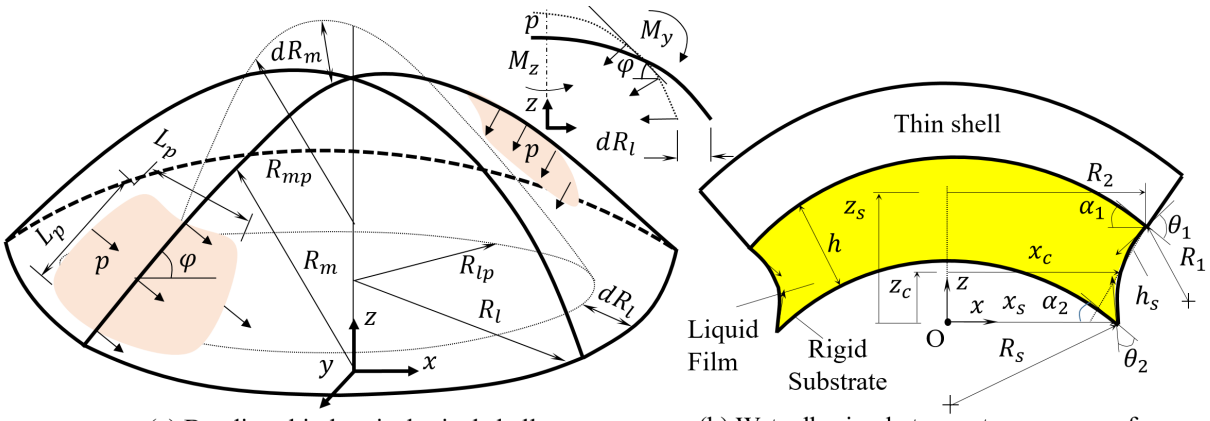

(a) Bending thin hemispherical shell (b) Wet adhesion between two curve surfaces

Figure 6.1: Schematic illustration of a thin shell under contact of the pads and the substrate. a) Bending a soft hemispherical shell with a thin thickness by two opposing fingers attaching the soft pads with area $L_p \times L_p$. Under the effects of the preload $P = pL_p^2$ in normal direction of the shell's surface, the shell deformed in mediator and latitude directions, corresponding with the entities dR_m and dR_l. b) Schematic illustration of the adhesion between two parallel curves of the contact interface: the thin-deformable shell and the hemispherical substrate at the interface gap h.

effects from the pads fixed at the robotic finger's tips. Let us denote $\kappa = Et^3/[12(1-\nu^2)]$ and $\kappa_1 = Et/(1-\nu^2)$, and subsequently, using Kirchhoff-Love equation [224] derives the moments M_y and M_z generated on the shell in the form:

$$\begin{bmatrix} M_y \\ M_z \end{bmatrix} = \kappa \begin{bmatrix} 1 & \nu \\ \nu & 1 \end{bmatrix} \begin{bmatrix} \chi_1 \\ \chi_2 \end{bmatrix}, \tag{6.1}$$

with $\chi_1 = 1/R_{mp} - 1/R_m$ and $\chi_2 = 1/R_{lp} - 1/R_l$ are the deformations of the thin shell in the mediator and latitude directions, respectively. Also, we have the following relation:

$$pL_p^2 = \kappa_1(\epsilon_1 + \nu\epsilon_2), \tag{6.2}$$

where ϵ_1 and ϵ_2 present the deformations of the thin shell, respectively, in the tangential and normal directions. Because p brings normal pressure to the shell's surface, the entity ϵ_1 is closed to 0; whereas, ϵ_2 approximate to $dR_l \sin\varphi/R_m$. Hence, from equation (6.2) we can obtain $p = \kappa_1 \nu dR_l \sin\varphi/(R_m L_p^2)$. Additionally, by synthesizing equations (6.1) and (6.2) we have the deformations and bending angle φ of the thin shell are directly proportional to the entities M_y, M_z, and p. Our research concentrates on evaluating the influence of the preload pressure p on the bending angle φ.

6.1.2 Wet Adhesion Between Two Parallel Curved Surfaces

In this scenario, we also investigate the underlying physics of adhesion for the contact between the thin shell and the hemispherical substrate (Fig. 6.1(b)). Herein, the process of forming capillary force from the liquid film for enhancement of the adhesion in the contact is explained in chapter 2. In figure 6.1(b), a thin-deformable shell in contact with its hemispherical substrate through a capillary bridge with the interface gap h being same at each point in the contact. Hence, the assumption of R_1 equalling to the meridian circle's radius of the capillary as shown in figure 6.1(b) yields:

$$R_1 = z_s/[\cos(\theta_1 - \alpha_1) + \cos(\theta_2 + \alpha_2)]. \tag{6.3}$$

In addition, z_s, h is equal to $h_s \cos\alpha_1$ and $h_s(1-\sin\alpha_1 \sin\alpha_2)+(R_2-x_s)\sin\alpha_2$, respectively. Therefore, the radius R_1 in equation (6.3) is rewritten in:

$$R_1 = \frac{[h - (R_2 - x_s)\sin\alpha_2]\cos\alpha_1}{[\cos(\theta_1 - \alpha_1) + \cos(\theta_2 + \alpha_2)]\,(1 - \sin\alpha_1 \sin\alpha_2)}. \tag{6.4}$$

Usually, we have $R_1 << x_c$ for a tiny interface gap h. That is, the entity $1/x_c$ is close to zero. If α_1, α_2 are equal to $\alpha = \sin^{-1}(x_s/R_s)$, $R_2 \sim x_s$, and $\beta_1 = \theta_1 - \alpha$, $\beta_2 = \theta_2 + \alpha$, the normal wet adhesion force for the n-pad-c $F^c_{wn,n}$ becomes:

$$F^c_{wn,n} = \pi\gamma R_2 \left[2\sin\beta_1 + R_2 h^{-1}(\cos\beta_1 + \cos\beta_2)\cos\alpha\right]\hat{z}. \tag{6.5}$$

In equation (6.5), the normal surface tension $F_{st,n}$ and laplace force $F_{L,n}$ are equal to $2\pi\gamma R_2 \sin\beta_1$ and $R_2 h^{-1}(\cos\beta_1 + \cos\beta_2)\cos\alpha$; whereas the normal viscosity force is in the relation $F_{v,n} \approx 0$ because the pad velocity in normal direction $v_z \sim 0$ in case of grasping. The equation (6.5) makes a theoretical foundation for calculating the forces $F^c_{wn,n}, F^c_{wm,n}$ in the following steps.

6.1.3 Wet Adhesion In Grasping A Thin Hemispherical Shell

This section shows a scenario of the thin hemispherical shell with its curvature radius $R_m = R_s + t/2$, which was soaked in a tank containing preservative liquid and subsequently grasped and moved by two opposite pads in three conditions: inside the liquid (figures 6.2(a) and 6.3(a)), outside the liquid (figures 6.2(b) and 6.3(b)), and in contact with the substrate (figures 6.2(c) and 6.4). In equilibrium state, the grasp force F_g is in the relation:

$$F_g = (F_r + G - F_b)\hat{z}. \tag{6.6}$$

Herein, the contact force F_c and grasp F_g are calculated for specific cases during the process of grasping; whereas the bouyancy force F_b [225] is only estimated in case "shell in liquid".

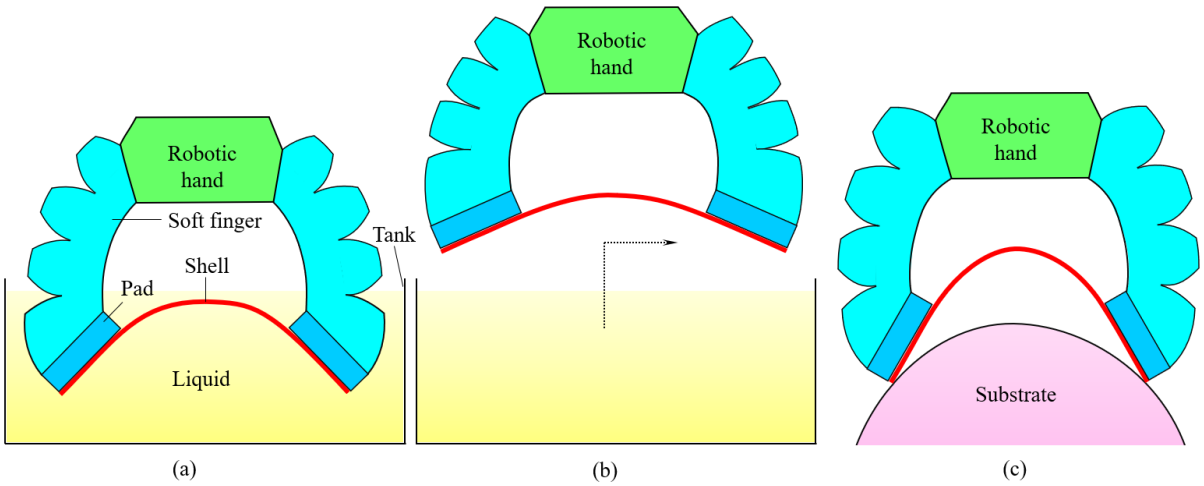

Figure 6.2: Schematic illustration of gripping and moving the thin shell in three conditions. a) The thin hemispherical shell immerses inside liquid. In this scenario, the pads grasp the hemispherical shell through the bending force produced by two opposite pad acting on the lateral side of the shell. Afterward, those such pads move upward to lift the hemispherical shell out of the tank. b) The thin hemispherical shell is outside the tank. In this situation, the thin shell is translated in lateral direction (x-axis) to approach the hemispherical substrate. Also, the couple pads gradually decreases the preload pressure p to expand the thin shell before dropping it for contacting the substrate. c) The thin hemispherical shell contacts the substrate mimicked the human eye. Finally, these pads generate preload P to peel the shell away the substrate.

6.1.3.1 Shell Inside Liquid

As shown in figure 6.3(a), the thin hemispherical shell which is soaked in preservative liquid having a small viscosity coefficient η, is grasped and moved out the tank along z-direction with velocity v_z. Herein, the thin shell with its radius in initial state R_l lies in the tank's bottom. The two opposite n-pads simultaneously makes symmetrical contact on the sides of the thin shell on z-axis and generates deformation dR_l for the shell. Let us consider that the the thin shell is much softer compared to that of with the pads. In other words, this shell is deformed under the preload pressure p produced by the n-pads as shown in figure 6.1.

Since the adhesion appertaining inside the liquid is extremely weak, the grasp force F_g in Eq. 6.6 majorly depends on the friction force $F_f^* = \mu^* p L_p^2$ between the contact interface of the shell and pad. Thus, to win the contact force F_c the grasp force $F_{g,z}$ in z-direction needs to satisfy:

$$F_{g,z} = 2\mu^* p L_p^2 \sin\varphi = (F_d + G - F_b)\hat{z}. \tag{6.7}$$

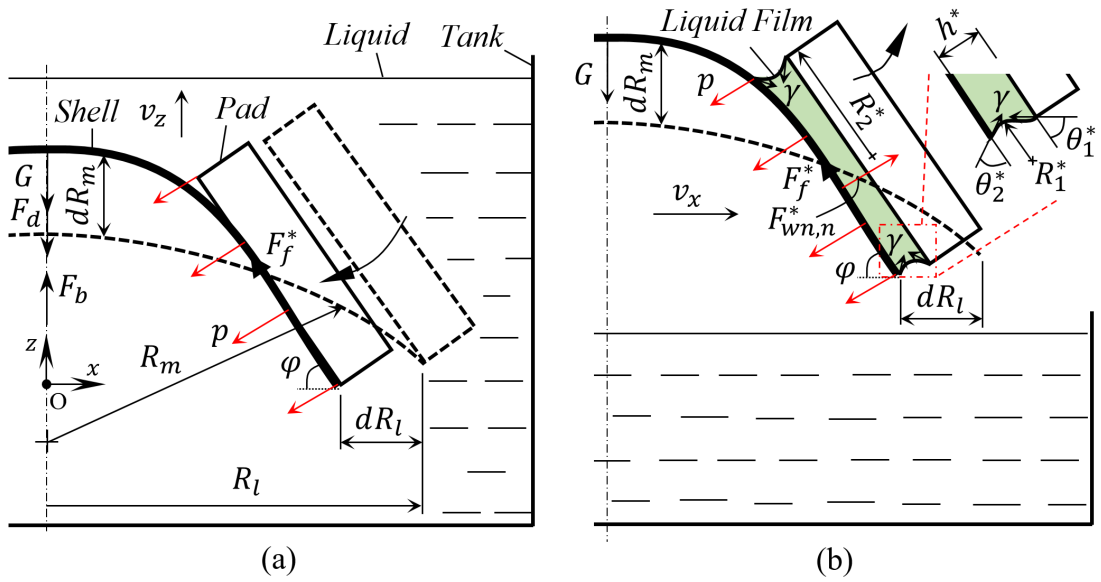

Figure 6.3: Mechanics of gripping and translating the thin hemispherical shell in different environments: inside a) and outside liquid b). Herein, because the pad directly contact the shell's surface, we can denote the interface gap, frictional force, contact angles and outside and inside radii of the meniscus curvature, respectively, by $h^*, F_f^*, \theta_1^*, \theta_2^*, R_1^*, R_2^*$. In addition, the preload pressure p is considered to be perpendicular to the shell surface motion.

In case the thin shell is safely gripped (without dropping), the force $F_{g,z}$ must be larger than the entity $F_d + G - F_b$, which is described as:

$$p \geq (0.5C\rho_l A_d v_z^2 + mg - \rho_l V g)/(2\mu^* L_p^2 \sin\varphi). \tag{6.8}$$

Here, we have the bouyancy and drag forces determined as $F_b = \rho_l V g$ and $F_d = 0.5C\rho_l A_d v_z^2$ [226]. Combining equations (6.2) and (6.8) yields the values of $\langle p, dR_m, dR_l \rangle$ of the thin shell. Rising the preload pressure p associates with strengthening the grasp force F_g in locking the thin shell.

6.1.3.2 Shell Outside Liquid

In this scenario, the thin hemispherical shell is translated from an initial place outside the tank (see Figs. 6.2(b) and 6.3(b)) to attach the substrate as shown in figure 6.2(c). After being lifted out of the preservative liquid, almost volume of the liquid flows off the shell's surface; whereas a tiny amount of the liquid remains inside the contact interface, which can generate the capillaries. This mechanism produces wet adhesion force F_{wn}^* to stick the n-pad to the shell with a lower preload pressure p. To achieve an efficient attachment between the thin shell and the substrate, the bending angle φ and deformation dR_l need to decrease before making the contacts between: the convex curvature of the substrate surface and the concave curvature of the shell surface. Therefore, by applying Eq. (2.42)

with the dry adhesion is zero yields the normal wet adhesion of the contact between the n-pad and the shell as follows:

$$F^*_{wn,n} = L_p\gamma\left[4\sin\theta^*_2 + L_p(\cos\theta^*_1 + \cos\theta^*_2)/h^*\right]\hat{z}. \tag{6.9}$$

Since the thin hemispherical shell is handled outside the tank containing the liquid, the grasp force F_g in equation (6.6) additionally includes the normal wet adhesion force $F^*_{wn,n}$; while the resistance force F_r eliminates the drag component F_d. Moreover, in case the n-pad has no complete contact with the hemispherical shell, the preload pressure p and the wet adhesion force $F^*_{wn,n}$ acting on the shell needs to be multiplied by a coefficient $k*$. Hence, in order to retain grasping this shell the grasp force $F_{g,z}$ has to be in the form:

$$F_{g,z} = 2\mu^* k^*(pL_p^2 + F^*_{wn,n})\sin\varphi\hat{z} = mg\hat{z}. \tag{6.10}$$

From equation (6.10) derives:

$$p = \left(\frac{mg}{2\mu^* k^*\sin\varphi} - F^*_{wn,n}\right)\frac{1}{L_p^2} < \frac{mg}{2\mu^* k^* L_p^2\sin\varphi}. \tag{6.11}$$

In case the wet adhesion appears, the preload pressure p in Eq. (6.11) may significantly decrease. This induces a smaller value of the deformation dR_l, which assists the pads to govern the situation of the thin shell before attaching the corresponding substrate.

6.1.3.3 Shell in Contact with a Hemispherical Substrate

In this situation, firstly the thin hemispherical shell is placed so that it makes a complete contact with the substrate mimicking the human eye. Subsequently, the pads contact and generate the preload pressure p on the thin shell as shown in figure 6.4 before gradually peeling this shell off the substrate. In the contact, the hemispherical shell sticks the substrate by the wet adhesion force F_w calculated in equation (6.5). The thin shell, in this scenario, consists of two kinds: shell-substrate and shell-pad where the contact area between the thin shell and the pads is smaller than that the shell and the substrate (Fig. 6.4(a)). Hence, in order to peel the thin shell off the substrate surface the soft pads require a preload pressure p integrating with the wet adhesion force $F^*_{wn,n}$.

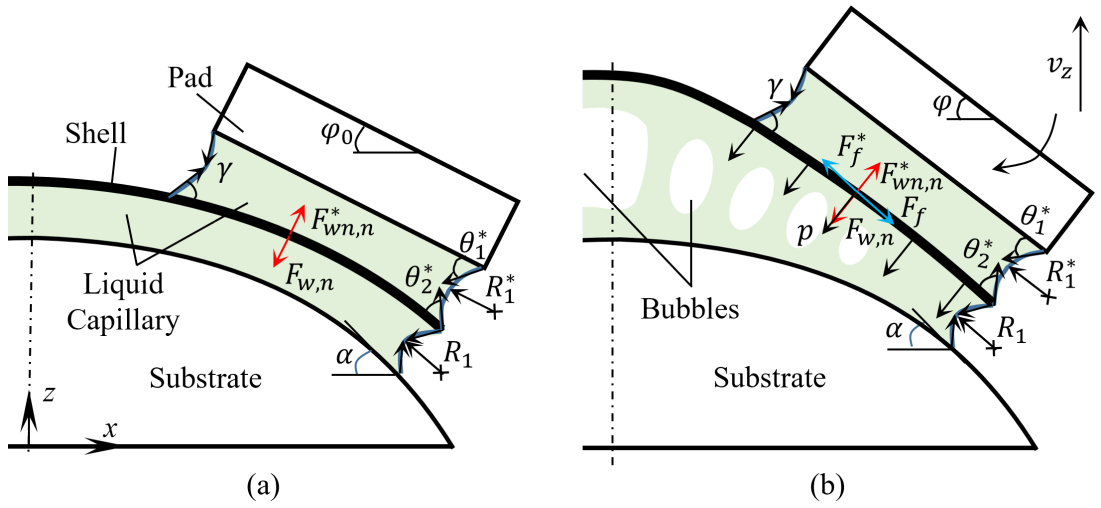

Figure 6.4: Schematic illustration of peeling the thin hemispherical shell off the substrate. The n-pads contact the thin hemispherical shell a) and generate preload pressure for removing the shell.

As there is no deformation for the thin hemispherical shell, the contact between the n-pads and this shell can be equal to the plane-sphere type. According to Lazzer [194], we have the normal wet adhesion of the plane-sphere as initial contact as follows:

$$F^*_{wn,n} \sim L_p\gamma \left\{4\sin\theta^*_2 + L_p\left[\cos\theta^*_1 + \cos\left(\theta^*_2 + \theta_s\right)\right]/h^*\right\}, \tag{6.12}$$

where the contact angle θ_s is calculated in $\sin^{-1}[L_p\pi^{-0.5}/(R_s + h + 0.5t)]$.

As the preload pressure p acts on the hemispherical substrate in the normal direction (Fig. 6.4(b)), the thin shell is gradually folded in lateral direction (x-axis). Also integration of the pad motion in z-axis and the two contacts: between the thin shell and the n-pad called plane-plane, and between this shell and the substrate named plane-sphere, makes the apex of the shell gradually separated from the substrate. By denoting $\Gamma = pL_p^2 + F^*_{wn,n}$ we have:

$$\mu^*\Gamma\sin\varphi = \mu(pL_p^2\sin\varphi + F_{w,n}) + 0.5mg. \tag{6.13}$$

When the contact area of the shell-pad is greater than that of the substrate-pad, the shell receives a bigger preload pressure than the substrate. Also, motion of the pads in the z direction induces the increase amount of the interface gaps h and h^*, which forms the appearance of bubbles (see chapter 2) inside the capillary as shown in figure 6.4(b). In this scenario, the normal wet adhesion forces $F_{w,n}$ and $F^*_{wn,n}$ quickly drop. Thus, we need to use a coefficient k to estimate the contact force of the substrate-shell. Additionally, the preload pressure p acting on the hemispherical shell is greater than that on the substrate that leads to a faster decline of the force $F_{w,n}$ than $F^*_{wn,n}$. This condition, on the other

hand, is equivalent to $k < k^*$. Furthermore, rising the bending angle φ varies the contact of the pad-shell in slightly plane-sphere to plane-plane. Therefore, the force $F^*_{wn,n}$ of equation (6.13) is more appropriate with equation (6.9) than equation (6.12). Hence, equation (6.13) is rewritten as follows:

$$\mu^* \Gamma k^* \sin\varphi = \mu k(pL_p^2 \sin\varphi + F_{w,n}) + 0.5mg. \tag{6.14}$$

In equation (6.14), the hemispherical shell is peeled off the substrate if the condition $F_{g,z} > \mu k(pL_p^2 \sin\varphi + F_{w,n}) + 0.5mg$ appears, being equivalent to:

$$p = \frac{0.5mg + \mu k F_{w,n} - \mu^* k^* F^*_{wn,n} \sin\varphi}{L_p^2(\mu^* k^* - \mu k)\sin\varphi}. \tag{6.15}$$

The preload pressure p in the left hand side of equation (6.15) is inversely and directly proportional to the forces $F^*_{wn,n}$ and $F_{w,n}$. When the interface gap h passes the peak h_p, the bubbles appear inside the capillary bridge of the contact substrate-shell. In this scenario, the normal wet adhesion force $F_{w,n}$ rapidly reduces, inducing a decrease of the coefficient k. On the contrary, the force $F^*_{wn,n}$ has no appreciable decline since the contact area in case the shell-pad is steady under elasticity force exerted by the hemispherical shell.

6.1.4 Grasping Interface With A Patterned Morphology

This section investigates the role of a micropatterned morphology on strengthening the wet adhesion interaction for decreasing the deformation of the thin hemispherical shell gripped by the soft robotic fingers (the pads). In this scenario, we designed a soft robotic hand with each fingertips attached by a micropattern pad (m-pad). Herein, the soft robot can carry out gripping a contact lens (showcase of the thin hemispherical shell) by soft fingers controlled by a pneumatic actuator. Because this contact lens has a very thin thickness t being much smaller than its radius, it can be accounted as the thin hemispherical shell. Therefore, the analytical model as aforementioned in the chapters 2 and 3 is appropriate to use.

6.1.4.1 Design of the Robotic Hand

In this situation, the proposed robotic hand comprised from a couple of opposite soft fingers as illustrated in Figure 6.5(a) constructed by a PneuNet structure for each. Additionally, the tip of each such finger was fixed the mincropatterned pad as shown in figure 6.5(b). In evaluated comparisons, we also designed another fingers having same structure and replaced the m-pad by the n-pad. When inputting the air pressure to the pneunet chambers, the m-pads (n-pads) moved towards each other, producing the grasp force to grasp/handle

the contact lens. Herein, the m-pads as shown in figure 6.5(b) included a square-pattern in micro scale deposited with a thin fluid film, having same design as described in Figure 3.1(b).

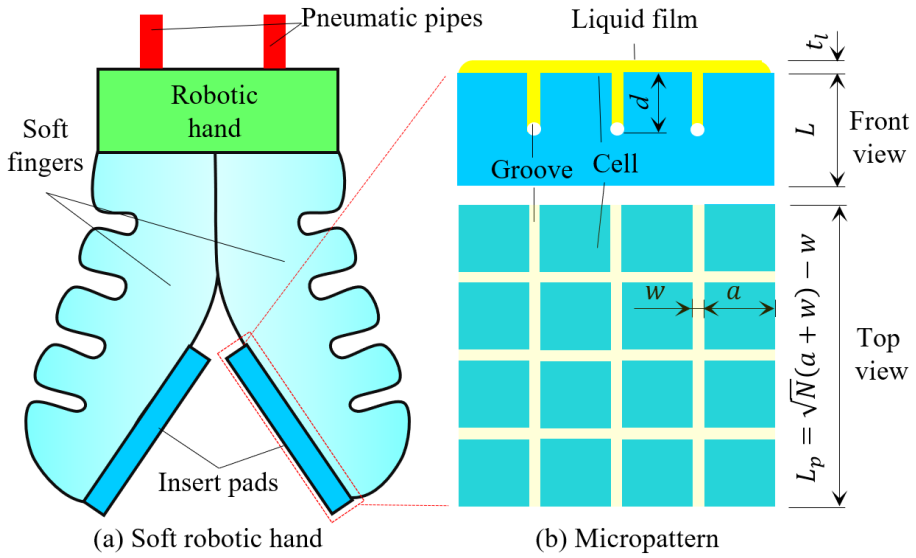

Figure 6.5: Proposed design of a soft robotic hand for gripping a contact lens. In this image, each finger's tip attached an m-pads with a micropatterned structure. a) Design of this robotic hand. b) The mcropatterned morphology of the m-pad having same structure in chapter 3.

6.1.4.2 Wet Adhesion for M-pad

Figure 6.5 showed the micropatterned pads gripping the contact lens in the same ways as the case: n-pad in figure 6.2. In this situation, in order to calculate the grasp force F_g for the contact case between the m-pad and the hemispherical shell the estimation carried out for that of the n-pad case as illustrated in figures 6.3 and 6.4 was replicated.

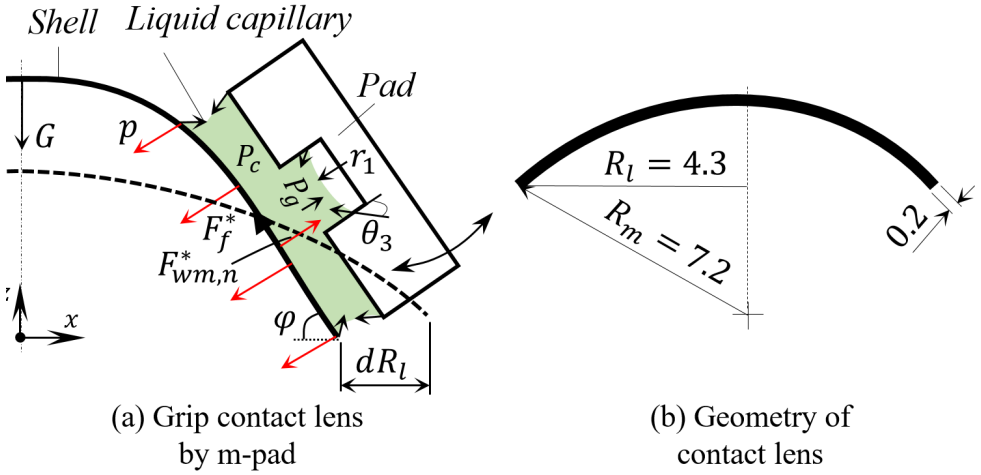

Figure 6.6: Schematic illustration of a) the m-pad gripping the thin hemispherical shell and b) a primary curvature of the contact lens.

Herein, the thin shell is assumed in stable contact with the micropatterned pads due to the elasticity force generated by the deformation. Hence, the variation of the interface gap h^* is neglected, while the slippery motion between the shell-pads is toward zero and the tangential wet adhesion force is in the relation $F^*_{wm,t} \approx 0$. Therefore, by applying Eq. (3.4) yields the normal wet adhesion force $F^*_{wm,n}$ for the m-pad as follows:

$$F^*_{wm,n} = 4Na\gamma \left[\psi \frac{\cos\theta_3}{2w} + \psi_1 + \frac{\sin\theta_1^*}{\sqrt{N}} + N^* \cos\theta_3 \right]. \tag{6.16}$$

Where $\psi = L_p^2/(aN) - a$, and $\psi_1 = a(\cos\theta_1^* + \cos\theta_2^*)/(4h^*)$. Generally, the normal wet adhesion force $F^*_{wm,n}$ in Eq. (6.16) is replace for the normal wet adhesion force of the n-pad case $F^*_{wn,n}$ in equations (6.10) and (6.14) when calculating the grasp force for the case m-pads in, respectively, the two other conditions of the contact lens's states: outside the liquid, and in contact with the substrate. Abolishing the infinitesimal entities derives the increment ratio r_n of the normal wet adhesion force between the micropatterned and normal pads in equations (6.16) and (6.9) in the form:

$$r_n \approx 1 + \frac{(h^*/w - 1)(21/k + w^2 a^{-2}) + 2Nh^*/a}{(1 + 1/k)^2}. \tag{6.17}$$

The increment ratio r_n shown in equation (6.17) is greater than 1 since the width of the groove satisfies $w < \langle h^*, a \rangle$. In other words, the pad having micropatterned structure can strengthen the wet adhesion force $F^*_{wm,n}$ of r_n times higher than the normal surface in gripping the thin shell. Assuming that the coefficient k has same value as k^* as griping in both cases: with the n- and m-pad. Hence, in order to investigate the role of the micropatterned morphology on declining the preload pressure p in the two cases of gripping the thin hemispherical shell: outside the liquid and in contact with the substrate, we use the formulation $F^*_{wm,n} = r_n F^*_{wn,n}$ obtained from equations (6.11) and (6.15). Therefore, by dividing the right hand side of equations (6.16) and (6.11) yields the reduction ratio r_{p1} as follows:

$$r_{p1} = 1 - \frac{2F^*_{wn,n}\mu^* k^* (r_n - 1)\sin\varphi}{mg + 2\mu^* k^* \sin\varphi} < 1, \tag{6.18}$$

and repeat this work for equations (6.16) and (6.15) derives the reduction ratio r_{p2} in the form:

$$r_{p2} = 1 - \frac{\mu^* k^* F^*_{wn,n}(r_n - 1)\sin\varphi}{0.5mg + \mu k F_{w,n} - \mu^* k^* F^*_{wn,n}\sin\varphi} < 1. \tag{6.19}$$

As illustrated in equations (6.18) and (6.19), both the reduction ratios $\langle r_{p1}, r_{p2} \rangle$ are lower than 1 since the increment ratio r_n is larger than 1. Thus, grasping the thin shell by using the micropatterned pad requires a lower preload pressure p than that using the normal pad. That is, to achieve a stable grasp, the m-pad generates less deformation for the shell. In case the normal wet adhesion forces $F^*_{wn,n}$ and $F^*_{wm,n}$ extremely enlarge,

using a preload pressure $p < 0$ may rise deformation of the hemispherical shell ($\varphi < \varphi_0$), which inverts the reduction ratio r_{p1} in equation (6.18). Therefore, as the relation $r_{p1} > 1$ appears, the micropatterned pad generates stronger wet adhesion force for contacting with the substrate than the normal pad.

6.1.5 Estimated Results

In order to evaluate the preload pressure p acting on the hemispherical shell by the m- and n-pads, the parameters mentioned in the analytical model are substituted with concrete values of water and the real contact lens. Herein, the contact lens made from silicon hydrogel Acuvue® advance material [72, 227] has parameters of: Young modulus $E = 1.1\,\text{MPa}$, Poisson ratio $\nu = 0.45$, $\mu \sim \mu^* = 0.028$, $\alpha = 0.44$, $\theta_1 - \alpha_1 = 1.13$, $\theta_1^* = 0.86$, $\theta_2 + \alpha = 1.2$, $m = 0.75\,\text{g}$, $\theta_1^* \sim \theta_3 = 1.13$.

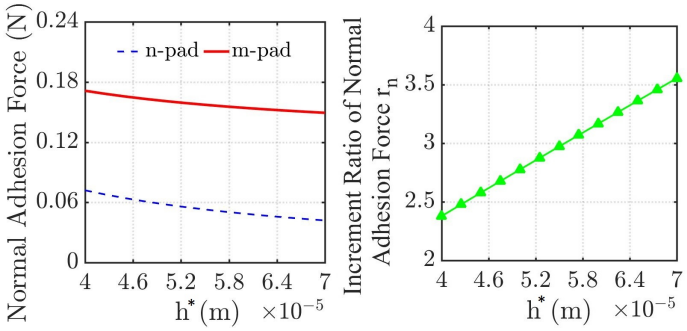

Figure 6.7: Normal wet adhesion forces of the contact between the n- and m-pads with the thin shell through variation of the interface gap h^*, respectively, output from equations (6.12) and (6.16) a), and the ratio r_n output from equation (6.17).

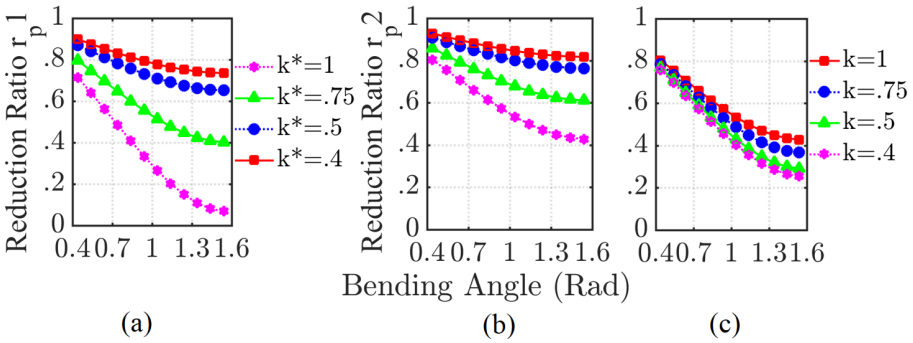

Figure 6.8: Influence of the coefficient k^* in the reduction ratio r_{p1} shown in equation (6.18) for the contact between the m- and n-pads with the thin shell by bending angle φ a). Influence of the coefficient k^*, k in the reduction ratio r_{p2} shown in equation (6.19) by bending angle φ in b) and c), respectively.

Figure 6.7 shows that the normal wet adhesion force in case the contact between the micropatterned pad with the hemispherical shell was 2 times higher than that of the case normal pad. When rising the interface gap h^*, the normal wet adhesion force decreases for

both those such pads (Fig. 6.8). Also, the ratio r_{p1} reduces when the bending angle φ and the coefficient k^* rises as shown in Fig. 6.8. Hence, it reveals that as the bending angle φ rises the m-pad can significantly decrease the shell's deformation compared with the n-pad case, contrasting to the trend of reducing the contact area of the contact lens-pad. Additionally, this relation is appropriate for explaining the trend in case the reduction ratio r_{p2} as illustrated in figure 6.8. As the contact lens is peeling off the substrate, the reduction ratio r_{p2} (Fig. 6.8(a)) marginally decreases for two cases of the pads in gripping the contact lens; while that shown in Fig. 6.8(b) has significant declines.

The obtained results in this section show that the pad having micropatterned morphology can strengthen grasp force F_g due to increasing the wet adhesion. In other words, if grasping the thin shell requires a value of F_g, the m-pad can decrease the preload pressure p through the reduction ratios r_{p1}, r_{p2}. Therefore, using the micropatterned pads help the soft robotic hand grip a contact lens with requirement of the pressure preload p of $1.2 \div 2$-times lower than that of using the n-pads.

6.1.6 Results Of Preliminary Experiments

6.1.6.1 Prototype

In this situation, in order to make the micropatterned pad as shown in figure 6.5 we utilized the method as aforementioned in chapter 4. In addition, the soft fingers were cast from silicon rubber (Smooth-on Dragon Skin 10) in the molds fabricated by printing the ABS plastic of 3D printer Zotrax M200. Afterward, the fabricated pads were attached to the tips of those such fingers through a thin film of a glue.

6.1.7 Experimental Setup

Setting the experiments is to verify the role of the micropatterned morphology on achieving the stronger wet adhesion force for decreasing the minimum value of the preload pressure p needed to grasp the contact lens. In figure 6.9, the experimental system consists of following equipment: one contact lens, a tank containing water, one hemispherical substrate, one syringe pump for generating pressure control, and one camera to record the contact lens's deformation in the meridian curve. These equipment were controlled via the controller linked to a computer. The obtained images illustrated the contact lens's deformation via the variation of the bending angle φ. In addition, those such deformation datum of the contact lens were compared for two contact cases between the n- and m-pads. Also, the contact lens was in three different conditions in the measurements: 1) immersed inside water (liquid), 2) outside the water, and 3) contact with the rigid hemispherical substrate.

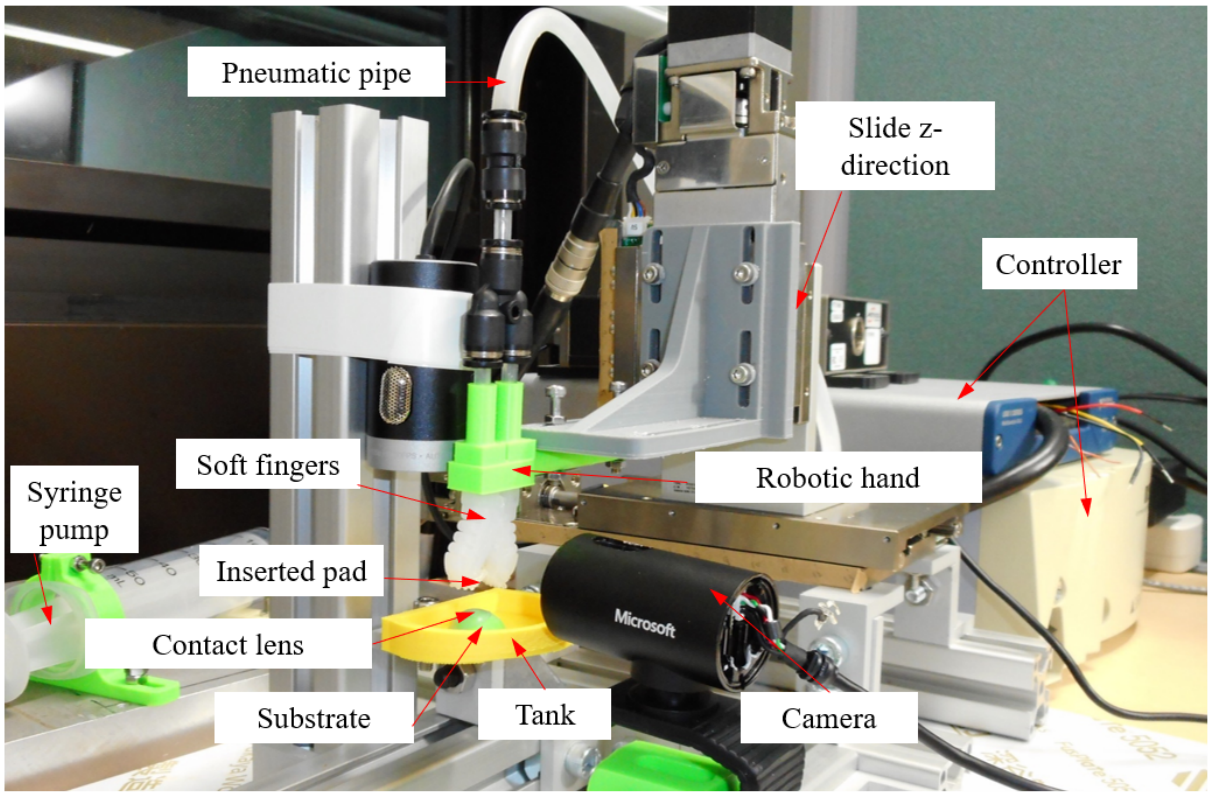

Figure 6.9: Measuring setup of testing the contact lens's deformation under acting of the grasp force F_g generated by the two fingers.

6.1.7.1 Contact Lens Inside Liquid

In the initial state, the n- and m-pads were separated above the bottom tank at a gap distance of 10 mm where the contact lens lied down. Those such pads moved downward of 9 mm at a normal velocity v_z of 0.5 mm/s. Subsequently, the pump input air pressure to toward bend these pads for grasping the contact lens. As the contact lens was stably gripped at the minimum value of preload pressure p, the n- and m-pads returned to their initial position. The camera recorded the deformation datum of the contact lens during this progress.

6.1.7.2 Contact Lens Outside Liquid

In this phase, these soft pads kept the contact lens at a distance 10 mm above the tank bottom where put the contact lens. Afterward, the syringe pump decreased the air pressure until this contact lens was released. The contact lens's deformation was recorded in this process.

6.1.7.3 Contact Lens in Contact with the Substrate

In this phase, the contact lens already stuck with the substrate. Hence, the soft pads moved down 7 mm to make contact and exert the preload pressure p on the contact lens. After that, these pads returned backward 7 mm for peeling the contact lens off the substrate. In this scenario, when the contact lens has just been separated from the substrate, the contact lens's deformation was recorded by the camera.

6.1.8 Preliminary Results

This section illustrated the validation of the preload pressure p generated by the soft pads when gripping the contact lens in three conditions according to testing the resultant bending angle φ in equation (6.2). Herein, the bending angle φ_0 shown in figures (6.10), (6.11) and (6.12) presented for that at initial state of the contact lens. When rising the preload pressure p, the bending angle φ_0 becomes φ. In other words, the greater values of the bending angle φ indicated the higher values of the preload pressure p acting on the contact lens.

6.1.8.1 Contact Lens Inside Liquid

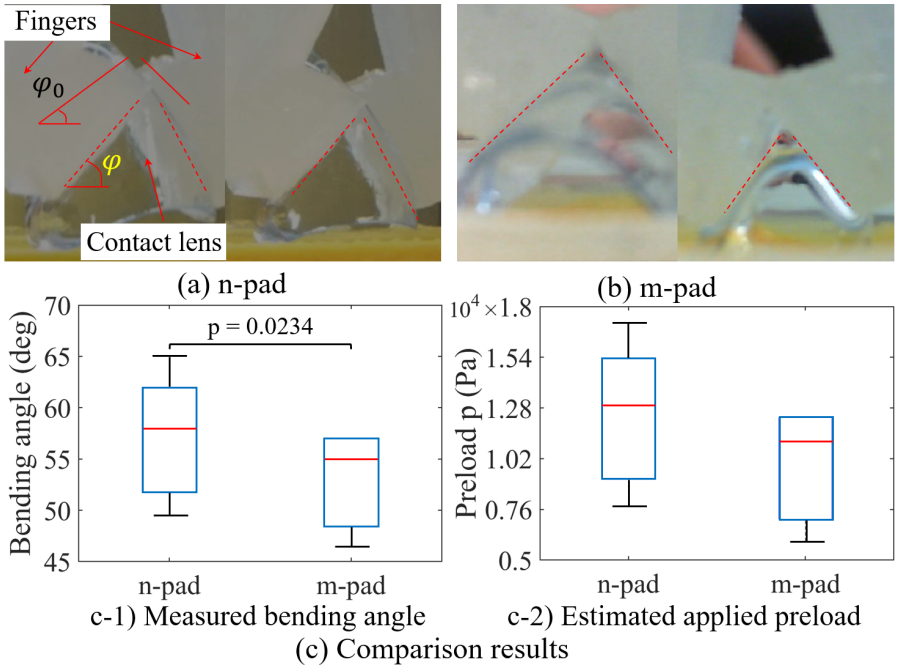

Figure 6.10: Comparison of the bending angle φ of the contact lens corresponding to the preload pressure p generated by the n- and m-pads to contact lens in the condition inside liquid. Pictures of φ under preload pressure p in cases n- a) and m-pads b). c) Results of comparing c-1) the experiment of the bending angle φ got from a) and b), and c-2) calculated preload pressure p (grasping the contact lens) through substituting φ in c-1) to equation (6.2). In this scenario, the angle $\varphi_0 = 0.64$ corresponded to the force $F_g = 0$.

Figure 6.10(c-1) illustrates that the angle φ of the contact lens gripped by the normal pad was about 10% larger than that by the micropatterned pad. That yields the preload pressure p imposing on the contact lens produced by the m-pad approximated 1.1 times lower as shown on figure 6.10(c-2). This also induced less deformation of the contact lens. Hence, the wet adhesion force generated from the contact between the m-pad and the thin shell was larger than that of between the n-pad during gripping the contact lens.

In case of gripping the thin hemispherical shell inside liquid as illustrated in figure 6.10, the influences of the drag force F_d by the liquid and low friction on the contact the contact lens-pads were combined with the weak role of wet adhesion force. This led to enlarging the dependence of the grasp force F_g on the preload pressure p. In this scenario, despite of being a difficult problem to govern the contact lens curvatures, the pad having micropatterned morphology manipulated the deformed surface of the contact lens better than did the normal pad, thanks to resulting in the lower deformation of the contact lens (figure 6.10(a-b)).

6.1.8.2 Contact Lens Outside Liquid

When grasping the contact lens in the condition: outside liquid as illustrated in figure 6.11, the grasp force F_g was more dependent on the wet adhesion than the preload pressure. Thanks to the significant role of the wet adhesion force, the contact lens can achieve a deformation with $\varphi < \varphi_0$ under the preload pressure $p < 0$ (grasping the contact lens). Because the relation $F^*_{wm,n} > F^*_{wn,n}$ appeared in equation (6.17), under the condition $p < 0$, the contact lens's deformation was over 1.5 times larger for the normal pad than the micropatterned pad as shown in figure 6.11(c-1). Moreover, the pulling preload pressure p generated by the pad having micropatterned morphology rose roughly two-fold that of the pad without any pattern in figure 6.11(c-2).

Thus, the micropatterned morphology can strengthen the wet adhesion force which was in contract with the estimation in equation (6.18). Because gripping the thin shell by using the m-pad output the a smaller value of bending angle φ compared to utilizing the n-pad (figure 6.11(b)), the m-pad can achieve more efficient outcome of attaching the contact lens to the hemispherical substrate than the n-pad.

6.1.8.3 Contact Lens in Contact with a Substrate

As the contact lens was in contact with the hemispherical substrate as shown in figure 6.12, the bending angle φ of the contact lens generated by the m-pad was slightly lower than by the n-pad (with the statistical value $p = 0.1446$, see figure 6.12(c-1)). This was caused from the major dependence of the grasp force F_g on the preload pressure p and the friction forces F_f, F^*_f when the relations $k^* \sim 0.75$ and $k \sim 0.3$ appear. In addition, the preload pressure p (figure 6.12(c-2)) produced by the m-pad is smaller than that of by the

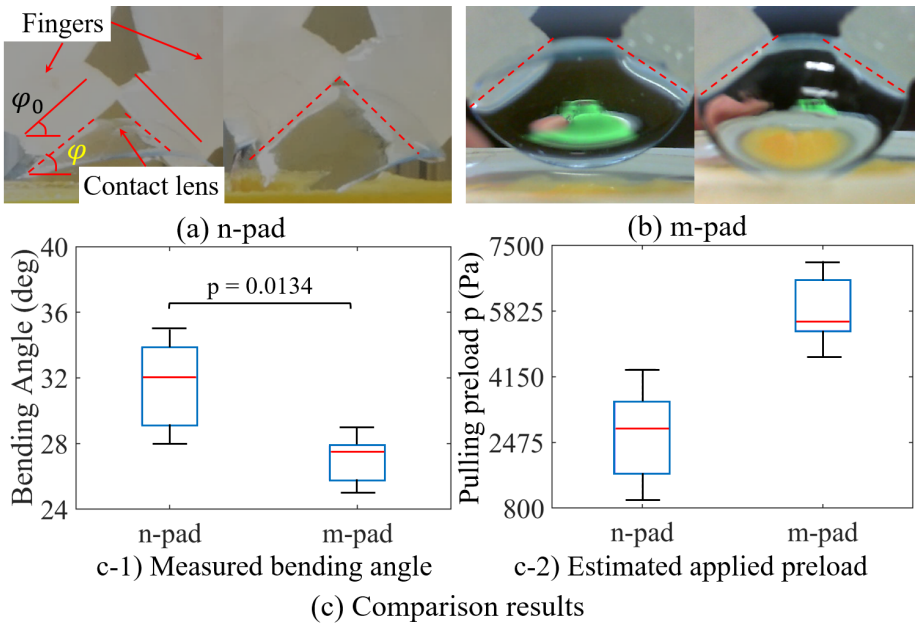

Figure 6.11: Comparison of the bending angle φ of the contact lens corresponding to the preload pressure p generated by the n- and m-pads to contact lens in the condition outside liquid. Pictures of φ under preload pressure p in cases n- a) and m-pads b). c) Results of comparing c-1) the experiment of the bending angle φ got from a) and b), and c-2) calculated preload pressure p (ulling contact lens) through substituting φ in c-1) to equation (6.2).

n-pad at the ratio $r_{p2} = 0.706$. This agreed with calculated results as shown in figure 6.8 in range $0.5 < k^* < 0.75$ and equation (6.19).

In general, the testing results of this model were valid. Although the given experiments focused on the contact lens as a showcase of the thin hemispherical shell, our study presented the vital role of the micropatterned morphology on strengthening the wet adhesion force in gripping the pliable object. Through illustrating the advantage properties in the wet adhesion interaction, the pads having micropatterned morphology needed smaller preload pressure which led to the less deformation for the contact lens. When expanding the contact lens with $\varphi < \varphi_0$ to facilitate attaching the hemispherical substrate, the micropatterned pad can enlarge the expansion of the contact lens with a smaller value of φ than the normal pad. Thus, those such models are potential to evaluate gripping other thin pliable objects in a diverse conditions (see video at: `https://www.youtube.com/watch?v=cMkQ40DDQ_8&t=1s`, consisting of dry, wet and with prolific substrates.

6.2 Design Soft Robotic Hand for Grasping Soft-Fragile Objects

This section investigates the role of a micropattern on decreasing the deformation, thanks to reducing of the applied compressing load, of a fragile object gripped by a soft robotic hand.

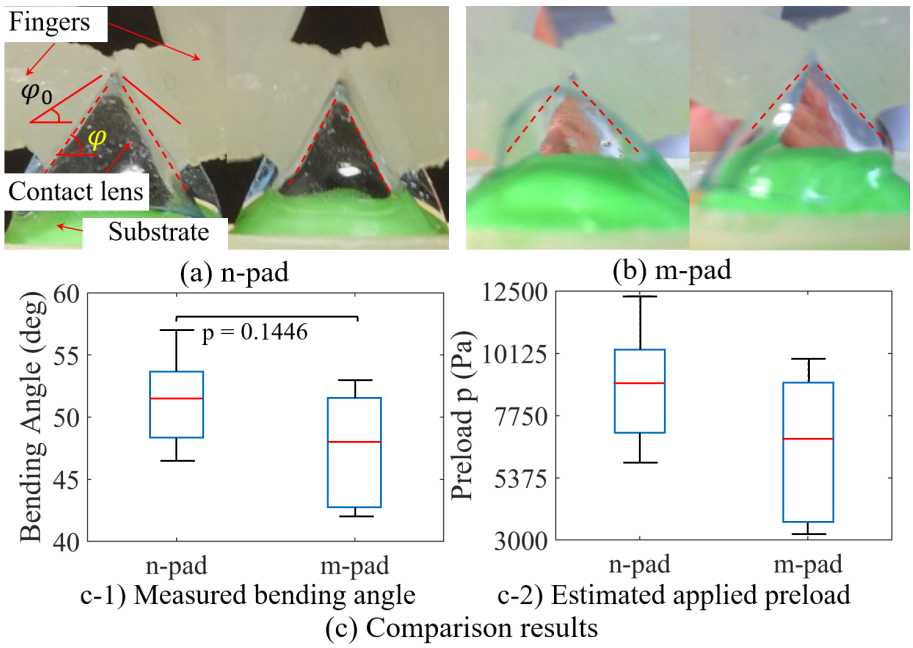

Figure 6.12: Comparison of the bending angle φ of the contact lens corresponding to the preload pressure p generated by the n- and m-pads to contact lens in the condition contact with the substrate. Pictures of φ under preload pressure p in cases n- a) and m-pads b). c) Results of comparing c-1) the experiment of the bending angle φ got from a) and b), and c-2) calculated preload pressure p (pressing the contact lens) through substituting φ in c-1) to equation (6.2).

An estimation was conducted to evaluate the grasp forces concerned for manipulating a soft, wet block by two soft-fingers in two cases: flat and micro-patterned fingertip pad. In this scenario, the object had an available thin film of liquid; whereas the pad was completely dry. Grasping the block was conducted in three steps: the pad (of the robotic finger) approaching the substrate (Fig. 6.13(a-1)), the pad attaching to the substrate (Fig. 6.13(a-2)) and the pad detaching from the substrate (Fig. 6.13(a-3)). When contacting the substrate, the grooves can suck the fluid film according to the wet adhesion mechanism of the tree's frog sole toe. Hence, we designed a robotic hand and carried out corresponding experiments to validate the estimation by grasping a tofu block as an actual application.

6.2.1 Revisit Theory of Viscoelastic Deformation

In manipulating a fresh tofu block, the tofu (considered as a fragile block object) is grasped and released by a soft gripper (Fig. 6.13), which results in deformation of the tofu block [75]. Also, water is always available at all surfaces of the fresh tofu, whic cause the surface slippy, as well as wet adhesion in the interface with the finger. This section discussed two such cases through formulations that can explain the underlying physics of such phenomena.

A deformation model of the tofu block is considered in this section. Tofu contains primary ingredients from the soy protein and 90%water. One can find out the physico-

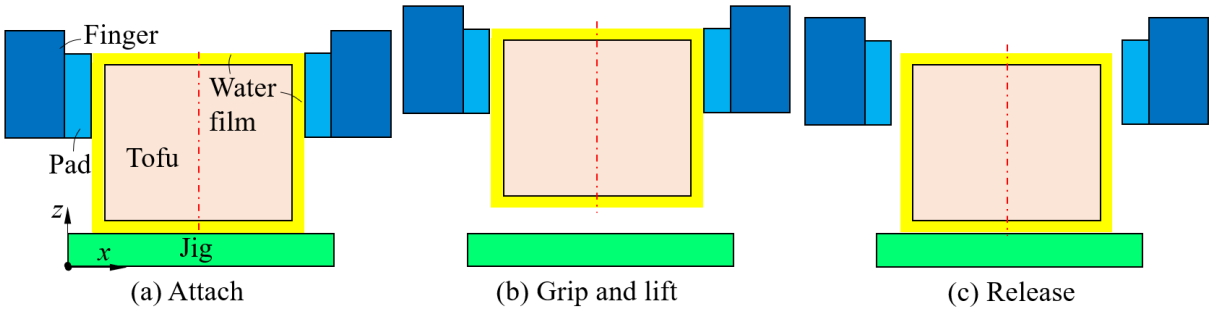

Figure 6.13: Scheme of grasping a tofu block by the soft robotic fingers: (a) The fingers approaching. (b) Gripping and lifting the tofu block away from the jig. (c) Releasing the tofu on the jig.

chemical properties for many types of the tofu in [73]. In addition, Cheng [74, 228] showed that tofu can be considered as a viscoelastic materials that includes two components: viscosity and elasticity upon deformation.

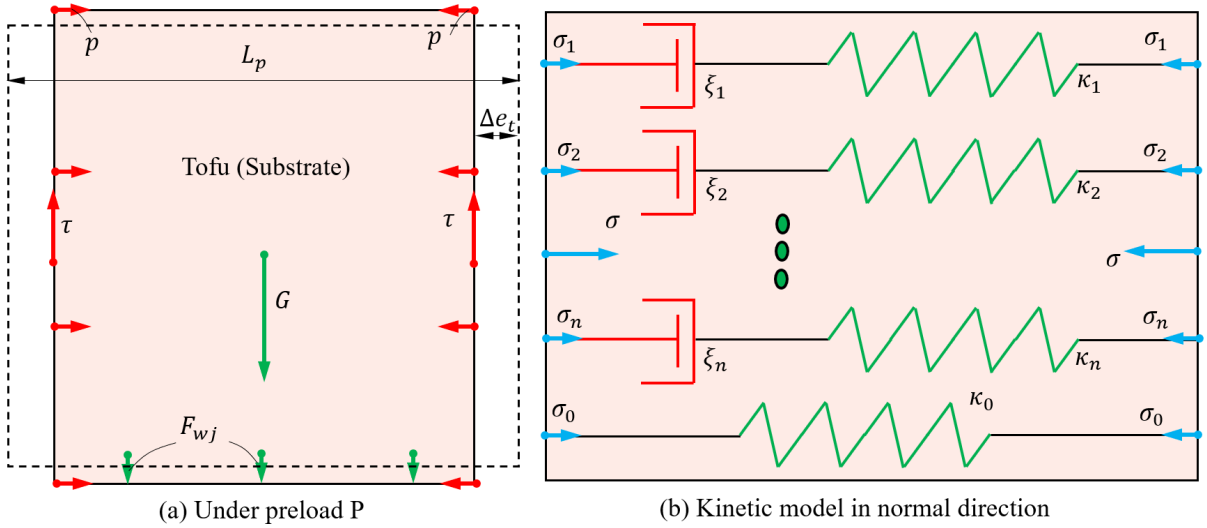

Figure 6.14: Deformation model of the tofu block in grasping. a) Deformation of the tofu under external forces. b) Modelling the tofu by a spring element κ_0 and series of parallel viscoelastic elements comprising of a spring (κ_i) and a dashpot (ξ_i).

As shown in Fig. 6.14(a), the tofu block, which has a roughly cubic shape with its edge side is L_p, is compressed by the preload $P = pL_p^2$ by each of the pads to create the grasp force F_g. This generates the normal deformations of the sample Δe_t with the internal stress σ. Also, to keep the object from falling down the tangential stress τ balancing with the gravity force $G = mg$ and the wet adhesion force of the jig F_{wj} that appears on the contact interface of the substrate. Let us virtually divide the volume of the tofu into one independent spring having stiffness coefficient κ_0 and n parallel elements each consisting two minor connecting elements: a dashpot (damping coefficient ξ_i) and a spring (stiffness coefficient κ_i) as shown in Fig. 6.14(b). Additionally, each such element and the whole

tofu are in turn exerted by the normal stress σ_i and the total normal stress σ. Hence, according to [229] the relationship between the pressure and the strain can be shown as follows:

$$\sigma = \sigma_0 + \sum_{i=1}^{n} \sigma_i = \kappa_0 \epsilon_0 + \sum_{i=1}^{n} \frac{\kappa_i \xi_i \dot{\epsilon}_i}{\kappa_i + \xi_i \dot{\epsilon}_i}, \tag{6.20}$$

with $\epsilon_i, \dot{\epsilon}_i$ are respectively the strain and its deviation by time t of the element i. And the apparent modulus $\kappa(t)$ of the sample in relaxation state satisfies the followed expression:

$$\kappa(t) = \kappa_0 + \sum_{i=1}^{n} \kappa_i e^{-t\kappa_i/\xi_i}. \tag{6.21}$$

The Eqs. (6.20) and (6.21) show the scenarios of the sample in cases: a small and a large (relaxation stress) deformations. As the grasp force F_g in this study does not generate a large deformation for the tofu ($\epsilon_i < 10\%$ [74]), we can neglect variation of the elastic modulus in Eq. (6.21).

6.2.2 Mechanics of Grasping with Wet Adhesion

6.2.2.1 Design Robotic Hand

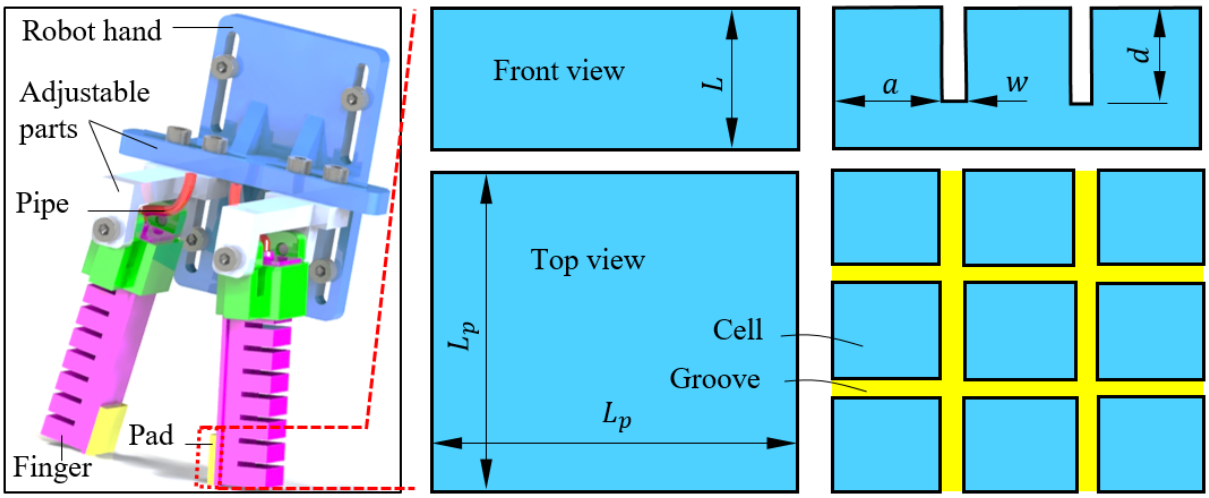

Figure 6.15: Design of a soft robotic hand with two types of the fingertip pad: a) n-pad (normal pad or the pad without any pattern) and b) m-pad (the pad that has micropattern).

As shown in Fig. 6.15(a), the design of a soft robotic hand comprises of two soft fingers with their morphology was constructed from a PneuNet structure, and fingertip pads were designed in two cases for evaluation: a normal flat surface (n-pad) in Fig. 6.15(b) and a micro-machined pattern surface (m-pad) in Fig. 6.15(c). Two kinds of pad have a square

shape with a same size of edges: L_p and thickness L and materials. For the m-pad, it is patterned by N square cells, which the edge size is a, interspaced by a network of the grooves, which width and depth of each groove are w and d, respectively. Then, this hand was fixed to a linear motorized stage functioned as a robotic arm for approaching the hand to the object. When the fingers were pressurized, the pads approach towards sides of the object for creation of the grasp force F_g.

6.2.3 Modelling Grasping of a Wet Object

This section concerns role of the wet adhesion in grasping the fragile wet object (tofu) by the soft pads (Fig. 6.16) in two cases: n-pad (normal pad) and m-pad (micropattern pad). For the m-pad, upon contacting with the tofu block, the water film on the tofu surface is sucked into the grooves when the width of the grooves is smaller than the interface gap h ($w < h$). This phenomena can be explained in chapter 2 that the Laplace pressure inside the groove and at the contact interface between cell and the substrate, in this situation, are $P_{Lg} \sim 2\gamma \cos\theta_3/w$ and $P_{Lc} \sim \gamma(\cos\theta_1 + \cos\theta_2)/h$, respectively (see Fig. 6.16).

In each of the corresponding contact interface, the grasp force $\mathbf{F}_g$ generates the friction force $\mathbf{F}_f$, and the wet adhesion force $\mathbf{F}_w$ increases the stick ability with the pads. We also consider that the couple interfaces between the pad and the tofu's surfaces is completely parallel to z axis in the grasping scenario. In the equilibrium state, the tofu is lifted only if the tangential contact force $\mathbf{F}_{r,t}$ generated from the pad (the total of $\mathbf{F}_f$ and the tangential wet adhesion force $\mathbf{F}_{w,t}$) satisfies the followed conditions:

$$0.5(\mathbf{G} + \mathbf{F}_{wj}\hat{z}) \leq \mathbf{F}_{w,t} + \mathbf{F}_f = \mathbf{F}_{r,t}. \tag{6.22}$$

The module of gravity force $\mathbf{G}$ in Eq. (6.22) is considered constant, and that of the wet adhesion force with the jig $F_{wj} \approx \gamma(\cos\theta_{j1} + \cos\theta_{j2})\pi r_{wj}^2/h_j + \gamma \sin\theta_{j1} 2\pi r_{wj}$. Thus, it is necessary to determinate other components in the right hand side of Eq. (6.22). This equation is utilized to compare the minimum preload pressure $\{p_n, p_m\}$ causing deformation on the tofu.

6.2.3.1 In Normal Direction (along $x - axis$)

In Fig. (6.16), as there are no slip between the pad and the substrate, the capillary's shape has no significant change and the related velocity between the pad and the substrate $\dot{x}, \dot{z}$ are neglected. According to chapter 2, by synthesizing the wet adhesion force F_w the Eq. (6.22) the normal wet adhesion force in case the n-pad $F_{wn,n}$ is generally calculated as followed:

$$F_{wn,n} = L_p 4\gamma \left(L_p \vartheta + \sin\theta_1\right), \tag{6.23}$$

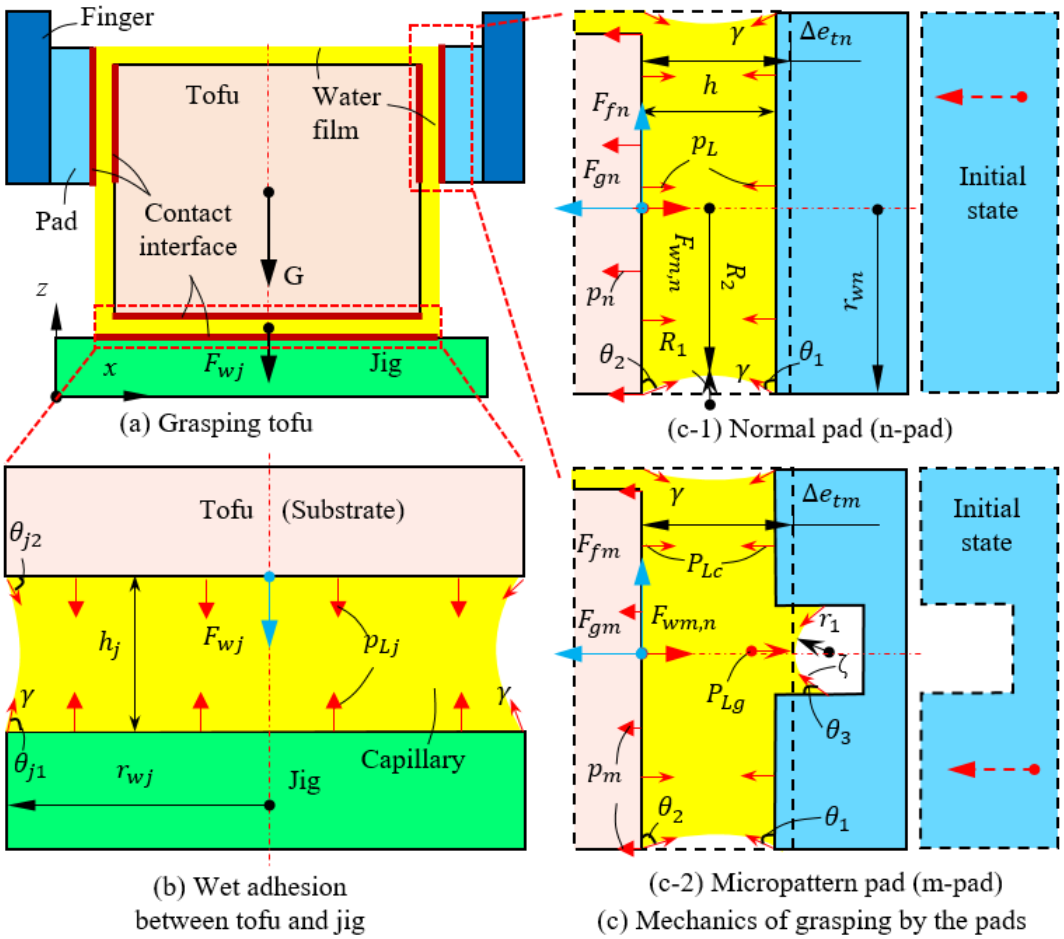

Figure 6.16: Mechanics of grasping a tofu block by the soft robotic fingers: (a). Model of contact interfaces between pads of the gripper and surfaces of the tofu. (b) Contact model of the tofu block's bottom with the jig. (c) Zoom-in illustration of contact interfaces in two cases: (c-1) contacting with the n-pad, and (c-2) contacting with the m-pad. The preload p_n, p_m from the n-pad and m-pad, which exert on the normal direction of the tofu's surfaces, causes the deformation of the tofu Δe_{tn} and Δe_{tm}. The dash lines and the dash-red arrows, in turn, show the original states of the pads and the substrate, and the moving direction of the pads. Additionally, $\theta_1, \theta_2, \theta_3, \theta_{j1}, \theta_{j2}$ and r_w, r_{wj} are the contact angles and wet radii, respectively.

where $\vartheta = 0.25(cos\theta_1 + cos\theta_2)/h, \vartheta_1 = L_p^2/(aN) - a$. Differing to the n-pad, in the case the m-pad, the normal wet adhesion force $F_{wm,n}$ includes the Laplace, surface tension and Stefan forces of the cells and the grooves. Hence, the force $F_{wm,n}$ equals to:

$$F_{wm,n} = 4Na\gamma\left(\vartheta_1\frac{\cos\theta_3}{2w} + a\vartheta + \frac{sin\phi_1}{\sqrt{N}} + n_c\cos\theta_3\right). \tag{6.24}$$

Note that $\psi_n = F_{wn,n}$ and $\psi_m = F_{wm,n}$ which are respectively in the left hand side of Eqs. (6.23) and (6.24), then the grasp forces F_g for the n-pad case F_{gn} and m-pad case F_{gm} become:

$$\begin{cases} F_{gn} = \pi r_w^2 p_n + \psi_n, \\ F_{gm} = \pi r_w^2 p_m + \psi_m \end{cases}. \tag{6.25}$$

Eq. (6.25) shows that the grasp forces $\{F_{gn}, F_{gm}\}$ depend on both preload pressure $\{p_n, p_m\}$ and the wet adhesion force $\{F_{wn,n}, F_{wm,n}\}$. The increment ratio of the grasp force in this scenario $r_g = F_{gm}/F_{gn}$ is:

$$r_g = 1 + \frac{2\gamma \cos\phi \left[(2 + 2n_c - 1/m)/a + 1/h\right]}{p(1 + 1/k)^2 + 2\gamma \cos\phi (1 + 1/k)^2/h}, \tag{6.26}$$

where $k = a/w, m = h/w, n_c = 1 - N^{-0.5}$ (N is the number of cells on m-pad), and we assume that $\phi = \theta_1 = \theta_2 = \theta_3$. Because the width of the groove was designed so that it is satified $w < h$, the increment ratio r_g in Eq. (6.26) is always larger than one in case the preload pressure $p_m = p_n = p$. In other words, in case grasping the tofu by the m-pad, the normal wet adhesion force $F_{wm,n}$ significantly enhances the grasp force F_{gm} than that of grasping by the n-pad. This plays an important role in the following sections as the normal force is a principal component in grasping.

6.2.3.2 In Tangential Direction (along $z - axis$)

The grasp force $\{F_{gn}, F_{gm}\}$ in Eq. (6.25) generates the friction force F_f and the wet adhesion force in tangential direction $F_{w,t}$. This study only focuses on investigating the tangential contact force $F_{c,t}$ in incipient slip ($\dot{z} = 0, F_{w,t} \sim 0$). Also we have $F_f = \eta F_{gn}$ with η is the friction coefficient. By projecting Eq. (6.22) in z axis yields the tangential contact force $F_{c,t}$ in case the n-pad as follows:

$$F_{cn,t} = \eta_n (pL_p^2 + \psi_n). \tag{6.27}$$

And the tangential contact force in case the m-pad becomes:

$$F_{cm,t} = \eta_m (pL_p^2 + \psi_m). \tag{6.28}$$

From the Eqs. (6.27) and (6.28), the increment ratio of the tangential contact force $r_t = F_{rm,t}/F_{rn,t}$ is calculated as follows:

$$r_t = \frac{\eta_m}{\eta_n} \left[1 + \frac{2\gamma \cos\phi \left[(2 + 2n_c - 1/m)/a + 1/h\right]}{\lambda_{21}(p + 2\gamma \cos\phi/h)}\right], \tag{6.29}$$

with $\lambda_{21} = (1 + 1/k)^2, \lambda_{22} = w(2 + 1/k)/a$. It is similar to the conclusion in Eq. (6.26), r_t in Eq. (6.29) is also larger than the ratio of the friction coefficients η_m/η_n. On the other hands, comparing the value of r_t with 1 depends on the ratio $\{\eta_m/\eta_n\}$. When $\eta_m = \eta_n$, r_t becomes r_g. That reveals the micropattern can create a stronger enhancement of the wet adhesion in tangential contact force than that of the normal surface. Replacing Eqs.

(6.27) and (6.28) into Eq. (6.22) yields the preload pressure p_n of the n-pad as follows:

$$p_n \geq 0.5(G + F_{wj})L_p^{-2}/\eta_n - \psi_n/L_p^2, \tag{6.30}$$

and that of the m-pad case is:

$$p_m \geq 0.5(G + F_{wj})L_p^{-2}/\eta_m - \psi_m/L_p^2. \tag{6.31}$$

Dividing the right hand side of Eq. (6.31) into that of Eq. (6.30) yields the reduction ratio of the minimum preload pressure $r_p = min\{p_m\}/min\{p_n\}$ as follows:

$$r_p = \frac{\eta_n}{\eta_m}\left\{1 - \frac{1 + [\lambda_{22}(k-1) + 2n_c m/k]/\lambda_{21}}{0.5(G + F_{wj})/\psi_n - 1}\right\}. \tag{6.32}$$

The ratio r_p in Eq. (6.33) is smaller than 1 that is equivalent to $min\{p_m\} < min\{p_n\}$ because we consider $\eta_m = \eta_n$ (friction coefficient of m-pad and n-pad, respectively) and $k > 1$. In addition, this ratio gradually decreases as $\eta_m > \eta_n$. The deformation of the tofu, in this study, is so small for concerning the relaxation stress. Thus, the apparent elastic modulus $\kappa(t)$ in Eq. (6.21) can be neglected. For simplicity, let us assume that the preload pressure is similar at every point on the contact interfaces, which leads to the same strain ϵ_i in Eq. (6.20) at all contact points. Combining Eqs. (6.20) and (6.32) yields the reduction ratio $r_s = \epsilon_{im}/\epsilon_{in}$ for the strains between the m-pad case and the n-pad case as shown in Eq. (6.33):

$$r_s = 1 - \frac{p_n L_p^2(1 - r_p) + \sum_{i=1}^{n} \xi_i \kappa_i^2 (\dot{\epsilon_{im}} - \dot{\epsilon_{in}})/(\chi_{in}\chi_{im})}{p_n L_p^2 - \sum_{i=1}^{n} \kappa_i \xi_i \dot{\epsilon_{in}}/\chi_{in}}, \tag{6.33}$$

where $\chi_{in} = \kappa_i + \xi_i \dot{\epsilon_{in}}, \chi_{im} = \kappa_i + \xi_i \dot{\epsilon_{im}}$

Consequently, gripping the tofu with the m-pad requires a smaller value of the applied preload P exerting on the tofu's surfaces. In addition, the Eq. (6.33) reveals that grasping in case the m-pad has less damage for the substrate.

6.2.4 Experimental Setup

This section reports the experiment evaluation of the reduction of the applied preload pressure exerting on the tofu's surfaces using m-pad (micropattern pad) compared to that of n-pad (normal flat pad). Apparatus setup and experimental method described in this section can be utilized for evaluation of grasping other wet, fragile objects like tofu.

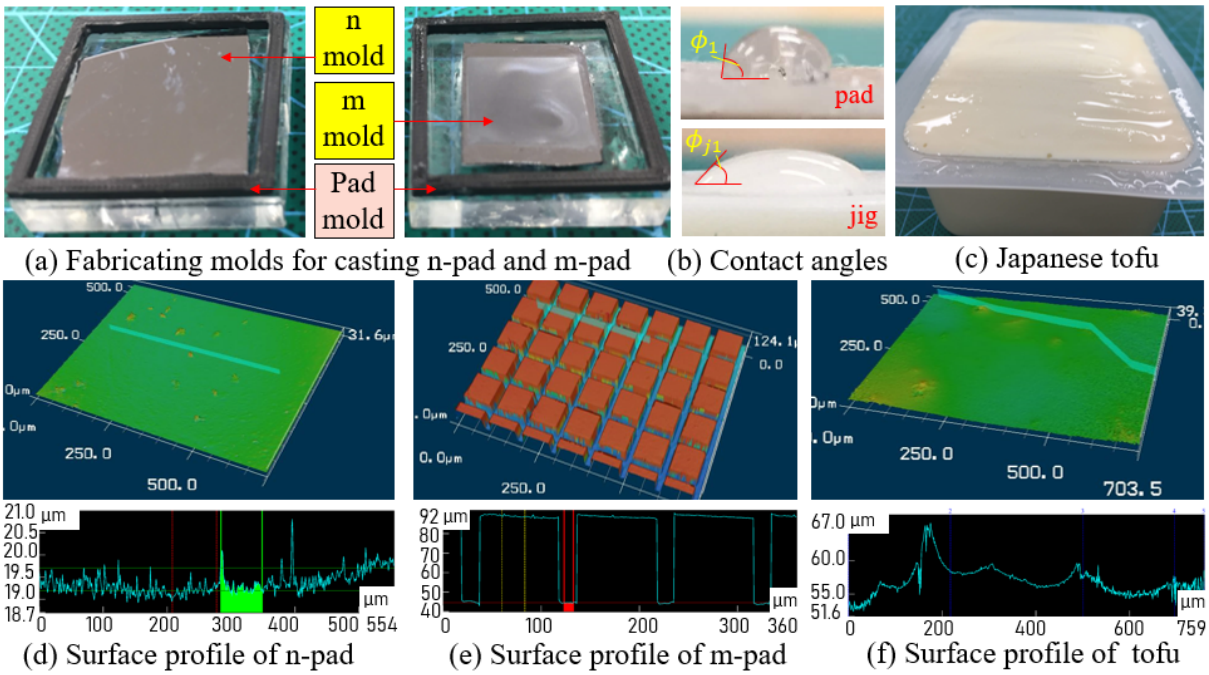

Figure 6.17: Fabrication processing of the pad and preparing sample. The n-pad and m-pad molds a) were fabricated by fixing the silicon substrates on the glasses with their walls printed by 3D Zotrax M200. b) Measuring the contact angles of the pad and the jig. c) A Japanse tofu as a sample for experiments. d), e) and f) the surface profiles of the n-pad, m-pad and the tofu under observed in microscope. Error of w is roughly 15%.

6.2.4.1 Fabrication

A micro-patterned mold (m-mold) was fabricated by a lithography method, with size of $12\times12\,\mathrm{mm}^2$ was fabricated as shown in chapter 4. The obtained micro-pattern mold was then fixed in a larger mold for casting silicon rubber (Ecoflex 00-50, SmoothOn, USA) to create the m-pad with thickness of 1 mm (Fig. 6.17(a)). Cells on the m-pad have the size of $85\,\mu\mathrm{m}\times85\,\mu\mathrm{m}$, separated by a network of channels (grooves) with 15μm in width and $44\,\mu$m in depth. The surface of m-pad, n-pad and the substrate were observed in laser scan microscope (VK-9710, Keyence, Japan) in Figs. 6.17(d-f). Generally, the cell's surfaces of the m-pad is more smooth than that of the n-pad and the tofu. There are a very small ratio of high roughness areas on the surfaces of the n-pad (maximum $\sim 1\mu m$) and the tofu (maximum $\sim 12\mu m$). The fingers were made from DragonSkin 00-10 following the Pneunet structure, and the cover layer was made from DragonSkin 00-20. The other parts of the robotic hand were printed by 3D Zotrax M200 with using ABS plastics. Also we cut a Japanese tofu with it dimensions: $19.6\times19.6\times15\,\mathrm{mm}^3$ as a sample to carrying out for the test as illustrated in Fig. 6.17(c). The surface having edge's size $19.6\times19.6\,\mathrm{mm}^2$ was implanted by black markers (ABS plastic) for tracking the deformation of the sample (see Fig. 6.22 for details).

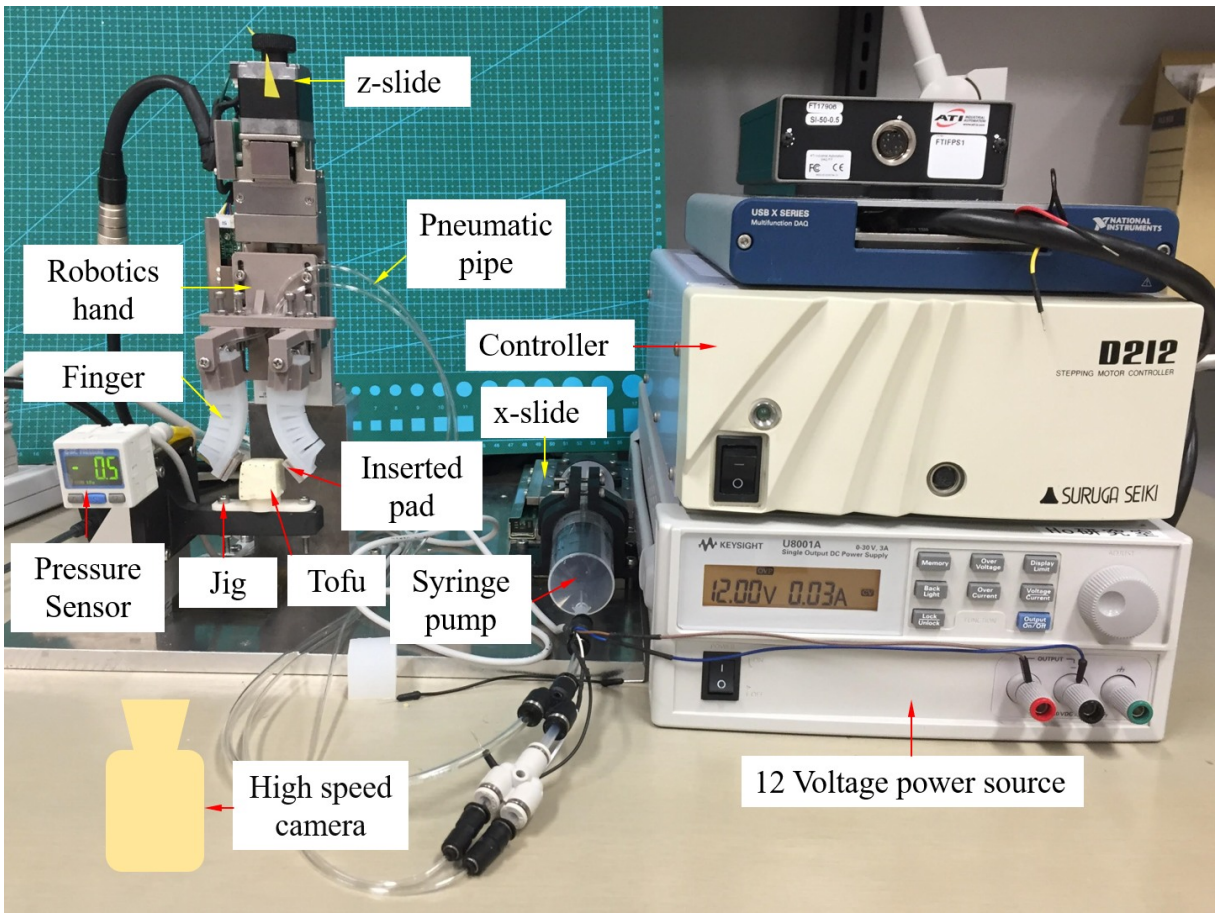

Figure 6.18: Scheme of experimental set-up for measuring the preload.

6.2.4.2 Experimental setup

An experiment was conducted for evaluating the preload resulted from the interaction between the m-pad/n-pad and a piece of fresh tofu. The fabricated pads (m-pads or n-pads) were fixed on the tips of a pair of soft pneumatic fingers. The robotic hand was attached to a motorized linear stage which can provide precise movement along vertical z-axis. The two soft fingers were connected through plastic pipes to a syringe pump whose plunger is fixed onto a horizontal linear stage (x-slide). Both of the linear stages were driven by a stepping motor controller (Suruga Seiki D212). The formation of the pneumatic fingers' grasping pose, as well as wide range of initial loads exerting on the piece of tofu at the fingertips, were regulated by varying air pressure, using the syringe pump. The acting pressure was measured by a pressure sensor (SMC ISE30A). Moreover, in order to evaluate the deformation of the piece of tofu under a designated acting pressure, a high-speed camera (Sony DSC-RX10M4) is used to capture black markers attached onto the surface of the tofu block. The experiment set-up is shown in Fig. 6.18.

During the evaluation process, there are two main phases by which the wet adhering capabilities of the n-pad and m-pad were examined. The adhering capabilities of the two

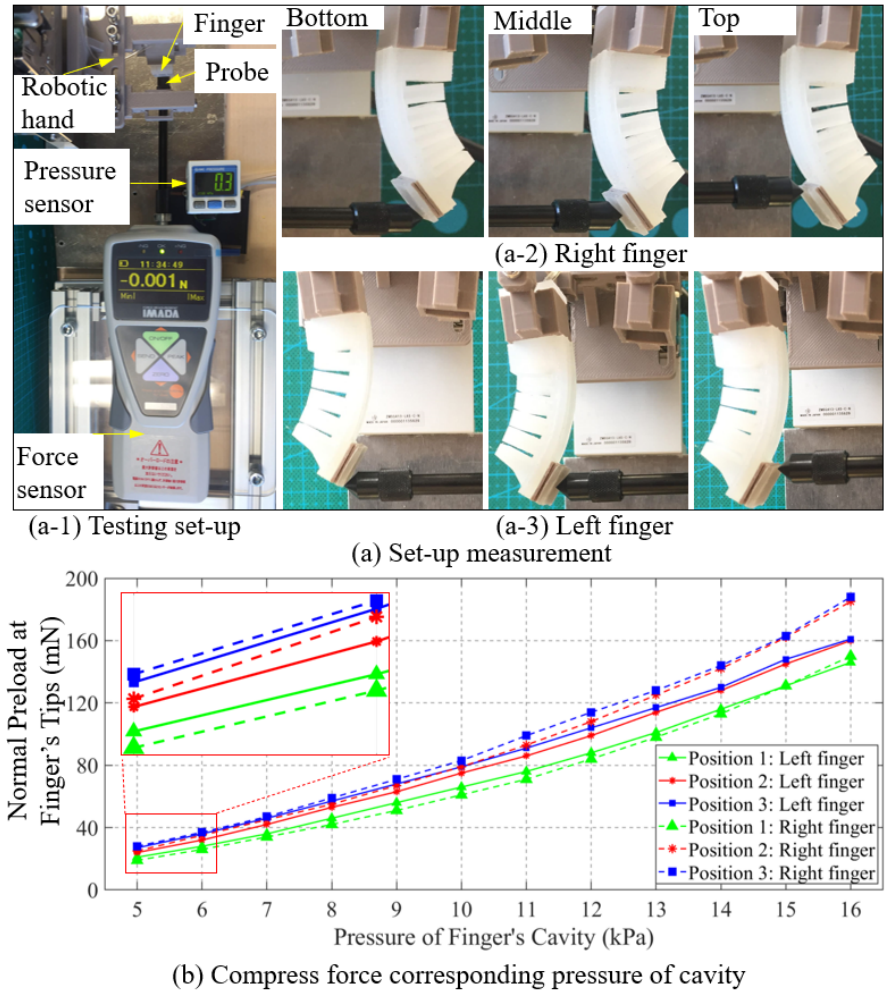

Figure 6.19: Measuring the preload by calibrating the pressure inside the Pneunet structure of the robotic fingers. The measurement set-up in a) including a pressure sensor and a force sensor a-1). Also the tests were performed at three points: bottom, middle and top on both two fingers a-2) and a-3). b) Results of the force calibration.

soft pads are evaluated and compared through two criteria: grasping pressure and releasing pressure. In the first phase, a minimum pressure (*i.e.*, grasping pressure) was determined, which was just sufficient enough to lift the tofu block out of the jig and then firmly held it without being slipped, while the hand was kept at a certain height. In order to obtain this *grasping pressure* value, at first, the robotic hand moved down to the piece of tofu. Next, the soft fingers were actuated so that the air pressure (*i.e.*, initial load) exerting on the tofu was gradually increased. In the second phase, once the robotic hand moved the tofu to a certain height, the exerting pressure was being steadily reduced until the tofu started sliding on the surfaces of the soft pads. The pressure at which the slippage occurred was defined as *releasing pressure*. Then, the preload P exerting on the surfaces of the pads were obtained by calibration the input pressure inside the chamber of each fingers as shown in Fig. 6.19(a). The calibration tests returned results for the preload

at 3 positions: top, middle and bottom of the pad as illustrated in Fig. 6.19(a-2)(a-3). The value of preload was almost similar for two fingers as the low pressure ($P < 10\,pa$); whereas, as ($P >> 10\,pa$), the preload of right finger is 10 % higher than that of the left finger (Fig. 6.19(b)). This error came from the accumulated error at large deformation of the fingers, which generated the different slope angle of the pad along z-direction. The difference in fabrication of two fingers may also be a reason.

6.2.5 Evaluation results

6.2.5.1 Grasping pressure

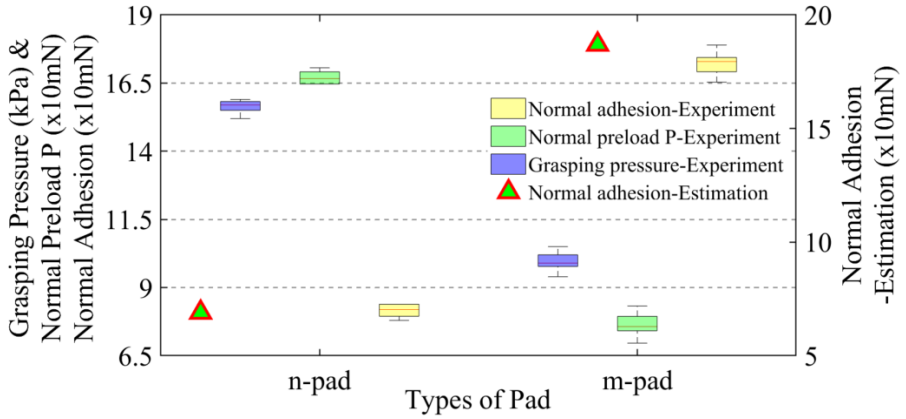

Figure 6.20: Comparison of the the force value from the pads exerting on the tofu between two cases: n-pad and m-pad. In this figure, the grasping pressure and its corresponding normal preload P was obtained from the mean value of the left and right fingers at middle position (Fig. 6.19(b)). Also the normal adhesion force was derived from Eq. (6.22) with replacing the experimental value of the preload P (equals to the grasp force F_{gn}, F_{gm}). The normal adhesion forces of the n-pad and the m-pad were, in turn, calculated in Eqs. (6.23) and (6.24). The condition for this calculation is: $\phi = \theta_1 = \theta_2 = \theta_3$=1.414 (rad) and $\theta_{j1} = \theta_{j2}$=0.7679 (rad) was measured in Fig. 6.17(b), $\eta_n = \eta_m$= 0.35, h=25 μm, h_j=30 μm, πr_{wj}^2=45.396 mm^2, $2\pi r_{wj}$=90.79 mm, μm, γ=0.073 N/m and m=5.537 g.

The grasping pressure and the resulted normal preload by which the designed robotic hand could stably lift the piece of tofu were experimentally observed in 5 trials for each type of the soft pads (m-pad or n-pad). The obtained data is statistically processed and shown in the Fig. 6.20. It reveals that the soft pad without micro pattern (n-pad) needs a higher grasping pressure to firmly lift the tofu, at approximately 15.7 kPa, thus leading to the normal preload of 168 mN. Whereas, with the m-pad, the grasping pressure of the robotic hand required for safely handling the tofu is smaller than that of the n-pad, with the mean value of 10 kPa and its corresponding normal preload is at about 75 mN.

From the initial conditions in Fig. 6.20, we have gravity force of the tofu G= 0.054 N and F_{wj}= 0.12 N. By replacing the obtained results of the preload in the Fig. 6.20 into Eqs.

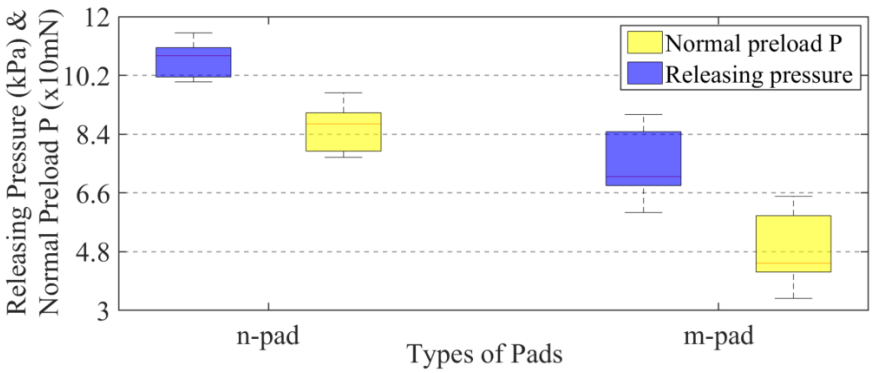

Figure 6.21: Releasing pressure and its corresponding normal preload P of the n-pad and the m-pad. The preload P was obtained in the same way as shown in Fig. 6.20.

(6.22), (6.27) and (6.28) we had the experimental data of the adhesion forces with $\bar{F}_{wn,n}$= 0.0812 N, $\bar{F}_{wm,n}$= 0.173 N. The testing values of the the normal adhesion force were utilized to validate the estimation in Eqs. (6.23) and (6.24) which returned wet adhesion forces of m-pad and n-pad are $F_{wn,n}$= 0.0692 N and $F_{wm,n}$= 0.187 N, respectively. The comparison showed a good agreement between the analytical model and the evaluation experiment, when the errors of the normal adhesion force are -14.8% and 8.09% for the n-pad and m-pad, respectively. This reveals that the m-pad needs lower applied preload into the tofu comparing with that of the n-pad ($\bar{r_p}$= 7.57 N/0.1667 N=0.454<1, respectively). In other words, the ratios $\{r_g, r_t, r_p\}$ in Eqs. (6.26), (6.29) and (6.32) are both appropriate with the actual tests.

6.2.5.2 Releasing pressure

The result of the examination of releasing pressure was determined at the moment the tofu started sliding relatively to the surface of the soft pads, judged through high-speed camera. Fig. 6.21 shows the releasing pressure for two cases of pads: n-pad and m-pad. For each type of the pads, the experimental process was repeatedly in 5 trials. For the n-pad, the recorded releasing pressure slightly fluctuates around 10.7 kPa, then its resulting normal preload is at 94 mN, which is lower than the grasping pressure and the preload by 5 kPa and 74 mN, respectively. Regarding the m-pad-type hand, the releasing pressure varies greatly, ranging from 6.5 to 8 kPa with the mean value of roughly 7 kPa, and thus differentiating from the grasping one by more or less 3 kPa. Also, the corresponding normal preload of 41 mN observed in the releasing state is lower than that of the grasping state, by 34 mN.

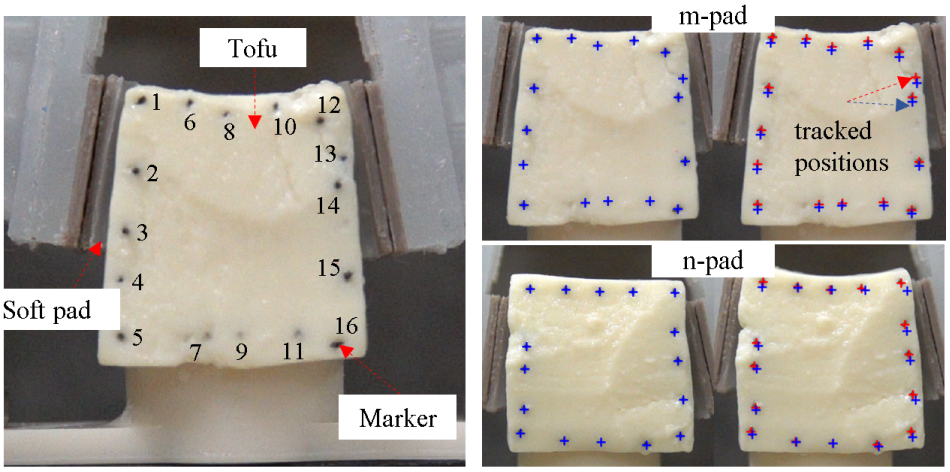

(a) Set-up for tofu-deformation evaluation (b) Pre-grasp state (c) Deformed state

Figure 6.22: The figure (a) shows the high-speed camera view for marker tracking which is used for determination of tofu deformation, (b) illustrates the tracked markers' positions in the original state of the tofu and (c) demonstrates the changes in markers' positions when the tofu is subjected to an acting force, and then gets to the deformed state. The m-pad and n-pad highlight the process of tofu deformation as gripping the tofu with and without micro-pattered pad, respectively.

6.2.5.3 Tofu Deformation

In this section, we report evaluation on how the piece of tofu was deformed under a preload (*i.e.*, grasping pressure), exerted by the robotic hand equipped with the normal n- and micro-patterned pad, in turn. Black markers (16 in total) were arranged on the front surface of the tofu, with ordinal numbers as shown in Fig. 6.22(a), then their relative positions could be tracked and measured using the Image Processing tool in MATLAB software.

The deviation of markers' positions (marked as red 'plus' sign) on the tofu under the acting force (*i.e.*, deformed state in Fig. 6.22(c)) from that of the original state (marked as blue 'plus' sign in Fig. 6.22(b)) was measured to assess the change in the tofu shape in terms of two-dimensional deformation. The deformation was observed in two cases: the tofu was gripped by the m-pad and the n-pad under a grasping pressure of 10 kPa and 15.7 kPa, respectively.

Because the markers are not arranged neatly onto the surface of the tofu, whose shape is badly defined in the pre-grasp state as well, it is hard to observe and evaluate the changes in the tofu shape under the grasping forces. In order to recognize the deformed tofu shape, therefore, we modelled the piece of tofu by translating the tracked markers' position to new calculated ones such that the original modelled tofu would transform to a square shape (c_0). With the same translation for tracked markers in the deformed state, the model shows that in the both cases under the preload, the upper and bottom sides

of the tofu are substantially deformed so that their contours would fit well as parabolic curves (c_1) (Fig. 6.23(a-1)). However, experiencing a large force - in the case of n-pad, the tofu is by more deformed at the corners and edges, which are modelled into the contour of (c_2) (Fig. 6.23(a-2)). Moreover, the deformation is analytically evaluated by measuring maximum strains with respect to x-axis and z-axis, which are calculated by the changes in length (ΔL=L-L_0) of the specific axis over the initial one (L_0) (Fig. 6.23(a-2)). According to the figure of two-dimensional deviation presented in Fig. 6.23(b) and the original lengths of the tofu (L_{0x}=19.6mm, L_{0z}=19.6mm), the maximum changes in length in terms of the case 1 (m-pad) are by -0.22mm (ΔL_x=Δx_{12}-Δx_5, the minus sign means the length reduced over the initial length) and 0.09mm (ΔL_z=Δz_5-Δz_1) along the x and z direction, respectively, and consequently the strains in turn are 1.14% and 0.47%.

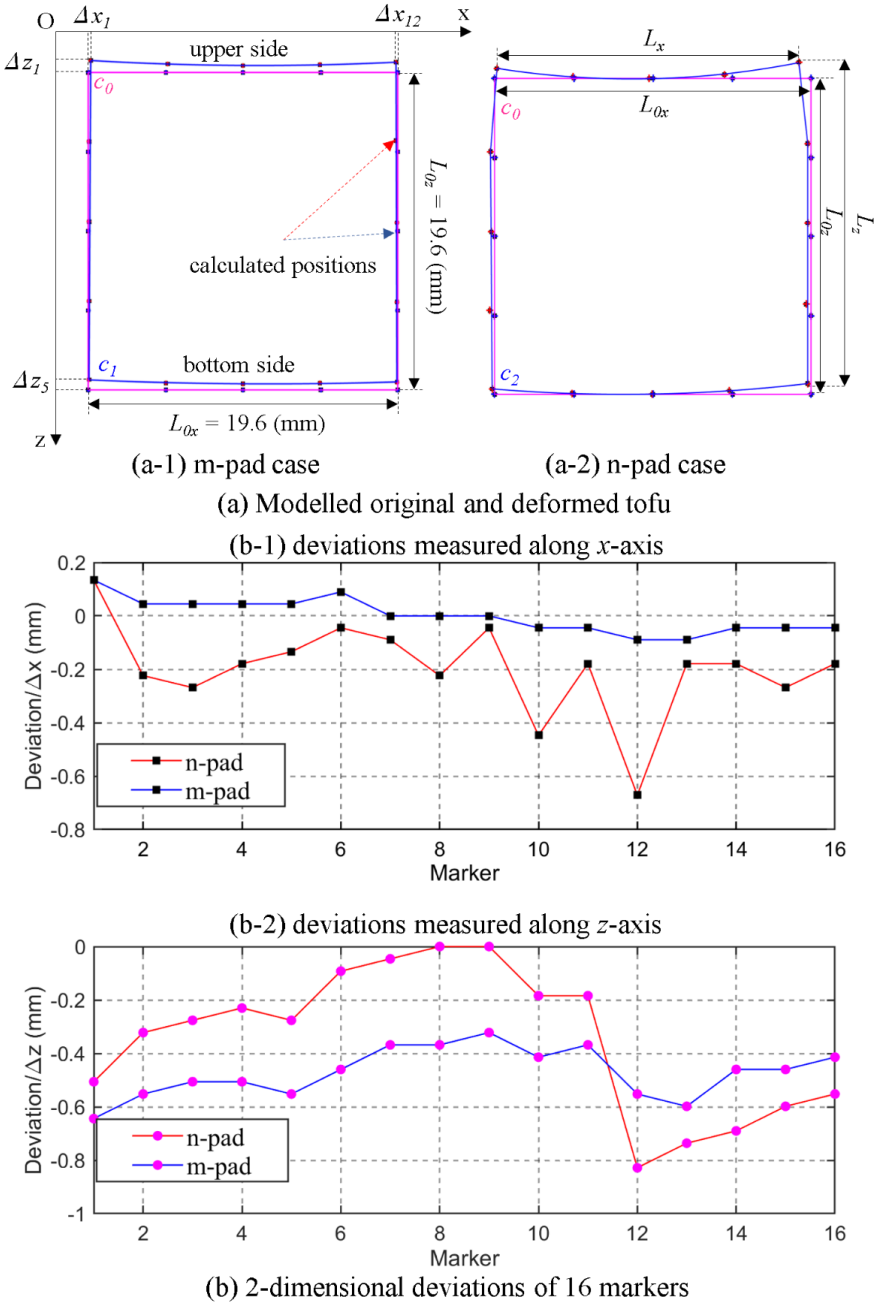

Figure 6.23: The figure (a) illustrates the model of the tofu seen from the front side after translating the tracked markers' positions to the calculated ones. The (a-1) and (a-2) are the tofu models derived from the experiment with case 1) m-pad and case 2) n-pad, in which (c_0), (c_1) and (c_2) are original and deformed tofu contours in case 1 and case 2, respectively. (b) the graph shows the deviation of the original markers from the deformed ones with respect to the 16 markers, which are measured in two dimensions, the (b-1) x-axis (Δx_1 to Δx_{16}) and the (b-2) z-axis (Δz_1 to Δz_{16}).

The deformation in the case 2 (n-pad) is considerably larger in comparison to the first case, that is, the maximum strains calculated in that case are 4.11% along the x direction and 1.41% along the z one. Also, the changes in length are nearly four times as large in

the x direction as that of the m-pad gripping case, at -0.81mm (ΔL_x=Δx_{12}-Δx_5) and twice in the z direction, at 0.28mm (ΔL_z=Δz_{16}-Δz_{12}). These obtained results repeatedly reveal that the m-pad exerted a smaller preload P which caused the major deformation of the tofu, comparing with that of the n-pad. In other words, testing the strain of the tofu also contracted with the reduction ratios $\{r_p, r_s\}$ in Eqs. (6.32) and (6.33).

CHAPTER 7

DISCUSSION, CONCLUSION AND VISIONS

7.1 Discussion

7.1.1 Adhesion of Flat Contact Interface

7.1.1.1 Analytical Model

In this thesis, the adhesion principle of the contact between the m-pad and the substrate having flat surface was investigated. Our proposed model showed the high dependence of the contact force on the pad morphological design, the properties of the liquid film, and relative motion between the couple surfaces in the contact interface. In addition, the surface roughness of the substrate influenced to the adhesion interaction of the contact, including dry and wet adhesion. We proposed the analytical model of the contact including: "wet without dry adhesion" and "wet with dry adhesion" as a general case. However, determining the ratio of the dry and wet adhesion force in the total adhesion was extremely complicated. This thesis limited case study for the substrate having very smooth surface and the liquid film entirely covered the substrate (neglected the dry adhesion) for calculating the adhesion force. Utilizing the proposed model was able to estimate the underlying physics of the adhesion in two cases of the contact: tangential and normal directions. The results illustrate that the pad having microppaterned morphology provides superior the adhesion force compared to that of the pad having no patterned morphology in the those directions. Moreover, the estimated model facilitates evaluating mechanical and geometrical properties of the wet contact interface in strengthening the wet adhesion interaction. Hence, this model is potential to be used for investing the wet adhesion for diverse contact interfaces, for instance, grasping, locomotion, and so on.

7.1.1.2 Parameters

The ultimate objective of our project is to come up with a bio-inspired robotic hand with its soft fingers designed for stably gripping/handling objects in wet conditions. Hence, the the contact interface's parameters are considered to appropriate to gripping actions, for example: low velocities and small displacements; in two cases: normal and tangential contacts. Herein, we chose water as the liquid film deposited on the contact surface, since it is one of the most common liquid existing in human daily life. In specific purposes involving the liquids with higher viscosity such as: oil in industry, blood in surgery, and so on, the wet adhesion will significantly rise, and thus this model can enable to describing similar phenomenon.

7.1.1.3 Experimental Results

The experimental results presented good agreement with the analytical ones achieved from our proposed model. Nonetheless, there were several inconsistencies points in the comparing results which were resulted from the nonlinearity of the silicon rubber utilized for making the m-pad, and the volume reduction, due to evaporation, of the liquid between the testing trials.

In addition, the obtained results of the adhesion in our study were compared with previous outcomes as shown in table 7.1. In [130], the square-patterned pad comprises of $100 \times 100\,\mu m^2$ cells interspaced by the network of the grooves with the width and depth of, in turn, $15 \times 10\,\mu m^2$, enhancing the normal and tangential adhesion force by 2- to 3-fold bigger than the pad having no patterned morphology. Also, the squared pattern in [132] rose the frictional force and coefficient roughly 30 % more than did the normal pad. The authors [127] revealed that the increment ratio of friction force in wet condition between a pad having hexagonal-patterned design and a normal pad was around three times.

Table 7.1: Comparison of the increment ratios of wet adhesion forces with previous work.

Our results Square	[130] Square	[132] Square	[127] Hexagon	[128] Hexagon	[104] Hexagon
Normal wet adhesion force					
2	2÷3	-	-	-	1
Tangential wet adhesion force					
1.2÷1.4	2	1.3	3	4	4

Authors in [104, 128] illustrated that using hexagonal pattern pads in the hydrophilic state can strengthen the friction force around 4-fold compared to a normal surface; whereas this force was decreased around 25 % in the hydrophobic state. In general, our obtained results demonstrated good agreement with those of previous researches for showing the m-pad's roles in increasing the contact force with adhesion interaction, in case square

pattern morphology. Thus, the adhesion force in case using the hexagonal patterns is different from that using square patterns. Therefore, the role of micropatterns in rising the wet adhesion interaction should be evaluate for many parameters: material properties of the pad and the substrate, patterned morphology, the liquid film and so on.

7.1.1.4 Morphology of the Micropattern Pad

In my thesis, the morphological design of the m-pad was the square pattern instead of other shapes of the shell, for instance, pentagon or hexagon as shown in the microstructure inside the sole of tree-frog toe. This is due to the fact that the square is the symmetrical shape, and easy to fit in the pad surface. Moreover, the square shape can exert a uniform load along the main axes. Also, it helps decrease the complexity in optimizing the m-pad morphology, for adapting diverse application objectives. On top of that, we aim to investigate the mechanics of the adhesion with various shapes of the micropattern morphology in the future researches.

7.1.2 Adhesion of Curved Contact Interface

7.1.2.1 Analytical Model

The role of micropattern on enhancement of contact force in cases with curved surfaces was investigated using a proposed analytical model in various scenarios. The proposed model showed dependence of contact force (with adhesion) on pad form, liquid film, and applied preload. Applying this model, one can investigate the underlying physics of wet adhesion to objects with a curved surface: concave and convex (with and without preload). The obtained results demonstrated the micropattern soft pad provided superior wet adhesion efficiency compared to that of the smooth flat/plain pad in all cases. Thus, this model may be utilized in estimation of wet adhesion for many complex grasping interfaces such as in grasping; objects in the human body, food, and so on. One such application is grasping a contact lens as described in chapter 6.

However, this model limited to the normal direction of the substrate has no investigation of the shear or tangential contact force because of followed reasons:

1 As the pad moves as shown in Figs. 7.1(b-d), the difference of interface gap inside the capillary changes significantly the capillary's curvature R_1, R_2. That is, we may not apply the Young-Laplace equation (2.20) and other components in estimating the adhesion force F_a.

2 At small interface gap h in Fig. 7.1(a), a small movement of the pad in x-direction can generate large deformation of the soft pad. In this scenario, the pad morphology

will change and lead to difficulties for applying the proposed theory in the current research.

3 At large interface gap h in Fig. 7.1(b) the wet adhesion force is infinitesimal for contribution in grasping objects.

Currently, there is no theory related to answering this problem, and we aim to carry out this work as our future works.

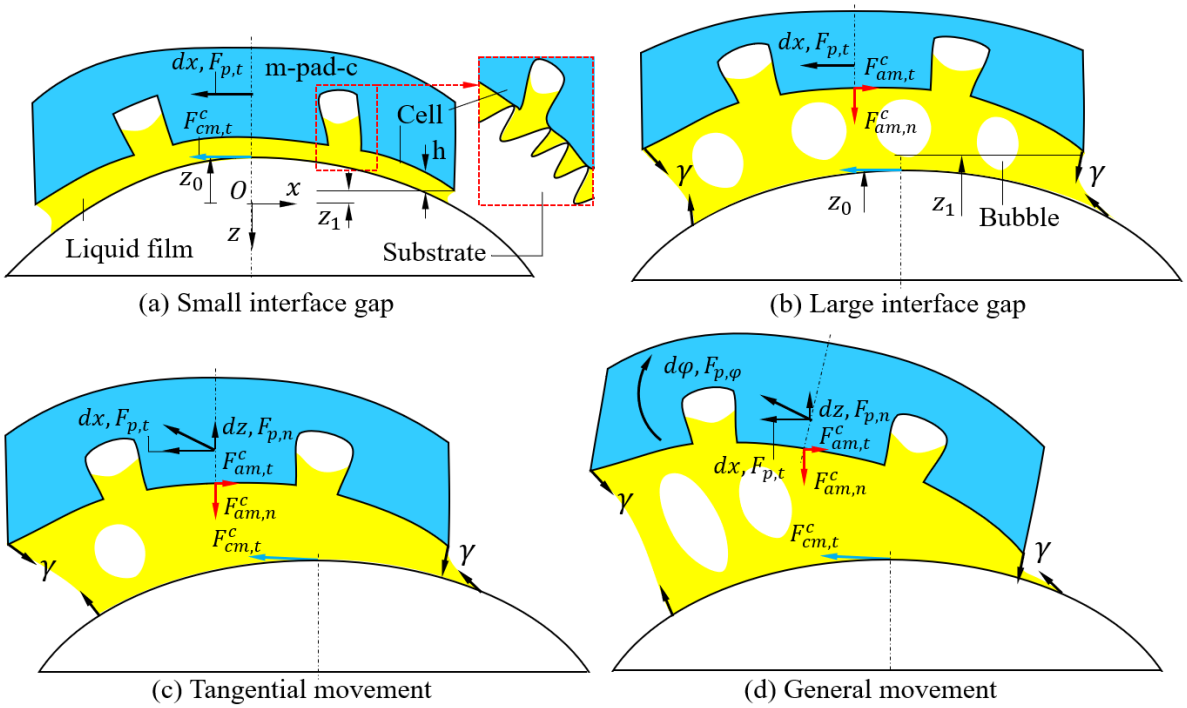

Figure 7.1: Four cases of estimating tangential contact force in curved contact interface. a) and b) the pad moves in x-direction at small and large interface gap h. The pad moves in tangential direction with the substrate surface c) and general direction d).

7.1.2.2 Obtained Results

Our obtained values of normal adhesion forces were agreement with the analytical models in this study. In addition, those results were lower than previous findings regarding plane interfaces in contact (table 7.1). This resulted from the pad morphology being significantly changed during contacting the substrates. The parameters of the substrates also influence to the results, which reveals that the micropattern pad can significantly increase the contact force for grasping actual objects.

7.1.3 Role of Viscosity

The liquid film used in this investigation is water, which has low viscosity coefficient ($\eta =$ 1 mPas). Thus, the contribution of the viscous force is smaller than that of the surface

tension and Laplace force. Herein, the capillary number in this study n_{ca} in Eq. (2.48) is about 0.00000694. By using honey ($\eta \geq 2\,\text{Pas}$ [230]) would we get $n_{ca} \geq$0.014. In this scenario, the viscosity force will make a significant contribution in the adhesion force comparing with the others. Changing liquid induces varying the property of surface tension γ, viscosity coefficient η, contact angle θ and other properties of the wet and dry adhesion (van der Waals and Casimir forces).

7.1.4 Contribution of the Dry Adhesion in Adhesion Force

This research aims to enhance the adhesion force for grasping soft, fragile objects, which usually have random and large roughness surfaces. In this scenario, the dry adhesion force may also exist in the interface accompanying with wet adhesion. However, figure 5.1 shows that its contribution in micro scale is infinitesimal to the wet adhesion force. Currently, we focus on manipulating objects with high surface roughness such as: food, human soft tissues or medical objects. In other words, the dry adhesion can be neglected in the validation of contact or grasp force. This force will be certainly concerned as the objects have low surface roughness or in dry condition, which also is an important content of our future works.

7.1.5 Role of Preload

In grasping/manipulating, the soft robotic fingers need the preload P acting on the object surfaces for handling. Depending on the stiffness of the contact, this force can change the interface gap h through varying the actual contact area A_{di} and A_{wi} at each asperity point i. Due to the influence of the groove network, the pad having micropattern is softer, achieves higher actual contact area and smaller interface gap h than that of the normal pad. Additionally, increasing the preload P leads to reducing the groove width w, which enhances the wet adhesion inside the grooves. In other works, the m-pad can achieve higher adhesion force comparing with the case of n-pad when increasing the preload P. However, the variation of w may not be same in entire contact when we deposit a large value P in curved interface (n-pad-c(v) and m-pad-c(v)). In this scenario, there are bigger deviations of the wet adhesion force between the estimations and experiments. Therefore, it is necessary to concern the contact model 2.5.2 and 2.5.3 for calculating the adhesion and contact forces.

7.2 Conclusion

My thesis proposed the model of the soft contact mechanics with considering the role of the adhesion in varying the pad morphology such as: flat and curved contact interfaces.

The principle design inspired by the wet attachment mechanism of tree-frog toes to its surrounding environment. The experimental and estimated results illustrate the good agreement which expresses the role of the micropattern on strengthening the adhesion force in a wet conditions. Also, it suggests a novel way for carrying out the morphological optimization in case the soft contact mechanics regarding the adhesion contributions. Although we investigated two cases of the contact interface: flat and curve, our research majorly concentrated on evaluating the adhesion forces for only one type of the micropattern like square shape. However, it is very useful to construct the new models of the contact mechanics for other patterns having diverse morphology. The increment ratios showing the ability of enhancing the wet adhesion for the m-pad compared with that of the n-pad are generally complicated. In this scenario, we transformed such equations into the function of the patterned morphology; whereas the other parameters of the liquid are constant. Further investigations are necessary to optimize the morphological surfaces of those such soft pads (the m-pad) for achieving the better enhancement of the adhesion interaction in both dry and wet conditions. That is, the grasping/manipulation of the soft-fragile objects can reduce the preload/reaction force acting on the substrate's surfaces, causing damages or risk for the outcomes. This was revealed through the grasping thin shell (showcase: gripping the contact lens) and the soft-fragile (showcase: gripping the tofu) objects by the soft robotic hands having their fingers inspired by wet adhesion of the tree frog toes. Finally, the parameters of the liquid properties, shape and tribological characteristics of the substrate should be considered for fabrication of actual applications in robotic fields such as: grasping, locomotion, haptics and so on in the future.

7.3 Visions

My thesis is expected to make many meaningful impacts to both science and tech. Currently, theoretical models of the wet adhesion with micropttterned surface are scare, while the experimental evidences have been gradually given from previous researchers. Thus, our works develop the theoretical foundations, which are necessary to predict the role of the micropattern on the enhancement of wet adhesion in the contact. Hence, the researchers in other fields can follow and develop their own models. For instance, authors in [124, 231, 232] in materials and biological sciences, and Li [233] in robotics referred our publications to their articles, although we have published recently in a different field.

In robotic manipulation, grasping rigid objects is popular. Recently, many researchers have attempted to find out effect ways for handling the soft-fragile objects such as: food, fruit, human soft tissues, medical equip and so on. In order to answer the given problems, there are a number of grasping mechanisms proposed. Among them, the robotic finger having micropatterned pad proposed in my thesis preliminary showed its advantage

points as grasping objects in wet conditions. This research direction is very novel and prospective in soft robotics, which may appeal many researchers, since its content relates to interdisciplinary collaborations of: mechanics, mechanical engineering, robotics and materials. However, many other related researchers may not follow currently due to requiring expensive equipment for fabricating the micropatterns as well the measurement devices. This can be overcome when making the micropattern becomes more simply.

In the future, we are going on developing our current research in both analytical models and applications as followed:

1. *Analytical model*: Besides optimization of the micropatterned morphology, it necessary to concern the deformation of the pad when exerting the preload P in the contact mechanics even though this deformation is very small. In this scenario, the JKR and GW models can be applied to the estimation in the cases flat and roughness surfaces. Then, this model is combined with the motion of the robot hand, in which the pads are fixed. In addition, the liquid film should have higher value of viscosity comparing with water that enhances the role of wet adhesion in grasping. Of course, the selected liquid has to be safe with the objects and environment. Also, we aim to find out another materials (polymers), which their adhesive ability are stronger than that of the silicon rubbers.

2. *Applications*: We will improve our current designs of the soft robotic hand in gripping contact lens and tofu toward the actual applications in daily life and food production lines. Furthermore, the soft fingers are diversely designed so that they can adapt with various environments having wet and dry conditions.

Our future work is fully supported by JSPS Kakenhi No 20J14910.

APPENDIX A

PUBLICATIONS AND AWARDS

A.1 Journals

1. **Pho Van Nguyen** and Van Anh Ho, "Grasping Interface with Wet Adhesion and Patterned Morphology: Case of Thin Shell", *IEEE Robotic and Automation Letters (RA-L)*, Vol. 4, Issue 2, pp. 792-9, 2019. **IF: 3.608, rank 6/28**.

2. **Pho Van Nguyen** and Van Anh Ho, "Mechanics of Wet Adhesion in Soft Interaction with Patterned Morphology", *Bioinspiration & Biomimetics*, Vol. 14, No. 1, 2018. **IF: 3.375, rank 10/28**.

A.2 Peer-review International Conference

1. **Pho Van Nguyen**, Quan Luu and Van Anh Ho, "Wet Adhesion of Micropattern Interface in Grasping Fragile Objects", *IEEE/RSJ International Conference on Intelligent Robots and Systems (IROS)*, No. 2080, Las Vegas, US, 2020.10. **Rank A, 2st in Robotics**. (accepted).

2. **Pho Van Nguyen** and Van Anh Ho, "Grasping Interface with Wet Adhesion and Patterned Morphology: Case of Thin Shell", *International Conference on Robotics and Automation (ICRA)*, No. 2711, Montreal, Canada, 2019.5. **Rank A, 1st in Robotics**.

3. **Pho Van Nguyen**, Tue Trong Phan, Ngoc Van Huynh and Van Ho," Soft Grasping with Wet Adhesion: Preliminary Evaluation", *The first IEEE- RAS International Conference on Soft Robotics (RoboSoft)*, pp. 418-23, Livorno, Italy, 2018.4. **1st in Soft Robotics**.

A.3 Peer-reviewed International Workshop

1. **Pho Van Nguyen**, Van Anh Ho *et al*, "Toward a Platform for Simulation and Design Optimization of Underwater Anguilliform Movement: Case of Soft Robotic Eel", *Interdisciplinary Collaborative Case-studies at the ICRA2020 workshop "Beyond Soft Robotics-International Conference on Robotics and Automation (ICRA)*, Paris, France, 2020.5.

2. **Pho Van Nguyen**, "Grasping Interface with Wet Adhesion and Patterned Morphology: Case of Thin Shell", *ICRA 2019 Workshop on soft haptic Interaction*, Canada, 2019.5.

3. **Pho Van Nguyen** and Van Anh Ho, "Soft Grasping with Wet Adhesion: Preliminary Evaluation", *Workshop Soft haptics: what's been done, be done*, Italy, 2018.4.

A.4 Domestic Conference and Symposiums

1. **Pho Van Nguyen**, "Grasping Curved Surfaces by Soft Robotic Finger with Micropattern Integrated Wet Adhesion", *Tokyo-Ishikawa Scientific Meeting*, Tokyo, 2020.3.

2. **Pho Van Nguyen**, "Soft Robotics: Potential in Developing Digital Economy", *Vietnamese Young Global Forum 2th-Technology and Management in Digital Economy*, Ha Noi, Viet Nam, 2019. 11.

3. **Pho Van Nguyen**, "Soft Robotics: Perspective of Significant Contribution in Science and Technology", *Vietnamese Young Global Forum 2th-Vietnamese Sustainable Development*, Ha Noi, Viet Nam, 2019. 11.

4. **Pho Van Nguyen**, "Grasping Interface with Wet Adhesion and Patterned Morphology", *Japan-India Symposium on Materials Science*, Ishikawa, Japan, 2019.3.

5. **Pho Van Nguyen**, "Soft Robotics", *Scientific Meeting with Duy Tan University*, Danang city, Viet Nam, 2018.12.

6. **Pho Van Nguyen**, "Soft Grasping with Wet Adhesion", *Vietnam-Japan Scientific Meeting-Tohoku University*, Sendai, Japan, 2018.9.

7. **Pho Van Nguyen**, "Soft Robot in Grasping", *Tokyo-Ishikawa Scientific Meeting*, Tokyo, 2018.3.

8. **Pho Van Nguyen**, "Soft Grasping with Wet Adhesion: Preliminary Evaluation", *Japan-India Symposium on Materials Science, Japan*, 2018.3.

A.5 Other Journals

1. Pham HH and **Nguyen PV**, "Dynamic analysis of cam manufacturing", *J. of Applied Mechanical Engineering*, Vol. 6, No. 274, 2017.

A.6 Awards

1. 2020 IEEE Nagoya Chapter International Conference Research Presentation Awards, 2020. 4.
2. Grants-in-aid for Scientific Research (JSPS KAKENHI), No. 20J14910, 2020.4-2022.3.
3. JSPS (Japan Society for the Promotion of Science) DC2 in 2020.4-2022.3.
4. JAIST Off-campus research grant for research in INRIA Institute, Lille, France, 2019.4-9.
5. Student travel award by JAIST research grant, 2019.5
6. JAIST President award, 2018.9.
7. Student travel award by JAIST research grant, 2018.4.
8. Doctoral Research Fellow (JAIST), 2017.10-2020.9
9. Monbukagakusho honors scholarship, 2017.10-2018.3.

Bibliography

[1] Gianluca Antonelli. *Underwater Robots*. Springer, Switzerland, 2014.

[2] Marco Ceccarelli. *Service Robots and Robotics: Design and Application*. Engineering Science Reference, US, 2017.

[3] Mark R. Miller and Rex Miller. *Robots and Robotics Principles, Systems, and Industrial Applications*. Mc Graw Hill Education, US, 2017.

[4] Roland Siegwart, Illah R. Nourbakhsh, and Davide Scaramuzza. *Introduction to Autonomous Mobile Robots*. The MIT Press, London, 2011.

[5] A. K. Pandey and R. Gelin. A mass-produced sociable humanoid robot: Pepper: The first machine of its kind. *IEEE Robotics Automation Magazine*, 25(3):40–48, 2018.

[6] Mordechai Ben-Ari and Francesco Mondada. *Robots and Their Applications*, pages 1–20. Springer International Publishing, 2018.

[7] Baxter Paul, Ashurst Emily, Robin Read, Kennedy James, and Belpaeme Tony. Robot education peers in a situated primary school study: Personalisation promotes child learning. *PLOS ONE*, 12, 2017.

[8] Tomáš Krajník, Vojtěch Vonásek, Daniel Fišer, and Jan Faigl. Ar-drone as a platform for robotic research and education. In *Research and Education in Robotics - EUROBOT 2011*, pages 172–186. Springer Berlin Heidelberg, 2011.

[9] Brian Davies. Robotic surgery – a personal view of the past, present and future. *International Journal of Advanced Robotic Systems*, 12(5):54, 2015.

[10] Robert Bogue. Robots that interact with humans: A review of safety technologies and standards. *Industrial Robot: An International Journal*, 44:531–536, 2017.

[11] Softbankrobotics. `https://www.softbankrobotics.com/emea/en/pepper`.

[12] Honda robotics. `https://global.honda/innovation/robotics/ASIMO.html`.

[13] D. Falanga, K. Kleber, S. Mintchev, D. Floreano, and D. Scaramuzza. The foldable drone: A morphing quadrotor that can squeeze and fly. *IEEE Robotics and Automation Letters*, 4(2):209–216, 2019.

[14] Deepak Trivedi, Christopher D. Rahn, William M. Kier, and Ian D. Walker. Soft robotics: Biological inspiration, state of the art, and future research. *Applied Bionics and Biomechanics*, 5(3):99–117, 2008.

[15] Chiwon Lee et.al. Soft robot review. *International Journal of Control, Automation and Systems*, 15(1):3–15, 2017.

[16] Sangbae Kim, Cecilia Laschi, and Barry Trimmer. Soft robotics: a bioinspired evolution in robotics. *Trends in Biotechnology*, 31(5):287–294, 2013.

[17] Hongbo Wang, Massimo Totaro, and Lucia Beccai. Toward perceptive soft robots: Progress and challenges. *Advance Science*, 5(1800541), 2018.

[18] Daniela Rus and Michael T. Tolley. Design, fabrication and control of soft robots. *Nature*, 521:467–475, 2015.

[19] Stephen Coyle, Carmel Majidi, Philip LeDuc, and K. Jimmy Hsia. Bio-inspired soft robotics: Material selection, actuation, and design. *Extreme Mechanics Letters*, 22:51–59, 2018.

[20] N. Elango1 and A. A. M. Faudzi. A review article: Investigations on soft materials for soft robot manipulations. *Int. J. Adv. Manuf. Technol.*, 80:1027–1037, 2015.

[21] Carmel Majidi. Soft robotics: A perspective—current trends and prospects for the future. *Soft Robotics*, 1(1), 2013.

[22] Jennifer C. Case, Edward L. White, and Rebecca K. Kramer. Soft material characterization for robotic applications. *Soft Robotics*, 2(2), 2015.

[23] C. Liu, H. Qinb, and P. T. Mather. Review of progress in shape-memory polymers. *Journal of Materials Chemistry*, 17:1543–1558, 2007.

[24] Carmel Majidi. Soft-matter engineering for soft robotics. *Adv. Mater. Technol.*, 4(1800477), 2019.

[25] Soo Jin Adrian Koh, Xuanhe Zhao, and Zhigang Suo. Maximal energy that can be converted by a dielectric elastomer generator. *Applied Physics Letter*, 94(262902), 2009.

[26] S. Diaham *et. al.* Dielectric breakdown of polyimide films: Area, thickness and temperature dependence. *IEEE Transactions on Dielectrics and Electrical Insulation*, 17(1), 2010.

[27] Andreas Lendlein and Robert Langer. Biodegradable, elastic shape-memory polymers for potential biomedical applications. *Science*, 296(5573):1673–1676, 2002.

[28] Z. Wang and S. Hirai. Soft gripper dynamics using a line-segment model with an optimization-based parameter identification method. *IEEE Robotics and Automation Letters*, 2(2):624–631, 2017.

[29] Stephen A. *et. al* Morin. Camouflage and display for soft machines. *Science*, 337(6096):828–832, 2012.

[30] Ameer Hamza Khan, Zili Shao, Shuai Li, Qixin Wang, and Nan Guan. Which is the best pid variant for pneumatic soft robots? an experimental study. *IEEE/CAA Journal of Automatica Sinica*, 7(JAS-2019-0257), 2020.

[31] O. Goury and C. Duriez. Fast, generic, and reliable control and simulation of soft robots using model order reduction. *IEEE Transactions on Robotics*, 34(6):1565–1576, 2018.

[32] E. Coevoet *et al.* Software toolkit for modeling, simulation, and control of soft robots. *Advanced Robotics*, 31(22):1208–1224, 2017.

[33] Guillaume Saupin, Christian Duriez, and Stephane Cotin. Contact model for haptic medical simulations. In Fernando Bello and P. J. Eddie Edwards, editors, *Biomedical Simulation*, pages 157–165. Springer Berlin Heidelberg, 2008.

[34] Hadrien Courtecuisse *et al.* Real-time simulation of contact and cutting of heterogeneous soft-tissues. *Medical Image Analysis*, 18(2):394 – 410, 2014.

[35] K. J. *et al* Cho. Review of manufacturing processes for soft biomimetic robots. *Int. J. Precis. Eng. Man.*, 10:171–181, 2009.

[36] H. Lipson and M. Kurman. *The New World of 3D Printing.* Wiley, 2013.

[37] Y. Xia and G. M. Whitesides. Soft lithography. *Annu. Rev. Mater. Sci.*, 28:153—-184, 1998.

[38] J. G. Cham, S. A. Bailey, J. E. Clark, R. J. Full, and M. R. Cutkosky. Fast and robust: hexapedal robots via shape deposition manufacturing. *Int. J. Robot. Res.*, 21:869–882, 2002.

[39] B.S. *et al* Homberg. Robust proprioceptive grasping with a soft robot hand. *Auton Robot*, 43:681–696, 2019.

[40] S. Hirai, T. Masui, and S. Kawamur. Prototyping pneumatic group actuators composed of multiple single-motion elastic tubes. *Proceedings 2001 ICRA. IEEE International Conference on Robotics and Automation (ICRA)*, 4:3807–3812, 2001.

[41] P. Paoletti, G. W. Jones, and L. Mahadevan. Grasping with a soft glove: intrinsic impedance control in pneumatic actuators. *J. R. Soc. Interface*, 14(20160867), 2017.

[42] Brown *et al.* Universal robotic gripper based on the jamming of granular material. *Proceedings of the National Academy of Sciences (PNAS)*, 107(44):18809–18814, 2010.

[43] V. Ho and S. Hirai. Design and analysis of a soft-fingered hand with contact feedback. *IEEE Robotics and Automation Letters*, 2(2):491–498, 2017.

[44] V. A. Ho. Grasping by wrapping: Mechanical design and evaluation. *2017 IEEE/RSJ International Conference on Intelligent Robots and Systems (IROS)*, pages 6013–6019, 2017.

[45] Jun Shintake, Vito Cacucciolo, Dario Floreano, and Herbert Shea. Soft robotic grippers. *Adv. Mater.*, 1707035, 2018.

[46] Z. Wang and S. Hirai. Soft gripper dynamics using a line-segment model with an optimization-based parameter identification method. *IEEE Robotics and Automation Letters*, 2(2):624–631, 2017.

[47] Charbel Tawk, Marc in het Panhuis, Geoffrey M. Spinks, and Gursel Alici. Soft pneumatic sensing chambers for generic and interactive human–machine interfaces. *Adv. Intell. Syst.*, 1(1900002), 2019.

[48] Ozgur Atalay, Asli Atalay, Joshua Gafford, and Conor Walsh. A highly sensitive capacitive-based soft pressure sensor based on a conductive fabric and a microporous dielectric layer. *Adv. Mater. Technol.*, 1700237, 2017.

[49] Christopher J. Payne *et al.* An implantable extracardiac soft robotic device for the failing heart: Mechanical coupling and synchronization. *Soft Robotics*, 4(3):241–250, 2017.

[50] Van Anh Ho, Dzung Viet Dao, Susumu Sugiyama, and Shinichi Hirai. Development and analysis of a sliding tactile soft fingertip embedded with a microforce/moment sensor. *IEEE Transactions On Robotics*, 27(3):411–424, 2011.

[51] Q. Qi, S. Hirai, and V. A. Ho. Wrinkled soft sensor with variable afferent morphology. *IEEE Robotics and Automation Letters*, 4:1908–1915, 2019.

[52] L. Van Duong, R. Asahina, J. Wang, and V. A. Ho. Development of a vision-based soft tactile muscularis. *2019 2nd IEEE International Conference on Soft Robotics (RoboSoft)*, pages 343–348, 2019.

[53] Blickhan Reinhard, Dabiri John Oluseun, Gordon Malcolm S., and Videler John. *Animal locomotion : physical principles and adaptations*. CRC Press, 2017.

[54] M. Calisti, G. Picardi, and C. Laschi. Fundamentals of soft robot locomotion. *Journal of The Royal Society Interface*, 14:418–423, 2017.

[55] Shepherd Robert F. *et al.* Multigait soft robot. *Proceedings of the National Academy of Sciences*, 108(51):20400–20403, 2011.

[56] Ariel A Calder *et al.* An earthworm-inspired soft robot with perceptive artificial skin. *Bioinspiration & Biomimetics*, 14(5), 2019.

[57] Altendorfer R. et al. Rhex: A biologically inspired hexapod runner. *Autonomous Robots*, 11:207—213, 2001.

[58] Bartlett Nicholas W. *et al.* A 3d-printed, functionally graded soft robot powered by combustion. *Science*, 349(6244):161–165, 2015.

[59] Vasista Srinivas, Tong Liyong, and Wong K. C. Realization of morphing wings: A multidisciplinary challenge. *Journal of Aircraft*, 49(1):11–28, 2012.

[60] Ma Kevin Y., Chirarattananon Pakpong, Fuller Sawyer B., and Wood Robert J. Controlled flight of a biologically inspired, insect-scale robot. *Science*, 340(6132):603–607, 2013.

[61] K. H. Low, J. Yang, A. P. Pattathil, and Y. Zhang. Initial prototype design and investigation of an undulating body by sma. *2006 IEEE International Conference on Automation Science and Engineering*, pages 472–477, 2006.

[62] Shuxiang Guo, T. Fukuda, and K. Asaka. A turtle-like swimming robot using a smart soft composite (SSC) structure. *IEEE/ASME Transactions on Mechatronics*, 8(1):136–141, 2003.

[63] Alex Villanueva, Colin Smith, and Shashank Priya. A biomimetic robotic jellyfish (robojelly) actuated by shape memory alloy composite actuators. *Bioinspiration & Biomimetics*, 6(3), 2011.

[64] Roche Ellen T. *et al.* A bioinspired soft actuated material. *Advanced Materials*, 26(8):1200–1206, 2014.

[65] R. K. Kramer, C. Majidi, and R. J. Wood. Wearable tactile keypad with stretchable artificial skin. *2011 IEEE International Conference on Robotics and Automation*, pages 1103–1107, 2011.

[66] Yong-Lae Park *et al.* Design and control of a bio-inspired soft wearable robotic device for ankle–foot rehabilitation. *Bioinspiration & Biomimetics*, 9(1):016007, 2014.

[67] Appiah Clement *et al.* Living materials herald a new era in soft robotics. *Advanced Materials*, 31(36), 2019.

[68] Ioannis Ieropoulos, Iain A. Anderson, Todd Gisby, Cheng-Hung Wang, and Jonathan Rossiter. Microbial-powered artificial muscles for autonomous robots. In *Electroactive Polymer Actuators and Devices (EAPAD) 2009*. SPIE.

[69] Nawroth J. *et al.* A tissue-engineered jellyfish with biomimetic propulsion. *Nat Biotechnol*, 30:792–797, 2012.

[70] Hyung-Jung Kim, Sung-Hyuk Song, and Sung-Hoon Ahn. A turtle-like swimming robot using a smart soft composite (SSC) structure. *Smart Materials and Structures*, 22(1), 2012.

[71] Hydrogel: Preparation, characterization, and applications: A review. *Journal of Advanced Research*, 6(2):105–121, 2015.

[72] Lily Cheng, Susan J. Muller, and Clayton J. Radke. Wettability of silicone-hydrogel contact lenses in the presence of tear-film components. *Current Eye Research*, 28(2):93–108, 2004.

[73] K.A. Khatib, F.M. Aramounp, T.J. Herald, and J.E. Boyer. Physicochemical characteristics of soft tofu formulated from selected soybean varieties. *Journal of Food Quality*, 25(4):289–303, 2002.

[74] Yongqiang CHENG, Naoto SHIMIZU, and Toshinori KIMURA. Texture evaluation of tofu (soybean curd) by viscoelastic tests. *Journal of the Japanese Society of Agricultural Machinery*, 64(6):137–144, 2002.

[75] Pho Van Nguyen, Quan Khanh Luu, Yuzuru Takamura, and Van Anh Ho. Wet adhesion of micro-patterned interfaces for stable grasping of deformable objects. *Proceeding IROS 2020IEEE/RSJ International Conference on Intelligent Robots and Systems*, (2080), 2020.

[76] P. V. Nguyen and V. A. Ho. Grasping interface with wet adhesion and patterned morphology: Case of thin shell. *IEEE Robotics and Automation Letters*, 4(2):792–799, 2019.

[77] K. *et al* Autumn. Adhesive force of a single gecko foot-hair. *Nature*, 405(1870):681–685, 2000.

[78] Cecilia Laschi *et al*. Soft robot arm inspired by the octopus. *Advanced Robotics*, 26(7):709–727, 2012.

[79] Stanislav N Gorb. Biological attachment devices: exploring nature's diversity for biomimetics. *Philosophical Transactions of the Royal Society A: Mathematical, Physical and Engineering Sciences*, 366(1870):1557–1574, 2008.

[80] S. Kim *et al*. Whole body adhesion: hierarchical, directional and distributed control of adhesive forces for a climbing robot. pages 1268–1273, 2007.

[81] Eppner C. *et al*. Four aspects of building robotic systems: lessons from the amazon picking challenge 2015. 42:1459–1475, 2018.

[82] Mazzolai Barbara *et al*. Octopus-inspired soft arm with suction cups for enhanced grasping tasks in confined environments. *Advanced Intelligent Systems*, 1(6), 2019.

[83] E. W. Hawkes, D. L. Christensen, Amy Kyungwon Han, H. Jiang, and M. R. Cutkosky. 2015 ieee international conference on robotics and automation (icra). pages 2305–2312, 2015.

[84] Jun Shintake, Samuel Rosset, Bryan Schubert, Dario Floreano, and Herbert Shea. Versatile soft grippers with intrinsic electroadhesion based on multifunctional polymer actuators. *Advanced Materials*, 28(2):231–238, 2016.

[85] Donald Ruffatto, Aaron Parness, and Matthew Spenko. Improving controllable adhesion on both rough and smooth surfaces with a hybrid electrostatic/gecko-like adhesive. *Journal of The Royal Society Interface*, 11(93), 2014.

[86] Jun *et al* Lou. Preliminary in vivo experiments on adhesion of geckos. *Journal of Nanomaterials*, 2008, 2008.

[87] Varenberg Michael, Pugno Nicola M., and Gorb Stanislav N. Spatulate structures in biological fibrillar adhesion. *Soft Matter*, 6:3269–3272, 2010.

[88] Gorb E. V., Hosoda N., Miksch C., and Gorb S. N. Slippery pores: anti-adhesive effect of nanoporous substrates on the beetle attachment system. *Journal of The Royal Society Interface*, 7(52):1571–1579, 2010.

[89] Peng Z., Wang C., and Chen S. The microstructure morphology on ant footpads and its effect on ant adhesion. *Acta Mech*, 227:2025–2037, 2016.

[90] Jiao Y., Gorb S., and Scherge M. Adhesion measured on the attachment pads of tettigonia viridissima (orthoptera, insecta). *Journal of Experimental Biology*, 203(12):1887–1895, 2000.

[91] Macner Ashley M. and Steen Paul H. Adaptive adhesion by a beetle: Manipulation of liquid bridges and their breaking limits. *Biointerphases*, 9(1), 2014.

[92] Shirtcliffe Neil J., Glen McHale, and Newton Michael I. Wet adhesion and adhesive locomotion of snails on anti-adhesive non-wetting surfaces. *PLOS ONE*, 7, 2012.

[93] Federle Walter, Riehle Mathis, Curtis Adam S.G., and Full Robert J. An Integrative Study of Insect Adhesion: Mechanics and Wet Adhesion of Pretarsal Pads in Ants. *Integrative and Comparative Biology*, 42(6):1100–1106, 2002.

[94] Dirks Jan-Henning and Federle Walter. Mechanisms of fluid production in smooth adhesive pads of insects. *Journal of The Royal Society Interface*, 8(60):952–960, 2011.

[95] Newar Janu and Ghatak Archana. Studies on the adhesive property of snail adhesive mucus. *Langmuir*, 31(44):12155–12160, 2015.

[96] Zhong Tianyi, Min Liu, Wang Zhiyuan, Zhang Feng, and Zuo Baoqi. Controlled self-assembly of glycoprotein complex in snail mucus from lubricating liquid to elastic fiber. *RSC Adv.*, 8:13806–13812, 2018.

[97] B N J Persson. Wet adhesion with application to tree frog adhesive toe pads and tires. *Journal of Physics: Condensed Matter*, 19, 2007.

[98] W.J.P. *et al* Barnes. Elastic modulus of tree frog adhesive toe pads. *J Comp Physiol A*, 197(969):689–697, 2011.

[99] Barnes W. Jon. P., Baum Martina, Peisker Henrik, and Gorb Stanislav N. Comparative cryo-sem and afm studies of hylid and rhacophorid tree frog toe pads. *Journal of Morphology*, 274(12):1384–1396, 2013.

[100] Michael Kappl, Farzaneh Kaveh, and W Jon P Barnes. Nanoscale friction and adhesion of tree frog toe pads. *Bioinspiration & Biomimetics*, 11(3), 2016.

[101] Scholz Ingo, Barnes W. Jon P., Smith Joanna M., and Baumgartner Werner. Ultrastructure and physical properties of an adhesive surface, the toe pad epithelium of the tree frog, litoria caerulea white. *Journal of Experimental Biology*, 212(2):155–162, 2009.

[102] Green David M. Adhesion and the toe-pads of treefrogs. *JSTOR*, 1981(4):790–796, 1981.

[103] Federle W, Barnes W.J.P, Baumgartner W, Drechsler P, and Smith J.M. Wet but not slippery: boundary friction in tree frog adhesive toe pads. *Journal of The Royal Society Interface*, 3(10):689–697, 2006.

[104] Drotlef Dirk-Michael, Lukas Stepien, Kappl Michael, Barnes W. Jon P., Butt Hans-Jürgen, and del Campo Aránzazu. Insights into the adhesive mechanisms of tree frogs using artificial mimics. *Advanced Functional Materials*, 23(9):1137–1146, 2013.

[105] Drotlef Dirk M. *et al.* Morphological studies of the toe pads of the rock frog, staurois parvus (family: Ranidae) and their relevance to the development of new biomimetically inspired reversible adhesives. *Interface Focus*, 5(1), 2015.

[106] Valerie V. Ernst. The digital pads of the tree frog, hyla cinerea. i. the epidermis. *Tissue and Cell*, 5(1):83–96, 1973.

[107] Pho Van Nguyen and Van Anh Ho. Mechanics of wet adhesion in soft interaction with patterned morphology. *Bioinspiration & Biomimetics*, 14(1), nov 2018.

[108] P. Van Nguyen, N. Van Huynh, T. T. Phan, and V. A. Ho. Soft grasping with wet adhesion: Preliminary evaluation. *2018 IEEE International Conference on Soft Robotics (RoboSoft)*, 2018.

[109] Crawford Niall, Thomas Endlein, and Barnes W. Jon P. Self-cleaning in tree frog toe pads; a mechanism for recovering from contamination without the need for grooming. *Journal of Experimental Biology*, 215(22):3965–3972, 2012.

[110] Endlein Thomas *et al.* The use of clamping grips and friction pads by tree frogs for climbing curved surfaces. *Proceedings of the Royal Society B: Biological Sciences*, 284(1849), 2017.

[111] Hill Iain D. C., Dong Benzheng, Barnes W. Jon P., Ji Aihong, and Endlein Thomas. The biomechanics of tree frogs climbing curved surfaces: a gripping problem. *Journal of Experimental Biology*, 221(5), 2018.

[112] Manzano Adriana S., Abdala Virginia, and Herrel Anthony. Morphology and function of the forelimb in arboreal frogs: specializations for grasping ability? *Journal of Anatomy*, 213(3):296–307, 2008.

[113] Koch Kerstin, Bhushan Bharat, and Barthlott Wilhelm. Diversity of structure, morphology and wetting of plant surfaces. *Soft Matter*, 4:1943–1963, 2008.

[114] Holgate M. W. The wetting of insect cuticles by water. *Journal of Experimental Biology*, 32(3):591–617, 1955.

[115] Julian FV Vincent and Ulrike G. KWegst. Design and mechanical properties of insect cuticle. *Arthropod Structure & Development*, 33(3):187–199, 2004.

[116] K.D. Wells. *The ecology & behaviour of amphibians*. The University of Chicago Press, Chicago, US, 2007.

[117] Drechsler P.H. *Mechanics of adhesion and friction in stick insects and tree frogs*. PhD thesis, Julius-Maximilians-Universität Würzburg, Würzburg, Germany, 2008.

[118] Julian K A Langowski *et al.* Estimating the maximum attachment performance of tree frogs on rough substrates. *Bioinspiration & Biomimetics*, 14(2):025001, 2019.

[119] Peter van Assenbergh *et al.* Pull-off and friction forces of micropatterned elastomers on soft substrates: the effects of pattern length scale and stiffness. *Beilstein Journal of Nanotechnology*, 10:79–94, 2019.

[120] Langowski J. *et al.* Tree frog attachment: mechanisms, challenges, and perspectives. *Front Zool*, 15(32), 2018.

[121] Liu Quan *et al.* Tree frog-inspired micropillar array with nanopits on the surface for enhanced adhesion under wet conditions. *ACS Applied Materials & Interfaces*, 0(ja):null, 2020.

[122] L. *et al* Xue. Humidity-enhanced wet adhesion on insect-inspired fibrillar adhesive pads. *Nat Commun*, 6(6621), 2015.

[123] Xue Longjian *et al.* Hybrid surface patterns mimicking the design of the adhesive toe pad of tree frog. *ACS Nano*, 11(10):9711–9719, 2017.

[124] Meng F. *et al.* Tree frog adhesion biomimetics: Opportunities for the development of new, smart adhesives that adhere under wet conditions. *Philosophical Transactions of the Royal Society A: Mathematical, Physical and Engineering Sciences*, 377(2150), 2019.

[125] Ling Gong, Haiwu Yu, Xuan Wu, and Xiaojie Wang. Wet-adhesion properties of microstructured surfaces inspired by newt footpads. *Smart Materials and Structures*, 27(11), 2018.

[126] Meng Li, Jun Xie, Qingwen Dai, Wei Huang, and Xiaolei Wang. Effect of wetting case and softness on adhesion of bioinspired micropatterned surfaces. *Journal of the Mechanical Behavior of Biomedical Materials*, 78:266–272, 2018.

[127] Varenberg Michael and Gorb Stanislav N. Hexagonal surface micropattern for dry and wet friction. *Advanced Materials*, 21(4):483–486, 2009.

[128] Iturri Jagoba *et al.* Torrent frog-inspired adhesives: Attachment to flooded surfaces. *Advanced Functional Materials*, 25(10):1499–1505, 2015.

[129] K. Mizushima, T. Nishimura, Y. Suzuki, T. Tsuji, and T. Watanabe. Surface texture of deformable robotic fingertips for a stable grasp under both dry and wet conditions. *IEEE Robotics and Automation Letters*, 2(4):2048–2055, 2017.

[130] B. He, Z. Wang, M. Li, K. Wang, R. Shen, and S. Hu. Wet adhesion inspired bionic climbing robot. *IEEE/ASME Transactions on Mechatronics*, 19(1):312–320, 2014.

[131] J. C. Norton, J. Boyle, A. Alazmani, P. Culmer, and A. Neville. Macro-scale tread patterns for traction in the intestine. *IEEE Transactions on Biomedical Engineering*, 2020.

[132] Chen Huawei, Zhang Liwen, Zhang Deyuan, Zhang Pengfei, and Han Zhiwu. Bioinspired surface for surgical graspers based on the strong wet friction of tree frog toe pads. *ACS Applied Materials & Interfaces*, 7(25):13987–13995, 2015.

[133] Hans-Jürgen Butt and Michael Kappl. *Surface and Interfacial Forces*. John Wiley & Sons, Ltd, 2010.

[134] George Wypych. *Handbook of Adhesion Promoters*. ChemTec Publishing, 2018.

[135] Kaveh F. *Wet Bioadhesion of Tree Frogs*. PhD thesis, Johannes Gutenberg-Universität, Germany, 2014.

[136] Petr Klapetek. *Quantitative Data Processing in Scanning Probe Microscopy. SPM Applications for Nanometrology*. William Andrew,, 2012.

[137] Duane Roller and Roller D.H.D. *The development of the concept of electric charge: Electricity from the Greeks to Coulomb*. Cambridge, Harvard University Press, 1954.

[138] Subhash Mahajan. *Encyclopedia of Materials: Science and Technology*. Pergamon, 2001.

[139] A.A. Abrikosov, L.P. Gorkov, and I.E. Dzyaloshinsky. *Methods of Quantum Field Theory in Statistical Physics*. Pergamon Press, 1965.

[140] Peter Atkins and Julio de Paula. *Physical Chemistry for the Life Sciences*. Oxford University Press, 2011.

[141] Martin Silberberg. *Principles of General Chemistry*. McGraw-Hill Education, 2012.

[142] Keesom W. H. The second virial coefficient for rigid spherical molecules whose mutual attraction is equivalent to that of a quadruplet placed at its center. *Proceedings of the Royal Netherlands Academy of Arts and Sciences*, 18:636–646, 1915.

[143] Leite F.L. *et al.* Theoretical models for surface forces and adhesion and their measurement using atomic force microscopy. *Int. J. Mol. Sci.*, 13:12773–12856, 2012.

[144] Rosenkrans J. P., Linder B., and Kromhout R. A. Two-temperature van der waals potentials. *The Journal of Chemical Physics*, 49(7):2927–2933, 1968.

[145] F. London. The general theory of molecular forces. *Trans. Faraday Soc.*, 33, 1937.

[146] Autumn Kellar and Peattie Anne M. Mechanisms of Adhesion in Geckos1. *Integrative and Comparative Biology*, 42(6):1081–1090, 2002.

[147] Loskill *et al.* Macroscale adhesion of gecko setae reflects nanoscale differences in subsurface composition. *Journal of The Royal Society Interface*, 10(78), 2013.

[148] Daniel Soto, Ginel Hill, Aaron Parness, Noé Esparza, Mark Cutkosky, and Tom Kenny. Effect of fibril shape on adhesive properties. *Applied Physics Letters*, 97(5), 2010.

[149] Kim Seok and Sitti Metin. Biologically inspired polymer microfibers with spatulate tips as repeatable fibrillar adhesives. *Applied Physics Letters*, 89(26), 2006.

[150] Emerson Sharon B. and Dielh Diana. Toe pad morphology and mechanisms of sticking in frogs. *Biological Journal of the Linnean Society*, 13(3):199–216, 2008.

[151] J. Mahanty and B. W. Ninham. *Dispersion Forces.* Academic Press, New York.

[152] Hans-Jürgen Butt, Karlheinz Graf, and Michael Kappl. *Physics and Chemistry of Interfaces.* Wiley-VCH, 2003.

[153] H. C. Hamaker. The london-van der Waals attraction between spherical particles. *Physica*, 4:1058–1072, 1937.

[154] Douglas Henderson, Der-Ming Duh, Xiaolin Chu, and Darsh Wasan. An expression for the dispersion force between colloidal particles. *Journal of Colloid and Interface Science*, 185(1):265 – 268, 1997.

[155] Robert J. Hunter. *Foundations of Colloid Science.* Oxford University Press, 2001.

[156] I.E. Dzyaloshinskii, E.M. Lifshitz, and L.P. Pitaevskii. The general theory of van der waals forces. *Advances in Physics*, 10(38):165–209, 1961.

[157] Jacob N. Israelachvili. Van der waals forces in biological systems. *Quarterly Reviews of Biophysics*, 6(4):341–387, 1973.

[158] L.B. Boinovich. The forces determining the stability of thin wetting films of solutions with nonpolar solvent. *Advances in Colloid and Interface Science*, 37(3):177 – 193, 1992.

[159] Umar Mohideen Michael Bordag, Galina Leonidovna Klimchitskaya and Vladimir Mikhaylovich Mostepanenko. *Advances in the Casimir Effect*. Oxford University Press, 2009.

[160] Sung Nae Cho. *Casimir Force in Non-Planar Geometric Configurations*. PhD thesis, Virginia Polytechnic Institute and State University, 2004.

[161] Evans DF and Wennerstrom H. *he colloidal domain*. Wiley-VCH, New York, second edition, 1999.

[162] Verwey E. J. W. Theory of the stability of lyophobic colloids. *The Journal of Physical and Colloid Chemistry*, 51(3):631–636, 1947.

[163] Donald H. Napper. *Polymeric Stabilization of Colloidal Dispersions*.

[164] Grasso D. *et al*. A review of non-dlvo interactions in environmental colloidal systems. *Reviews in Environmental Science and Biotechnology*, 1(2):17–38, 2002.

[165] Hugo K. Christenson. Non-dlvo forces between surfaces -solvation, hydration and capillary effects. *Journal of Dispersion Science and Technology*, 9(2):171–206, 1988.

[166] A. D. McNaught and A. Wilkinson. *Compendium of Chemical Terminology*. Blackwell Scientific Publications, Oxford, 1997.

[167] Arieh Ben-Naim. *Hydrophobic Interactions*. Springer, US, 1980.

[168] K. W. Allen. *Encyclopedia of Physical Science and Technology - Materials*. Elsevier, 2001.

[169] Young Thomas. An essay on the cohesion of fluids. *Philosophical Transactions of the Royal Society of London*, 95:65–87, 1805.

[170] Marko Popovic. *Biomechatronics*. Academic Press, 2019.

[171] Fuji Masayoshi, Machida Kotoe, Takei Takashi, Watanabe Tohru, and Chikazawa Masatoshi. Effect of wettability on adhesion force between silica particles evaluated by atomic force microscopy measurement as a function of relative humidity. *Langmuir*, 15(13):4584–4589, 1999.

[172] Guoping Lian and Jonathan Seville. The capillary bridge between two spheres: New closed-form equations in a two century old problem. *Advances in Colloid and Interface Science*, 227:53 – 62, 2016.

[173] K.P. Galvin. A conceptually simple derivation of the kelvin equation. *Chemical Engineering Science*, 60(16):4659 – 4660, 2005.

[174] Zhang Shi, Yi Zhang, Mingchao Liu, Dorian A.H. Hanaor, and Yixiang Gan. Dynamic contact angle hysteresis in liquid bridges. *Colloids and Surfaces A: Physicochemical and Engineering Aspects*, 555:365 – 371, 2018.

[175] Malcolm E. Schrader. Young-dupre revisited. *Langmuir*, 11(9):3585–3589, 1995.

[176] Jacob Israelachvili. *Intermolecular and Surface Forces*. Academic Press, 2011.

[177] Hans-Jürgen Butt and Michael Kappl. Normal capillary forces. *Advances in Colloid and Interface Science*, 146(1):48 – 60, 2009.

[178] Jan-Henning Dirks. Physical principles of fluid-mediated insect attachment - shouldn't insects slip? *Beilstein Journal of Nanotechnology*, 5:1160–1166, 2014.

[179] Halsey Thomas C. and Levine Alex J. How sandcastles fall. *Phys. Rev. Lett.*, 80:3141–3144, 1998.

[180] Bocquet L. *et al.* Moisture-induced ageing in granular media and the kinetics of capillary condensation. *Nature*, 396(3):735–737, 1998.

[181] Cai Shaobiao and Bhushan Bharat. Meniscus and viscous forces during separation of hydrophilic and hydrophobic smooth/rough surfaces with symmetric and asymmetric contact angles. *Philosophical Transactions of the Royal Society A: Mathematical, Physical and Engineering Sciences*, 366(1870):1627–1647, 2008.

[182] P. Kralchevsky and K. Nagayama. *Particles at Fluid Interfaces and Membranes*. Elsevier Science, 2001.

[183] Adam Neil Kensington. *The Physics and Chemistry of Surfaces*. Oxford University Press, 1941.

[184] De Souza E. J., Brinkmann M., Mohrdieck C., Crosby A., and Arzt E. Capillary forces between chemically different substrates. *Langmuir*, 24(18):10161–10168, 2008.

[185] De Souza E. J., Gao L., McCarthy T. J., Arzt E., and Crosby A. J. Effect of contact angle hysteresis on the measurement of capillary forces. *Langmuir*, 24(4):1391–1396, 2008.

[186] Warren J. Jasper and Nadish Anand. A generalized variational approach for predicting contact angles of sessile nano-droplets on both flat and curved surfaces. *Journal of Molecular Liquids*, 281:196 – 203, 2019.

[187] Warren J. Jasper and Srinivasan Rasipuram. Relationship between contact angle and contact line radius for micro to atto [106 to 1018] liter size oil droplets. *Journal of Molecular Liquids*, 248:920 – 926, 2017.

[188] Bruce M. Law *et al.* Line tension and its influence on droplets and particles at surfaces. *Progress in Surface Science*, 92(1):1 – 39, 2017.

[189] J.C. Walraven. *Aggregate interlock: A theoretical and experimental analysis*. PhD thesis, Delft University Press, 1980.

[190] Shaobiao Cai and Bharat Bhushan. Meniscus and viscous forces during normal separation of liquid-mediated contacts. *Nanotechnology*, 18(46):465704, 2007.

[191] M Resch and R Scheidl. A model for fluid stiction of quickly separating circular plates. *Proceedings of the Institution of Mechanical Engineers, Part C: Journal of Mechanical Engineering Science*, 228(9):1540–1556, 2014.

[192] Labonte David and Federle Walter. Scaling and biomechanics of surface attachment in climbing animals. *Philosophical Transactions of the Royal Society B: Biological Sciences*, 370(1661), 2015.

[193] Maeda Nobuo, Israelachvili Jacob N., and Kohonen Mika M. Evaporation and instabilities of microscopic capillary bridges. *Proceedings of the National Academy of Sciences*, 100(3):803–808, 2003.

[194] de Lazzer A., Dreyer M., and Rath H. J. Particlesurface capillary forces. *Langmuir*, 15(13):4551–4559, 1999.

[195] Xue Xiaojie and Polycarpou Andreas A. Meniscus model for noncontacting and contacting sphere-on-flat surfaces including elastic-plastic deformation. *Journal of Applied Physics*, 103(2), 2008.

[196] Jin Qian, Ji Lin, and Mingxing Shi. Combined dry and wet adhesion between a particle and an elastic substrate. *Journal of Colloid and Interface Science*, 483:321 – 333, 2016.

[197] Valentin L. Popov. *Contact Mechanics and Friction Physical Principles and Applications*. Springer, Verlag Berlin Heidelberg, 2010.

[198] Carbone G. and Bottiglione F. Contact mechanics of rough surfaces: a comparison between theories. *International Journal of Solids and Structures*, 51(25):557–565, 2011.

[199] Boris Lorenz. *Contact Mechanics and Friction of Elastic Solids on Hard and Rough Substrates*. PhD thesis, Forschungszentrum Jülich GmbH, 2012.

[200] Johnson Kenneth Langstreth, Kendall Kevin, Roberts A. D., and Tabor David. Surface energy and the contact of elastic solids. *Proceedings of the Royal Society of London. A. Mathematical and Physical Sciences*, 324(1558):301–313, 1971.

[201] Ciavarella M., J. Joe, Papangelo A., and Barber J. R. The role of adhesion in contact mechanics. *Journal of The Royal Society Interface*, 16(151), 2019.

[202] Greenwood J. A., Williamson J. B. P., and Bowden Frank Philip. Contact of nominally flat surfaces. *Proceedings of the Royal Society of London. Series A. Mathematical and Physical Sciences*, 295(1442):300–319, 1966.

[203] Fuller K. N. G. and Tabor David. The effect of surface roughness on the adhesion of elastic solids. *Proceedings of the Royal Society of London. A. Mathematical and Physical Sciences*, 345(1642):327–342, 1975.

[204] G. Carbone and F. Bottiglione. Asperity contact theories: Do they predict linearity between contact area and load? *Journal of the Mechanics and Physics of Solids*, 56(8):2555 – 2572, 2008.

[205] Giuseppe Carbone. A slightly corrected greenwood and williamson model predicts asymptotic linearity between contact area and load. *Journal of the Mechanics and Physics of Solids*, 57(7):1093 – 1102, 2009.

[206] B. N. J. Persson. Theory of rubber friction and contact mechanics. *The Journal of Chemical Physics*, 115(8):3840–3861, 2001.

[207] B.N.J. Persson. Contact mechanics for randomly rough surfaces. *Surface Science Reports*, 61(4):201 – 227, 2006.

[208] Ho Anh-Van and Hirai Shinichi. *Mechanics of Localized Slippage in Tactile Sensing And Application to Soft Sensing Systems*. Springer, 2014.

[209] Gao Jianping *et al.* Frictional forces and amontons' law: From the molecular to the macroscopic scale. *The Journal of Physical Chemistry B*, 108(11):3410–3425, 2004.

[210] Yu *et al.* Friction and adhesion of gecko-inspired pdms flaps on rough surfaces. *Langmuir*, 28(31):11527–11534, 2012.

[211] Douglas-Hamilton *et al.* Particle distribution in low-volume capillary-loaded chambers. *Journal of Andrology*, 26(1):107–114, 2005.

[212] A del Campo and C Greiner. Su-8: a photoresist for high-aspect-ratio and 3d submicron lithography. *Journal of Micromechanics and Microengineering*, 17(6):81–95, 2007.

[213] M. Lajvardi, H. Eshghi, M.E. Ghazi, M. Izadifard, and A. Goodarzi. Structural and optical properties of silicon nanowires synthesized by ag-assisted chemical etching. *Materials Science in Semiconductor Processing*, 40:556 – 563, 2015.

[214] Kim Jungkil, Kim Young Heon, Choi Suk-Ho, and Lee Woo. Curved silicon nanowires with ribbon-like cross sections by metal-assisted chemical etching. *ACS Nano*, 5(6):5242–5248, 2011.

[215] Lin L. *et al.* Synthesis and photoluminescence properties of porous silicon nanowire arrays. *Nanoscale Res Lett*, 5(1822), 2010.

[216] Permittivity. `https://en.wikipedia.org/wiki/Relative_permittivity`.

[217] Optical liquid silicon rubber (lsr). `https://www.simtec-silicone.com/optical-liquid-silicone-rubber/`.

[218] Refractive index. `https://en.wikipedia.org/wiki/Refractive_index`.

[219] Refractive index of polymers by index. `https://scientificpolymer.com/technical-library/refractive-index-of-polymers-by-index/`.

[220] Extrand C. W. and Moon Sung In. Contact angles on spherical surfaces. *Langmuir*, 24(17):9470–9473, 2008.

[221] Schay Geza and Peter Szor. Stress-Strain Relation in Rubber Blocks under Compression. I. *Rubber Chemistry and Technology*, 32(2):409–419, 1959.

[222] Jong Beom Suh and S. Graham Kelly. Stress response of a rubber block under vertical loading. *Journal of Engineering Mechanics*, 138(7):770–783, 2012.

[223] Strutture aeronautiche: Shells with membrane behavior, ch. 3, 2017. `http://web.archive.org/web/20080207010024/http://www.808multimedia.com/winnt/kernel.htm`.

[224] C. R. Calladine. *Theory of Shell Structures*. Cambridge University Press, 2007.

[225] F M S Lima. Using surface integrals for checking archimedes law of buoyancy. *European Journal of Physics*, 33(1):101–113, 2011.

[226] Blevins Robert D. *Applied Fluid Dynamics Handbook*. Krieger Publishing Co, 2003.

[227] Atul Tiwari and Mark D. Soucek. *Concise Encyclopedia of High Performance Silicones*. Krieger Publishing Co, 2014.

[228] Yongqiang Cheng, Naoto Shimizu, and Toshinori Kimura. The viscoelastic properties of soybean curd (tofu) as affected by soymilk concentration and type of coagulant. *International Journal of Food Science & Technology*, 40(4):385–390, 2005.

[229] Danton G. L. *Engineering viscoelasticity*. Springer US, 2014.

[230] S. Yanniotis, S. Skaltsi, and S. Karaburnioti. Effect of moisture content on the viscosity of honey at different temperatures. *Journal of Food Engineering*, 72(4):372 – 377, 2006.

[231] Julian K A Langowski, Dimitra Dodou, Peter van Assenbergh, and Johan L van Leeuwen. Design of tree-frog-inspired adhesives. *Integrative and Comparative Biology*, 2020.

[232] J. *et al* Li. Mechanisms underlying the biological wet adhesion: Coupled effects of interstitial liquid and contact geometry. *J Bionic Eng*, 17:448–456, 2020.

[233] M. Li, D. Melville, E. Chung, and H. Stuart. Milliscale features increase friction of soft skin in lubricated contact. *IEEE Robotics and Automation Letters*, 2020.